

*The structure of binary molten salt mixtures :
a neutron diffraction study*

Thesis submitted for the degree of Doctor of Philosophy at the University of
Leicester

by

Yaspal Singh Badyal
Physics & Astronomy department
University of Leicester

Submitted December, 1994

UMI Number: U072802

All rights reserved

INFORMATION TO ALL USERS

The quality of this reproduction is dependent upon the quality of the copy submitted.

In the unlikely event that the author did not send a complete manuscript and there are missing pages, these will be noted. Also, if material had to be removed, a note will indicate the deletion.



UMI U072802

Published by ProQuest LLC 2015. Copyright in the Dissertation held by the Author.
Microform Edition © ProQuest LLC.

All rights reserved. This work is protected against
unauthorized copying under Title 17, United States Code.



ProQuest LLC
789 East Eisenhower Parkway
P.O. Box 1346
Ann Arbor, MI 48106-1346



For Reena and Harkirat

"They are ill discoverers that think there is no land,
when they can see nothing but sea."

Francis Bacon *The Advancement of Learning*

"Discovery consists of seeing what everybody has seen and thinking
what nobody has thought."

Albert Szent-Gyorgi *The Scientist Speculates* (1962)

Contents

	Page
Thesis abstract	vi
Acknowledgements	vii
List of tables	viii
List of figures	ix
List of abbreviations	xi
Chapter 1. Introduction	
1.1 Background to the study of molten salt mixtures	1
1.1.1 Review of structural studies to date	2
1.1.2 The first sharp diffraction peak and intermediate range order	4
1.2 Overview of thesis contents	5
1.3 References	7
Chapter 2. Theory	
2.1 Introduction - describing liquid structure	8
2.2 Theoretical background to neutron diffraction	9
2.2.1 The differential scattering cross-section	9
2.2.2 Coherent and incoherent scattering and the static structure factor $S(Q)$	10
2.2.3 The Fourier transform relationship between $S(Q)$ and $g(r)$	12
2.2.4 The static approximation and $S(Q)$	13
2.2.5 Scattering from multicomponent liquids	15
2.3 Theoretical models of liquid structure	18
2.3.1 Introduction	18
2.3.2 Integral equations for the pair distribution function	20
2.3.3 Computer modelling	22
2.4 References	25
Figures	

Chapter 3. Experimental Method

3.1 Introduction	26
3.2 Sample preparation	27
3.2.1 Preparing the pure salts	27
3.2.2 Preparing the mixtures	29
3.3 The neutron diffraction experiment	30
3.3.1 Conducting the experiment	30
3.3.2 The LAD instrument	32
3.3.3 The SANDALS instrument	33
3.4 References	35
Tables	
Figures	

Chapter 4. Data analysis

4.1 Introduction	36
4.2 General procedure for the analysis of TOF data	36
4.2.1 Correction for counter deadtime and normalising to the incident neutron spectrum	36
4.2.2 Measuring the wavelength-dependent total cross-section	37
4.2.3 Corrections for multiple scattering	38
4.2.4 Corrections for attenuation	38
4.2.5 Smoothing the vanadium scattering	39
4.2.6 Calculating the differential cross-section	39
4.2.7 Inelasticity (Placzek) corrections	40
4.2.8 Merging the data	40
4.2.9 Fourier transformation : $F(Q) \Rightarrow G(r)$	41
4.2.10 Checks on $F(Q)$ and $G(r)$	42
4.3 Analysis of LAD data	43
4.4 Analysis of SANDALS data	45
4.5 References	48

Tables

Figures

Chapter 5. The reverse Monte Carlo method

5.1 Introduction - modelling disordered structures	49
5.2 The basic RMC method	50
5.2.1 The RMC algorithm	50
5.2.2 The role of physical constraints in RMC modelling	55
5.2.3 The nature of RMC models	56
5.2.4 Summary of the RMC method	57
5.3 Application of the RMC method	59
5.3.1 Details of RMC modelling	59
5.3.2 The effects of systematic errors - reasons for not achieving fits	61
5.3.3 Characterising the RMC solution structure	63
5.4 References	65

Figures

Chapter 6. Structural modification in molten divalent metal chloride and alkali chloride mixtures

Abstract

6.1 Introduction	66
6.2 Experimental details	68
6.3 Discussion	69
6.3.1 The structure of pure NiCl ₂	69
6.3.2 The structure of molten NiCl ₂ -LiCl and ZnCl ₂ -LiCl	71
6.3.3 Structural modification in NiCl ₂ -KCl	73
6.3.4 The effect of the alkali cation on intermediate range order	76
6.4 Summary	77
6.5 References	78

Tables

Figures

Chapter 7. Isotopic substitution study of NiCl₂-KCl and ZnCl₂-KCl binary molten salt mixtures

Abstract

7.1 Introduction	79
7.2 Experimental details	81
7.3 Discussion	82
7.3.1 The structure of molten NiCl ₂ -KCl	82
7.3.2 The structure of molten ZnCl ₂ -KCl	87
7.3.3 The structures of the pure ZnCl ₂ and NiCl ₂ melts	90
7.4 Summary	91
7.5 References	93

Tables

Figures

Chapter 8. The structure of liquid AlCl₃ and structural modification in AlCl₃-MCl (M=Li,Na) molten salt mixtures

Abstract

8.1 Introduction	94
8.2 Experimental details	96
8.3 Discussion	97
8.3.1 The structure of pure liquid AlCl ₃	97
8.3.2 Structural modification in the mixtures	104
8.3.3 Intermediate range order	107
8.4 Concluding remarks	109
8.5 References	111

Tables

Figures

Chapter 9. Summary and further work

9.1 Summary of main research findings	113
---------------------------------------	-----

9.2	Further work : charge-ordered structures in molten salts	114
9.2.1	Structural modification in divalent metal chloride-alkali halide melts	114
9.2.2	Structural modification in chloro-aluminate melts	115
9.2.3	Trivalent metal halides and their mixtures	116
9.2.4	Thermodynamic-related studies	117
9.2.5	Quasi-elastic and inelastic studies	118
9.3	Concluding remarks	119
9.4	References	121
 Appendices		
A1	Calculating the differential cross-section : case I	122
A2	Calculating the differential cross-section : case II	123

The structure of binary molten salt mixtures :
a neutron diffraction study

by

Yaspal Singh Badyal

Abstract

Structural modification in a series of polyvalent metal chloride - alkali chloride binary molten salt mixtures has been investigated using the pulsed neutron diffraction technique. Structure factors have been measured for $\text{NiCl}_2\text{-KCl}$, $\text{NiCl}_2\text{-LiCl}$ and $\text{ZnCl}_2\text{-LiCl}$ samples spanning the entire composition range. The key finding was that the degree of structural modification is dependent on the relative size and polarising power of the two cation species. The mixtures of NiCl_2 and ZnCl_2 with LiCl largely appear to be admixtures of the two pure salt structures, whereas adding KCl to NiCl_2 results in a better ordered, more regularly tetrahedral local structure around the metal cation and enhancement of the first sharp diffraction peak (FSDP). A simple model involving charge ordering of discrete tetrahedral units by alkali counter-ions is proposed as an explanation for the enhanced intermediate range order.

In order to identify some of the partial structure factor contributions to the enhanced FSDP, the scattering was measured for three isotopically-enriched $\text{NiCl}_2+2\text{KCl}$ samples. A complementary isotopic substitution experiment was performed on three $\text{ZnCl}_2+2\text{KCl}$ samples. The results generally confirm the findings of the composition study, with a strong similarity between the two molten salt systems also being evident. In addition, RMC modelling supports the proposed model for intermediate range order in the mixtures.

Structure factors were also measured for $\text{AlCl}_3\text{-LiCl}$ and $\text{AlCl}_3\text{-NaCl}$ samples covering the entire composition range. Several features consistent with strong charge ordering of discrete tetrahedral units by alkali counter-ions were identified. In addition, RMC modelling of the data for pure AlCl_3 strongly challenges the 'established' view of the structure and an alternative 'sparse network liquid' model is proposed which emphasises the similarity to ZnCl_2 .

Acknowledgements

I would like to thank the following.

- i) Dr R.A. Howe for his guidance and inspiration throughout the course of my doctoral research.
- ii) Dr D.A. Allen for providing technical instruction, especially at the start of my Ph.D, in sample preparation and the collection and analysis of neutron diffraction data.
- iii) The isotope preparation unit at the H.H. Wills laboratory (University of Bristol), in particular Dr H. Tromp, for the preparation of isotopically-enriched samples and checks of isotopic composition using mass spectrometry.
- iv) The scientific and technical staff at Rutherford ISIS, especially Dr W.S. Howells and Dr A.K. Soper, for their assistance in performing experiments and helpful discussions on experimental technique and data analysis.
- v) Dr R.L. McGreevy, M.A. Howe and J.D. Wicks for providing the RMC software and prompt responses to my stream of questions and requests.
- vi) The technical staff at the Physics department (University of Leicester), in particular Mr S. Thornton, for their general technical advice and assistance. I would also like to thank Mr R. Batchen for providing glass-working services and instruction.
- vii) My colleagues, especially Dr S. Baker, Mr S. Thornton and Mr B.T. Williams, for patiently listening to my research ideas.
- viii) The SERC for awarding me a studentship to carry out this work.

Last, but not least, I am indebted to my wife, Harkirat, and daughter, Reena, for their support and understanding during my late nights and long weekends away from them - this thesis is dedicated to them.

List of tables

- 3.1 Details of the vacuum drying procedure for the single salts.
- 3.2 Details of the preparation of the mixtures.
- 3.3 The design and actual complement of detectors on ISIS SANDALS.

- 4.1 Typical Q ranges and renormalisation factors for LAD detector groups.
- 4.2 Typical Q ranges and renormalisation factors for SANDALS groups.

- 6.1 Data analysis parameters used for the pure salts.
- 6.2 Comparison of real-space structural parameters for NiCl_2 and ZnCl_2 .
- 6.3 Structural parameters for the estimated $g_{\text{Ni-Cl}}(r)$ partials.
- 6.4 Structural parameters for $g_{\text{Ni-Cl}}(r)$ after taking $g_{\text{K-Cl}}(r)$ into account.
- 6.5 The r_{--}/r_{+-} ratios in $G(r)$ for the NiCl_2 -KCl mixtures.

- 7.1 Coherent scattering lengths for the isotopic enrichments.
- 7.2 Comparison of ion sizes for NiCl_2 and ZnCl_2 .
- 7.3 Next nearest neighbour coordinations of Ni^{2+} .
- 7.4 Results of bond network analysis.

- 8.1 Data analysis parameters for the pure salts.
- 8.2 Parameters for the Al_2Cl_6 molecular structure.
- 8.3 Comparison of the results of bond network analysis for RMC models I and II.
- 8.4 Structural parameters for the Al-Cl principal peak in real space.
- 8.5 Best-fit weightings of the Cl-Cl pure salt partial structures.
- 8.6 The systematic shift in position of the FSDP.

List of figures

- 2.1 The process of neutron scattering from a single static nucleus.

- 3.1 The sublimation-drying kit used in preparation of AlCl_3 .
- 3.2 Comparison of the vapour pressures of solid AlCl_3 and ice I.
- 3.3 Diagram of the ISIS LAD instrument.
- 3.4 Diagram of the ISIS SANDALS instrument.

- 4.1 Flow diagram of the main steps in TOF data analysis.
- 4.2 Numerical method used to calculate attenuation coefficients.
- 4.3 High- Q droop on DCS data covering the 5° - 35° LAD detector banks.
- 4.4 Comparison of normalised counts for sample, furnace etc. (SANDALS).
- 4.5 Diagram of basic furnace geometry.
- 4.6 Structure factors (liquid AlCl_3) compared for SANDALS groups 1-6.

- 5.1 The effects of varying composition on RMC modelling.

- 6.1 Comparison of total structure factors for pure NiCl_2 .
- 6.2 Total structure factors for molten NiCl_2 - LiCl mixtures.
- 6.3 Total pair distribution functions for molten NiCl_2 - LiCl mixtures.
- 6.4 Comparison of ZnCl_2 - LiCl structure factors with model $F(Q)$.
- 6.5 Comparison of ZnCl_2 - LiCl pair distributions with model $G(r)$.
- 6.6 Normalised principal peak height as a function of alkali halide concentration for NiCl_2 - LiCl and ZnCl_2 - LiCl mixtures.
- 6.7 Anion-anion peak position as a function of alkali halide Cl-Cl partial weighting.
- 6.8 Estimated $S_{\text{Ni-Ni}}(Q)$ contribution to FSDP as a function of alkali halide concentration.
- 6.9 Total structure factors for the molten NiCl_2 - KCl mixtures.
- 6.10 Total pair distribution functions for molten NiCl_2 - KCl mixtures.

- 7.1 $F(Q)$ data for isotopically-enriched NiCl_2 - KCl samples compared to the RMC fits.
- 7.2 $G(r)$ data for isotopically-enriched NiCl_2 - KCl samples compared to the RMC fits.
- 7.3 Direct first- and second-order differences compared to RMC solutions.
- 7.4 Real-space comparison of direct differences and the RMC solutions.
- 7.5 RMC partial structure factors for NiCl_2 - KCl and pure NiCl_2 compared.
- 7.6 RMC pair distribution functions for Ni-Ni and Ni-K.

- 7.7 Bond angle distributions pertaining to intermediate range order.
- 7.8 Illustration of likely effect of K^+ ions on linked tetrahedral units.
- 7.9 Ni-Cl radial distribution functions for $NiCl_2$ -KCl and pure $NiCl_2$.
- 7.10 'Slice' through a typical RMC model-F equilibrium configuration.
- 7.11 RMC Coordination number and bond angle distributions relevant to local structure.
- 7.12 RMC Coordination number and bond angle distributions relevant to the anion structure.
- 7.13 Total structure factors for isotopically-enriched $ZnCl_2$ -KCl samples.
- 7.14 Total pair distribution functions for the isotopic $ZnCl_2$ -KCl samples.
- 7.15 RMC partial structure factors for $ZnCl_2$ -KCl and pure $ZnCl_2$ compared.

- 8.1 Total structure factor data for pure liquid $AlCl_3$.
- 8.2 Total pair distributions corresponding to figure 8.1.
- 8.3 Comparison of RDFs for $g_{Al-Cl}^{AlCl_3}(r)$ and $g_{Zn-Cl}^{ZnCl_2}(r)$.
- 8.4 Al_2Cl_6 molecular structure of liquid $AlCl_3$.
- 8.5 RDF from neutron data for liquid $AlCl_3$ compared to earlier X-ray data.
- 8.6 Raman spectra of GaI_3 , $GaBr_3$, $AlBr_3$ and $AlCl_3$.
- 8.7 $F(Q)$ data for liquid $AlCl_3$ compared with the RMC fits.
- 8.8 $G(r)$ data for liquid $AlCl_3$ compared with the RMC fits.
- 8.9 Bond angle distributions relevant to local structure.
- 8.10 Coordination number distribution of anions around Al^{3+} .
- 8.11 'Slice' through RMC model-I configuration for liquid $AlCl_3$.
- 8.12 Bond angle distributions relevant to the wider $AlCl_3$ structure.
- 8.13 'Slice' through RMC model-II configuration.
- 8.14 $F(Q)$ data for $AlCl_3$ -LiCl molten salt mixtures.
- 8.15 $G(r)$ data for $AlCl_3$ -LiCl molten salt mixtures.
- 8.16 $F(Q)$ data for $AlCl_3$ -NaCl molten salt mixtures.
- 8.17 $G(r)$ data for $AlCl_3$ -NaCl molten salt mixtures.
- 8.18 High- r regions of $G(r)$ data for 50% LiCl, and 45% NaCl mixtures.
- 8.19 Charge ordering of neighbouring $AlCl_4^-$ tetrahedra by Li^+ cation.

List of common abbreviations

ANS	Anomalous neutron scattering
AXS	Anomalous X-ray scattering
DCS	Differential scattering cross-section
EXAFS	Extended X-ray absorption fine structure
FSDP	First sharp diffraction peak
FWHM	Full-width half maximum
F-Z	Faber-Ziman
HNC	Hypernetted Chain
HSPY	Hard-sphere Percus-Yevick
IRO	Intermediate range order
LAD	Liquids and amorphous materials diffractometer
MD	Molecular dynamics
MEM	Maximum Entropy method
MMC	Metropolis Monte Carlo
MSA	Mean spherical approximation
PY	Percus-Yevick
PSF	Partial structure factor
RMC	Reverse Monte Carlo
SANDALS	Small angle neutron diffraction for amorphous and liquid samples
TOF	Time-of-flight
YBG	Yvon,Born,Green

Chapter 1

Introduction

1.1 Background to the study of molten salt mixtures

In contrast to the large number of structural studies which have been undertaken on pure molten salts, comparatively little work has been done on molten salt mixtures. This is despite the fact that molten salt mixtures often exhibit attractive properties such as low-temperature eutectics of possible relevance to energy storage and other commercial applications¹. The relatively low-melting mixtures of aluminium chloride with alkali chlorides, which are the subject of chapter 8, form a particularly good case in point. Such molten salt mixtures are also of interest because they are part of a class of complexing binary systems whose thermodynamic and physical properties display strong compositional dependences which are not completely understood. The comparative lack of structural information on such mixtures is largely due to the increased complexity of binary systems. In the general case of a binary mixture containing four components, ten partial structure factors are required to describe the structure. However, in the case of the metal chloride - alkali chloride molten salt mixtures described in this thesis, which have all been studied using time-of-flight neutron diffraction, the number of partial structures falls to six because of the common anion species.

This chapter begins with a brief survey of molten salt studies to date starting with investigations of the pure salt structures before moving on to consider binary mixtures. This is followed by some background concerning the topics of central interest to this investigation, namely, the first sharp diffraction peak (FSDP) and intermediate range order. Finally, there is an overview of thesis contents.

¹ A good source of information about the range of applications of molten salts is Lovering [1.1].

1.1.1 Review of structural studies to date

Molten salts form one of the simplest classes of so-called ionic liquids and as such have always attracted a great deal of interest from both experimentalists and theorists. In 'simple' liquids such as condensed inert gases the ordering is largely determined by rather weak van der Waals' forces combined with the ubiquitous short-range repulsive forces preventing overlap of atoms. Consequently, the experimental observations can be explained adequately using interaction potentials of the simple Lennard-Jones type (see, for example, Yarnel *et al* [1.2]). In ionic liquids, however, longer range Coulombic forces are also at work and these play a major role in determining the structure and dynamics of the liquid. The long-range forces give rise to charge-charge correlations beyond first neighbours. This ordering can, at least to a first-order approximation, be modelled using a simplified 'bare' potential, $\phi_{\alpha\beta}(r)$, whose general form for rigid ions can be written as

$$\phi_{\alpha\beta}(r) \approx -\frac{Z_{\alpha}Z_{\beta}e^2}{r} + \phi_{\alpha\beta}^{SR}(r) \quad (1.1)$$

where the second term represents the short-range, mainly repulsive, contribution (see, for example, Rovere and Tosi [1.3]). $\phi_{\alpha\beta}^{SR}(r)$ may also incorporate terms for the van der Waals contribution and for the effects of ionic motion.

Using potentials of this form, excellent agreement has been obtained between experiment and theory for the structures of the simplest molten salts, the monovalent alkali halides. Analyses of the experimental results for alkali chlorides have suggested a trend in local coordination from octahedral to tetrahedral as the cation size decreases from CsCl to LiCl [1.4, 1.5]. This has been supported by Monte Carlo and Molecular Dynamics simulations using both rigid and polarisable (shell model) ion potentials [1.6, 1.7]. However, this approach has been less successful in modelling the data for divalent metal halides, particularly with respect to the cation distribution (see, for example, Pastore *et al* [1.8]). Extensive neutron scattering studies of alkaline earth and transition metal halides have revealed trends in local and intermediate order as a function of cation size which are not readily explained using a simple ionic model [1.9]. In the case of MX_2 melts with small cations, such as ZnCl_2 [1.10], the first peak in $g_{++}(r)$ virtually coincides with that in $g_{--}(r)$, whereas for melts containing larger cations, such as BaCl_2 [1.11], the peak is at higher r as would

be expected from the requirement to maximise the separation of doubly charged cations. Also evident in the case of small cations, but not for large cations, is a FSDP at $Q \sim 1 \text{ \AA}^{-1}$ in $S_{++}(Q)$ usually taken to be indicative of intermediate range ordering involving the cations. Although Wilson and Madden [1.12] have recently put forward a polarisable anion model which can reproduce the observed trends, it still appears necessary to invoke 'covalency' effects [1.9] to account for *all* the features of divalent salts in both the liquid and solid phases (see section 7.3.3). The incorporation of 'covalency corrections' into theoretical structure factors and radial distribution functions remains one of the most pressing theoretical problems in the field of molten salt studies.

More recently, there has been increased interest in molten trivalent metal halides which in some cases depart even further from the simple ionic model and are probably best described as molecular fluids. Attempts have been made to relate the limited neutron and X-ray diffraction data to the distinct melting behaviours of lanthanide trichlorides, YCl_3 , AlCl_3 and SbCl_3 using Pettifor's phenomenological chemical scale as a measure of the covalent character of bonding [1.13-1.15]. Theoretical attention has focussed on AlCl_3 , which is of special interest because of the anomalous increase in molar volume upon melting, despite there being no reliable diffraction data on the liquid prior to this doctoral study (see, for example, Abramo & Caccamo [1.16]). As will be seen in chapter 8, there is little evidence to support the 'established' view of the liquid structure, implicitly assumed in all theoretical studies to date, as consisting predominantly of discrete dimers.

For the reasons mentioned earlier, the binary molten salt mixtures which have been most closely studied using diffraction methods are also those containing AlCl_3 (see chapter 8 and references therein). Although Saboungi and co-workers were able to show by MD simulation [1.17, 1.18] that structural features of AlCl_3 - NaCl melts normally attributed to 'covalency' could be reproduced using an ionic model, it is now recognised that polarisation effects play a major role in determining structure (again, see chapter 8). There is also considerable thermodynamic and spectroscopic evidence for halide 'complex' formation in the alkali chloro-aluminate melts and, generally, for both divalent and trivalent metal chloride mixtures with alkali chlorides. Ferrante *et al* [1.19] discuss the thermodynamic stability of such halo-complexes using the concept of an effective length over which the units are screened by the surrounding ionic liquid. However, for the results described in this thesis, a simpler approach based on a consideration of the relative polarising power of the two cation species has been adopted, which also generates insights regarding intermediate range order in

the mixtures. The next section provides some general background on the FSDP and its relationship to intermediate range order.

1.1.2 *The first sharp diffraction peak and intermediate range order*

A FSDP or 'prepeak' is observed at values of Q in the range $0.5 - 2 \text{ \AA}^{-1}$ in the X-ray or neutron structure factors of a diverse range of glasses and liquids. This is widely recognised as indicating the occurrence of intermediate range order (IRO) on a length scale of $r \sim 2\pi/Q$ in such materials (the width of the FSDP also provides a measure of the real-space coherence length). In the case of molten salts where the FSDP usually occurs at $Q \sim 1 \text{ \AA}^{-1}$, this suggests fluctuations in density of period approximately $5-10 \text{ \AA}$ in real space. The FSDP is also anomalous in that its behaviour as a function of temperature and pressure may differ markedly from that of other peaks in the total structure factor. For example, in chalcogenide glasses the FSDP exhibits a (reversible) increase in intensity with temperature rather than the expected Debye-Waller behaviour [1.20]. With increasing pressure, the FSDP diminishes rapidly and shifts to higher Q , unlike the other peaks in the structure factor [1.21]. At present, controversy still surrounds the *general* origin of the FSDP although it must be noted that there is no reason why the structural origin should be the same for all materials .

Most proposals for the structural origin of the FSDP can be divided into three broad categories : quasi-crystalline (layer-type) structures, the formation of clusters, or ordered voids within a network structure. The first of these was suggested because the crystal structures of many glass-forming chalcogenides (for example, GeSe_2) are layer-like [1.20]. However, a layer-like structure is not a general explanation for the FSDP since this feature is also observed in the diffraction patterns of glasses such as SiO_2 which are not believed to have such a structure. The second explanation, involving correlations between clusters, again only seems to apply in those cases where the formation of such structures is clearly evident (for example, in arsenic sulphide thin films [1.22]). The third suggestion ascribes the FSDP to the existence of low-density regions or voids in the structure [1.23]. The attraction of this theory is that it provides a natural explanation in terms of changes in void volume for the anomalous pressure and temperature dependences of the FSDP in chalcogenide glasses. However, Salmon [1.24] points out that in most molten and glass binary systems, AB_2 , the predominant contribution to the FSDP is from the A-A partial structure factor and thus concludes that A-A correlations are generally responsible for IRO.

The ubiquitous nature of the FSDP has also prompted the suggestion that the feature arises from random packing of structural units (see Price *et al* [1.25]). In the case of molten ZnCl_2 , however, the units will be ZnCl_4^{2-} tetrahedra and the requirements of stoichiometry necessitate some sharing of Cl^- ions which will inevitably give rise to correlations between neighbouring units and hence deviations from randomness. In addition, the results of reverse Monte Carlo (RMC) modelling of isotopic data for molten ZnCl_2 suggest the FSDP is due to definite correlations of cations rather than random packing of structural units [1.26]. It has been suggested by Wood and Howe [1.27] that the FSDP in the Zn-Zn partial structure factor for molten ZnCl_2 arises from the angular dependence of interionic forces. This implies the effect of adding a 'network breaking' alkali halide to molten ZnCl_2 would be to destroy IRO because the isolated ZnCl_4^{2-} units formed in such mixtures would no longer be constrained by the need to share anions. However, Allen *et al* [1.28] actually observed enhancement of the FSDP with increasing alkali halide in their total structure factor data for ZnCl_2 -KCl melts.

The principal aim of the research in this thesis was to explore, in detail, the nature of intermediate range order in metal chloride - alkali chloride molten salt mixtures. Diluting network-forming polyvalent melts by adding alkali halide was also intended to be a means of probing the stability of local structural units and of possibly shedding new light on the structure of the pure liquids.

1.2 Overview of thesis contents

In chapter 2, the theoretical background to the neutron diffraction technique is described. This chapter also contains an overview of the theoretical models used to describe liquid structure and explains the role of computer modelling.

Details of sample preparation and the method of collecting data on the ISIS LAD and SANDALS instruments are given in chapter 3. The particular checks and tests employed in each phase of experimentation are emphasised.

The data analysis procedure used once the data had been collected, is outlined in chapter 4. The problems peculiar to each of the ISIS instruments, and the methods used to overcome them, are highlighted. The problems encountered with SANDALS are particularly worthy of note.

The RMC technique, used to model some of the data presented in chapters 7 and 8, is the subject of chapter 5. A description of the method and an extended discussion of its characteristics and limitations is presented.

The research is described in three parts beginning with the results of composition studies of the NiCl₂-KCl, NiCl₂-LiCl and ZnCl₂-LiCl molten salt mixtures in chapter 6. Analysis of trends in peak height and position reveals the contrasting effect of alkali cation type on the local order and geometry of the Ni²⁺ ion. A model involving charge ordering between NiCl₄²⁻ tetrahedra and K⁺ counter-ions is proposed as an explanation for the enhanced IRO observed in the NiCl₂-KCl melts.

In chapter 7, the results of isotopic substitution studies on molten NiCl₂-KCl and ZnCl₂-KCl samples of the same (nominal) 2/3 alkali halide concentration are described. RMC modelling of the NiCl₂-KCl data lends further support to the charge-ordered model proposed as an explanation for enhanced intermediate range order in the mixtures. RMC modelling also highlights the strong structural similarities between the two molten salt mixtures.

The results of composition studies of AlCl₃-LiCl and AlCl₃-NaCl molten salt mixtures are described in chapter 8. A shift in FSDP position to higher Q with increasing alkali halide is observed, which is consistent with strong charge ordering between tetrahedral AlCl₄⁻ units and alkali counter-ions. In addition, RMC modelling of the data for pure liquid AlCl₃ challenges the 'established' view of the structure of this anomalous liquid. A new structural model is proposed which emphasises the similarities to molten ZnCl₂.

The final chapter contains a summary of the key points emerging from the research presented in this thesis. In addition, suggestions for future work are provided in the form of a programme of study centred on exploring in further detail the links between strongly charge-ordered molten salt structures and intermediate range order.

1.3 References

- [1.1] D.G. Lovering (editor), 1982, 'Molten salt technology', 1st edition, Plenum Press, New York
- [1.2] J.L. Yarnell, M.J. Katz, R.G. Wenzel & S.H. Koenig, 1973, *Phys. Rev. A*, **7**, 2130
- [1.3] M. Rovere & M.P. Tosi, 1986, *Rep. Prog. Phys.*, **49**, 1001
- [1.4] J-C. Li, J.M. Titman, G.E. Carr, N. Cowlam & J-B. Suck, 1989, *Physica B*, **156**, 168
- [1.5] M.A. Howe & R.L. McGreevy, 1988, *Phil. Mag. B*, **58**, 485
- [1.6] M. Dixon & M.J. Gillan, 1981, *Phil. Mag. B*, **43**, 1099
- [1.7] A. Baranyai, I. Ruff & R.L. McGreevy, 1986, *J. Phys. C: Solid State Phys.*, **19**, 453
- [1.8] G. Pastore, P. Ballone & M.P. Tosi, 1986, *J. Phys. C: Solid State Phys.*, **19**, 487
- [1.9] J.E. Enderby & A.C. Barnes, 1990, *Rep. Prog. Phys.*, **53**, 85
- [1.10] S. Biggin & J.E. Enderby, 1981, *J. Phys. C: Solid State Physics*, **14**, 3129
- [1.11] F.G. Edwards, R.A. Howe, J.E. Enderby & D.I. Page, 1978, *J. Phys. C: Solid State Phys.*, **11**, 1053
- [1.12] M. Wilson & P.A. Madden, 1994, *J. Phys. : Condens. Matter*, **6**, A151-A155
- [1.13] M.P. Tosi, 1994, *J. Phys. : Condensed Matter*, **6**, A13-A28
- [1.14] Z. Akdeniz & M.P. Tosi, 1992, *Proc. R. Soc. Lond. A*, **437**, 85-96
- [1.15] M.-L. Saboungi, D.L. Price, C. Scamehorn & M.P. Tosi, 1991, *Europhys. Lett.*, **15**(3), 283-288
- [1.16] M.C. Abramo & C. Caccamo, 1994, *J. Phys. : Condensed Matter*, **6**, 4405
- [1.17] M. Blander, M.-L. Saboungi & A. Rahman, 1986, *J. Chem. Phys.*, **85**, 3995
- [1.18] M.-L. Saboungi, A. Rahman & M. Blander 1984, *J. Chem. Phys.*, **80**, 2141
- [1.19] A. Ferrante, L. Wang & M.P. Tosi, 1988, *Phil. Mag. A*, **58**(1), 13-25
- [1.20] L.E. Busse, 1984, *Phys. Rev. B*, **29**, 3639
- [1.21] K. Tanaka, 1988, *Phil. Mag. Lett.*, **57**, 183
- [1.22] J.C. Phillips, 1981, *J. Non-Cryst. Solids*, **43**, 37
- [1.23] S.R. Elliott, 1992, *J. Phys. : Condensed Matter*, **4**, 7661
- [1.24] P.S. Salmon, 1992, *Proc. R. Soc. Lond. A*, **437**, 591
- [1.25] D.L. Price, S.C. Moss, R. Reijers, M.-L. Saboungi & S. Susman, 1988, *J. Phys. C: Solid State Physics*, **21**, L1069
- [1.26] R.L. McGreevy & L. Pusztai, 1990, *Proc. R. Soc. Lond. A*, **430**, 241-261
- [1.27] N.D. Wood & R.A. Howe, 1988, *J. Phys. C: Solid State Physics*, **21**, 3177
- [1.28] D.A. Allen, R.A. Howe, N.D. Wood & W.S. Howells, 1992, *J. Phys. C: Condens. Mat.*, **4**, 1407-1418

Chapter 2

Theory

2.1 Introduction - describing liquid structure

Because liquids are amorphous their microscopic structure is best represented mathematically by some form of distribution function. The one most commonly used, and arguably the most useful, is the pair distribution function, $g(\underline{r})$ (sometimes known as the pair correlation function). This is defined such that given an atom¹ centred at the origin $|\underline{r}| = 0$ then the probability of finding another atom centred in a small element of volume dV at position \underline{r} is given by

$$\rho_o g(\underline{r}) dV \quad (2.1)$$

where ρ_o is the mean atomic number density. The distribution function $g(\underline{r})$ obviously represents an average over time because the instantaneous positions of atoms vary, particularly in the case of a fluid. An immediate simplification is possible in the case of liquids (and other non-crystalline samples such as glasses) where the structure is usually isotropic so that $g(\underline{r})$ depends on the magnitude but not the direction of the \underline{r} vector, hence $g(\underline{r})$ can be replaced by $g(r)$ (which is an average over spherical polar angle coordinates and the entire volume of the sample).

The discussion in this chapter is divided into two main sections. The first covers the theoretical background to the experimental determination of $g(r)$ functions using neutron diffraction. The second concentrates on theoretical models of liquid structure produced by calculation or computer simulation and the comparison of the resulting model $g(r)$ with experimental functions.

¹ The discussion in this chapter refers to atoms although it is equally valid for ions and molecules.

2.2 Theoretical background to neutron diffraction

2.2.1 The differential scattering cross-section

The pair distribution function is derived from the angle-dependent differential scattering cross-section (per unit solid angle) which is defined as

$$\frac{d\sigma}{d\Omega}(\lambda, 2\theta) = \frac{\text{flux scattered into solid angle } d\Omega \text{ at angle } 2\theta}{\text{incident flux of wavelength } \lambda * d\Omega} \quad (2.2)$$

and is the quantity actually measured in a neutron diffraction experiment. This cross-section can be related to the structure of a sample by using the wave-like properties of the neutron. If the incident neutrons are considered as plane waves described by a wave-function of the form

$$\Psi_{\text{inc}} = e^{i\mathbf{k}_o \cdot \mathbf{r}} \quad (2.3)$$

where \mathbf{k}_o is the wave-vector ($|\mathbf{k}| = 2\pi/\lambda$), then the scattered wave from a static nucleus j at point \mathbf{r}_j , measured at position \mathbf{r} (with respect to an arbitrary origin close to j), will be spherically symmetric and of the form

$$\Psi_{\text{sc}}(\mathbf{r}) = \frac{-b_j}{|\mathbf{r} - \mathbf{r}_j|} e^{i\mathbf{k}' \cdot (\mathbf{r} - \mathbf{r}_j)} \quad (2.4)$$

([2.1], section 1.4)

where \mathbf{k}' is the wave-vector after scattering. The process of scattering from a single fixed nucleus is illustrated in figure 2.1. The quantity b_j is defined as the scattering length and although in general it is a complex quantity the imaginary component, which can make b vary rapidly with neutron energy, is only important for a few highly absorbing nuclei ([2.2], section 2.2). Hence for most scattering experiments, b is independent of \mathbf{k}_o . In addition, because the wavelength of thermal neutrons is very large compared to the dimensions of nuclei then it is a basic result from diffraction theory that scattering is isotropic (spherically symmetric) so b is also independent of angle. Thus the scattering length usually only depends on the type of nucleus.

The scattering from an assembly of N nuclei is obtained simply by summing over all the atoms so that

$$\Psi_{sc}(r) = \sum_j^N \frac{-b_j}{|r-r_j|} e^{ik'_o \cdot (r-r_j)} e^{ik_o \cdot r_j} \quad (2.5)$$

where the second exponential term is the phase of the incident wave at nucleus j . In practise, the distance $|r|$ from the sample to the detectors is large compared to $|r_j|$ so using the far-field approximation ($|r-r_j| \cong r$) the above equation becomes

$$\Psi_{sc}(r) \cong -\frac{e^{ik_o \cdot r}}{r} \sum_j^N b_j e^{i\underline{Q} \cdot r_j} \quad (2.6)$$

where $\underline{Q} = \underline{k}_o - \underline{k}'$ is the scattering vector and $\hbar\underline{Q}$ is the momentum transferred to the nucleus j by the scattered neutron. The differential scattering cross-section is effectively the ratio of the scattered and incident neutron wave intensities after normalising for the $1/r^2$ dependence of $|\Psi_{sc}|^2$ hence

$$\frac{d\sigma}{d\Omega} = r^2 \frac{|\Psi_{sc}|^2}{|\Psi_{inc}|^2} = \left\langle \sum_j^N \sum_k^N b_j b_k e^{i\underline{Q} \cdot (r_j - r_k)} \right\rangle \quad (2.7)$$

([2.3], section 1.2).

Since cross-sections are measured over a period of time which is much longer than the lifetime of thermal fluctuations, the above quantity is a thermal average (as denoted by $\langle \dots \rangle$). This equation is central to all diffraction experiments - the spatial information about nuclear positions is reflected in phase shifts between scattered waves giving rise to observable interference.

2.2.2 Coherent and incoherent scattering and the static structure factor $S(Q)$

Because neutron scattering lengths vary even between isotopes of the same element, and, between different spin states of species with non-zero nuclear spin (since the neutron itself has non-zero spin), the measured scattering will include contributions from isotopic and spin incoherence. It is thus useful to express the total differential scattering cross-section as the sum of two terms consisting of a coherent and incoherent component.

For a collection of N static nuclei of the same element and assuming a random distribution of isotopes and spin orientations, the right hand side of eqn. 2.7 can be expanded and rewritten as

$$\frac{d\sigma}{d\Omega} = \bar{b}_j^2 \left| \sum_j^N e^{i\mathbf{Q}\cdot\mathbf{r}_j} \right|^2 + N(\overline{b_j^2} - \bar{b}_j^2) \quad (2.8)$$

([2.3], appendix 1).

The first term in the above equation depends on the mean scattering length, \bar{b}_j , and represents the coherent scattering since it contains the phase factor (reflecting structure) as if all nuclei were the same. The second term depends on the mean square deviation of the individual scattering lengths b_j from the mean and represents the incoherent scattering. Obviously, it contains no phase factor and hence positional information because of the assumed random distribution of isotopes and spins.

Integrating the first term in the differential scattering cross-section over all 4π steradians of solid angle gives the coherent scattering cross-section

$$\sigma_{coh} = 4\pi\bar{b}^2 \quad (2.9).$$

Similarly integrating the second term gives the incoherent scattering cross-section

$$\sigma_{inc} = 4\pi(\overline{b^2} - \bar{b}^2) \quad (2.10).$$

Thus the total scattering cross-section formed by the sum of the two is

$$\sigma_{sc} = 4\pi\overline{b^2} \quad (2.11).$$

Cross-sections are usually quoted in barns (bn or 10^{-28}m^2) and extensive data is available in the 'barn book' [2.4]. The differential scattering cross-section has units of barns per scattering unit per steradian ($\text{bn}\cdot\text{sr}^{-1}$).

Eqn. 2.8 can also be rewritten as

$$\frac{1}{N} \frac{d\sigma}{d\Omega} = \bar{b}_j^2 S(\underline{Q}) + (\overline{b_j^2} - \bar{b}_j^2) \quad (2.12)$$

where $S(\underline{Q})$ is the static structure factor explicitly defined as

$$S(\underline{Q}) = \frac{1}{N} \left| \sum_j^N e^{i\underline{Q} \cdot \underline{r}_j} \right|^2 \quad (2.13)$$

or, more rigorously, as

$$S(\underline{Q}) = \frac{1}{N} \left| \sum_j^N e^{i\underline{Q} \cdot \underline{r}_j} \right|^2 - N\delta_{\underline{Q},0} \quad (2.14)$$

(see [2.5])

where $N\delta_{\underline{Q},0}$ is the excluded forward scattering term corresponding to the intensity at $Q=0$. This term can be neglected because it is only significant in a very narrow region (hence the delta function) around $Q=0$ so it is never measured in a conventional diffraction experiment. The relationship between the static structure factor and the real-space pair distribution function is considered next.

2.2.3 The Fourier transform relationship between $S(Q)$ and $g(r)$

Because neutrons used in diffraction experiments have wavelengths several orders of magnitude larger than nuclear dimensions, the nuclei can be regarded as point scatterers so their positions may be represented using δ (delta) functions. Hence the following alternative definition of the pair distribution function

$$\rho(\underline{r}) = \rho_0 g(\underline{r}) = \frac{1}{N} \left\langle \sum_j^N \sum_k^N \delta[\underline{r} - (\underline{r}_j - \underline{r}_k)] \right\rangle - \delta(\underline{r}) \quad (2.15)$$

([2.6])

where $\rho(\underline{r})$ is the radial density function giving the probability of finding two nuclei separated by \underline{r} . The $\delta(\underline{r})$ term, generated when $\underline{r}=0$ and $\underline{r}_j = \underline{r}_k$, is subtracted to exclude self correlation.

Since $g(\underline{r}) \rightarrow 1$ for large values of $|\underline{r}|$, we can use the expression $\rho(\underline{r}) = \rho_0[g(\underline{r}) - 1] + \rho_0$ to rearrange eqn. 2.15 as

$$\frac{1}{N} \left\langle \sum_j^N \sum_k^N \delta[r - (r_j - r_k)] \right\rangle - \rho_o = \rho_o [g(r) - 1] + \delta(r) \quad (2.16).$$

Using Fourier transformation, we now obtain (see [2.6], pages 8-9 for details of the mathematical relations used)

$$\frac{1}{N} \left\langle \sum_j^N \sum_k^N e^{-i\underline{Q} \cdot (r_j - r_k)} \right\rangle - N\delta_{\underline{Q},0} = 1 + \rho_o \int_0^\infty [g(r) - 1] e^{-i\underline{Q} \cdot r} dr = S(\underline{Q}) \quad (2.17)$$

where the expression on the left hand side is clearly identical to that for the structure factor in eqn. 2.14. Thus, there is a Fourier transform relationship between $S(\underline{Q})$ and $g(r)$ ($S(\underline{Q})/\rho$ is to be regarded as the density of points in reciprocal space just as $\rho_o g(r)$ is the density of points in real space). The above definition of the structure factor is valid for all types of sample whether crystalline or amorphous. However, as was mentioned in the introduction, we can assume spherical symmetry in the case of liquids. $S(\underline{Q})$ and $g(r)$ then depend only on the magnitude of \underline{Q} and r , respectively, so the integral over spherical polar angular coordinates can be performed directly to give

$$S(Q) = 1 + 4\pi\rho_o \int_0^\infty r^2 [g(r) - 1] \frac{\sin(Qr)}{Qr} dr \quad (2.18).$$

The inverse transform is given by

$$g(r) = 1 + \frac{1}{2\pi^2\rho_o} \int_0^\infty Q^2 [S(Q) - 1] \frac{\sin(Qr)}{Qr} dQ \quad (2.19).$$

Note that the limits of the integral in eqn. 2.19 imply that data covering the entire range of Q from 0 to ∞ is required for a complete knowledge of the pair distribution function. In practise, Q_{\max} is of course finite and the approximation $S(Q) = 1$ at large Q is used. Nonetheless, it is desirable to measure the differential cross-section over as large a Q range as possible.

2.2.4 The static approximation and $S(Q)$

The discussion so far contains the implicit assumption of elastic scattering because only *static* nuclei (implying no energy transfer) have been considered. However, in real diffraction experiments, and, particularly in the case of

liquids where atoms do not remain in specific sites and diffusion occurs, there is strictly no elastic scattering.

The fraction of an incident neutron beam that is scattered into solid angle $d\Omega$ having interchanged energy within the range $\hbar d\omega$ is given by the double differential scattering cross-section, $d^2\sigma/d\Omega d\omega$. This is related directly to the 'scattering law', $S(Q, \omega)$, by the following equation

$$\frac{d^2\sigma}{d\Omega d\omega} = \frac{k'}{k_0} b^2 S(Q, \omega) \quad (2.20).$$

In general, diffraction experiments are performed without energy analysis and so measure the 'total scattering'. A detector at scattering angle 2θ will count all neutrons scattered into its direction irrespective of any energy transfer during the scattering process. With time-of-flight diffractometers (see 3.3.1 for an explanation of the underlying principles) there is the additional complication that each time channel is actually a sum over all incident and corresponding scattered neutron energies with an equal total flight time t . Hence the measured cross-section is the integral over all possible energy transfers, carried out at constant 2θ (and t), of $d^2\sigma/d\Omega d\omega$ weighted by the detector efficiency, $D(k)$, so that

$$\frac{d\sigma}{d\Omega} = \int_{\substack{-E_0/\hbar \\ \text{constant } 2\theta \\ \text{(constant } t)}}^{\infty} D(k) \frac{k'}{k_0} \frac{d^2\sigma}{d\Omega d\omega} d\omega \quad (2.21)$$

where E_0 is the incident neutron energy. The factor k'/k_0 is introduced because neutron flux depends on particle velocity (which is proportional to the wave-vector k).

The relationship between momentum transfer, $\hbar Q$, and energy transfer, $\hbar\omega$, for neutrons of mass m_n scattered through an angle 2θ is given by

$$\frac{(\hbar Q)^2}{2m_n} = 2E_0 - \hbar\omega - 2[E_0(E_0 + \hbar\omega)]^{1/2} \cos 2\theta \quad (2.22)$$

([2.3], pg. 43).

Thus a complicated cross-section is measured. However, if the incident neutron energy is large compared to that exchanged between the neutron and

the system, that is to say $E_o \gg \hbar\omega$, then the collision can be regarded as elastic ($|\underline{k}'| = |\underline{k}_o|$) and the scattering vector becomes

$$Q \equiv \frac{4\pi}{\lambda} \sin \theta \quad (2.23).$$

Thus integration at constant θ (and t) in equation 2.21 is now equivalent to integration at constant Q and the differential cross-section becomes, as required, a function of Q . This assumption is known as the 'static approximation' and is equivalent to an effective decoupling of the information on the structure from that on the dynamics. In the static approximation, and assuming the detector efficiency is the same for any scattered neutron energy, the measured cross-section is

$$\frac{d\sigma}{d\Omega} = \left\langle \left| \sum_j^N b_j e^{iQ \cdot r_j(t)} \right|^2 \right\rangle_t \quad (2.24)$$

([2.3], section 1.7).

This is the same expression as eqn. 2.7 but with nuclear positions, $r_j(t)$, monitored at time t , then averaged over all t , so we have the average *instantaneous* structure with no information on dynamics.

Deviations from the static approximation are negligible for X-rays because of the high photon energies at the wavelengths used in diffraction experiments. However, for thermal neutrons, which by definition have energies comparable to the thermal energies of atoms in a liquid, the deviations can be large so corrections for inelastic scattering are necessary. These are discussed in chapter 4 (section 4.2.7).

2.2.5 Scattering from multicomponent liquids

The discussion so far has been limited to single component systems and is now extended to the more general case of scattering from multicomponent samples. For this, it is convenient to reformulate the differential cross-section in terms of self, I^s , and distinct, $i(Q)$, scattering rather than the equivalent expression in terms of coherent and incoherent scattering introduced earlier. Thus eqn. 2.7 can be rewritten as

$$\frac{d\sigma}{d\Omega} = I^s(Q) + i(Q) = N\overline{b_j^2} + \overline{b_j^2} \sum_j \sum_{k \neq j}^N e^{iQ \cdot (r_j - r_k)} \quad (2.25)$$

and finally as

$$\frac{d\sigma}{d\Omega} = N\overline{b_j^2} + N\overline{b_j^2}(S(Q) - 1) \quad (2.26).$$

The distinct term (sometimes called the interference function) contains the information on atomic positions whereas the self term is the single atom scattering (when $j = k$).

For a multicomponent system there is a self and distinct term for each pair of atom types (α, β). The measured scattering is a linear sum of these terms weighted for concentration and scattering length so that

$$\frac{d\sigma}{d\Omega} = \sum_{\alpha} c_{\alpha} \overline{b_{\alpha}^2} + \sum_{\alpha, \beta} c_{\alpha} \overline{b_{\alpha}} c_{\beta} \overline{b_{\beta}} [S_{\alpha\beta}(Q) - 1] \quad (2.27)$$

([2.7], section 8.2.3)

where c_{α} is the atomic fraction and $\overline{b_{\alpha}}$ is the coherent scattering length for element α . The $S_{\alpha\beta}(Q)$ terms are the partial structure factors (PSFs) according to the definition of Faber and Ziman [2.8]. The PSF is related to the corresponding partial pair distribution function, $g_{\alpha\beta}(r)$, by Fourier transformation so

$$S_{\alpha\beta}(Q) = 1 + 4\pi\rho_o \int_0^{\infty} r^2 [g_{\alpha\beta}(r) - 1] \frac{\sin(Qr)}{Qr} dr \quad (2.28)$$

([2.6], pg. 11)

just as in the single component case (eqn. 2.18). The partial pair distribution function is then given by the inverse transform

$$g_{\alpha\beta}(r) = 1 + \frac{1}{2\pi^2\rho_o} \int_0^{\infty} Q^2 [S_{\alpha\beta}(Q) - 1] \frac{\sin(Qr)}{Qr} dQ \quad (2.29).$$

The function $g_{\alpha\beta}(r)$ gives the probability of finding a β type atom at a distance r from an α type atom located at the origin.

There are alternative definitions of the PSFs such as those of Bhatia and Thornton [2.9] which are derived from the Fourier transforms of the local number density and concentration fluctuations in the long-wavelength limit ($Q \rightarrow 0$). Although the Bhatia-Thornton PSFs have useful physical significance in the long-wavelength limit, where they are directly related to the thermodynamic properties of a system (see [2.6], appendix 4), it is the Faber-Ziman (henceforth referred to as F-Z) definition which has been adopted in this thesis.

The various definitions of the PSFs differ in their normalisation. Because the differential cross-section must approach the value of the first term in eqn. 2.27 (viz. the mean self scattering \bar{I}^s) at high Q , the second term, which we shall now call the total structure factor $F(Q)$, is asymptotic to zero as $Q \rightarrow \infty$. Hence the F-Z PSFs are normalised to unity at large values of Q .

For a two component system, with atoms of type a and b , $F(Q)$ can be written as

$$F(Q) = c_a^2 b_a^2 [S_{aa}(Q) - 1] + c_b^2 b_b^2 [S_{bb}(Q) - 1] + 2c_a c_b b_a b_b [S_{ab}(Q) - 1] \quad (2.30)$$

Since $S_{ab}(Q) = S_{ba}(Q)$ there is an additional coefficient of 2 in the last term. It should be noted that unlike $S(Q)$, which is dimensionless, $F(Q)$ has the dimensions of L^2 and is usually quoted in barns (10^{-28}m^2) per atom. Fourier transformation of $F(Q)$ gives the corresponding total pair distribution function, $G(r)$, written as

$$G(r) = 1 + \frac{1}{2\pi^2 \rho_0} \int_0^\infty Q^2 F(Q) \frac{\sin(Qr)}{Qr} dQ \quad (2.31)$$

which after substituting eqn. 2.29 can be re-written as

$$G(r) = 1 + c_a^2 b_a^2 [g_{aa}(r) - 1] + c_b^2 b_b^2 [g_{bb}(r) - 1] + 2c_a c_b b_a b_b [g_{ab}(r) - 1] \quad (2.32)$$

Not surprisingly, $G(r)$ is a linear sum of the various partial structures weighted for concentration and scattering, just as in the original $F(Q)$. The function is normalised to unity at high r . The exact form of the above equations is of course only valid for pure molten salts with two types of atom, such as liquid AlCl_3 . Generally, for a system with n components there are $n(n+1)/2$ distinct pairs of atom types and hence PSFs contributing to the

measured $F(Q)$. The molten salt mixtures mainly studied in this thesis contain three components so six partial structures have to be considered.

The PSFs and the corresponding partial pair distribution functions can be extracted from the measured total structure factor data using the method of isotopic substitution. This involves varying the coefficients of, for example, the partials in eqn. 2.30 by changing the coherent scattering lengths, \bar{b}_α , of particular elements using different isotopic enrichments. The result is a set of total structure factors, with known coefficients for the $S_{\alpha\beta}(Q)$ terms, which form a set of simultaneous equations that can be solved to determine the unknowns - the PSFs. There are other methods to determine PSF information such as anomalous X-ray scattering (AXS) [2.10], and possibly in the near future, anomalous neutron scattering (ANS). These involve varying f (the X-ray form factor) or \bar{b} by working near the absorption edge for a particular element. Finally, there is isomorphic substitution where one type of atom is replaced by another of similar size so there is a difference in f or \bar{b} because of the different atomic numbers. However, this last method assumes chemical similarity and is probably the least reliable.

A detailed description of the data analysis procedure, including the corrections, used to derive the $F(Q)$ and $G(r)$ functions presented in this thesis is provided in chapter 4. The technique of isotopic substitution is discussed in detail by D.A. Allen in his doctoral thesis [2.11].

2.3 Theoretical models of liquid structure

2.3.1 Introduction

A successful theory of the liquid state will be one which explains the macroscopic properties of the liquid from a knowledge of the (microscopic) forces between atoms - calculated ideally from a first-principles quantum mechanical treatment of the electronic system. This is, as yet, an unsolved problem². In order to test theories based on the interaction between particles, equations relating the potential function, $\phi(r)$, and $g(r)$ are essential so that theoretical functions may be compared with those derived experimentally. However, to do this, several drastic approximations have to be made. Firstly, the interactions between particles are usually assumed to be pairwise so that

² In the sense that there is no comprehensive theory of the liquid state which works well for all types of liquid under all conditions of temperature and pressure.

the total potential energy of the system, $\phi(r_1, r_2, \dots, r_N)$, is given by the sum of two-body interactions over all $N(N+1)/2$ pairs i.e.

$$\phi(r_1, r_2, \dots, r_N) = \sum_{1 \leq i < j \leq N} \phi(r_{ij}) \quad (2.33).$$

It is also assumed that the potential $\phi(r)$ is spherically symmetric so that $r_{ij} = |r_i - r_j|$.

The assumption of pairwise additivity only holds if the potential between any pair of particles is unaffected by the presence of others. In real liquids this assumption may break down if, for example, ions are polarised by other nearby ions. Furthermore, in order to relate $g(r)$ to $\phi(r)$ it is necessary to make another assumption about a higher order distribution function in the generalised force equation

$$-\frac{\partial U(r_{12})}{\partial r_1} = -\frac{\partial \phi(r_{12})}{\partial r_1} - \int \frac{n^{(3)}(r_1, r_2, r_3)}{\rho_0^2 g(r_{12})} \frac{\partial \phi(r_{13})}{\partial r_1} dr \quad (2.34)$$

([2.12])

where the function $U(r_{12}) = -K_B T \ln[g(r_{12})]$ and is called the potential of mean force. The above equation implies the mean force on particle 1 is the direct effect of particle 2 plus the net effect of all the other particles (the first and second terms, respectively, on the right hand side of eqn. 2.34), represented by particle 3, hence the inclusion of the three-body number density function, $n^{(3)}(r_1, r_2, r_3)$. This density function is defined such that the probability of volume elements centred at positions r_1 , r_2 and r_3 being occupied by particles is given by $n^{(3)}(r_1, r_2, r_3) dr_1 dr_2 dr_3$. Clearly, in order to solve eqn. 2.34, and, because pair scattering theory can not provide any information about three-body (or higher) correlation functions, some form of approximation for $n^{(3)}$ is required. However, this step, usually referred to as the 'closure approximation', means any disagreement between theory and experiment becomes more difficult to pinpoint - it could be due to a problem in the choice of $\phi(r)$ or the particular form of the closure approximation itself.

Methods based on some form of closure approximation lead to integral equations which, given a choice of pair potential, can be solved for $g(r)$. The main schemes used in this analytical approach are considered next.

2.3.2 Integral equations for the pair distribution function

The Born-Green equation [2.13], one of the first to be proposed, used the superposition approximation due to Kirkwood [2.14] for the three-body density function as the product of only pair distribution terms such that

$$n^{(3)}(\underline{r}_1, \underline{r}_2, \underline{r}_3) = \rho_0^3 g(r_{12})g(r_{23})g(r_{31}) \quad (2.35).$$

The use of the above approximation leads to the soluble YBG (Yvon, Born, Green) equation. An iterative approach to solving for $g(r)$ is usually adopted. The physical meaning of the superposition approximation is that in a triplet of particles each pair correlates independently of the third. This assumption is only likely to be true in certain limiting cases such as low densities where the particles are effectively uncorrelated. The YBG equation rarely works well (it has been shown to be characterised by numerical instabilities [2.15]) and has not even been applied to ionic liquids - which are usually of high density and strongly coupled.

Of more importance to the study of molten salts have been the Percus-Yevick (PY) and Hypernetted Chain (HNC) equations and modifications thereof. Both the PY and HNC approximations involve carrying out a cluster expansion for $n^{(3)}$ and then neglecting certain terms which make the summation difficult ([2.16], chapter 5). In order to describe these equations, it is convenient to introduce the direct correlation function, $c(r)$, and relationships first proposed by Ornstein and Zernike [2.17]. They suggested the division of the total correlation function, $h(r)$, which is simply defined as $h(r) = g(r) - 1$, into two parts ; a direct pair term and an indirect one representing the effect of the remaining particles³ so that

$$h(r) = c(r) + \rho_0 \int c(|\underline{r} - \underline{r}'|)h(r')d\underline{r}' \quad (2.36).$$

The latter term represents a convolution of $h(r)$ and $c(r)$. The usefulness of the function $c(r)$ lies in the fact that it is both accessible experimentally and has a shorter range (than $h(r)$) comparable to that of the pair potential function. In the PY approximation, $c(r)$ is linked to $\phi(r)$ and $g(r)$ by

$$c(r) = g(r) \left[1 - e^{\phi(r)/K_B T} \right] \quad (2.37)$$

³ The separation is analogous to that in the generalised force equation (eqn. 2.34).

, whereas with the HNC approximation, the relationship becomes

$$c(r) = h(r) - \ln[g(r)] - \phi(r)/K_B T \quad (2.38).$$

Again, these approximations work best at low densities but are more accurate than the YBG equation. The HNC method has been generally favoured because it retains one extra term in the cluster expansion (compared with the PY) and so might be expected to yield more accurate results. However, the PY equation is known to be superior when repulsive forces are dominant because of partial cancelling in the excluded terms. This advantage is highlighted by the crude, but useful, hard-sphere solution of the PY equation or HSPY ([2.6], pg. 22).

A third useful approximation is the mean spherical approximation (MSA) of Waisman and Lebowitz [2.18]. The pair potential is assumed to consist of a repulsive hard core and a coulomb tail so that

$$\begin{aligned} g(r) &= 0 & r < \sigma_0 \\ c(r) &= -\frac{\phi(r)}{K_B T} & r > \sigma_0 \end{aligned} \quad (2.39)$$

where σ_0 is the charged hard-sphere diameter. Because the MSA is a theory for charged hard spheres it cannot relate the properties of molten salts to realistic interatomic potentials. Real ions interact through continuous, finite (except at $r=0$) potentials whereas the MSA model assumes infinite repulsion when $r < \sigma_0$. Not surprisingly, the success of MSA models depends critically on a proper choice of σ_0 .

It is now generally accepted that for multicomponent systems any comparison between theory and experiment should be made either at the level of the PSF or the partial pair distribution function - if these are available. The integral equation methods described above can of course be generalised for multicomponent liquids to link partial pair potential functions, $\phi_{\alpha\beta}(r)$, to $g_{\alpha\beta}(r)$ functions. However, in recent years a different approach to studying liquid structure based on computer modelling has become popular. These methods are described in the next section.

2.3.3 Computer modelling

Computer modelling methods have the advantage of not requiring any form of closure approximation. These methods are exact in the sense that, because the positions and velocities of all the particles are known, there is no need to make assumptions about higher order distribution functions and the equations governing the behaviour of the system can be solved to as high an accuracy as desired for a given form of $\phi(r)$. The Monte Carlo (MC) and Molecular Dynamics (MD) methods are the two basic techniques commonly used. They both involve modelling the behaviour of a large number of particles under the influence of a specified interatomic potential. They differ in that the MC method uses the pair potential directly in the computational process whereas MD uses the derivative of the function.

Finite computing power restricts the number of particles to typically of the order of $N \sim 10^3 - 10^4$ corresponding to a simulation cube with sides of length $L \sim 10 - 20$ atomic diameters. The limited simulation size gives rise to a statistical error, which can be minimised by collecting statistically-independent configurations, as well as surface effects which are minimised through the use of periodic boundary conditions. The usual method (sometimes referred to as 'ghosting') is to surround the simulation cube with images of itself so that a particle leaving through one side re-enters via the opposite side with the same velocity - this also preserves the number density constraint. A brief description of the main simulation techniques will be provided next as the details are amply covered elsewhere (see, for example, [2.16], chapter 3).

The principle of the MC method is to produce a statistical ensemble of atoms with a Boltzmann distribution of energies. This is done by generating a series of atomic configurations from sequential, random displacements of the N particles in the model. A configuration is accepted or rejected according to a criterion which ensures that a given configuration occurs with a probability proportional to the Boltzmann factor, $e^{-U_j/k_B T}$, for that configuration, where U_j is the total potential energy of the system and the temperature T is fixed. This method of sampling configuration space was devised by Metropolis *et al* [2.19] and is widely used hence Metropolis Monte Carlo (MMC) is often synonymous with MC. Usually, between 10^5 and 10^6 configurations need to be generated for adequate statistics. No time scale is involved and the order in which the configurations occur has no special significance. The equilibrium properties are found by averaging over the set of accepted configurations.

In the MD method, Newton's equations of motion are solved for each particle moving under the influence of all its neighbours (the forces between atoms being calculated from the specified potential). Starting from a set of initial coordinates and velocities, usually chosen randomly, the trajectories of each particle are computed and the new positions and velocities after a short time step, Δt , are determined. The process then continues to be repeated and the time evolution of the configurational and velocity distributions is followed. Once the transient effects of the initial starting configuration have died out⁴ the equilibrium properties can then be calculated as time-averages over the configurations which arise after subsequent time steps. The MD method has the great advantage (over MC) of allowing time-dependent phenomena, as well as thermodynamic equilibrium properties, to be studied. However, the relaxation time for the process needs to be significantly smaller than the time-scale of the simulation - usually limited to $\sim 10^{-11}$ s with a time step between configurations of $\Delta t \sim 10^{-14}$ s.

The MC and MD methods are not, in principle, restricted to pairwise additivity of the potential function although this is usually assumed in order to simplify calculation. Ideally, explicit knowledge of the electronic ground state is required to obtain a correct description of the interatomic forces. In conventional computer methods, as described above, no attempt is made to solve this complex many-body problem, instead, interactions between atoms are modelled using *empirical* potentials. However, in recent years considerable progress has been made in combining the conventional MD technique with interatomic potentials derived from a first-principles treatment of the quantum electronic system - an approach based on methods introduced by Car and Parrinello [2.20]. Currently, these methods are restricted to systems consisting of only a few hundred atoms (even with the use of supercomputers) so they remain of limited value. Details of recent developments of the *ab initio* MD technique and some of the results of its application can be found in Galli [2.21].

Certain fundamental limitations apply to all computer modelling methods. The most obvious of these is the finite simulation size. This restricts the accuracy of model pair distribution functions (and their transforms) since r_{\max} is set by $\frac{1}{2}L$; beyond $r = \frac{1}{2}L$, the distribution is distorted by the periodic boundary condition. This can limit the usefulness of computer methods in the study of ionic liquids where there are long-range interactions. It is also

⁴ The simulation evolves rapidly and a Maxwellian distribution of particle velocities is usually attained, on average, after 6-10 collisions per particle.

impossible to study spatial fluctuations of wavelength greater than L . In the MD method, the boundary conditions can lead to spurious time-recurrences as local disturbances propagate through the periodic system. Despite these difficulties, computer methods have been successfully applied, for example, to the study of molten alkali halides [2.22] with generally good agreement between the pair distribution functions derived from MC simulation and experiment. This is mainly a reflection of the good choice of interatomic potentials. In general, choosing the 'correct' potential and obtaining more than just qualitative agreement with the data poses a severe challenge with conventional computer methods. Iterative techniques [2.23, 2.24] to improve on the initial choice of $\phi(r)$ have been developed but greatly increase the computational burden.

The reverse Monte Carlo (RMC) method does not require an interatomic potential and so avoids the problem of choosing the 'correct' one. It is a method for producing three-dimensional models of the structure of disordered materials that agree quantitatively with the diffraction data. The reduced computational demands of this technique can allow the limitation on simulation size to be eased. Details of the RMC method and its practical use are given in chapter 5.

2.4 References

- [2.1] G.L. Squires, 1978, " Introduction to the theory of thermal neutron scattering", Cambridge university press, Cambridge
- [2.2] G.E. Bacon, 1975, " Neutron diffraction", 3rd edition, Clarendon press, Oxford.
- [2.3] C.G Windsor, 1981, " Pulsed neutron scattering", 3rd edition, Taylor & Francis, London.
- [2.4] V.F. Sears, 1984, " Thermal neutron scattering lengths and cross-sections for condensed matter research", *Atomic Energy of Canada Ltd.*, Report AECL-8490, Chalk river nuclear labs.
- [2.5] N.W. Ashcroft & J. Lekner, 1966, *Phys. Rev.*, **145**, 83
- [2.6] Y. Waseda, 1980, " The structure of non-crystalline materials", 3rd edition, McGraw-Hill Inc., New York.
- [2.7] P. Chieux, 1978, in " Neutron diffraction", edited by H. Dachs, Springer-Verlag, New York.
- [2.8] T.E. Faber & J.M. Ziman, 1965, *Phil. Mag.*, **11**, 153
- [2.9] A.B. Bhatia & D.E. Thornton, 1970, *Phys. Rev.* , **2B**, 3004
- [2.10] P.H. Fuoss, P. Eisenberger, W.K. Warburton & A. Bienenstock, 1981, *Phys. Rev. Lett.*, **46**,1537
- [2.11] D.A. Allen, 1989, 'A neutron diffraction study of the structure and structural modification of molten zinc halides and nickel halides', PhD thesis, University of Leicester, chapter 4
- [2.12] N.H. March, 1968, " Liquid metals", Pergamon press inc., New York.
- [2.13] M. Born & H.S. Green, 1946, *Proc Roy. Soc.* , **A188**, 10
- [2.14] J.G. Kirkwood, 1935, *J. Chem. Phys.* , **3**, 300
- [2.15] M. Tanaka, 1977, *Institute of Physics Conference Series No. 30*, IOP publishing, Bristol, p. 164
- [2.16] J.P Hansen & I.R. McDonald, 1986, " Theory of simple liquids", 2nd edition, Academic Press, London.
- [2.17] L.S. Ornstein & F. Zernike, 1914, *Proc Acad. Sci. Amsterdam*, **17**, 793
- [2.18] E. Waisman & J.L Lebowitz, 1972, *J. Chem. Phys.*, **56**, 3093
- [2.19] M. Metropolis, A.W. Rosenbluth, M.N. Rosenbluth, A.N. Teller & E. Teller, 1953, *J. Chem. Phys.*, **21**, 1087
- [2.20] R. Car & M. Parrinello, 1985, *Phys. Rev. Lett.*, **55**, 2471
- [2.21] G. Galli, 1993, *J. Phys.: Condens. Matter*, **5**, pp. B107-B116
- [2.22] A. Baranyai, I. Ruff & R.L. McGreevy, 1986, *J. Phys. C: Solid State*, **14**, 453
- [2.23] M. Dzugotov, K.E. Larsen & I. Ebbsjö, 1988, *Phys. Rev. A*, **38**, 3609
- [2.24] L. Reatto, D. Levesque & J.J. Weiss, 1986, *Phys. Rev. A*, **33**, 3451

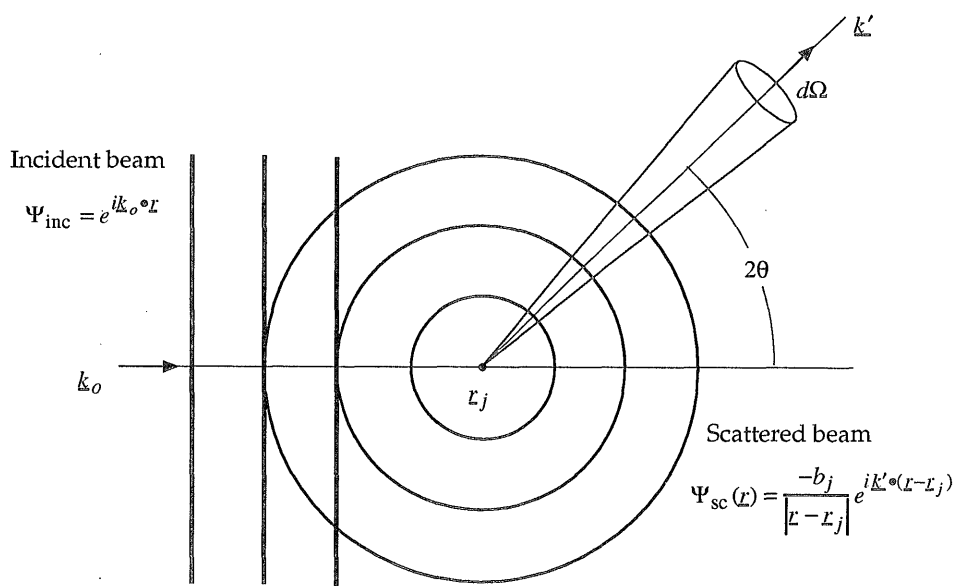


Figure 2.1. The process of scattering from a single fixed nucleus at position r_j . The nucleus acts as a point scatterer so the incident plane wave is scattered into a spherical wave. The differential scattering cross-section, $d\sigma/d\Omega$, is effectively the normalised fraction of the incident flux scattered into an element of solid angle, $d\Omega$.

Chapter 3

Experimental Method

3.1 Introduction

The aim of experiment was to derive reliable pair distribution functions from accurately measured structure factors. This necessitated both care in the preparation of samples and a suitable instrument for the neutron diffraction experiment. It is appropriate to consider these basic requirements in a little more detail before proceeding to describe how they were actually met.

The essential requirement in sample preparation was to produce mixtures to an accurate chemical composition using pure, anhydrous ingredients. In addition, the final samples had to be thoroughly mixed and homogeneous. Furthermore, isotopic substitution experiments required samples of the correct isotopic enrichment to ensure optimum conditioning for the experiment.

The specifications of the diffractometer also had to be adequate in certain regards. Firstly, in order to derive a satisfactory $G(r)$, the Q range had to be sufficiently large. Q_{\max} was required to extend beyond $\sim 15 \text{ \AA}^{-1}$, to avoid truncation of structure and subsequent loss of information in the Fourier transform. Q_{\min} , ideally, had to extend below $\sim 0.5 \text{ \AA}^{-1}$ so that the structure factor could be reliably extrapolated to the long-wavelength limit as a check on normalisation. Count rate of the instrument was important especially in isotopic substitution experiments where high statistical accuracy was required for reliable differencing. High Q resolution was not a critical requirement although it still had to be good enough to check there were no Bragg peaks i.e. the sample had completely melted.

The remainder of this chapter is divided into two main sections. The first deals with sample preparation and the second gives details of the diffractometers and how they were used.

3.2 Sample preparation

3.2.1 *Preparing the pure salts*

The first (lengthy) stage in preparing the mixtures was the drying of the pure single salts. Because inorganic salts are invariably hygroscopic and 'ultrapure' (≥ 99.99 mole %) raw chemicals were used, absorbed moisture is the most significant impurity. The water content of samples had to be minimised for several reasons. Firstly, molten salts are highly reactive and high vapour pressure products, such as HCl gas, resulting from the hydrolysis of absorbed water can cause sealed sample tubes to explode. Furthermore, the hydrogen in water is a strong scatterer of neutrons hence contributing to background as well as being the optimum moderating element so giving rise to significant inelastic scattering. For these reasons it was essential the salts were dried and, during subsequent handling, kept dry.

The low vapour pressure salts were dried by heating them gently under vacuum. The salt was first loaded into a test tube, under a dry argon atmosphere, in an evacuable glovebox. Research grade (≥ 99.998 % VPM¹ purity) argon was used to refill the glovebox after it had been 'rough' pumped down to a pressure of less than 1×10^{-1} torr over a period of at least 8 hours, prior to handling the salt. The salt was crushed to improve the efficiency of drying. A leak-tight transfer vessel was used to move the loaded salt to a vacuum drying rig. Once the transfer vessel had been pumped down to 'rough' vacuum, heating could begin. Initially the salts were slowly heated to no more than about 70°C and left at that temperature for at least 24 hours. This was to allow most of the absorbed water in the salt to be driven off at low temperature whilst limiting any reaction with the salt (which would upset the stoichiometry of the substance). The pressure would then be reduced using a diffusion pump. The outgassing, primarily of water, from the heated salt would delay attainment of base pressure by the diffusion pump so pressure measurements provided an indication of when the salt was sufficiently dry. Raising the temperature of the salt incrementally would naturally cause a corresponding increase in vacuum pressure. However, unless the pressure soon began to fall again after each step in temperature, it was assumed that the original increase was due entirely to the raised vapour pressure of the salt itself i.e. not due to a temporary surge from liberalisation of trapped water vapour. Once a safe maximum temperature was attained

¹ Volume parts per million.

vacuum drying was continued for at least a couple of days thereafter. In the case of ZnCl_2 , which has a high vapour pressure, the maximum temperature used for drying was limited to about 100°C so, to compensate, the salt was vacuum dried for a longer period than usual. The specific details of the vacuum drying procedure for each type of salt are given in table 3.1.

The vacuum drying technique could not be used for AlCl_3 because it sublimates at 180°C under normal atmospheric pressure and has a significant vapour pressure (~ 1 torr) even at 100°C . Instead, a technique of drying by sublimation was employed and the apparatus used is shown in figure 3.1. The salt was slowly heated over 3 days to a final temperature of $\sim 150^\circ\text{C}$ with a diffusion/rotary pump combination being used to draw the sublimed salt to the cold trap (an ice/water bath) where it condenses. The principle of the technique can be understood from figure 3.2 which compares the vapour pressures of AlCl_3 and Ice I. At temperatures above 100°C the vapour pressure of AlCl_3 becomes appreciable and significant amounts of the salt and absorbed water are liberated to travel down to the cold trap. At the temperature of the cold trap ($\sim 0^\circ\text{C}$) the vapour pressure of AlCl_3 is $\approx 1 \times 10^{-6}$ torr. Given, that this is approximately the base pressure attainable with a diffusion pump and that the pressure in the trap will be at least an order of magnitude higher than this, the AlCl_3 vapour may be expected to condense readily. However, the vapour pressure of Ice I is ≈ 4.6 torr at the same temperature and so water vapour will tend not to condense in the trap and continues on towards the pump. In practise, the pressures registered by the Penning gauge positioned near the inlet of the diffusion pump were in the region of $2-5 \times 10^{-5}$ torr, or even higher, depending on the AlCl_3 heating temperature. The effectiveness of drying by sublimation was checked using CHN combustion microanalysis². The water content of a small sample of AlCl_3 collected from the cold trap was estimated at $\sim 0.5\%$ by weight - this must be regarded as an upper limit because of the likelihood of absorption of water during subsequent storage and handling of the sample.

Once dried, by whichever method, the pure salt was returned to the glovebox in the leak-tight transfer vessel. The glovebox would now be evacuated using a diffusion pump rather than just being 'roughed' out since a better vacuum was required once the salts had been dried. The glovebox would then be refilled with research grade argon to a slight overpressure against atmospheric (so any leaks tend to be outward) before handling. Working as

² CHN stands for carbon, hydrogen and nitrogen.

quickly as possible (to minimise absorption of residual moisture) the dried salt powder was loaded into necked, transparent fused quartz tubes and sealed temporarily using a rubber tube and clamp before removal from the glovebox. The clamped tubes were reduced in argon pressure down to about 0.5 atm. before sealing off at the neck using a gas torch. The sealed salt powder usually contained considerable 'dead' space and was melted in order to reduce this. The resulting solid cast was much easier to handle than the powder and the survival, without exploding, of such 'pre-melted' salts provided a very crude check that they were, to some extent, dry.

3.2.2 *Preparing the mixtures*

The mixtures were made by weighing out the appropriate masses of the dried, 'pre-melted' pure salts required for a given composition and loading them into fused quartz containers before sealing off. This was done using glovebox and sealing-off procedures similar to those described above for handling the dried salts. The sealed mixtures were 'pre-mixed' by heating to at least 25°C above the liquidus (according to the relevant phase diagram) and maintaining at that temperature for more than 18 hours. The aim was to ensure the samples were thoroughly mixed and homogenous. These were then cooled as rapidly as possible, to minimise phase separation. In the final glovebox operation, the 'pre-mixed' samples were re-tubed into quartz sample containers, usually of 6 mm internal diameter and 1 mm wall thickness, before sealing off in the usual manner. At this stage, the samples were visually inspected to check for homogeneity and the quartz container checked for signs of chemical attack by the molten mixtures. Table 3.2 details the preparation of the mixtures and indicates if there were signs of chemical attack (such as pitting of the quartz surface and bonding between sample and quartz).

Fused quartz was used for sample containment mainly because of its general resistance to chemical attack. However, molten salts can be highly corrosive and effects on quartz such as devitrification (recrystallisation) may be expected to occur at high temperatures ($\geq 1000^\circ\text{C}$). The extent of such change depends of course on the precise temperature and time hence the checks after samples have been 'pre-mixed'. Another advantage of quartz is the extremely low coefficient of thermal expansion and the related property of high thermal shock resistance. In addition, because quartz lacks a distinct melting point (like most glasses) and softens over a broad temperature range it is an easy material to handle and shape ([3.3] gives further details on the properties of

quartz). The main disadvantage of quartz is that it is not a featureless scatterer of neutrons, so container peaks may be confused with those of the sample if the background subtractions or corrections are significantly in error. More suitable materials from this point of view, such as Ti-Zr alloy and vanadium, are prone to chemical attack (vanadium also presents problems with inelasticity corrections at high temperatures). Reducing the wall thickness of the quartz containers would have been the best means of minimising the problem but because of the high vapour pressures encountered, particularly with the NiCl₂ and AlCl₃ mixtures, a wall thickness of 1.0 mm was retained.

3.3 The neutron diffraction experiment

3.3.1 *Conducting the experiment*

Although the aim was to obtain accurate structure factors what is actually measured in a neutron diffraction experiment is the differential scattering cross-section (see chapter 2 - theory) of the sample. This was done by the usual method of normalising the sample scattering to the incoherent scattering of a vanadium reference sample after first normalising for the total incident flux (by dividing by the appropriate monitor count n) and subtracting relevant backgrounds. The general method is summarised in the following equation

$$\left(\frac{d\sigma}{d\Omega}\right)_s = \frac{N_v}{N_s} \left(\frac{d\sigma}{d\Omega}\right)_v \frac{S/n_s - C/n_c}{V/n_v - B/n_b} \quad (3.1)$$

where S , C , V and B refer to the sample, container (empty), vanadium and background scattering respectively and the N_s and N_v terms are the numbers of sample and vanadium atoms in the beam. The above simplified expression neglects the necessary corrections for absorption, multiple scattering and inelasticity. Details of these corrections and how they were applied are given in the next chapter which discusses data analysis.

The series of empty container, vanadium and background measurements required for the analysis of each sample were usually undertaken first. In the case of the empty container (a quartz tube of dimensions closely matching those of the sample containers) the scattering was measured at the same temperatures as the molten samples. This allowed a test of the Leicester furnace sample environment [3.4] used for heating, before risking actual samples. The vanadium scattering was usually measured in the furnace at room temperature using a rod of 8.0 mm diameter thus intercepting

approximately the same beam profile as the contained samples (typically of the same diameter). The furnace background was also measured at close to room temperature.

The sample scattering was measured at least 20°C above the melting point of pure salt samples or the temperature of the liquidus in the case of mixtures. The disappearance of Bragg peaks in the highest Q resolution (viz. highest scattering angle) bank of detectors was taken as indication of complete melting. Data was then collected in short (2-4 hour) scans so any time-dependent changes in sample or container scattering from incomplete mixing, chemical attack or devitrification could be monitored. Only scans which agreed (perhaps, after renormalisation) were used. Detector stability was also monitored by comparing the integrated (over all Q) counts from each detector in a group, scan by scan. The counts from unstable detectors were omitted. The measured samples were cooled quickly to just below the melting point of the composition before being cooled more gently (to avoid thermal shock to the sample container or the furnace element). The aim was to minimise phase separation so that a visual check of the homogeneity of the sample could be made after the run. It was also possible to check, very crudely, the liquid density of the sample by comparing the estimated height of liquid in the container against the often visible liquid tide-mark.

The diffractometers used in these experiments were both time-of-flight (TOF) instruments exploiting the pulsed beam of the Rutherford ISIS neutron source. The principle of TOF neutron diffraction can be understood from the equation for elastic scattering (eqn. 2.23) which suggests how to measure the scattering as a function of Q . Standard steady-state diffraction uses a continuous flux of neutrons of a fixed wavelength, selected from the white beam of a thermal reactor neutron source, to measure scattering as a function of Q by scanning in angle 2θ . In TOF neutron diffraction, however, a pulsed beam of neutrons with a distribution of velocities and hence wavelengths is used to measure scattering as a function of Q at fixed angle detector banks. From their arrival times at the detectors the scattered neutrons are sorted according to their time of flight over a known flight path (which depends on their velocity) hence effectively scanning in λ . Details of the TOF technique can be found in specialised texts such as [3.5].

TOF neutron diffraction has some advantages over the steady-state method. For example, the fast neutron background can be avoided by stopping counters between pulses (reactor sources must rely on shielding which is

never completely effective). The TOF method also makes efficient use of all wavelengths of neutrons generated in the pulsed beam. However, it is the high epithermal flux available from accelerator-based pulsed sources that provides the principal advantage of TOF over steady-state diffraction where the neutron beam is usually limited to thermal energies. The result is a higher Q_{\max} for TOF instruments like LAD (Liquids and Amorphous materials Diffractometer) although newer diffractometers like SANDALS (Small Angle Neutron Diffraction for Amorphous and Liquid Samples), by concentrating detectors at low scattering angles, have been more closely optimised to exploit epithermal neutrons. The LAD and SANDALS instruments, both used for the research in this thesis, are described in detail in the remainder of this chapter.

3.3.2 The LAD instrument

LAD is a total scattering instrument optimised for the study of amorphous solids and liquids. The wavelengths of incident neutrons, emerging from a liquid methane (100K) moderator, typically cover the range 0.1 - 7.0 Å. The Q range available is 0.2 - 100 Å⁻¹, although in practise data is only collected up to ~ 40 Å⁻¹. Figure 3.3 shows the layout of the instrument and the positioning of the detectors. There are 7 banks of detectors at mean scattering angles of $\pm 5^\circ$, 10° , 20° , 35° , 58° , 90° and 150° making a total of 14 detector groups. ³He gas-filled detectors make up the banks at 5° , 10° and 150° whereas the rest are scintillator banks. The resolution $\Delta Q/Q$ of the instrument³ varies from 0.5% at the 150° detector bank down to 10% at the 5° bank. The detectors are collimated to a width of about 4 cm at the sample position. The incident beam is usually collimated to a rectangular shape of maximum height 40 mm and width 20 mm, although this can be altered by the use of beam-defining slits.

The count rate of an instrument can be gauged from the 'C-number' (count rate per Q bin per unit volume of a standard vanadium scatterer) which, in the case of TOF diffractometers, varies as a function of Q and also depends on the scattering angle 2θ (particularly when there are different types of fixed detectors). The count rate on LAD, when counts from all detector groups are integrated, matches that of the D4B diffractometer but only in a narrow region of Q around 1 Å⁻¹. Reference [3.7] (appendix B) provides a detailed explanation of the 'C-number' as a performance index and also provides

³ The quantity $\Delta Q/Q$ is approximately constant for a given 2θ detector angle.

measured values (pg. 1.10) for each of the LAD detector banks at a given value of Q .

Experience with conducting experiments on LAD has highlighted some recurrent problems with detector stability and normalisation. The scattering (calibrated to vanadium) from some of the opposing groups of detectors would often show a normalisation error of as much as 20%. In addition, the data from the 5° and 10° banks was often unusable not only because of low Q resolution but also the poor match, even after renormalisation, with the scattering from other groups.

3.3.3 *The SANDALS instrument*

SANDALS is a high performance, low angle, total scattering instrument for the measurement of structure factors in amorphous solids and liquids. The instrument exploits the high epithermal flux from ISIS thus benefiting from reduced sample absorption and improved statistics. The wavelength range of incident neutrons, emerging from a poisoned liquid methane (100K) moderator, is typically 0.05 - 4.0 Å. The use of epithermal neutrons allows the detectors to be concentrated at low scattering angles and yet still provide an acceptable Q range. The combination of high neutron energies and low scattering angles minimises the magnitude of the recoil corrections necessary and thus facilitates the study of materials containing light atoms.

Figure 3.4 shows the layout of SANDALS and the positioning of detector groups. The detectors are of a ZnS scintillator type and use coincidence counting from photomultiplier tubes to reject spurious background. They are arranged on the inside of a slightly tapered cylinder forming a surface of near constant resolution ($\Delta Q/Q \sim 3\%$). This is because the detectors set at lower scattering angle have a longer flight path, although the corollary of this is that they also have poorer statistics. The full design complement of detectors (see table 3.3), arranged in four banks, will eventually cover the range of scattering angles from 3° to 41° in a continuous span. A limited detector complement was available at the time of the SANDALS experiments described in this thesis (the AlCl_3 mixtures study in chapter 8). The measurements of the AlCl_3 -NaCl mixtures were conducted on an instrument with 360 detectors arranged to give continuous coverage of the scattering angle range 11° - 21°. For the purposes of data analysis the detectors were grouped into 6 at average angles 11.79°, 13.07°, 14.61°, 16.23°, 18.09° and 20.12°. The AlCl_3 -LiCl mixtures experiment conducted later, benefited from additional detectors covering the

scattering angle range $3^\circ - 11^\circ$. These detectors provided another 4 groups at average angles 3.88° , 5.02° , 6.75° and 9.34° . The usable Q range of the data collected in these experiments was $\sim 0.4 - 25 \text{ \AA}^{-1}$. The statistics of the instrument peaked at $Q \approx 1.0 \text{ \AA}^{-1}$ and the 'C-number' (integrated for all detectors) was already equal to or better than D4B up to $\sim 5.0 \text{ \AA}^{-1}$ [3.8] at the time of these experiments.

The major problem encountered with the use of this instrument was the very large furnace background which often accounted for as much as 60% of the total scattering measured from a sample. Clearly, because this is a small angle scattering instrument a large background is to be expected since the detectors view more of the furnace directly illuminated by the neutron beam than at high angles. However, the use of epithermal neutrons, with their negligible absorption cross-sections, gives rise to severe problems with any attempt to collimate either the detectors or the incident beam. Collimating the detectors leads to a greatly increased instrument background because of the scattering from the collimators themselves, even when made of highly absorbing BC_4 . Consequently, the detectors on SANDALS were left uncollimated and have an effectively unrestricted view of the entire furnace. The circular (32 mm diameter) main beam was defined by a series of collimators placed well back from the sample position so any background was stopped by the surrounding massive shielding.

An attempt was made in a series of tests aimed at reducing the furnace background, conducted with the assistance of A.K. Soper (instrument scientist), to match the shape of the incident beam more closely to the sample geometry by using a rectangular aperture (thereby minimising the amount of illuminated furnace vanadium). However, the resulting reduced furnace background was at the expense of increased background from the instrument. Since neither effective collimation of the incident beam nor of the sample scattering to the detectors was possible, a reliable furnace correction scheme was essential for successful analysis of the SANDALS data. The following chapter on data analysis gives further details of the tests conducted to establish the precise sources of the large furnace background and of the furnace correction scheme developed to deal with this problem. Even with a reliable furnace correction there was significant disagreement at low Q between the spectra from different detector groups. This is believed to be due to a modified background when there is a sample in the beam. Fortunately, the effect appears to be confined to increased slopes on the data which were readily removed in a manner also described in the next chapter.

3.4 References

- [3.1] T.G. Dunne & N.W. Gregory, 1958, *J. Am. Chem. Soc.*, **80**, pp.1526-1530
- [3.2] D.R. Lide (editor), 1991, "CRC handbook of chemistry and physics", 72nd edition, CRC press, Boston
- [3.3] Catalogue, 1990, "Scientific, laboratory glassware, in clear fused quartz", Multi-lab LTD., Tynevale works, High street, Newburn, Newcastle upon Tyne NE15 8LN
- [3.4] N.D. Wood, 1987, 'The study of the structure of molten nickel halides by neutron scattering', Ph.D thesis, University of Leicester, chapter 3
- [3.5] C.G Windsor, 1981, "Pulsed neutron scattering", 3rd edition, Taylor & Francis, London.
- [3.6] B. Boland & S. Whapham, 1992, "ISIS user guide - experimental facilities", Rutherford Appleton Laboratory, Chilton, Didcot
- [3.7] A.K. Soper, W.S. Howells & A.C. Hannon, 1989, "ATLAS - analysis of time-of-flight diffraction data from liquid and amorphous samples", RAL report RAL-89-046
- [3.8] A.K. Soper, 1992, private communication

<u>Vacuum drying parameters</u>			
Salt	Max. temp. (°C)	Duration (days)	Final vacuum pressure (torr)
NiCl ₂	300	7	6. x 10 ⁻⁶
ZnCl ₂	100	14	2. x 10 ⁻⁶
KCl	250	7	5. x 10 ⁻⁶
LiCl	250	7	4. x 10 ⁻⁶
NaCl	250	7	1. x 10 ⁻⁶

Table 3.1. Details of the vacuum drying procedure for the single salts. The maximum temperatures reached and the duration of the drying process are shown. The final vacuum pressures attained, with no liquid nitrogen in the cold trap of the diffusion pump, are also shown.

<u>Mixing parameters</u>			
Mixtures	Mixing temp. (°C)	Duration (hours)	Comments
NiCl ₂ -LiCl	1040	18	Sample tubes crack on cooling (possible expansion of solid?). Some roughening of quartz surfaces although solid can be removed cleanly.
NiCl ₂ -KCl	1040	18	High temperature needed to melt NiCl ₂ and ensure mixing. Little sign of chemical attack especially at high KCl concentration where solid comes away cleanly from quartz.
ZnCl ₂ -LiCl	500	18	Little sign of chemical attack and solid comes away cleanly from quartz.
ZnCl ₂ -KCl	550	18	Some tendency to stick to quartz, indicating limited bonding.
AlCl ₃ -LiCl	300	48	Extra time needed to mix two liquids present in AlCl ₃ -rich compositions. Samples 'pre-mixed' at least twice. No signs of chemical attack - quartz surfaces remain smooth.
AlCl ₃ -NaCl	300	48	Again, extra time needed to mix two liquid phases. No signs of chemical attack.

Table 3.2. Details of the preparation of the mixtures, including typical temperatures and durations of mixing, along with comments concerning signs of chemical attack etc.

Bank	Number of detectors		Resolution
	Design	Actual (1992)	$\Delta Q/Q$
3° - 11°	300	100	0.03 -0.16
11° - 21°	600	360	0.03
19° - 31°	400	0	0.03
29° - 41°	200	0	0.02

Table 3.3. The design and actual complement of detectors on ISIS SANDALS, as of December 1992 [3.6]. There is provision for additional detectors to be installed up to a scattering angle of 120°.

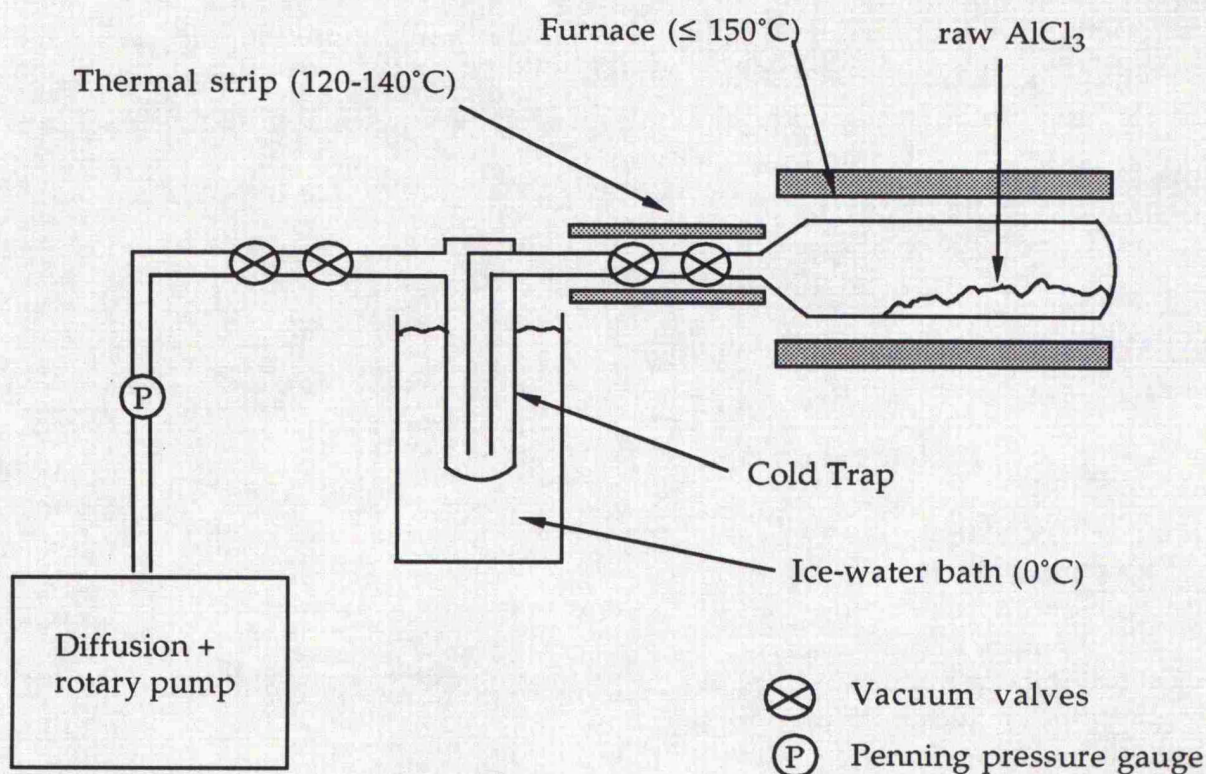


Figure 3.1. Schematic diagram of the sublimation-drying kit used in the preparation of AlCl_3 . The thermal strip was essential to prevent premature condensation of the sublimed AlCl_3 before it reached the trap.

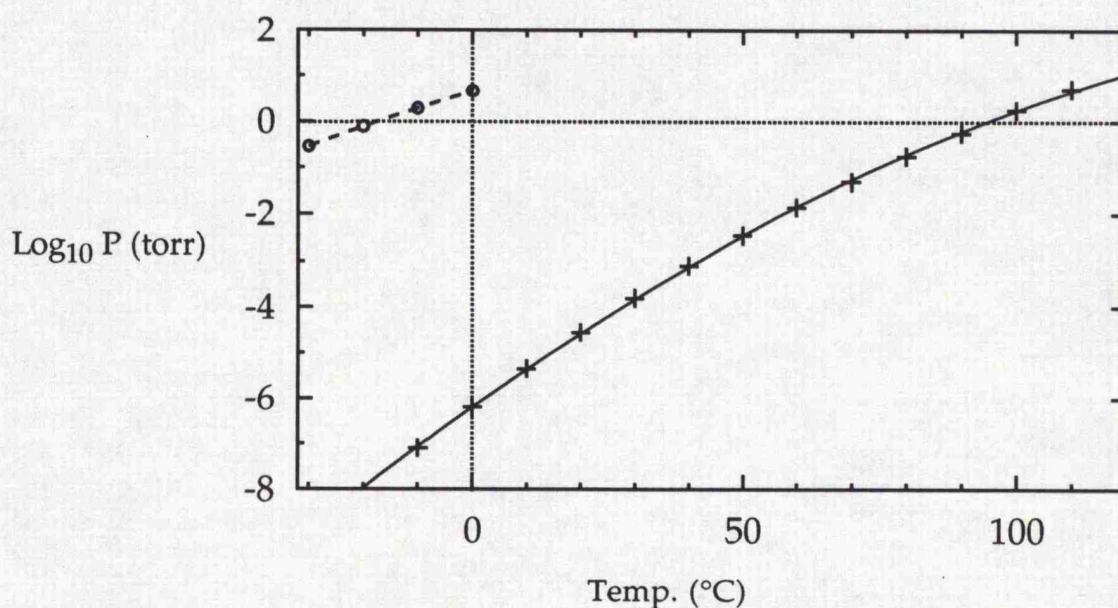


Figure 3.2. Comparison of the vapour pressures of solid AlCl_3 (+ and solid curve)[3.1] and ice I (o and dashed curve)[3.2].

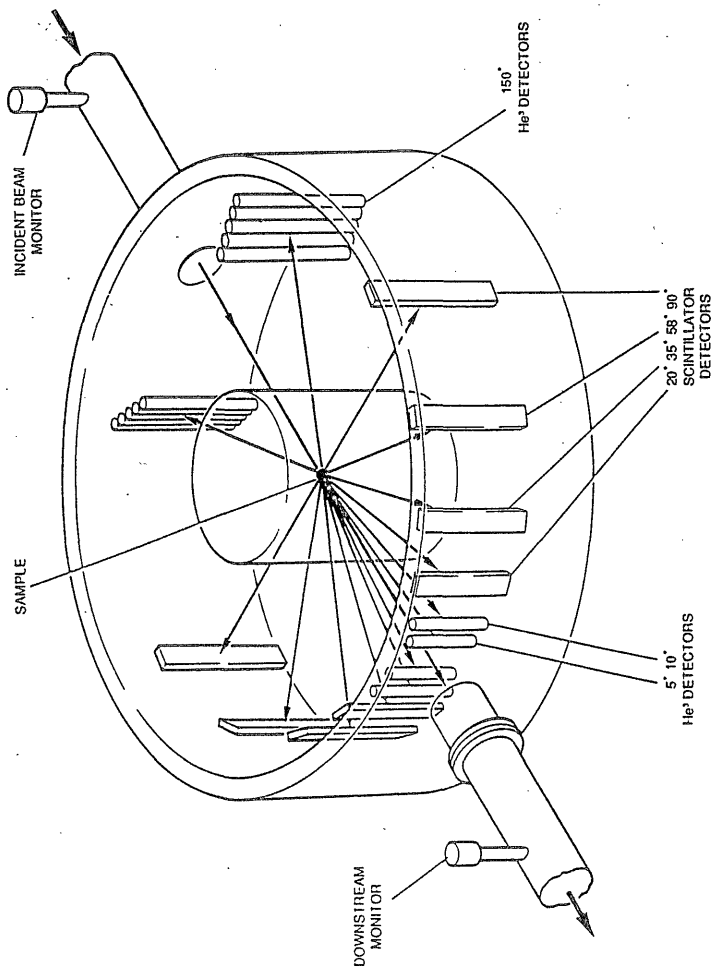


Figure 3.3. Diagram of the LAD instrument [3.6], showing the sample position and layout of detectors as of December 1992. Note there is a monitor for the transmitted as well as the incident beam ; together these are used to calculate sample cross-sections.

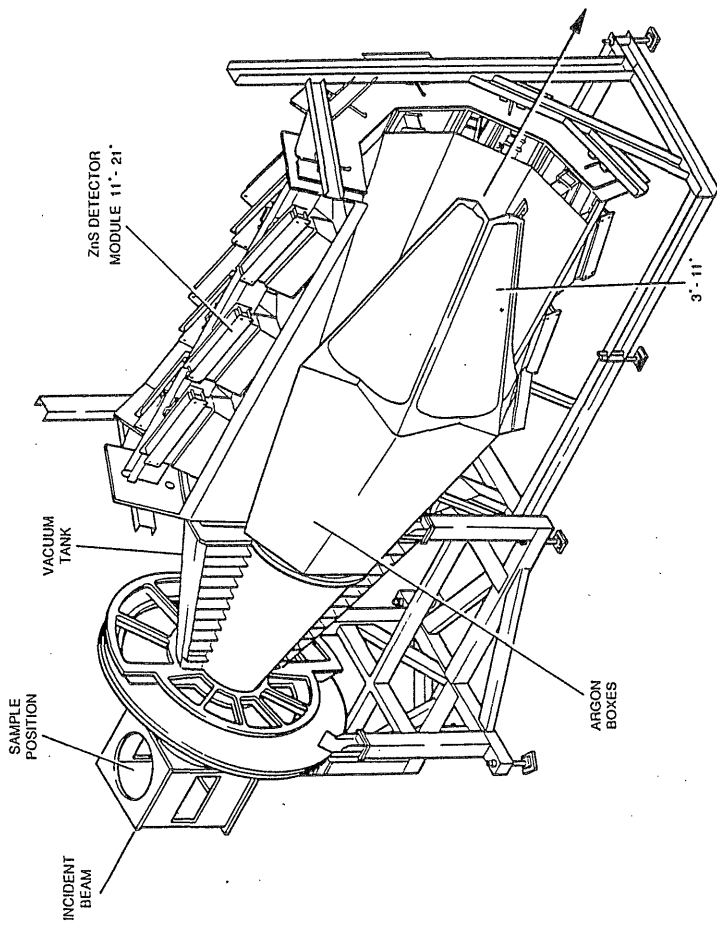


Figure 3.4. Diagram of the SANDALS instrument [3.6], showing the sample position and layout of detectors as of December 1992. There is a monitor for the incident beam but this is not shown as it is much further 'upstream' in the beam guide.

Chapter 4

Data analysis

4.1 Introduction

In the previous chapter, the importance of obtaining accurate structure factors and reliable pair distribution functions was emphasised. In practise, this entails making corrections to the raw data (which also has to be normalised) for counter deadtime, detector efficiencies, background scattering, multiple scattering, attenuation and inelasticity. The first part of this chapter provides an outline of the general TOF data analysis procedure, in particular the corrections, and is followed by a discussion of the specific problems with data reduction encountered on the LAD and SANDALS instruments.

4.2 General procedure for the analysis of TOF data

The data was analysed using the Rutherford ISIS ATLAS package for which further details can be found elsewhere [4.1]. The steps in the general sequence of analysis, as shown by the flow diagram of figure 4.1, are now described in turn.

4.2.1 *Correction for counter deadtime and normalising to the incident neutron spectrum*

The first correction to be applied is for counter deadtime. This is because all detectors are 'dead' and unable to record another neutron event for a short period after a neutron has been counted. The deadtime correction is normally only of the order of a few percent and so can be made using a simple formula (see [4.1], pg. 2-3). Having corrected for counter deadtime, the usual next step is to normalise to the incident neutron spectrum. This is done by dividing the sample counts by the counts registered by a monitor detector positioned in the incident beam just ahead of the sample. This has the effect of

normalising for the wavelength distribution of the incident beam as well as for the time-integrated flux deposited on the sample. The reason it is performed at this stage is to take into account the small (1-2%) variations in the incident spectrum due to changes in proton beam steering and moderator temperature. The normalised scattering is now in the form of count rate per Q -bin.

4.2.2 Measuring the wavelength-dependent total cross-section

The total cross-section for neutrons, $\sigma_T(\lambda)$, arises from the two main processes of scattering and absorption such that

$$\sigma_T(\lambda) = \sigma_{sc}(\lambda) + \sigma_a(\lambda) \quad (4.1)$$

where $\sigma_{sc}(\lambda)$ is the total scattering cross-section and $\sigma_a(\lambda)$ is the absorption cross-section. Although the wavelength dependence of absorption, resulting from the inverse linear relationship between probability of capture and neutron velocity, is common knowledge, the dependence of the scattering cross-section on neutron energy is less widely appreciated. This dependence arises because the scattering cross-section actually represents the integral of the differential scattering cross-section, at a given wavelength, over all scattering angles i.e.

$$\sigma_{sc}(\lambda) = \int \frac{d\sigma}{d\Omega}(\lambda) d\Omega = 4\pi \int \frac{d\sigma}{d\Omega}(\lambda) \sin 2\theta d\theta \quad (4.2)$$

in the static approximation. Hence $\sigma_{sc}(\lambda)$ will deviate from its 'bound' value (as usually quoted in tables such as that of Sears [4.2]) for materials with structure. Furthermore, $\sigma_{sc}(\lambda)$ will also vary dramatically between its 'bound' and 'free' values with neutron energy for samples containing light atoms. Since $\sigma_T(\lambda)$ clearly depends on the details of $S(Q, \omega)$ and thus the thermodynamic state of the sample, it should (ideally) be measured for each sample during the diffraction experiment itself. An accurate $\sigma_T(\lambda)$ leads to improved corrections for multiple scattering and attenuation¹. In order to measure $\sigma_T(\lambda)$, a transmission monitor is usually placed after the sample. The energy dependence of the total cross-section is determined from the incident and transmitted neutron spectra.

¹ Sometimes the term absorption is used in place of attenuation although the latter is more precise since the scattering process also contributes to a reduction in neutron flux.

4.2.3 Corrections for multiple scattering

Clearly, some neutrons will scatter from the sample more than once before being detected, and, since single scattering is assumed in the theory, corrections must be made for such multiple scattering. The multiple scattering contribution to the differential scattering cross-section (DCS) can't be evaluated exactly because this requires detailed knowledge of sample structure and dynamics (if inelastic scattering is significant). Hence the usual approaches to calculation involve making some assumptions particularly about primary scattering. In the ATLAS algorithm, the scattering cross-section, as determined from $\sigma_T(\lambda)$, is used to calculate the multiple scattering at each wavelength which, in the isotropic approximation, is assumed to be uniform with scattering angle. Improved calculations, perhaps using a Monte Carlo algorithm as described by Sears [4.3], are needed to deal with thick samples. However, the general consensus is that the isotropic approximation will give acceptable results if the sample scatters less than $\sim 20\%$ of the incident beam. As all the thesis experiments used samples which were approximately 10% scatterers, the ATLAS algorithm was appropriate in all cases.

4.2.4 Corrections for attenuation

Corrections for attenuation are necessary because of the reduction of the incident and scattered neutron flux by the sample itself (self shielding) as well as furnaces, shields, container etc. thus the experimental scattering intensity, I_{sc}^e , for the simple case of a sample in a container is given by

$$I_{sc}^e = A_{s,sc}I_s + A_{c,sc}I_c \quad (4.3)$$

where I_s and I_c represent the scattering from the separate sample and container, respectively. Instrument backgrounds, which are usually small anyway, have been neglected in the above simple formulation. The coefficients, $A_{i,j}$, are the usual Paalman and Pings [4.4] attenuation factors where the scattering occurs in region i and attenuation occurs in region(s) j . The attenuation factors depend only on sample geometry and the total cross-section so they can be calculated, in the static approximation, to whatever numerical precision is required. The ATLAS package uses the formalism of Soper and Egelstaff [4.5] which involves numerical integrations to estimate the corrections for a cylindrical geometry (as illustrated in figure 4.2). The

advantage of this formalism is that it is sufficiently general as to allow additional corrections for furnaces and radiation shields to be incorporated if these are significantly absorbing or scattering.

4.2.5 *Smoothing the vanadium scattering*

A standard vanadium sample is used to independently calibrate for instrument factors, such as detector efficiencies, because vanadium has a largely incoherent scattering cross-section ($\sigma_{inc} = 5.08$ bn) so the DCS for this element can, in theory, be estimated reasonably accurately. In fact, the scattering from vanadium exhibits the usual statistical noise plus some weak Bragg peaks due to the small coherent cross-section ($\sigma_{coh} = 0.018$ bn). Since the sample scattering has to be divided by the vanadium calibration, steps must be taken to ensure neither effect is propagated to the data. To do this, an expansion in terms of Chebyshev polynomials, with zero weighting of points in the regions of Bragg peaks, is used in the routine VANSM to produce a best fit to the normalised vanadium scattering. This has the effect of smoothing out the noise while simultaneously removing the Bragg peaks. The order of the polynomials fitted were adjusted to give the optimum smooth fit (as judged from the residuals) without introducing spurious ripples.

4.2.6 *Calculating the differential cross-section*

The smoothed vanadium scattering is divided by the calculated calibration correction which takes into account multiple scattering, attenuation and also includes a vanadium inelasticity (Placzek) correction. The resulting vanadium calibration, $CAL_V(Q)$, can be written as

$$CAL_V(Q) = \frac{E_d(K)}{E_m(K)} \Delta\Omega \quad (4.4)$$

([4.1], pg. 2-14)

where E_d and E_m are the detector and monitor efficiencies, respectively. It is now possible to evaluate the sample DCS by applying the calculated multiple scattering and attenuation corrections when subtracting the backgrounds from the sample scattering and finally calibrating to vanadium. The algorithm used in the routine ANALYSE to calculate the DCS for the simple case of sample in a container is shown in appendix A1. Note that the sequence of steps is critical. For example, the multiple scattering must be

subtracted before the attenuation corrections can be applied because the theory for the latter assumes only single scattering. The final step (5) accounts for the number of scattering centres i.e. atoms in the neutron beam so that the final DCS is in units of barns per unit steradian per atom.

4.2.7 Inelasticity (Placzek) corrections.

As explained in section 2.2.4, the assumption of wholly elastic scattering i.e. the static approximation means that (theoretically) the integration of the double differential cross-section occurs at constant Q . In practise, what is actually measured is the very complicated TOF differential cross-section (see [4.1], eqn. 1.2.12) and an inelasticity correction for the difference between this and the desired $F(Q)$ is required. Ideally, the correction would be determined from a knowledge of the dynamical structure factor, $F(Q, \omega)$, but this would obviate the need for a diffraction experiment ! Fortunately, Placzek [4.6] showed that for large atoms (those having masses much greater than that of a neutron) the inelasticity correction is essentially independent of the detailed dynamics of the system and is related to simple parameters such as nuclear mass, sample temperature etc. Inelasticity corrections based on the Placzek approach only compensate for the recoil of single particles and do not take into account the effects of any collective (phonon) modes in the sample. The Placzek correction, $P(Q, \theta)$, is largest for light atoms and larger scattering angles as the energy integration path deviates further from constant Q . The ATLAS routine PLATOM uses a modification of the Powles formula [4.7] derived by Howe *et al* [4.8]. The correction is calculated solely for the self scattering, I^s , and the corrected function, I_{corr}^s , is subtracted (using the INTERFERE routine) from the DCS to give the distinct scattering corresponding to the second term in eqn. 2.25. Note that because the DCS is theoretically asymptotic to $\bar{\sigma}_s/4\pi$ at high Q (see section 2.2.4), the measured cross-section is normalised to this level prior to subtracting I_{corr}^s .

4.2.8 Merging the data

The counts from all the detectors, which up to this point have been ordered into detector groups centred at nominal scattering angles, need to be merged to form a single composite $F(Q)$ with improved statistics and an optimum Q range. In practise, the choice of Q -ranges for each detector group to be included depends to a some extent on the judgement of the experimentalist. The general approach adopted was to only merge those regions of each

spectrum which overlapped with at least one other neighbouring group at lower or higher scattering angle. Good agreement between the spectra from neighbouring groups provides confidence in the accuracy of the corrections employed especially those which vary greatly with scattering angle i.e. attenuation and Placzek. If a spectrum differed markedly from most of the others it could be rejected entirely. The merging of data is achieved in the MERGE routine by a flux-weighted averaging over the specified Q -ranges.

4.2.9 Fourier transformation : $F(Q) \Rightarrow G(r)$

The composite $F(Q)$ has now to be Fourier transformed (see eqn. 2.30) into the corresponding total pair distribution function². However, the limitations of an experimental $F(Q)$ function lead to systematic errors in the calculated $G(r)$. The finite upper limit of the diffraction data, Q_{\max} , gives rise to spurious termination ripples of period π/Q_{\max} throughout real space. This is because $F(Q_{\max})$ is invariably not quite zero so that, in effect, the structure factor is multiplied by a step window function with a value of unity up to Q_{\max} and zero there-after. Obviously, a careful choice of the Q_{\max} to be used in transformation needs to be made so as to minimise truncation at high Q and any possible loss of structural information. In addition, the statistical noise at high Q will also contribute significantly to termination ripple because of the Q^2 dependence of the Fourier transform (conversely, this also means that the extrapolated low- Q portion of $F(Q)$ has little effect on $G(r)$). The finite Q_{\max} also limits the resolution of peaks in real space to $\Delta r = 2\pi/Q_{\max}$. By varying Q_{\max} it is possible to begin to distinguish between ripple and data from the resulting transforms. It is also possible to suppress termination ripple by using a window function, $W(Q)$, that tapers $F(Q)$ smoothly to zero at Q_{\max} . However, the $G(r)$ is now convoluted by a peak shape function with increased side-lobes leading to a further worsening of the real space resolution. The window function used for some of the results in this thesis was the cosine function which is of the form

$$W(Q) = \left\{ \frac{1}{2} + \frac{1}{2} \cos \left[\frac{\pi(Q-Q')}{(Q_{\max}-Q')} \right] \right\}^n \quad \text{for } Q' < Q \leq Q_{\max} \quad (4.5)$$

² Prior to transformation, the missing low- Q portion of the data was always fitted with a smooth curve leading to the theoretical long-wavelength limit if this was known - otherwise it was simply extrapolated.

with $W(Q)$ being equal to unity up Q' (n is simply the adjustable order of the cosine function). The window function was always applied over the smallest fraction of the data as possible i.e. Q' close to Q_{\max} . Although the use of a window function has the advantage that its effects on $G(r)$ are predictable, in practise it was usually found that removal of most of the ripple entailed an unacceptable broadening of the data peaks. For this reason, an alternative approach involving smoothing of the structure factor data at high Q was generally favoured. This was done by fitting a piece-wise cubic spline with knots of non-uniform spacing as defined by the equation $a+bQ^2$. The transform of the smoothed $F(Q)$ was always compared to the original and with the result of using the window function, in order to confirm that mainly ripple was removed with marginal effect on the 'real' peaks (see figures 8.1-2).

4.2.10 Checks on $F(Q)$ and $G(r)$

Given the likelihood of errors in parameters such as density, the actual amount of sample and sample container in the beam etc. it is necessary to employ a few simple rules to check the results of data analysis. Below is a brief outline of the main rules and constraints usually employed.

- i) As mentioned earlier, at high Q the DCS should be asymptotic to the theoretical self scattering - if not, the data is renormalised to this level. Once the self scattering is subtracted, the resulting $F(Q)$ should oscillate about zero at high Q .
- ii) At low Q , $F(Q)$ should be asymptotic to the thermodynamic long-wavelength limit as given by

$$F(Q \rightarrow 0) = \delta - \sum_{\alpha=1}^n c_{\alpha} \bar{b}_{\alpha}^2 \quad (4.6)$$

where α is the atomic species and δ takes account of the small contribution from isothermal compressibility.

- iii) At low r , the total pair distribution function should tend to the theoretical base-level dependent on sample composition as given by

$$G(r \rightarrow 0) = \left(\sum_{\alpha=1}^n c_{\alpha} \bar{b}_{\alpha} \right)^2 \quad (4.7).$$

In practise, $G(r)$ oscillates about this value at low r because of termination ripple and also often exhibits prominent artefacts due to spurious slopes on the $F(Q)$ data.

iv) $G(r)$ should also exhibit peaks at the distances expected from a knowledge of sample composition and atom sizes. Definite peaks or troughs at $r \sim 1.6$ and ~ 2.6 Å usually indicate container under/over-subtraction since they correspond to the Si-O and O-O nearest neighbour distances for quartz.

4.3 Analysis of LAD data

The most significant problem encountered with LAD data was the presence of an unexpected droop at high Q in the DCS spectra generated using the routine ANALYSE. The DCS had been expected to be asymptotic to a single value at high Q , with some renormalisation usually required to make this equal to the theoretical self scattering level. However, as can be seen from figure 4.3, the DCS falls off with increasing Q and this high- Q droop generally becomes more pronounced with decreasing scattering angle. These observations make it possible to discount any link with inelasticity effects although they do indicate a correlation with neutron energy (the fall-off seems to start at around $\lambda = 0.1$ Å). The link with neutron energy suggests that at high Q we may be in the wings of a broad absorption resonance. However, in the case of our samples the only possible species that could be responsible for this is chlorine and other users have not always observed a pronounced high- Q droop with their samples also containing chlorine. Another possible cause is the vanadium calibration which is usually performed at close to room temperature (to minimise the difficult correction for inelasticity) and may be inappropriate for the high temperatures of our samples. However, this implies that heat from the water-cooled furnace affects the stability of the detectors which seems rather improbable. The difference between the actual and measured backgrounds for the vanadium and sample scattering is much more likely to be the cause of the high- Q droop. In our experiments, the scattering for the vanadium rod was always greater than for the sample. In addition, the sample-dependent background may be expected to increase with neutron energy (because there is less absorption) and with decreasing scattering angle as more of the furnace

becomes visible. Although sample-dependent backgrounds would explain the trends observed with the high- Q droop phenomenon they still might not be the true explanation - further work is necessary to fully resolve this matter.

As regards processing the data, a droop at high Q obviously makes determination of the true asymptotic level, and thus the correct renormalisation factor, rather difficult. The approach taken to dealing with this problem was to rely on the renormalised high-angle detector groups (least affected by droop) as a guide to renormalising the remaining spectra. In the case of the mixtures described in chapter 6, the regions of the data clearly affected by droop were not used in the merged structure factor. However, for the isotopic data discussed in chapter 7, the SUBSELF program (described in more detail in section 4.4 below) was used to remove the spurious slopes in the DCS spectra thus allowing better statistics at high Q in the final structure factors. An inevitable consequence of high- Q droop is increased uncertainty in the absolute normalisation, which is reduced to probably no better than approximately $\pm 5\%$. The uncertainty was compounded by the fact that in most cases no isothermal compressibility data was available so it was not possible to check the absolute normalisation using the long-wavelength limit.

Some of the other difficulties associated with LAD data analysis were :

i) Obtaining a reliable total cross-section ; this was because the LAD transmission monitor does not sample the beam uniformly but uses a square grid of elements spaced 5 mm apart. This problem was tackled by always using a vanadium rod of similar diameter (8 mm) to the samples so as to cast a similar shadow on the transmission monitor. This allows the effective beamwidth (i.e. the value which gives the theoretical 'free' scattering and capture cross-sections for vanadium from the transmission calculation) to be determined (see [4.1], pg. 3-24).

ii) The poor coverage at low Q ; this arises, in part, because the 5° detector banks agreed poorly with the others and were consequently almost unusable. In addition, the 10° bank included relatively few detectors so that the bulk of the counts in the important region of the FSDP usually came from just the 20° bank (see table 4.1).

iii) Large variations in the relative normalisation of some detector groups ; the reasons for which are not clear. Table 4.1 illustrates this point with the 10

and 20° banks showing large differences in the renormalisation factors for opposite groups of detectors. The most likely cause is detector instability.

4.4 Analysis of SANDALS data

The first problem encountered in the analysis of SANDALS data was the presence of Bragg peaks in the incident monitor spectrum. These peaks were due to the vanadium beads used to scatter neutrons into the path of the monitor detector positioned to one side of the incident beam. The Bragg peaks meant that the measured scattering could not simply be divided by the monitor spectrum as described earlier in section 4.2. An alternative method of normalising each measurement for the integrated incident flux had to be adopted and this involved adjusting the way the DCS was calculated. The modified scheme simply involved taking the ratio of the monitor spectra so that the calculation for the sample DCS was *effectively* equivalent to the following simple formula

$$DCS(Q) = \left(\frac{I_{sc}(Q) - I_c(Q) \frac{m_{sc}}{m_c}}{I_v(Q) - I_b(Q) \frac{m_v}{m_b}} \right) \frac{m_v N_v}{m_s N_s} \quad (4.8)$$

where the subscript v refers to vanadium, the other subscripts are as in appendix A1, the symbol m refers to the incident monitor spectrum and the corrections for attenuation etc. have been omitted for clarity. This method assumes that the monitor spectra all retain the same shape so the neutron to proton ratio had to be carefully observed for the duration of the experiment and any scans coincident with apparent instabilities in moderator temperature etc. had to be discarded. A further problem with SANDALS was the lack of a transmission monitor so the $\sigma_T(\lambda)$ function used to calculate the corrections was always a theoretical one (assuming no structure). The experimental DCS could have been used to calculate a more realistic total cross-section via eqn. 4.2 but this refinement did not appear necessary given the excellent agreement eventually obtained between the data from different detector groups.

As pointed out in chapter 3, a large furnace background is an inevitable consequence of the geometry of the SANDALS instrument which is optimised for small-angle scattering and to use epithermal neutrons. Typically, the scattering from the empty furnace was approximately two-

thirds of that obtained from a measurement including a sample (see figure 4.4). Tests were conducted in order to establish the main sources of this background and these revealed that removing all the radiation shields only reduced the scattering by about 15% but removing the thick (~ 0.5 mm) vanadium foil windows on the front and back of the furnace holder (see figure 4.5 for details of the furnace geometry) lowered the furnace background by one-third. These results suggest that the biggest single contribution (~ 50%) to the furnace background arises from the furnace element. This is not surprising given that the diameter of the element is less than the width of the incident beam. Reducing the amount of furnace vanadium in the beam by making cut-outs in the strongly scattering sides of the element or increasing its diameter were not viable options because both would have affected furnace performance adversely and increased the risk of thermal inhomogeneities in heated samples. It has recently become possible to significantly reduce furnace background by halving the thickness of the vanadium foil windows although this improvement came too late to benefit the experiments in this thesis. Since it was not possible to substantially reduce the background, an accurate furnace correction scheme had to be employed (appendix A2 shows the modified algorithm for calculating the DCS³). For the purposes of the correction, all the furnace vanadium was considered to be integrated into a single annulus at the appropriate weighted-average distance from the sample. Clearly, the correct dimensions for this representative vanadium annulus were required. The approach used to solve this problem was to systematically vary first the radius and then the thickness of the annulus until the calculated DCS spectra for samples of pure molten LiCl (640°C) and NaCl (820°C) appeared to be consistent at low Q with the theoretical long-wavelength limits. The inner and outer annular radii obtained in this way were 10.0 and 10.05 cm, respectively, and these parameters were used in all subsequent analyses⁴.

Despite the use of an accurate furnace correction, there was poor agreement between the DCS spectra from different detector groups (see figure 4.6). This is

³ The algorithm strictly only applies to data analysis on LAD because of the complications with the SANDALS transmission monitor but it does show the general approach taken with furnace corrections.

⁴ Note that tests indicated the position of the annulus to be the most important parameter, with the thickness making comparatively little difference to the resulting DCS. This is because the ratio of the attenuation factors in step 4 of appendix A2 remains virtually unchanged when the thickness is altered. However, the calculated multiple scattering does change significantly but in practise this only affects the normalisation. The nominal thickness used was the sum of the thicknesses of the radiation shields and the furnace element.

believed to be due to sample-dependent background which in the case of SANDALS is particularly unpredictable because of the high epithermal flux. Detector groups 1 and 2, corresponding to mean angles of 11.79 and 13.07° (see table 4.2), are clearly divergent at low Q ($\leq 2.0 \text{ \AA}^{-1}$) compared to the remaining detector groups. Fortunately, the sample-dependent background is mostly in the form of monotonic slopes giving rise to spurious features at low r in real space. Thus it was possible to use a program, SUBSELF, developed by the SANDALS instrument scientist, A. K. Soper, to remove the slopes in Q space and greatly improve the agreement between detector groups. The program worked by first fitting a low order (usually $n=2$) polynomial to the data which was then subtracted in order to remove the high- Q droop (evident on SANDALS data as well as that from LAD). From the transform of the result, a correction for the low- r region to make it as close as possible to the theoretical flat $G(0)$ base-level was calculated and applied. The resulting DCS spectra match well for groups 2-5 across virtually the entire Q -range. However, spectra 1 and 6 do not match so well at low Q and their renormalisation factors differ markedly from the other groups (see table 4.2) suggesting there remains a problem with detector stability and/or residual sample-dependent background. In the case of the experiments where additional detectors covering the 3-11° range were available, the two lowest angle detector groups (3.88 and 5.02°) were often completely unusable. The generally good agreement between detector groups, especially at low Q , suggested an inelasticity correction would be redundant therefore no such correction was applied.

4.5 References

- [4.1] A.K. Soper, W.S. Howells & A.C. Hannon, 1989, " ATLAS - analysis of time-of-flight diffraction data from liquid and amorphous samples", RAL report RAL-89-046
- [4.2] V.F. Sears, 1992, *Neutron News*, **3**(3), 26-37
- [4.3] V.F. Sears, 1975, *Adv. Phys.*, **24**, 1
- [4.4] H.H. Paalman & C.J. Pings, 1962, *J. Appl. Phys.*, **33**, 2635
- [4.5] A.K. Soper & P.A. Egelstaff, 1980, *Nucl. Inst. Meth.*, **178**, 415-425
- [4.6] G. Placzek, 1952, *Phys. Rev.*, **86**, 377
- [4.7] J.G. Powles, 1978, *Mol. Phys.*, **36**, 1181
- [4.8] M.A. Howe, R.L. McGreevy & W.S. Howells, 1989, *J. Phys. : Condens. Matter*, **1**(22), 3433-3451

Detector group	Renormalisation factor	Merge ranges (\AA^{-1})	
		Q_{\min}	Q_{\max}
1 (+5°)	1.08	- unusable	-
2 (-5°)	1.12	1.5	5.35
3 (+10°)	1.02	0.4	9
4 (-10°)	1.03	0.4	9
5 (+20°)	1.05	1.5	20
6 (-20°)	0.95	7.0	20
7 (+35°)	1.0	1.25	25
8 (-35°)	1.02	1.20	25
9 (+60°)	1.02	1.85	25
10 (-60°)	1.02	1.85	25
11 (+90°)	1.0	5.30	25
12 (-90°)	1.03	5.25	25
13 (+150°)	1.03	11.0	25
14 (-150°)	1.04	10.2	25

Table 4.1. Typical renormalisation factors and Q -ranges used for merging spectra from different detector groups on LAD. The average scattering angle for each group is given in brackets.

Detector group	Renormalisation factor	Merge ranges (\AA^{-1})	
		Q_{\min}	Q_{\max}
1 (11.4°)	1.36	2.5	25
2 (13.7°)	1.14	0.5	25
3 (15.3°)	1.10	0.425	6.95
4 (16.9°)	1.06	0.425	22.5
5 (18.9°)	1.16	0.425	20
6 (22.1°)	1.34	1.5	18

Table 4.2. Typical renormalisation factors and Q -ranges used for merging spectra from different detector groups on SANDALS. Again, the average scattering angle for each group is given in brackets.

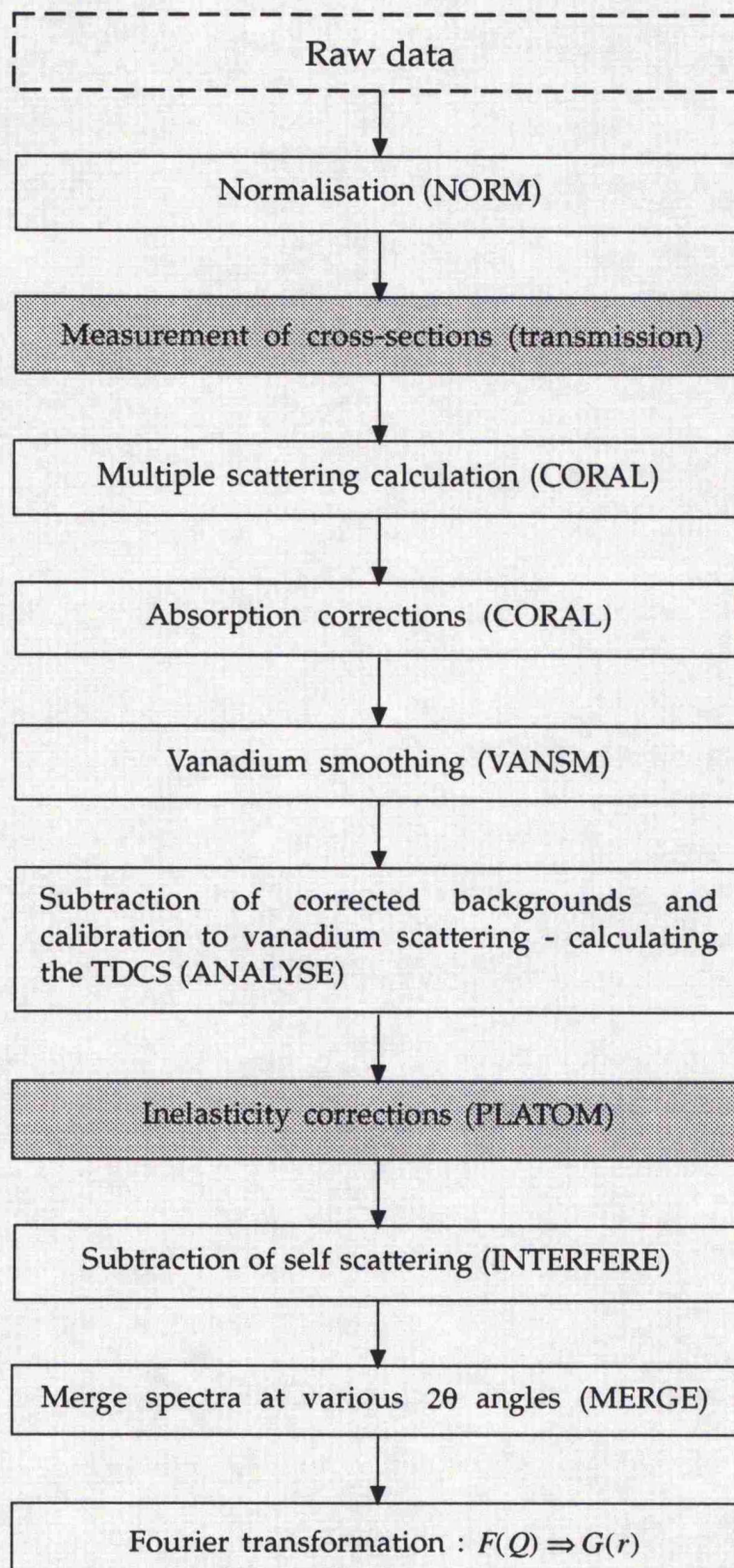


Figure 4.1. Flow diagram showing the main steps in the analysis of TOF neutron data. The names of the ATLAS routines are given in brackets and the shaded boxes indicate steps which are skipped in the analysis of SANDALS data.

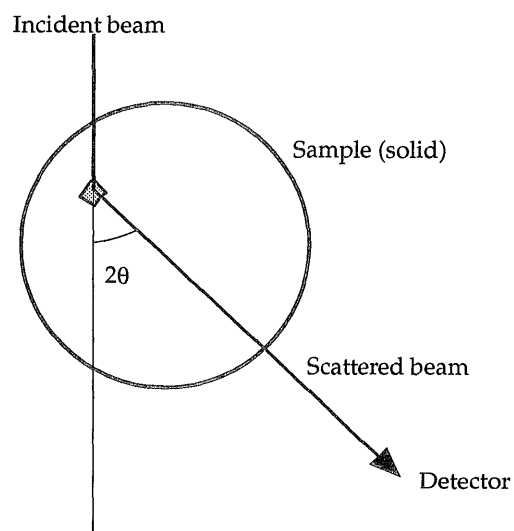


Figure 4.2. Illustration of the numerical method used to calculate attenuation coefficients. By dividing the sample and container into annuli and sectors thus forming elements of roughly equal size, the mean absorption factor over the entire sample can be evaluated. The scattering is assumed to occur at the centre of each element and the attenuation over the flight path in the sample is determined.

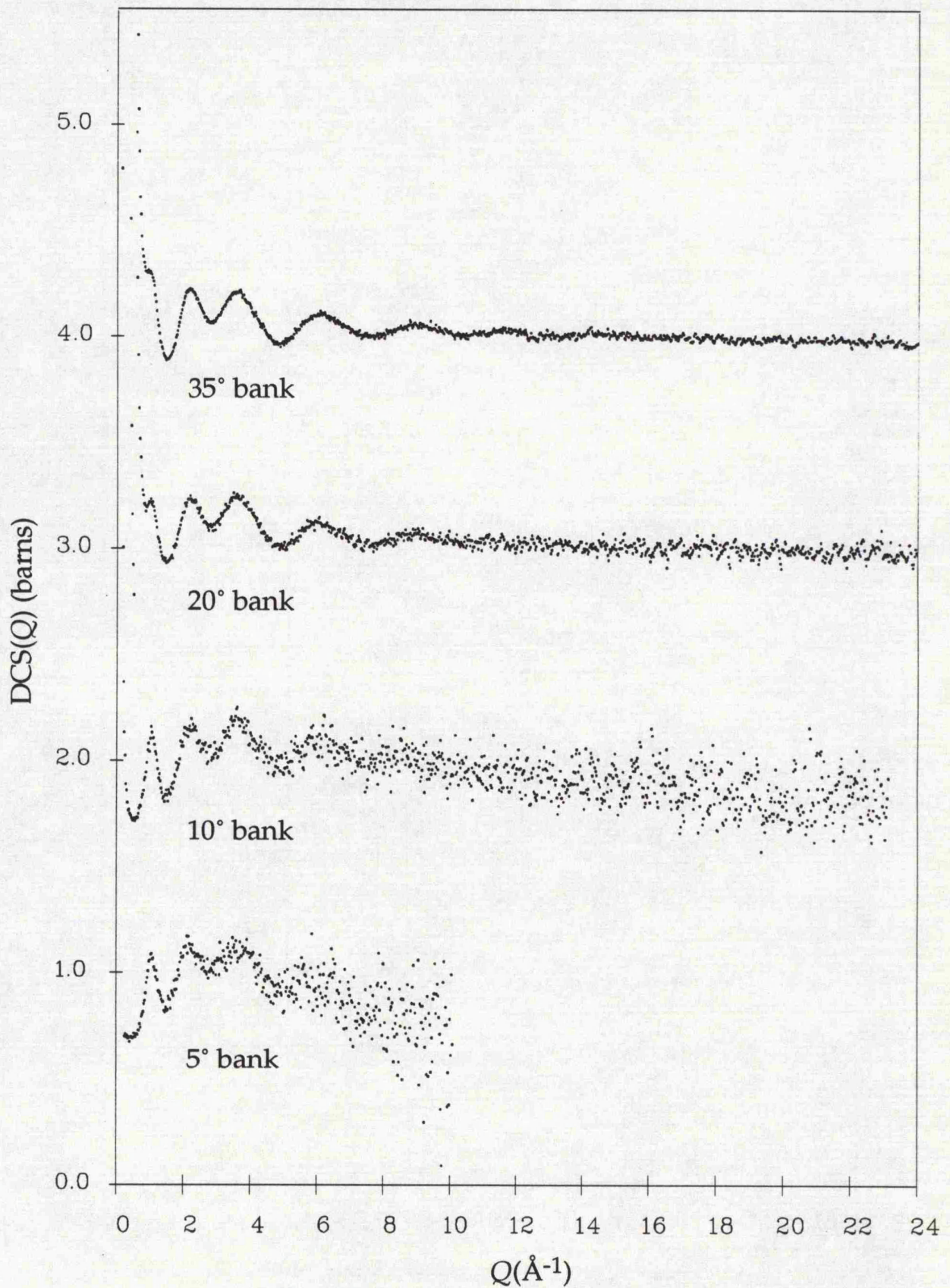


Figure 4.3. Differential cross-section data covering the 5° - 35° LAD detector banks for a molten $\text{NiCl}_2 + 60\% \text{KCl}$ sample at 650°C. The correlation between the severity of high- Q droop and decreasing scattering angle is readily apparent. The spectra from opposite pairs of detector groups have been averaged but no Placzek corrections have been applied.

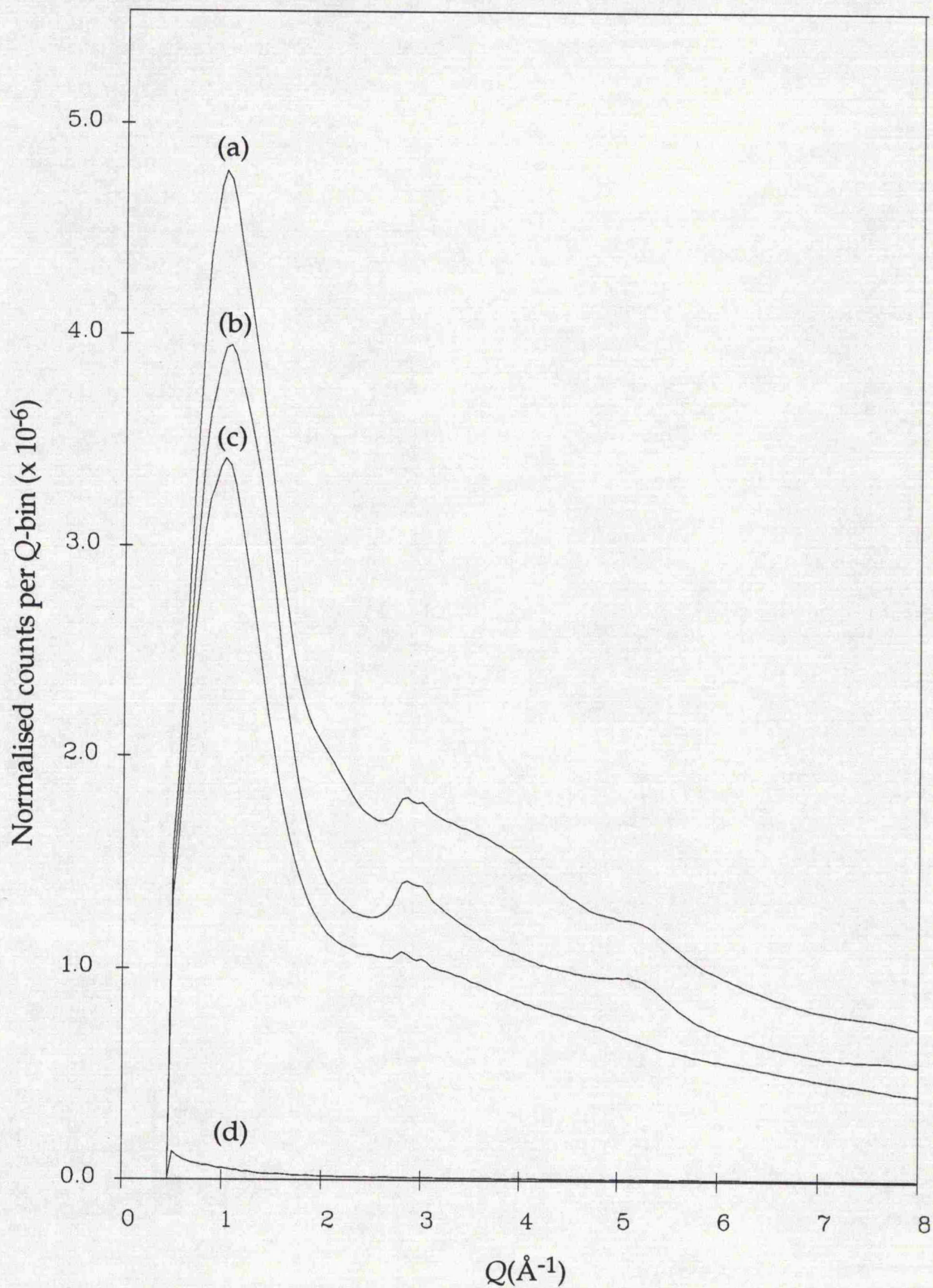


Figure 4.4. Comparison of the normalised counts (no corrections) for SANDALS detector group 1 ($2\theta=11.4^\circ$) for (a) the liquid AlCl_3 sample, (b) the empty container plus furnace, (c) empty furnace (including 3 radiation shields) and (d) the instrument background (i.e. no furnace). The spectra have been normalised to the vanadium scattering using the ratio of the monitor spectra.

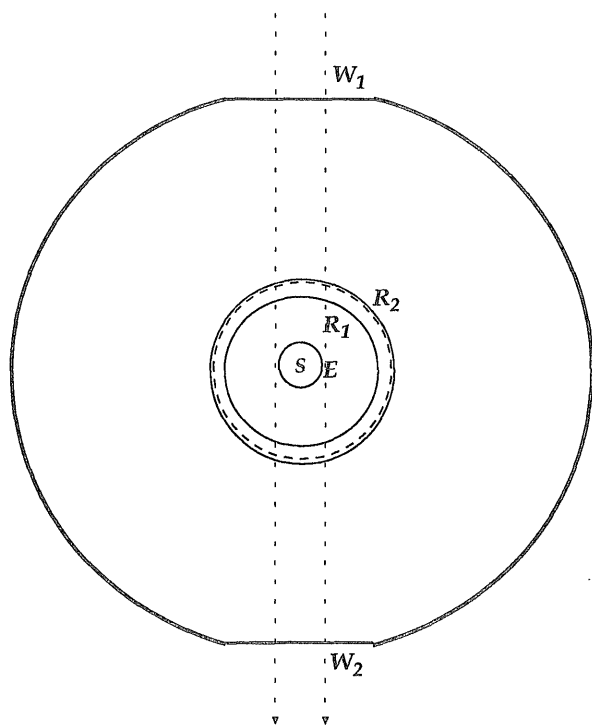


Figure 4.5. Schematic diagram of the basic furnace geometry drawn to scale. The symbol S denotes the sample position, E the furnace element, R_1 and R_2 the two positions of the radiation shields, and W_1 and W_2 are the vanadium foil windows stuck on the outside of the furnace holder. The dashed circle indicates the position of the average furnace annulus used in calculating the furnace correction. The width of the circular beam on SANDALS is indicated by the dashed lines.

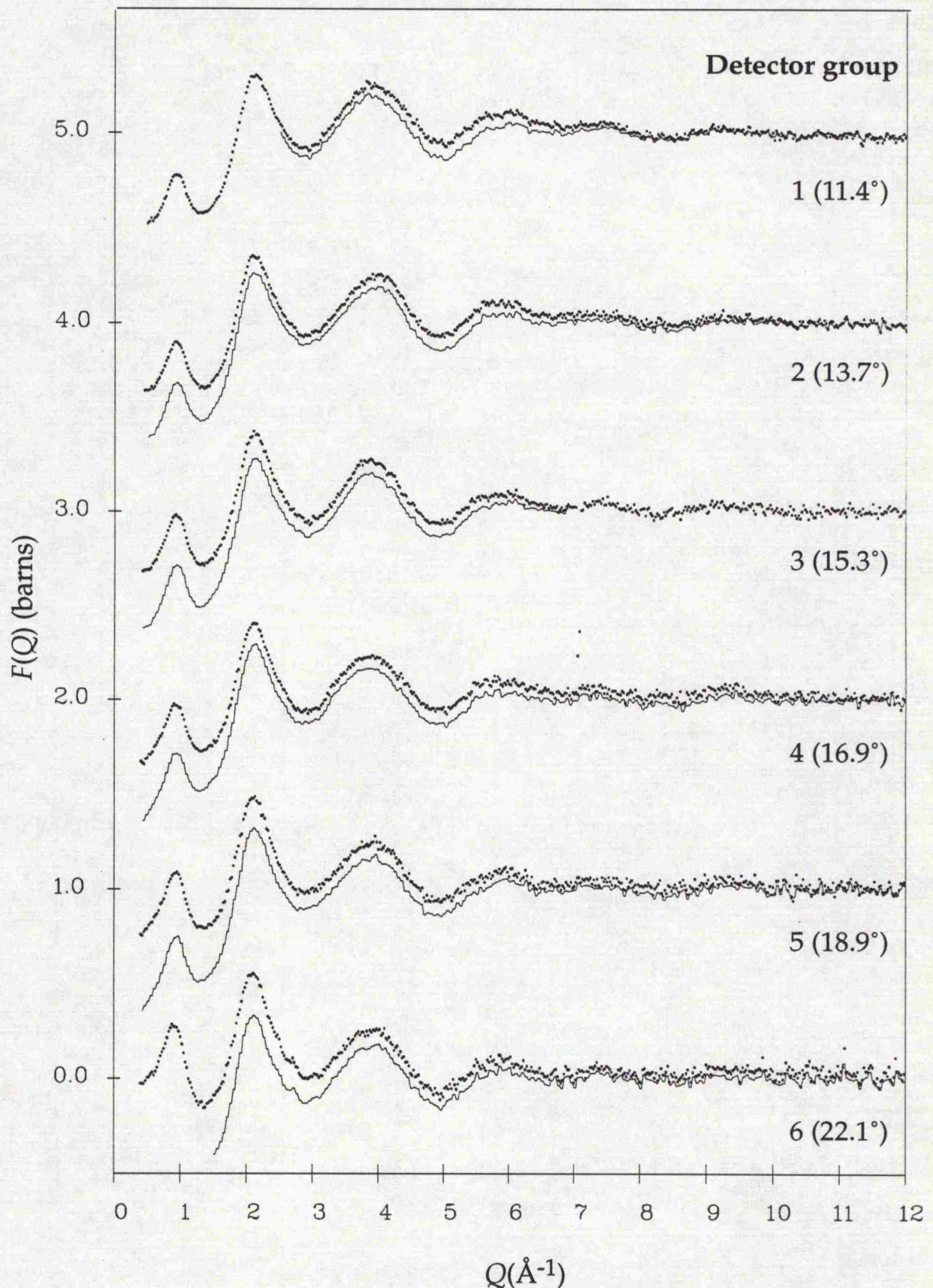


Figure 4.6. Structure factors for molten AlCl_3 (200°C) compared for SANDALS detector groups 1-6. The dotted curves show the result of data analysis *before* the SUBSELF routine was used to remove spurious slopes. The solid curves show the portions of each detector group $F(Q)$ that agreed closely *after* using SUBSELF and were consequently merged to form the composite structure factor.

Chapter 5

The reverse Monte Carlo method

5.1 Introduction - modelling disordered structures

An accurate determination of the structure is usually the first step towards understanding the properties of a material. However, in the case of disordered materials many experiments are conducted without any clear knowledge of the structure. The problem is that while there are several general methods for predicting crystal structures from diffraction data¹, there have been, until recently, no comparable methods available for non-crystalline materials. The approach usually adopted is to attempt to deduce the structure from a few features of the data such as peak positions and coordination numbers. However, this approach effectively discards much of the information content of the data and may give misleading results. The difficulty with Monte Carlo (MC) and Molecular Dynamics (MD) simulation is that these methods depend on choosing the 'correct' interatomic potential and so often agree only qualitatively with the data (see 2.3.3).

The reverse Monte Carlo (RMC) method [5.2] largely overcomes these problems. It is a general method for producing three-dimensional models of the structure of disordered materials. Because no interatomic potential is required and the method involves fitting directly to the data, *quantitative* agreement is possible. The discussion in the remainder of this chapter begins with details of the basic RMC method, followed by a consideration of the practical application of the method.

¹ For example, cyclic fourier refinement [5.1].

5.2 The basic RMC method

5.2.1 The RMC algorithm

The RMC algorithm is a variant of the standard Metropolis Monte Carlo (MMC) procedure first encountered in chapter 2 (section 2.3.3). Before describing the RMC algorithm, it is helpful to first consider the MMC in detail.

The principle of the standard MC method is to produce a statistical ensemble of atoms with a Boltzmann distribution of energies. Instead of generating and sampling configurations completely at random and weighting them with the Boltzmann factor, which is a very inefficient approach, a weighted sampling procedure (Markov chain) is used in MMC. This generates configurations with a frequency proportional to the Boltzmann factor which are then weighted equally. Certain requirements must be met for a true Markov chain (see [5.3], section 3.4) and these are achieved for an ensemble in which the number of particles N , volume V and temperature T are fixed, by the following algorithm.

1) An initial configuration is generated, usually randomly, consisting of N particles in a cell (normally cubic) with periodic boundary conditions. For a cube of side L , the value of N must satisfy the required density constraint $\rho = N/L^3$ for the system being modelled. The probability of this initial configuration P_o (subscript o = old) is given by

$$P_o \propto e^{(-U_o/K_B T)} \quad (5.1)$$

where U_o is the total potential energy as calculated using a specified interatomic potential.

2) A single atom is moved randomly. The probability of the resulting configuration P_n (subscript n = new) is given by

$$P_n \propto e^{(-U_n/K_B T)} \quad (5.2)$$

hence

$$\frac{P_n}{P_o} = e^{[-(U_n - U_o)/K_B T]} = e^{(-\Delta U/K_B T)} \quad (5.3).$$

3) If $\Delta U < 0$ the new configuration is accepted and becomes the starting point in the next iteration. If, however, $\Delta U > 0$ the new configuration is accepted with probability P_n/P_o , otherwise it is rejected and the old configuration is retained.

4) The procedure loops back to step 2.

In the normal course of a simulation, the value of U will decrease until it converges on an equilibrium value about which it will then fluctuate. The maximum size of random moves is usually adjusted to maintain the ratio of accepted to rejected moves close to unity once equilibrium has been reached. Only equilibrium configurations considered to be statistically independent, i.e. separated by least N accepted moves, are collected to generate the required ensemble.

In the RMC method, it is assumed that an experimentally measured structure factor, $S^E(Q_i)$, contains only statistical errors with a normal distribution². The difference between the real structure factor, $S^C(Q_i)$, (which can be calculated from a model of the true structure) and the one measured experimentally is given by

$$\varepsilon_i = S^C(Q_i) - S^E(Q_i) \quad (5.4)$$

with the probability

$$p(\varepsilon_i) = \frac{1}{\sqrt{2\pi}\sigma(Q_i)} e^{\left(-\varepsilon_i^2/2\sigma(Q_i)^2\right)} \quad (5.5)$$

where $\sigma(Q_i)$ is the standard deviation of the assumed normal distribution. The total probability of $S^C(Q)$ is then given by

$$P = \prod_{i=1}^m p(\varepsilon_i) = \left(\frac{1}{\sqrt{2\pi}\bar{\sigma}}\right) e^{\left(-\sum_{i=1}^m \varepsilon_i^2/2\sigma(Q_i)^2\right)} \quad (5.6)$$

where m is the number of Q_i data points in $S^E(Q)$. The mean deviation $\bar{\sigma}$ is defined as

² Obviously, experimental data can also contain systematic errors but this point will be discussed again later.

$$\bar{\sigma} = \left(\prod_{i=1}^m \sigma(Q_i) \right)^{\frac{1}{m}} \quad (5.7).$$

The structure corresponding to $S^E(Q)$ can be modelled by generating a statistical ensemble of atoms whose calculated structure factor conforms with the probability distribution P . The exponent in eqn. 5.6 can be rewritten as

$$\chi^2 = \sum_{i=1}^m \frac{(S^C(Q_i) - S^E(Q_i))^2}{\sigma(Q_i)^2} \quad (5.8)$$

so then

$$P \propto e^{(-\chi^2/2)} \quad (5.9).$$

The similarity to eqn. 5.1 is obvious and it can be seen that $\chi^2/2$ in RMC and $U/K_B T$ in MC are equivalent. Pursuing the analogy, since χ^2 takes the place of energy in the RMC then σ may be considered as an 'effective temperature'.

The algorithm for RMC is as follows.

- 1) Start from an initial configuration with the usual periodic boundary conditions and the correct density. Again, the positions of the atoms are usually chosen randomly, although a known crystal structure, theoretical model or a configuration from a different simulation³ may also be used.
- 2) The pair distribution function is calculated for this old configuration using the equation

$$g_o^C(r) = \frac{n_o^C(r)}{4\pi r^2 \Delta r \rho} \quad (5.10)$$

where $n_o^C(r)$ is the number of atoms whose centres lie at a distance between r and $r + \Delta r$ from an origin atom, averaged over all the atoms in the configuration. The size of the configuration cell should be sufficiently large that $g(r \geq L/2) = 1$ so that the model structure is not being (effectively)

³ These can be from the traditional methods such as MC and MD as well as RMC.

truncated. The pair distribution function is only calculated, as is usual (see 2.3.3), up to $r = \frac{1}{2}L$, with the nearest image convention ([5.3], pg. 49) being used to determine atomic separations.

3) Back-transform to obtain the structure factor.

$$S_o^C(Q) = 1 + 4\pi\rho \int_0^\infty r^2 (g_o^C(r) - 1) \frac{\sin(Qr)}{Qr} dr \quad (5.11)$$

4) Determine χ^2 from the difference between the calculated and measured structure factors using eqn. 5.8.

$$\chi^2 = \sum_{i=1}^m \frac{(S_o^C(Q_i) - S^E(Q_i))^2}{\sigma(Q_i)^2} \quad (5.12)$$

Note, that in practise, the experimental error, $\sigma(Q_i)$, is normally replaced by a uniform standard deviation, σ .

5) One atom is moved at random to generate a new pair distribution function $g_n^C(r)$. From this, a new structure factor, $S_n^C(Q)$, and hence χ_n^2 , is determined.

$$\chi_n^2 = \sum_{i=1}^m \frac{(S_n^C(Q_i) - S^E(Q_i))^2}{\sigma(Q_i)^2} \quad (5.13)$$

6) If $\chi_n^2 < \chi_o^2$, the move is accepted and the new configuration becomes the starting point in next iteration. However, if $\chi_n^2 > \chi_o^2$, then the move is only accepted with probability $e^{[-(\chi_n^2 - \chi_o^2)/2]}$ else it is rejected.

7) The process is repeated from step 5.

In the normal course of simulation, χ^2 will decrease until it settles on an equilibrium value about which it will fluctuate. The resulting equilibrium configuration should be a three-dimensional structure that is consistent with the data to within experimental error. Once equilibrium has been reached, statistically-independent configurations can be collected.

The analogy between RMC⁴ and MMC is apparent from the algorithms. The simple distinction between the two methods is that in RMC it is the χ^2 fit to the data which is being sampled, whereas with MMC, it is the total potential energy, U . It is important to note that because RMC uses a proper Markov chain the final structure is independent of the initial configuration. Algorithms similar to RMC have been tried in the past. For example, Averbach and co-workers [5.4, 5.5] calculated pair distribution functions from models consisting of a few hundred atoms but only converging moves ($\chi_n^2 < \chi_o^2$) were accepted. However, this makes the solution structure dependent on the initial choice of configuration so the method did not find favour.

The basic RMC algorithm, as described above, assumes that only a single set of diffraction data (obtained using neutrons, X-rays or electrons) for a one-component system is being modelled. However, the RMC method can be easily extended to use any set or sets of data which can be directly calculated from the structure. Thus, it may be applied to data-sets obtained either by isotopic substitution in neutron diffraction or using anomalous scattering in X-ray diffraction as well as to EXAFS and possibly NMR data. The only modification involved in modelling multiple data-sets simultaneously is to sum the individual χ^2 values (it is this total which is minimised in the simulation). In general, for a multicomponent system where the fit is to n different total structure factors (denoted by k) we have

$$\chi^2 = \sum_k^n \chi_k^2 = \sum_k^n \sum_{i=1}^m \frac{(F_k^C(Q_i) - F_k^E(Q_i))^2}{\sigma_k(Q_i)^2} \quad (5.14)$$

where the definition of F_k^E in terms of partial structure factors is given by eqn. 2.29 for the case of neutron diffraction data. The relative weighting assigned to each data-set is determined by the various values of σ_k . Different definitions of F_k^E apply for X-ray diffraction [5.6] and EXAFS data [5.7]. Note that it is possible to combine data obtained by different techniques using RMC (see, for example, [5.6, 5.8]), although there are potential problems with systematic errors.

⁴ Because RMC fits directly to the data rather than producing a model which can be compared with experiment *after simulation* as with MMC, this justifies the use of the term 'reverse'.

5.2.2 The role of physical constraints in RMC modelling

Although it is the data itself which provides the most fundamental constraint on the RMC model some simple, additional constraints are almost always used. The most common of these is constraints on the closest approach distance or 'cut-off', $r_{\alpha\beta}^c$, between a given pair of atom types (it is assumed now and in the remainder of the discussion that we are dealing with multicomponent systems) such as would be expected from a hard-sphere model. These are necessary because the experimental data may either lack information or contain systematic errors so that, by itself, it can not prevent atoms from moving too close together. Usually, sensible values for $r_{\alpha\beta}^c$ can be estimated from the direct transform of the data. Furthermore, it is often obvious from the simulation results whether a chosen cut-off distance is seriously in error ; the leading edge of the first peak in $g_{\alpha\beta}^c(r)$ will appear truncated if the value of $r_{\alpha\beta}^c$ is too high or, if it is set too low, spurious sharp peaks may be appear at the front of the partial. The simple cut-off constraint when used in conjunction with the fixed density constraint, has a powerful effect on limiting the range of structures which are consistent with the data. This is because, for most materials, packing considerations play a large part in determining the structure. Note, that in the case of multicomponent liquids, not only is there a fixed constraint on the overall density but also on the partial densities of each species since the composition is also fixed.

Another commonly used constraint is that on the coordination of atoms. If ions whose separation is less than the first minimum in $g_{\alpha\beta}(r)$ are defined as being within the first coordination shell then $C_{\alpha\beta}(n)$ is the fraction of ions of type α with n ions of type β in this shell. By choosing $C_{\alpha\beta}^{\text{Req}}(n_i)$ to be the required proportion with coordination n_i , an additional term of the form

$$\frac{\left(C_{\alpha\beta}^{\text{Req}}(n_i) - C_{\alpha\beta}^{\text{RMC}}(n_i)\right)^2}{\sigma_c^2} \quad (5.15)$$

may be added to χ^2 , where the σ_c parameter serves to weight this constraint relative to the data constraints. Multiple coordination constraints can be applied by simply adding further terms of the above form (in fact, a complete coordination number distribution may be defined). The same approach can be used to constrain average coordination numbers. The information needed for defining coordination constraints can be obtained from such methods as

Raman scattering, NMR, EPR or use of chemical knowledge. Although coordination constraints were not used in the RMC modelling work presented in this thesis, they are one of the most powerful 'tools' available for exploring the range of structures consistent with the data.

5.2.3 *The nature of RMC models*

At this point it is useful to point out some of the characteristics of RMC solution structures. Firstly, the method generates the most disordered structure that is still consistent with the data and constraints i.e. the configurational entropy is maximised. Following on from this it is clear that the usefulness of the resulting model is completely dependent on the quality of information in the data and constraints.

The three-dimensional structure generated by the RMC method is not unique - it is simply one of a range of structural models which are consistent with the data (and any additional constraints) to within experimental error. However, no model that reproduces structure factor data, whether generated by RMC, conventional MC and MD methods or from other sources (e.g. derived from crystal structures), is unique. The disadvantage of conventional simulation methods is that they rely on choosing the 'correct' potential and rarely agree with the data to within experimental error. This makes it difficult to determine whether the problem lies with the form of potential used or with systematic errors in the data. In contrast, the RMC solution, by definition, always agrees with the data to within experimental error. Providing the method is used properly, poor RMC fits are invariably due to problems with the data or the choice of sample parameters, such as density, used in the simulation.

Another question, related to the one above on uniqueness, is whether the RMC solution is path-dependent i.e. does the final structure depend in any way on the choice of starting configuration? In principle, the RMC solution structure is indeed independent of the starting configuration because the method uses a proper Markov chain. Extensive tests have confirmed this [5.9]. However, problems can arise if the RMC method is used incorrectly. For example, in the case of modelling close-packed systems like metallic glasses [5.10], final structures sometimes contain elements of long range order retained from crystalline starting configurations. Problems such as these can be alleviated by always using random initial configurations and always fitting to structure factor data (which is more sensitive to long range order than real-

space functions). It also helps to allow the simulation to continue for a long time after reaching equilibrium so it is as far removed from the starting point as possible. Nonetheless, care must be exercised in modelling dense systems where movement of the atoms is inevitably restricted.

Since the RMC solution is, like those from other methods, not unique, is it ever possible to determine the 'correct' structure? The answer is only in the special case of a system where the interatomic potential is purely pairwise additive and there is a functional relationship between $\phi(r)$ and the pair distribution function [5.11]. This means $g(r)$ uniquely determines $\phi(r)$ and since the potential determines the structure (including all higher correlation functions) then $g(r)$ uniquely determines the structure. Theoretical tests show that for an accurately defined $g(r)$, generated from conventional MC simulation, the RMC solution correctly reproduces the three-body correlations [5.12]. The RMC method, under these conditions, appears able to produce the 'correct' structure. Although potentials in real systems are never simply pairwise additive, these results suggest that accurate $F(Q)$ or $G(r)$ data may contain useful information about the three-dimensional structure which can be extracted using a method like RMC. Furthermore, where there are significant many-body contributions to the potential the effect of these may be taken into account using additional constraints. For example, in the case of molecular liquids, the expected types of molecule may be included explicitly in the starting configuration and coordination constraints applied to preserve these discrete units during simulation.

Given, that the RMC structure is neither unique nor necessarily 'correct', how should the method be applied? The only truly valid approach is to try to explore the range of possible structures consistent with the data and look for similar characteristics in these models [5.13]. However, this is rarely done in any form of simulation because of the computational expense. An often simpler strategy is to use constraints in order to determine whether an assumed or hypothetical structure is actually consistent with the data - a structural model which does not fit the data is unlikely to be 'correct'.

5.2.4 Summary of the RMC method

It is now possible to summarise the key points about the RMC method and thus highlight some of the reasons for its use in the research presented in this thesis.

1) RMC makes use of all the information available in diffraction data (not just a few specific features) in a quantitative way. This is particularly important in attempting to model complex multicomponent systems such as molten salt mixtures where it is necessary to extract the maximum possible amount of information.

2) RMC does not need a potential function. This greatly simplifies the problem of obtaining a structure which is in quantitative agreement with the experimental structure factors. The reduced computational requirements mean that RMC simulations can be larger than is typical with MC and MD methods. Large simulations have the advantage of being accurately transformable to $F(Q)$ so it is nearly always possible to fit directly to the diffraction data with RMC (MC and MD simulations often only fit to $G(r)$ data). This is particularly important for the research in this thesis because of the interest in intermediate range order, as indicated by the first sharp diffraction peak (FSDP) feature at $Q \sim 1. \text{ \AA}^{-1}$ in the structure factor, which is not prominent in the real-space transform.

3) Because RMC models a three-dimensional structure, subject to simple but powerful constraints on excluded volume (atom sizes) and density, the data must correspond to a possible physical structure. In the case of modelling isotopic data, this means additional, stringent conditions on the separated partial structures which now all have to be physically consistent with each other. This constraint can also improve the separation of partials when the separation matrix is poorly conditioned (see chapter 7). In the case where there is only a single structure factor for a multicomponent system, the physical constraints in the RMC method can, to some indeterminate extent depending on the quality of information in the data, compensate for the lack of isotopic data.

4) The RMC solution, although not unique, has the characteristic of maximum configurational entropy - which is not necessarily a disadvantage because it means any order in the model is due only to information extracted using the data and constraints. Alternative inverse methods such as the maximum entropy method (MEM) are actually promoted on the basis that they produce the 'least' structural solution [5.14]. However, such techniques lack the physical constraints of RMC and do not generate a three dimensional structure⁵.

⁵ A useful discussion of the relative merits of RMC and the MEM is given in [5.15].

5.3 Application of the RMC method

It is now possible to describe the use of the RMC method for the research presented in this thesis. The discussion will begin with the practical application of the method, followed by a consideration of the effects of errors on RMC simulation, and finally, how the solution structures were analysed. The original RMC program (RMCA, version 1.04) and configuration characterisation software (version 2) were provided by R.L. McGreevy of the Studsvik Neutron Research Lab., Sweden (at time of writing).

5.3.1 Details of RMC modelling

The first step was to create a random initial configuration which satisfied the required 'cut-off' and density constraints. The $r_{\alpha\beta}^c$ values were estimated from the direct transform of the data, and the dimensions of the (cubic) cell were defined to give the correct density with the chosen number of particles. Typically, about 2400 particles were used, giving an effective simulation size of $L/2 \sim 20\text{-}25 \text{ \AA}$. As explained earlier, the size of simulation is important particularly when fitting to structure factor data. Furthermore, simulation size in terms of number of particles is also important because this determines the statistical fluctuations in $g^C(r)$ and hence how many equilibrium configurations need to be collected for averaging.

Initially, a trial simulation was conducted by fitting to $G(r)$ data. This was faster than fitting to the structure factor and allowed the $r_{\alpha\beta}^c$ values to be adjusted. It also gave early indication of possible systematic errors. The value of σ was chosen to approximately match the amplitude of Fourier ripple. In order to speed convergence, a large value (usually 2.5 \AA) for the maximum size of random move, δ_r , was used in the early stages of simulation. δ_r was reduced to about $.5 \text{ \AA}$ once the configuration had become relatively well ordered (so few moves were being accepted with the initial large value of δ_r). It usually took about 20,000 accepted moves (out of $\sim 200,000$ actually tried) for the simulation to reach equilibrium⁶. Because of the CPU time required, the RMC program was executed in stages as computer batch jobs.

⁶ The figures quoted (for the typical number of moves needed for equilibrium) only really apply in the case of the highly structured data in this thesis. Data with less information content would naturally be easier and quicker to fit. It is also useful to make the distinction between tried and attempted moves : more moves will have been attempted and rejected, because they violate 'cut-off' constraints, than are tried for an improved fit.

The program was modified slightly (from version 1.04) to suit the definitions of $F(Q)$ and $G(r)$ used in this research. A further modification was made in the implementation of random number generation. The original program started by initialising the seed for the random number generator (the intrinsic Fortran function, RAN, as implemented by Silicon Graphics [5.16]) from the system clock. Since the program had to be run several times under a batch process, the random number seed would have been repeatedly re-initialised. It is not recommended [5.17] to keep re-initialising the seed. Individual sequences of pseudo-random numbers will have been checked for the statistical properties of randomness. However, randomness cannot be guaranteed between different sequences (resulting from different initial seeds). For this reason, the current value of the seed was kept between batch jobs thus preserving the same sequence.

If the RMC method was successful in fitting to real-space data, the next step was to fit directly to the diffraction data. However, this had to be free of spurious slopes and features that appear at low r in the real-space transform. The RMC simulation cannot reproduce these because of the obvious 'cut-off' constraints. The $F(Q)$ data was corrected for slopes by fitting the theoretical $G(0)$ base-level to the transform and back-transforming to calculate the correction to be applied in Q space. It was also essential that the data range did not extend below the minimum Q value that can be modelled as given by $Q_{\min}^C = 2\pi/L$. The effects of fitting to data points at Q values below Q_{\min}^C are unpredictable. The value of σ was determined from the obvious scatter (error bars) in the data points at high Q . The r spacing, Δr , used in the calculation of $g^C(r)$ (eqn. 5.10) was set at 0.1 Å.

Because of the interest in modelling intermediate range order (IRO), the RMC simulation was restarted from a random initial configuration when fitting to $F(Q)$ data. The initial fit to $G(r)$ was usually ineffective at reproducing the FSDP feature in Q space because it corresponds to shallow, long-period fluctuations in real space that are invariably masked by Fourier ripple. Even using the best-fit configuration obtained by modelling $G(r)$ data as a starting point for a refinement fit to $F(Q)$ was not deemed a reliable approach. This was because of the constraint of only being able to move one atom at a time. Once the configuration has become ordered, with units or clusters of atoms present, then it is difficult to move or re-orient these units to give the correct inter-unit distance corresponding to the position of the FSDP. For this reason, the definitive RMC simulation of the nickel isotopes

data (chapter 7) was obtained by fitting directly to all three data-sets starting from a random initial configuration.

The data will normally contain small systematic errors in the form of multiplicative constants. Fortunately, the RMC program includes a renormalisation option to take account of these. The renormalisation factor which minimised χ^2 is given by

$$\frac{\sum_i F^E(Q_i)F^C(Q_i)}{\sum_i F^E(Q_i)^2} \quad (5.16).$$

Renormalisation of the data was performed, as a refinement, only when the simulation was close to equilibrium. It was of particular importance in dealing with the nickel isotopes data where it was essential to have the correct relative normalisation between data-sets. In most cases, the renormalisation suggested by the RMCA program did not exceed $\pm 3\%$ (anything very much larger than $\pm 5\%$ would have indicated some problems with the data).

Fitting to $F(Q)$ data, even multiple data-sets, usually took a similar number of accepted and tried moves as fitting to the corresponding real-space data. The simulations were conducted in much the same way as the trial fits to $G(r)$, using a large initial value of δ , etc. However, because a Fourier transformation step was now included, the amount of CPU time (as well as elapsed time) required was much greater. Usually, about $2N$ accepted moves were allowed after equilibrium in order to confirm that χ^2 was actually fluctuating and also to reduce any possible dependence on the initial configuration. Subsequently, configurations separated by at least $2N$ accepted moves were collected for averaging of their structural properties.

5.3.2 *The effects of systematic errors - reasons for not achieving fits*

As stated earlier, the RMC algorithm assumes only statistical errors in the data. However, systematic errors will also be present and these may distort the RMC solution or, if they are severe enough, actually prevent a quantitative fit. In general, if a fit is not possible using the RMC method then the cause is usually systematic errors in the data. The RMC method can still be used if it were possible to identify the systematic error and perhaps localise

its effects to specific regions of Q space. Setting large values of $\sigma(Q_i)$ in the affected regions would ensure that they are effectively ignored in the fitting process. This kind of approach was used by McGreevy and Howe [5.18] when modelling isotopic data for molten LiCl. They deduced that inadequate inelasticity corrections were responsible for inconsistent main-peak heights in their isotopic data-sets and simply did not fit to data points near this feature.

Systematic errors in the data are not the only reasons for failing to achieve RMC fits. Errors involving the choice of adjustable parameters in the simulation can also cause problems. For example, choosing values of $r_{\alpha\beta}^c$ that are too large or physically inconsistent with each other could prevent a fit. For reasons already discussed in 5.2.2, the values of $r_{\alpha\beta}^c$ finally adopted are usually not in serious error.

Large errors in density may also prevent a fit. Configurations with a small void volume (e.g. glasses) would be particularly sensitive to this kind of error. Smaller errors would presumably allow a fit but distort the configuration. The effects of varying the nominal density (by $\pm 10\%$) were studied when modelling neutron data for molten AlCl_3 (see chapter 8). Analysis of bond networks, coordination number and bond angle distributions (see 5.3.3) suggests that varying the density, aside from causing a proportionate change in the mean local coordination number, affects the inter-molecular/unit void volume. Lowering the density appears to pull apart the configuration producing a more skeletal structure and, because of the need to produce the best fit to the data, RMC is likely to generate voids and clusters of a size corresponding to peaks in Q space below Q_{\min}^c . Naturally, increasing the density has the opposite effect and leads to a more compact structure. In addition, there might be problems of packing and closest approaches with some configurations, although not for molten AlCl_3 which has a large void volume. RMC may attempt to partially compensate for an error in density by renormalising the data (consider eqn. 2.31). If RMC suggests a renormalisation factor clearly larger than expected from the typical error in normalisation of about $\pm 5\%$ for neutron diffraction data, then this probably means a systematic error involving density or container subtraction etc.

Errors in the fractional densities, i.e. composition, of samples were a recurrent problem in RMC simulation. This was most clearly demonstrated

in modelling the nickel isotopes data (chapter 7). The results of fitting to a single $G(r)$ data-set for the 'natural' $\text{NiCl}_2\text{-KCl}$ sample, assuming nominal (67% KCl) and trial compositions, are shown in figure 5.1. The simulations assuming 67 and 55% KCl are clearly unable to fit the Ni-Cl principal peak at $r \sim 2.3 \text{ \AA}$. The results of fitting directly to the structure factor are also shown. In the case of 67% KCl, the transform of the Q -space fit shows a spurious, sharp peak at $r \sim 2.9 \text{ \AA}$, arising from the $g_{\text{K-Cl}}^{\text{C}}(r)$ partial, which is not present in the fit to $G(r)$. This is consistent with there being too many K^+ ions, and conversely too few Ni^{2+} ions, in the configuration so that RMC, in trying to fit $F(Q)$, pushes the 'excess' ions down to low r thereby minimising their effect in Q space. The spurious peak is not present in the 60% KCl simulation and the value of $59 \pm 1\%$ KCl determined by chemical analysis confirms this is approximately the true composition. Indications of a similar error in composition were also found when modelling data for a (nominally) 67% KCl + ZnCl_2 sample [5.19]. It is not surprising that RMC can be sensitive to such errors since the composition parameter would clearly affect the possibilities for packing, particularly if there were large differences in ion sizes.

5.3.3 Characterising the RMC solution structure

Once a satisfactory fit had been achieved, the RMC solution structure could be examined in detail. However, since the structures remained relatively disordered they were best characterised in terms of distributions rather than well-defined geometries.

Coordination number distributions, $C_{\alpha\beta}(n)$, were obtained by averaging over several statistically-independent configurations using the program NEXTTO. The average coordination number is simply

$$\sum_n n C_{\alpha\beta}(n) = \bar{n}_{\alpha\beta} \quad (5.17).$$

The average value, $\bar{n}_{\alpha\beta}$, is all that can be obtained directly from $g_{\alpha\beta}(r)$ so the advantages of having a three-dimensional model are apparent. An estimate of the range and relative probabilities of coordinations in the liquid could be obtained from $C_{\alpha\beta}(n)$. This made the precise definition of the coordination shell less important.

Bond angle distributions, $B_{\alpha\beta\gamma}(\cos\theta)$, were also obtained by averaging over several independent configurations, using the program TRIPLETS. The 'bonds' are actually vectors joining any two coordinated atoms i.e. a purely geometrical definition with no implications for chemical bonding. The three-body correlation function $g^{(3)}(r_1, r_2, r_3)$ can be written as $g^{(3)}(|r_1 - r_2|, |r_2 - r_3|, \cos\theta)$, where θ is the angle between bonds $|r_1 - r_2|$ and $|r_2 - r_3|$. Thus information on three-body correlations and geometrical structure is available from bond angle distributions. $B_{\alpha\beta\gamma}(\cos\theta)$ is defined as the average number of bond angles, per atom type β , with cosines in the range $\cos\theta$ to $\cos\theta + \Delta(\cos\theta)$, for triplets of type α, β and γ (the bond angle is formed by α and γ to the central atom β). For a two-component liquid like molten AlCl_3 there are six such distributions.

It was usually possible to identify the dominant local structure using the two types of distribution function, particularly bond angle, described above. However, in order to identify more complex structures, involving higher-order correlations, it was necessary to use the bond network analysis program CHAINS. This program works out the size and number of connected units (formed by coordinated atoms) and also determines whether they contain branches or loops. For example, in the case of the RMC solution structures obtained for molten AlCl_3 (see chapter 8), bond network analysis revealed that very few units corresponding to discrete Al_2Cl_6 dimers were present. Only 1-2% of the connected units were of 8 atoms size and included a loop (as expected for edge-sharing double tetrahedra). Bond network analysis was also used to check for long chains and clusters possibly associated with IRO.

Visual inspection provided some useful confirmation of the structure as indicated by the quantitative methods described above. However, this method did not provide a reliable means of determining the structure in the first instance. This was largely because of the complexity of the disordered RMC configurations. Visual inspection is more useful when *comparing* different RMC configurations - marked structural similarities or differences are then readily apparent.

5.4 References

- [5.1] D. Sherwood, 1976, " Crystals, X-rays & proteins", 1st edition, Longman, London, chapter 13
- [5.2] R.L. McGreevy & L. Pusztai, 1988, *Mol. Sim.*, **1**, 359-367
- [5.3] J.P. Hansen & I.R. McDonald, 1986, "Theory of simple liquids", 2nd edition, Academic Press, London.
- [5.4] R. Kaplow, T.A. Rowe & B.L. Averbach, 1968, *Phys. Rev.*, **168**, 1068
- [5.5] A.L. Renninger, M.D. Rehtin & B.L. Averbach, 1974, *J. Non-Cryst. Solids*, **16**, 1
- [5.6] D.A. Keen & R.L. McGreevy, 1990, *Nature*, **344**, 423-424
- [5.7] S.J. Gurman & R.L. McGreevy, 1990, *J. Phys.: Condens. Matter*, **2**, 9463-9474
- [5.8] R.L. McGreevy, 1993, *Int. J. Mod. Phys. B*, **7**, 2965-2980
- [5.9] R.L. McGreevy, 1991, private communication
- [5.10] E.W. Iparraguirre, J. Sietsma & B.J. Thijsse, 1993, *J. Non-Cryst. Solids*, **156**(2), 969-972
- [5.11] R. Evans, 1990, *Mol. Sim.*, **4**, 409
- [5.12] R.L. McGreevy & M.A. Howe, 1991, *Phys. Chem. Liq.*, **24**, 1-12
- [5.13] R.L. McGreevy, 1993, *J. Non-Cryst. Solids*, **156-158**, 949-955
- [5.14] D.A. Allen, 1989, Ph.D thesis, University of Leicester, 'A neutron diffraction study of the structure and structural modification of molten zinc halides and nickel halides', chapter 5 and references therein.
- [5.15] R.L. McGreevy, 1989, IOP conference series, **101**, 41-50
- [5.16] Silicon Graphics manual, 1991, "Fortran 77 programmer's guide", document number 007-0711-030, Silicon Graphics inc., California.
- [5.17] NAG manual, 1991, "NAG Fortran manual introductory guide, mark 15", 1st edition, Numerical Algorithms Group LTD, Oxford. chapter G05 and references therein.
- [5.18] R.L. McGreevy & M.A. Howe, 1989, *J. Phys. C: Condens. Matter*, **1**, 9957
- [5.19] D.A. Allen, R.A. Howe, N.D. Wood & W.S. Howells, 1992, *J. Phys. C: Condens. Matter*, **4**, 1407-1418

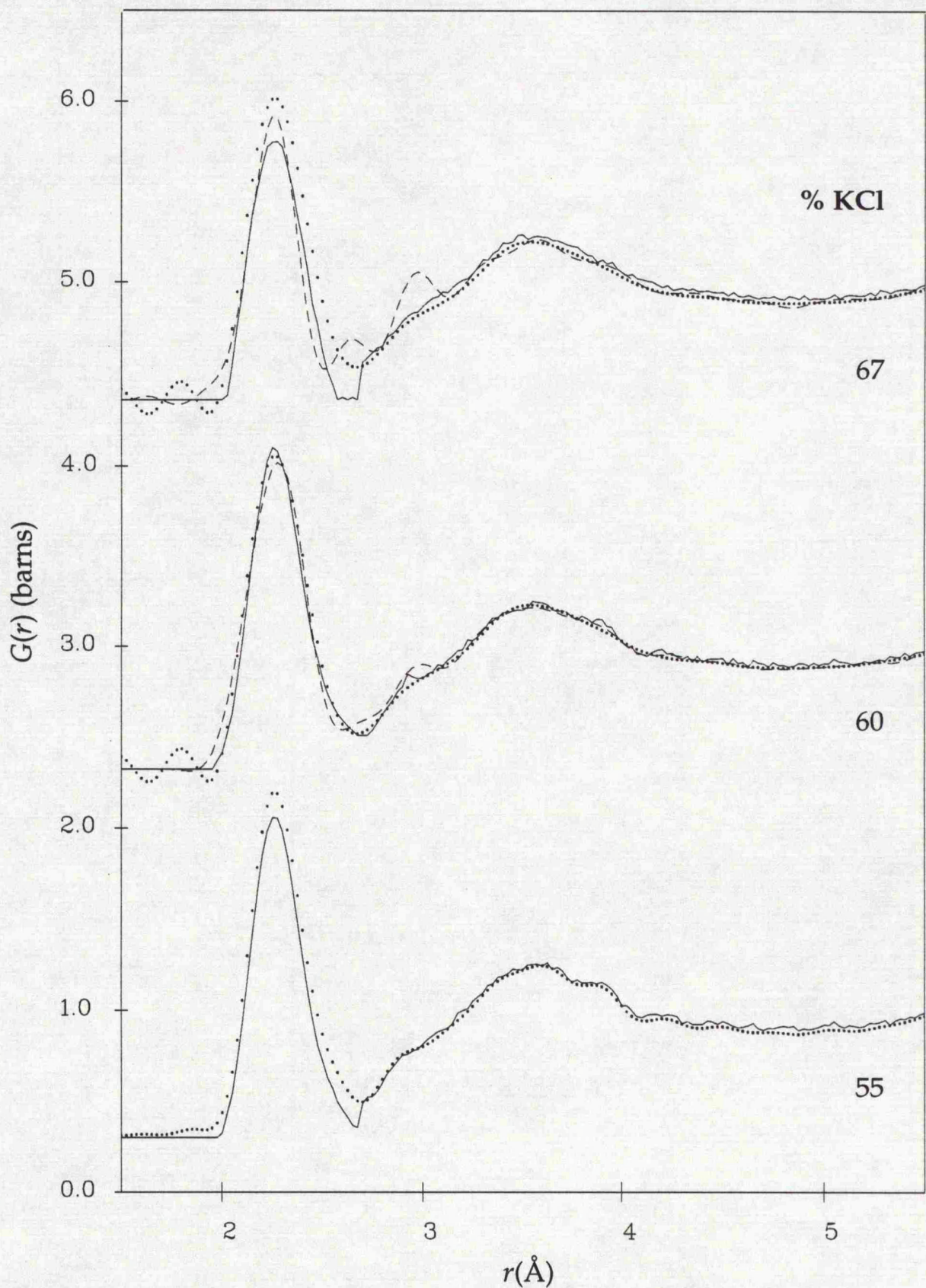


Figure 5.1. The effects of varying composition on RMC modelling of data (dotted) for a 'natural' molten $\text{NiCl}_2\text{-KCl}$ sample (see chapter 7). The real-space results of fitting to $G(r)$ (solid curves), and directly to the total structure factor (dashed curves) are shown.

Chapter 6

Structural modification in molten divalent metal chloride and alkali chloride mixtures

(Shortened version published in *J. Phys. : Condens. Mat.*, 1993, 5(39), 7189-7202)

Abstract

Structure factors have been measured by time-of-flight neutron diffraction for $\text{NiCl}_2\text{-KCl}$, $\text{NiCl}_2\text{-LiCl}$ and $\text{ZnCl}_2\text{-LiCl}$ binary molten salt mixtures. The results are consistent with those from earlier thermodynamic and spectrophotometric studies, in which the degree of structural modification was found to depend on the type of alkali cation. The $\text{NiCl}_2\text{-LiCl}$ and $\text{ZnCl}_2\text{-LiCl}$ systems appear to be almost ideal admixtures of the pure salts. In contrast, adding KCl to NiCl_2 results in enhancement of the local structure and intermediate range order. The first sharp diffraction peak at $Q \sim 1. \text{ \AA}^{-1}$ in pure NiCl_2 , which is more prominent than previously reported, appears to be enhanced by the addition of KCl up to a high concentration of alkali halide. No change is apparent in $\text{NiCl}_2\text{-LiCl}$ or $\text{ZnCl}_2\text{-LiCl}$.

6.1 Introduction

There have been a number of studies, by several techniques, of binary molten salt mixtures with the general formula $\text{MX}_2\text{-AX}$ (where M is a divalent metal, A is an alkali metal and X the common halide). Thermodynamic measurements indicate deviations from random mixing and the common formation in these systems of mainly tetrahedral MX_4^{2-} complexes at $2/3$ alkali halide concentration, with the degree and stability of complexing dependent on the size of alkali cation. Enthalpies of mixing data [6.1] for $\text{NiCl}_2\text{-ACl}$ (A = Li, Na, K, Rb and Cs) suggest that these mixtures exhibit strong deviations from ideality for the larger alkalis such as Cs, Rb and K, less so for Na and almost not at all for Li. Entropies of mixing [6.2] are also consistent with the formation of well-ordered, energetically-stable tetrahedral units with the reduction in partial molar entropy most pronounced for the largest alkali metal.

Optical absorption spectra for a transition metal ion like Ni^{2+} are sensitive indicators of the coordination geometry because the energy levels of the poorly shielded $3d$ electrons are strongly influenced by the local environment. In

spectrophotometric measurements of NiCl₂-ACl melts [6.3, 6.4] the characteristic absorption spectra of NiCl₄²⁻ becomes increasingly evident as the size of the alkali cation is increased from Li to Cs. X-ray diffraction measurements show that the nickel atoms are almost all tetrahedrally coordinated in crystalline Cs₃(NiCl₄)Cl so the similarity of the absorption spectra for solid and liquid phases of the compound provides evidence for the existence of the tetrahedral NiCl₄²⁻ unit in the melt [6.5]. Optical absorption studies [6.6] of dilute ternary solutions of NiCl₂ in KCl-LiCl reveal that adjusting the proportions of the two alkali halides affects the coordination geometry of the Ni²⁺ ion in a systematic way. Increasing KCl results in predominantly tetrahedral structural units whereas more LiCl leads to a less regular, probably octahedral, geometry.

Theoretical models, such as the simple complex anion model of Pelton [6.7], have been proposed which can reproduce the general features of the experimental enthalpies and entropies of mixing curves. These models attempt to explain the thermodynamic data solely in terms of the degree of complexing and ordering of the local structure of the metal cation. The question arises as to whether any of the reduction in entropy and enthalpy observed in these mixtures is due to structural correlations between complex units namely intermediate range order (IRO). The presence of a first sharp diffraction peak (FSDP) at $Q \sim 1. \text{ \AA}^{-1}$ in diffraction data for MX₂ melts with small cations has been taken as evidence of IRO arising from linked structural units. In the 'network liquid' model [6.8] (references therein) proposed for the ZnCl₂ melt, correlations between corner-sharing neighbouring units are thought to lead to correlations between the cations at the centres of these units. This model implies that adding alkali halide would break up the IRO and allow isolated structural units to be formed by reducing the need for anion sharing.

In order to obtain direct evidence of the structural modification of MX₂ salts by different alkali halides as indicated in previous studies, time-of-flight (TOF) neutron diffraction experiments were carried out on molten NiCl₂-KCl, NiCl₂-LiCl and ZnCl₂-LiCl samples covering a range of compositions. The availability of partials information for the pure salts and the dissimilarity in their total scattering functions makes it possible to interpret the mixtures data without using isotopic substitution. For example, the size and position of the FSDP can be followed as a function of composition to obtain information about the state of IRO in the mixtures.

6.2 Experimental details

The mixtures were prepared from anhydrous, pure ($\geq 99.99\%$) single salts heated gently under vacuum to minimise moisture content. Details of the vacuum drying procedure for the pure salts and the general method followed for preparing the mixtures are given in chapter 3. The samples were 'pre-mixed' by heating to at least 25°C above the liquidus (as indicated in the phase diagrams for $\text{NiCl}_2\text{-KCl}$ [6.9], $\text{NiCl}_2\text{-LiCl}$ [6.10] and $\text{ZnCl}_2\text{-LiCl}$ [6.11]) and maintained at that temperature for at least 24 hours. The prepared samples were loaded into quartz containers of approximately 5 mm internal diameter and 1 mm wall thickness before being sealed off under an argon pressure of $\sim .5$ atm. at room temperature¹. The lithium chloride used in mixtures with nickel chloride was isotopically enriched ($\geq 99.99\%$) in ^7Li to avoid the very large absorption cross-section for neutrons of the ^6Li isotope.

Total structure factors for samples of 0, 20, 40, 55, 70 and 80% KCl with NiCl_2 at a temperature of 1040°C (1050°C for pure NiCl_2) were measured on the LAD instrument at Rutherford ISIS. Samples of 33 and 67% LiCl with NiCl_2 were measured at the same temperature. In addition, 0, 33 and 67% LiCl with ZnCl_2 compositions were studied at 450°C . The $F(Q)$ for pure LiCl (@ 650°C) was obtained on ISIS SANDALS. Multiple scans were taken for each sample to check whether structural changes in sample or container, from incomplete mixing or chemical attack, occurred during data collection. Only scans that agreed to within statistical error were added together. Devitrification was noted in the scattering for molten $\text{NiCl}_2\text{-LiCl}$ samples from the increasing size, in successive scans, of sharp Bragg peaks at $Q \approx 1.5$ and 3 \AA^{-1} . Fortunately, these peaks appeared to be localised and thus could be removed by curve fitting. Data was collected for the empty container (@ 1040°C) and furnace backgrounds as well as a vanadium calibration.

The raw data was analysed using the Rutherford ATLAS package [6.12], without furnace corrections, in the manner described in chapter 4. Composite $F(Q)$ s were obtained by merging those Q ranges of adjacent detector groups which matched. The $\pm 5^\circ$ detector groups were invariably unreliable and never included but there was good agreement between opposite pairs of detector

¹ NiCl_2 sublimates before fusion at 973°C under normal atmospheric pressure. An argon over-pressure of about 1.5 atm at the melting point seems to be enough to ensure fusion. It should be noted that because NiCl_2 can only be melted in sealed containers above atmospheric pressure and at high temperature, the values of the density and melting point are uncertain in the literature.

groups at $\pm 10, 20, 35$ and 60° with good overlap between the different angles as well. No clear signs of excess or deficit of container scattering were noted in the $G(r)$ data. However, some problems were encountered with the data for the NiCl_2 mixtures where a marked fall off in scattering with increasing Q gives rise to a large slope in $F(Q)$. This systematic error is proportionately worse at lower detector angles and so appears to be related to neutron energy. It was corrected by fitting a theoretical $G(0)$ base-level to the $G(r)$ data and back-transforming to obtain a correction for the original $F(Q)$. However, the large slope has the effect of making renormalisation less accurate leading to a larger than usual error (say 5-10%) in the absolute normalisation of the data for the NiCl_2 mixtures. The lack of isothermal compressibility data precluded the use of the long-wavelength limit, $F(0)$, as a check on normalisation. The missing low- Q portion of the data was simply extrapolated. Because of the Q^2 dependence of the Fourier transform this makes little difference to the real-space picture.

The $G(r)$ functions were obtained by Fourier transformation of $F(Q)$ data which was smoothed at high Q (in the manner described in chapter 4). No window function was employed. Comparison of the $G(r)$ from smoothed and unsmoothed $F(Q)$ data confirmed that mainly Fourier ripple was removed with marginal effect on real peaks.

The data analysis parameters for the pure salts are given in table 6.1. Because of the lack of published measurements, number densities for the NiCl_2 mixtures were linearly interpolated from those of the pure salt endpoints at 1040°C . Density data for the ZnCl_2 - LiCl mixtures (and the pure salts) was obtained from Yoko *et al* [6.15].

6.3 Discussion

6.3.1 The structure of pure NiCl_2

Before considering the mixtures it is instructive to first examine the data for pure NiCl_2 . Total structure factors from the previous reactor diffraction investigation of Newport *et al* [6.16] and the current TOF study (henceforth referred to as I and II, respectively) are shown in figure 6.1 : clear differences are apparent, even when uncertainty in normalisation of the data is taken into

account². In particular, the FSDP in II is larger and more comparable in size to that of molten NiBr₂ [6.17]. If, as several studies indicate [6.17-6.19], the FSDP is a signature of directional bonding then a comparison of electronegativity differences suggests the feature should be a similar size in both nickel halides. Whereas Newport *et al* found only a small contribution to the FSDP from $S_{Ni-Ni}(Q)$, the current data suggests it could be as significant as in NiBr₂. Since a large FSDP is a consistent feature of the data for the mixtures (as will be seen later) the current data for pure NiCl₂ is preferred to that of Newport *et al* in the discussion that follows.

Differences in absolute normalisation and the phase of peaks are also apparent between I (the recombined partials) and II. The effects of this in real space can be gauged from comparison of the structural parameters as shown in table 6.2. Phase differences, corresponding to those in Q space, between I and II are apparent from the positions of principal and secondary peaks in $G(r)$.

Despite the differences between I and II, some real-space parameters remain in agreement and are unambiguous. The estimated coordination number is not significantly different and the r_{-}/r_{+} ratio in $g(r)$ remains almost identical at approximately 1.50. Newport *et al* used the naturally higher value of this ratio in $r^2g(r)$ of ~ 1.60 to support their conclusion that the local structure of molten NiCl₂ is approximately tetrahedral. However, reverse Monte Carlo (RMC) modelling [6.18] suggests that although the local structure in the melt is highly disordered it is probably best characterised as octahedral, as in the crystalline phase, with 1-2 vacancies. RMC modelling gives a tetrahedral geometry for pure molten ZnCl₂ which is again consistent with the known structure of the solid. Structural parameters for ZnCl₂ are shown in table 6.2 for comparison. The r_{-}/r_{+} ratios have been calculated *consistently* using peak positions in $g(r)$ and are clearly different for the two salts. It seems unlikely that they share a similar geometry as suggested by Newport *et al*.

The value of the r_{-}/r_{+} ratio for pure ZnCl₂ is in good agreement with the theoretical $\sqrt{8}/3$ (≈ 1.63) expected for a regular close-packed tetrahedron and is consistent with the RMC result. The ratio for pure NiCl₂ is about halfway between that for a regular tetrahedron and an octahedron ($\sqrt{2} \approx 1.41$). This is

² NB The Q_{\max} indicated in this and other figures (6.2, 6.4 and 6.9) was selected for display purposes and the actual Q_{\max} used in Fourier transformation was typically between 20 and 25 \AA^{-1} . In the same figures, the extrapolated region below Q_{\min} (typically between 0.3 and 0.4 \AA^{-1}) is identifiable from the smoothness of the fitted curves.

also consistent with the RMC result. A disordered octahedral structure with on average almost two vacancies (hence a mean coordination number close to four) and slightly distorted bond angles begins to resemble a distorted tetrahedral structure, which explains the intermediate value of the ratio. Since the RMC method fits a physical model to the whole of the data, it is inherently more reliable as a guide to local structure than any method based on particular features of the $G(r)$ data such as peak positions. However, it does seem that the r_{-}/r_{+} ratio in $g(r)$, taken together with the coordination number, indicates local geometries consistent with those from RMC³.

In the discussion of the mixtures data which follows, the local structure of pure NiCl_2 is taken to be irregular but probably best described as disordered octahedral with, on average, 1-2 vacancies. Although some structural parameters agree, because of the inconsistencies between I and II interpretation of the data for the NiCl_2 mixtures is based primarily on a consideration of the trends in peak position, height etc. as a function of composition rather than the absolute values. The RMC technique was not used because the constraint of a single $F(Q)$ data-set for each composition was not expected to yield structures sufficiently unambiguous to be useful in extending the analysis of such complex molten salt systems.

6.3.2 The structure of molten $\text{NiCl}_2\text{-LiCl}$ and $\text{ZnCl}_2\text{-LiCl}$

Total structure factors and real-space functions for the $\text{NiCl}_2\text{-LiCl}$ mixtures are shown in figures 6.2 and 6.3, respectively. The corresponding data for the $\text{ZnCl}_2\text{-LiCl}$ mixtures is presented in figures 6.4 and 6.5. Both systems appear to exhibit simple admixture behaviour. A gradual change with composition in the size and position of characteristic features of the pure salts is readily apparent in $F(Q)$.

The metal and alkali cations appear to retain their pure salt local structures in the mixtures. In real space, the positions of the principal peaks from $g_{\text{Ni-Cl}}(r)$ or $g_{\text{Zn-Cl}}(r)$ overlap almost exactly with $g_{\text{Li-Cl}}(r)$ (the Ni^{2+} , Zn^{2+} and Li^+ ions are very similar in size) so the contributions of the two partials cannot be easily

³ Using the positions of peaks in $r^2g(r)$ to calculate r_{-}/r_{+} would at first sight seem more correct. However, all such methods neglect the effect of vacancies in the structure which would particularly affect the r_{-} position in $r^2g(r)$ leading to an over-estimate of the true ratio relating to the local structure. The RMC solution includes the effect of vacancies through the use of the density constraint and consequently gives a more meaningful result. It should be noted that the ratio in $r^2g(r)$ for ZnCl_2 is about 1.7 which does not correspond to any obvious geometry.

distinguished. However, the normalised height H_c of the combined first peak in $G(r)$, which is defined by the following equation

$$H_c = c_M b_M (g_{M-Cl}(r) - 1) + c_{Li} b_{Li} (g_{Li-Cl}(r) - 1) \quad (6.1)$$

where M is the metal species, can be estimated and is shown as a function of composition in figure 6.6. A linear plot is to be expected if both partials remain unchanged in size and position between the endpoints. The results are clearly linear for ZnCl₂-LiCl and seem to be so for NiCl₂-LiCl too. In the case of the latter, uncertainty in number density and inconsistencies in the absolute normalisation of the data explains most of the deviation. Confirmation of the lack of change in $g_{Ni-Cl}(r)$ (and by implication in $g_{Li-Cl}(r)$) is provided by the $F(Q)$ data for NiCl₂-LiCl. The peak at $Q \sim 6 \text{ \AA}^{-1}$ in pure NiCl₂ can be uniquely ascribed to $S_{Ni-Cl}(Q)$ and, to lesser extent, the same is true of the peak at $Q \sim 3.6 \text{ \AA}^{-1}$. The heights of these peaks when scaled by the Faber-Ziman (F-Z) coefficient for $S_{Ni-Cl}(Q)$ remain approximately constant across the composition range.

Each type of cation has a characteristic anion structure so the second peak in $G(r)$ may be modelled as the weighted average of two pure salt partials - $g_{Cl-Cl}^{LiCl}(r)$ and $g_{Cl-Cl}^{MCl_2}(r)$ (the superscript refers to the pure salt). For the NiCl₂-LiCl mixtures, the position r_{Cl-Cl} of the main anion-anion peak in $G(r)$ has been plotted against the *ideal* weighting, i.e. according to the ratio of chlorine in the pure salts, of the $g_{Cl-Cl}^{LiCl}(r)$ partial, in figure 6.7. The excellent linear fit indicates simple averaging of the pure salt anion structures and is of course consistent with little or no change in local structure for both types of cation. Modelling the data for the ZnCl₂-LiCl mixtures using the pure salt partials⁴ [6.21, 6.22] weighted with the appropriate F-Z coefficients supports a similar conclusion for this system. Good fits to the anion-anion peak at $r \sim 3.75 \text{ \AA}$ are achieved using the *ideal* weighting of $g_{Cl-Cl}^{LiCl}(r)$ and $g_{Cl-Cl}^{ZnCl_2}(r)$. Although the primary peak in both partials is at virtually the same position, there is a significant difference in height so the fit does give an indication of the correctness of weighting. Alternative weightings such as cation ratios would clearly give worse fits, particularly at the 67% KCl composition.

The results also suggest that admixture behaviour extends to the FSDP and hence IRO. The estimated height H_p of the $S_{Ni-Ni}(Q)$ contribution to the FSDP is

⁴ The unknown Zn-Li partial has a small F-Z coefficient so it could be safely omitted.

plotted against composition for the NiCl₂-LiCl mixtures in figure 6.8. H_p is defined as

$$H_p = \frac{(H_Q - c_{Ni}c_{Cl}b_{Ni}b_{Cl}(0.4))}{(c_{Ni}b_{Ni})^2} \quad (6.2)$$

where H_Q is the total height of the FSDP in $F(Q)$. The contribution from $S_{Ni-Cl}(Q)$, which is assumed to remain unchanged from its value of about 0.4 ± 0.2 in pure NiCl₂, is subtracted from H_Q to give the FSDP from $S_{Ni-Ni}(Q)$ alone. The results, despite the large error bars, suggest H_p remains approximately constant. As regards the ZnCl₂-LiCl system, H_Q may be estimated in a consistent manner for both model and data and compared directly. The almost exact agreement obtained suggests that the contributions to the FSDP from both $S_{Zn-Zn}(Q)$ and $S_{Zn-Cl}(Q)$ simply scale with the F-Z coefficients across the composition range.

Despite the apparent differences in local structure between ZnCl₂ and NiCl₂, both salts exhibit a similar admixture behaviour with LiCl. The almost identical size of the Ni²⁺ and Zn²⁺ ions (with the alkali cation being only slightly smaller) prompts an explanation based on ion size and polarising power. In the pure divalent salts, each metal cation is competing for influence over surrounding anions with identical next nearest neighbour cations. As more LiCl is added, these neighbours are increasingly likely to be alkali rather than metal cations but there is apparently little effect on local structure even though doubly-charged ions have been replaced by singly-charged ones. However, the fractional number density of cations in pure LiCl is about twice that in the divalent metal chlorides. This implies that in the mixtures the local concentration of Li⁺ neighbours of Ni²⁺ or Zn²⁺ ions is also about twice what might be expected from simple replacement of metal cations. Thus the lower polarising power of singly-charged alkali cations is compensated for by the greater numbers of such ions. The lack of structural modification in the mixtures with LiCl is consistent with thermodynamic data for enthalpies and entropies of mixing for these and other MCl₂-LiCl systems where little or no deviation from ideality is observed.

6.3.3 Structural modification in NiCl₂-KCl

Total structure factors and corresponding real-space functions for the NiCl₂-KCl mixtures are shown in figures 6.9 and 6.10, respectively. In contrast to the LiCl mixtures, addition of KCl to NiCl₂ results in clear deviation from simple

admixing of the two pure salt structures. Characteristic features of pure NiCl_2 remain prominent in $F(Q)$ even up to 80% KCl.

The results indicate not just persistence but actual enhancement of the NiCl_2 local structure in the mixtures. When scaled by the F-Z coefficient, the heights of characteristic $S_{\text{Ni-Cl}}(Q)$ peaks at $Q \sim 6$ and 3.6 \AA^{-1} increase by approximately 30% between 0 and 80% KCl concentration. In real space, the principal peak from $g_{\text{Ni-Cl}}(r)$ remains prominent at the same position up to the highest KCl concentration. The $g_{\text{Ni-Cl}}(r)$ partial has been estimated for each composition by assuming that all the other partials in the expression for $G(r)$ (eqn. 2.32) are approximately zero at short distances. Structural parameters for partials generated by this method are given in table 6.3. The height of the principal peak in 80% KCl is about 30% greater than in pure NiCl_2 , which agrees closely with the aforementioned increase in the size of peaks in Q space, and there is some reduction in the FWHM. In addition, a gradual shift in the position of the first minimum to lower r with increasing KCl concentration is apparent.

However, the position of the first minimum will be affected by the gradual emergence of the principal peak from $g_{\text{K-Cl}}(r)$ which will also tend to shift the minimum down to lower r . In order to take account of this, the pure salt $g_{\text{K-Cl}}^{\text{KCl}}(r)$ partial [6.23] weighted with the appropriate F-Z coefficient was subtracted from each $G(r)$ function before proceeding, as outlined above, to derive $g_{\text{Ni-Cl}}(r)$. The structural parameters for the partials estimated by this method are shown in table 6.4. The first minimum not only still seems to shift slightly to lower r , it also becomes gradually deeper with increasing KCl. The absurd negative value⁵ for the height of the first minimum at 80% KCl implies that the principal peak of $g_{\text{K-Cl}}(r)$ in the mixtures is not, as assumed, the same height as in pure KCl but in fact smaller. The local structure of the K^+ ion thus seems to be significantly weakened even at low NiCl_2 concentration. Although over-subtracting $g_{\text{K-Cl}}(r)$ (by assuming it to be the same as $g_{\text{K-Cl}}^{\text{KCl}}(r)$) would exaggerate the reduction in height of the first minimum it would also lead to an under-estimate of the shift in position to lower r . As there is some shift even by this method it then follows that there must also be some definite reduction in the height of the first minimum since the two effects would be expected to occur together. It is apparent from these observations that in the presence of K^+ ions the local structure of the Ni^{2+} ion becomes better defined with less ionic exchange into and out of the first coordination shell.

⁵ The error bars quoted are the maximum possible errors (taking into account uncertainty in normalisation, density and the effect of FT ripple) so the height estimated for the 80% KCl concentration is almost certainly negative.

The results also indicate a gradual change in the local geometry of the metal cation in the mixtures. There is a continuous shift in the position r_{Cl-Cl} of the main anion-anion peak in $G(r)$ from its characteristic value in pure $NiCl_2$ to higher r with increasing KCl (see figure 6.7). This is clearly a trend in the average Cl-Cl separation associated with the local structure of the Ni^{2+} ion since the characteristic peak for pure KCl occurs at much higher r . The large difference in peak positions for the pure salts eliminates any possibility of the effect being due to averaging of the pure salt anion structures. Since the position of the principal peak remains unchanged, the trend in r_{Cl-Cl} implies a gradual change in local geometry. The r_{-}/r_{+-} ratio in $G(r)$ gradually increases to reach a value close to that found for pure $ZnCl_2$ at the higher KCl concentrations (see table 6.5). The local geometry of the Ni^{2+} ion thus appears to change from disordered octahedral (with vacancies) to almost regularly tetrahedral. The decrease in coordination number (integrating to r_{min} ; see table 6.3) from approximately 4.4 in pure $NiCl_2$ to 4.1 at 80% KCl seems to be consistent with such modification of the local geometry.

The height of the anion-anion peak in $G(r)$, associated with the local structure of the Ni^{2+} ion, stays approximately constant up to high alkali halide concentration when scaled by the *unweighted* F-Z coefficient for $g_{Cl-Cl}(r)$. In contrast, the anion-anion peak of pure KCl is diminished even at 80% alkali halide. These observations are evidence that a more stable and ordered local structure for the Ni^{2+} ion is attained at the expense of the K^+ ion and highlight the dominance of the nickel cation in the mixtures. The observations are also consistent with the formation of *isolated* structural units centred on Ni^{2+} ions with the surrounding K^+ ions occupying disordered sites. Isolated structural units imply reduced overlap of the 2nd shell with the 1st in $g_{Ni-Cl}(r)$, which is consistent with a reduction in height of the first minimum.

Taken together, the above findings suggest that adding KCl to $NiCl_2$ promotes the formation of stable, well-ordered, isolated and mainly tetrahedral $NiCl_4^{2-}$ structural units. An explanation for this can be given, as with the LiCl mixtures previously, in terms of the relative size and polarising power of the two cation species present. The large K^+ ion is almost twice the size of the Ni^{2+} ion and is comparatively weakly polarising. Consequently, the nearest neighbour K^+ ions around each Ni^{2+} ion cannot compete as effectively for influence over the surrounding anions. The result is a stronger and more stable local structure for the metal cation and conversely a weaker one for the alkali ion. The large K^+ ions would also be less effective at shielding the anions from their mutual electrostatic repulsion. This would lead to a tendency for the mean Cl-Cl

separation to increase and thus favour a tetrahedral geometry for the local structure of the Ni^{2+} ion. The physical size of the alkali cation would also cause a spacing apart and isolation of the NiCl_4^{2-} units and may be partly responsible for the observed increase in $r_{\text{Cl}-\text{Cl}}$. The findings for $\text{NiCl}_2\text{-KCl}$ are in good agreement with those from previous thermodynamic and optical absorption studies.

6.3.4 The effect of the alkali cation on intermediate range order

There is a contrasting effect on IRO in the mixtures depending on the type of alkali cation. The estimated height H_p of the contribution from $S_{M-M}(Q)$ to the FSDP appears to remain almost constant in $\text{NiCl}_2\text{-LiCl}$ and $\text{ZnCl}_2\text{-LiCl}$ whereas in $\text{NiCl}_2\text{-KCl}$ it increases right up to the highest alkali halide concentration (see figure 6.8). Such apparent enhancement is surprising since the addition of KCl also seems to promote the formation of isolated structural units and a reduction in Ni-Cl-Ni bridging. This implies that either IRO in pure NiCl_2 (and perhaps other MX_2 salts) does not arise from the need for anion sharing and the resulting structural correlations between units or that there is a different mechanism for IRO in the mixtures. It is of course possible that the increase in H_p is not just due to $S_{\text{Ni-Ni}}(Q)$, as assumed, but may have contributions from other partials such as $S_{\text{Ni-K}}(Q)$ and possibly $S_{\text{K-K}}(Q)$.

The origin of the FSDP has been attributed to the existence of long chains and clusters of electropositive species in several systems. From RMC simulation of molten ZnCl_2 , McGreevy & Pusztai [6.20] suggested a model involving chains of Zn^{2+} ions giving rise to fluctuations in cation density on a length scale of 5-10 Å and hence a FSDP at $Q \sim 1. \text{Å}^{-1}$. In a neutron diffraction study of the $\text{ZnCl}_2\text{-KCl}$ system, in which enhancement of the FSDP also seems to occur, Allen *et al* [6.8] suggested this was due to the formation of similar K^+ ion chains between the original Zn^{2+} ion ones in pure ZnCl_2 . A difficulty with this model is that it seems to depend on some retention of the 'network liquid' structure of pure ZnCl_2 even up to high KCl concentration. However, Raman studies [6.24] clearly indicate the formation of isolated ZnCl_4^{2-} units in the mixtures. Furthermore, the model seems even less credible in the case of $\text{NiCl}_2\text{-KCl}$ since pure NiCl_2 cannot be described as a 'network liquid' to begin with.

Another explanation for the FSDP in terms of the random packing of discrete poly-atomic units has been suggested by Price *et al* [6.25]. However, in $\text{NiCl}_2\text{-KCl}$ the isolated structural units appear to be complex anions and truly random packing of these charged entities will not occur. The NiCl_4^{2-} units will inevitably

be surrounded by a shell of large K^+ ions acting to space them apart from other similar units. It is proposed that such charge ordering gives rise to a disordered but somewhat 'lattice-like' arrangement. Hence there would be correlations in density between the well-ordered Ni^{2+} ions leading to an enhanced $S_{Ni-Ni}(Q)$ contribution to the FSDP. The model also implies the existence of (probably weaker) correlations involving $S_{Ni-K}(Q)$ and possibly $S_{K-K}(Q)$ so contributions to the FSDP could be expected from these partials too.

6.4 Summary

The effect of alkali cation type on structural modification in MCl_2 - ACl molten salt mixtures has been confirmed by direct structural measurement. With Li as the alkali, the results are best described as simple admixtures of the two pure salt structures. In contrast, considerable structural modification is observed with the larger alkali K. The presence of K^+ ions seems to promote the formation of stable, well-ordered, isolated and mainly tetrahedral $NiCl_4^{2-}$ units. These findings can be understood in terms of the competition between two types of cation species for anions and hence influence over their local structures. The small, highly polarising Li^+ ions seem to compete equally well with Ni^{2+} or Zn^{2+} metal cations for Cl^- ions so the local structure around each type of cation remains much the same as in the pure salts. However, the large and weakly polarising K^+ ion is unable to compete effectively with the Ni^{2+} ion. Consequently, the local structure of the Ni^{2+} ion is strengthened at the expense of that of the K^+ ion. Because enhancement of the FSDP is observed in $NiCl_2$ - KCl but not in either of the mixtures with $LiCl$, it appears that the K^+ ion also affects IRO. A model has been proposed in which the large K^+ ions act to both charge order and space apart the $NiCl_4^{2-}$ units thus giving rise to a less random, more 'lattice-like' structure and hence increased IRO involving the cations.

In order to ascertain the precise contributions of the various partials to the enhanced FSDP in the total scattering, detailed isotopic studies of $NiCl_2$ - KCl and $ZnCl_2$ - KCl molten salt mixtures of nominally $2/3$ alkali halide concentration were undertaken. The results, including the outcome of RMC modelling, are discussed in the next chapter.

6.5 References

- [6.1] G.N. Papatheodorou & O.J. Kleppa, 1970, *J. Inorg. Nuc. Chem.*, **32**(3), 889-900
- [6.2] D.C. Hamby & A.B. Scott, 1968, *J. Electrochem. Soc.*, **115**, 705
- [6.3] G.P. Smith & C.R. Boston, 1965, *J. Chem. Phys.*, **43**, 4051
- [6.4] G.P. Smith & C.R. Boston, 1967, *J. Chem. Phys.*, **46**, 412
- [6.5] C.R. Boston, J. Brynstad & G.P. Smith, 1967, *J. Chem. Phys.*, **47**, 3193
- [6.6] J. Brynstad, C.R. Boston & G.P. Smith, 1967, *J. Chem. Phys.*, **47**, 3179
- [6.7] A.D. Pelton, 1971, *Can. J. Chem.*, **49**, 3919
- [6.8] D.A. Allen, R.A. Howe, N.D. Wood & W.S. Howells, 1992, *J. Phys. C: Condens. Matter*, **4**, 1407-1418
- [6.9] V.M. Bazhenov, S.P. Raspopin & Y.F. Chervinskii, 1984, *Russ. Journ. Inorg. Chem. (trans.)*, **29**(12), 1814
- [6.10] M.S. Golubeva & B.S. Medvedev, 1962, *Russ. Journ. Inorg. Chem. (trans.)*, **7**(11), 1350
- [6.11] L.G. Macdonald, G.S. Perry, J.R. Smith & S.D. Wilcox (AWRE), 1986, *Thermochima Acta*, **97**, 29-35
- [6.12] A.K. Soper, W.S. Howells & A.C. Hannon, 1989, RAL report RAL-89-046
- [6.13] V.F. Sears, 1984, *Atomic Energy of Canada Ltd.*, Report AECL-8490
- [6.14] J. Galka, J. Moscinski & L. Suski, 1972, *J. Chem. Thermod.*, **4**, pp. 849-856
- [6.15] T. Yoko, R. Crescent, Y. Tsukagoshi & T. Ejima, 1978, *J. Japn. Inst. Met.*, **42**, 1179-1186
- [6.16] R.J. Newport, R.A. Howe & N.D. Wood, 1985, *J. Phys. C: Solid State Physics*, **18**, 5249-5257
- [6.17] N.D. Wood & R.A. Howe, 1988, *J. Phys. C: Solid State Physics*, **21**, 3177-3190
- [6.18] D.A. Allen, R.A. Howe, N.D. Wood & W.S. Howells, 1991, *J. Chem. Phys.*, **94**(7), 5071-5076
- [6.19] P.S. Salmon, 1992, *Proc. Royal. Soc. Lond. A*, **437** (1901), 591-606
- [6.20] R.L. McGreevy & L. Pusztai, 1990, *Proc. Royal. Soc. Lond. A*, **430** (1878), 241-261
- [6.21] S. Biggin & J.E. Enderby, 1981, *J. Phys. C: Solid State Physics*, **14**, 3129
- [6.22] R.L. McGreevy & M.A. Howe, 1989, *J. Phys. C: Condens. Matter*, **1**, 9957
- [6.23] J.Y. Derrien & J. Dupuy, 1975, *J. Physique*, **36**, 191
- [6.24] R.B. Ellis, 1966, *J. Electrochem. Soc.*, **113**, 485
- [6.25] D.L. Price, S.C. Moss, R. Reijers, M.-L. Saboungi & S. Susman, 1988, *J. Phys. C: Solid State Physics*, **21**, 1069-1072

Pure salt	Number density $\rho_o(\text{\AA}^{-3})$	F-Z coefficients		
		M-M	M-Cl	Cl-Cl
NiCl ₂	0.0367 ^a (1050°C)	0.118	0.0439	0.408
KCl	0.0223 (1040°C)	0.034	0.178	0.230
	0.0242 (820°C)	"	"	"
⁷ LiCl	0.0375 (1040°C)	0.012	-0.104	"
LiCl	0.0421 (640°C)	0.009	-0.091	"
ZnCl ₂	0.0327 (450°C)	0.036	0.242	0.408
	σ_c (barns)	σ_s (barns)	σ_a (barns) @ 1.8Å	
Nickel	13.3	18.5	4.49	
Potassium	1.73	1.98	2.1	
Chlorine	11.53	16.7	33.5	
⁷ Lithium	0.62	1.40	0.045	
Lithium	0.45	1.36	70.5	
Zinc	4.05	4.13	1.11	

The scattering cross-sections are from Sears [6.13].

^aGalka *et al* [6.14].

Table 6.1. Data analysis parameters used for the pure salts. The temperatures corresponding to the density figures are in brackets.

	NiCl ₂ I	NiCl ₂ II	ZnCl ₂
Coord num.	4.7 ±0.2	4.4 ±0.2	4.3 ±0.3
r_{Ni-Cl}	2.32±0.02	2.28±0.02	2.29±0.02
r_{Cl-Cl}	3.48±0.02	3.40±0.02	3.71±0.02
r_{--}/r_{+-}	1.50±0.03	1.49±0.03	1.62±0.03

Table 6.2. Comparison of real space structural parameters for pure NiCl₂ and ZnCl₂ [6.21]. The coordination number is for the anions around each metal cation.

% KCl	Principal peak		First min. position r_{\min} (Å)	Coordination number		FWHM
	position (Å)	height (Å ⁻¹)		by integration over $r^2 g(r)$ symmetric & to r_{\min}		
0	2.28±0.02	14±1.25	2.80±0.02	3.4±0.4	4.4±0.1	0.42±0.04
20	2.27±0.02	14±1.25	2.82±0.02	3.1±0.4	4.3±0.1	0.42±0.04
40	2.26±0.02	14±1.5	2.79±0.02	3.1±0.4	4.2±0.1	0.45±0.04
55	2.25±0.02	16±1.7	2.75±0.05	3.5±0.4	4.25±0.05	0.42±0.04
70	2.27±0.02	18±2.2	2.65±0.05	3.9±0.5	4.1±0.1	0.37±0.04
80	2.26±0.02	18±2.7	2.64±0.05	3.5±0.4	4.1±0.15	0.37±0.04

Table 6.3. Structural parameters for the estimated $g_{\text{Ni-Cl}}(r)$ partials. All parameters refer to $4\pi\rho_0 r^2 g(r)$. The coordination number is for the anions around nickel. The error bars quoted for the height of the principal peak include the effect of errors due to normalisation, uncertainty in density and FT ripple. The positional errors have been estimated by varying FT parameters such as Q_{\max} and window function settings. The same approach was used for errors in the FWHM.

% KCl	First Minimum		Coord. num. integrating over $r^2g(r)$ to r_{\min}
	position (\AA) r_{\min}	height (\AA^{-1})	
0	2.80 ± 0.02	4.4 ± 0.4	4.4 ± 0.1
20	2.85 ± 0.05	3.5 ± 0.5	4.25 ± 0.1
40	2.85 ± 0.05	3.1 ± 0.7	4.1 ± 0.1
55	2.82 ± 0.05	1.4 ± 0.9	4.0 ± 0.02
70	2.81 ± 0.05	0.4 ± 0.5	4.0 ± 0.02
80	2.82 ± 0.05	-0.7 ± 1.0	4.0 ± 0.1^a

^a integration to r_{\min} was not possible in his case - actually used 2.77\AA .

Table 6.4. Structural parameters for the $g_{Ni-Cl}(r)$ partials. All parameters refer to $4\pi\rho_0r^2g(r)$. The coordination number is for the anions around nickel.

% KCl	0	20	40	55	70	80
r_{--}/r_{+-}	1.50 ± 0.03	1.52 ± 0.03	1.58 ± 0.03	1.61 ± 0.03	1.61 ± 0.03	1.65 ± 0.03

Table 6.5. The r_{--}/r_{+-} ratios in $G(r)$ for the NiCl_2 -KCl mixtures.

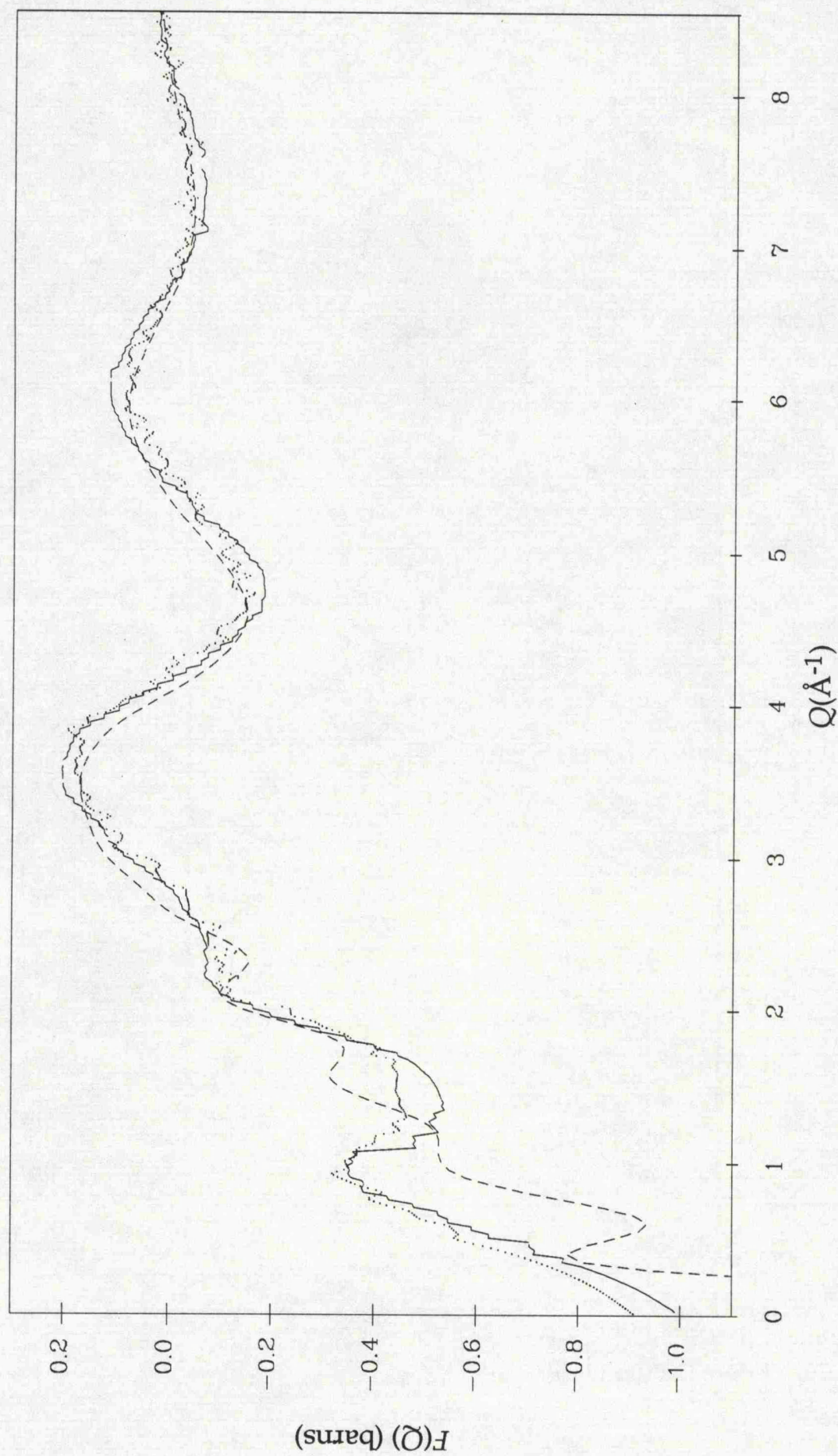


Figure 6.1. Comparison of total structure factors for pure NiCl_2 : current study I I (full curve) and both the original data (dotted curve) and recombined partials (broken curve) from the previous study I by Newport *et al* [6.16]. The $F(Q)$ from the recombined partials in I is usually referred to in the literature but is clearly flawed when compared with the original data - the FSDP has been lost and the phase of peaks is altered.

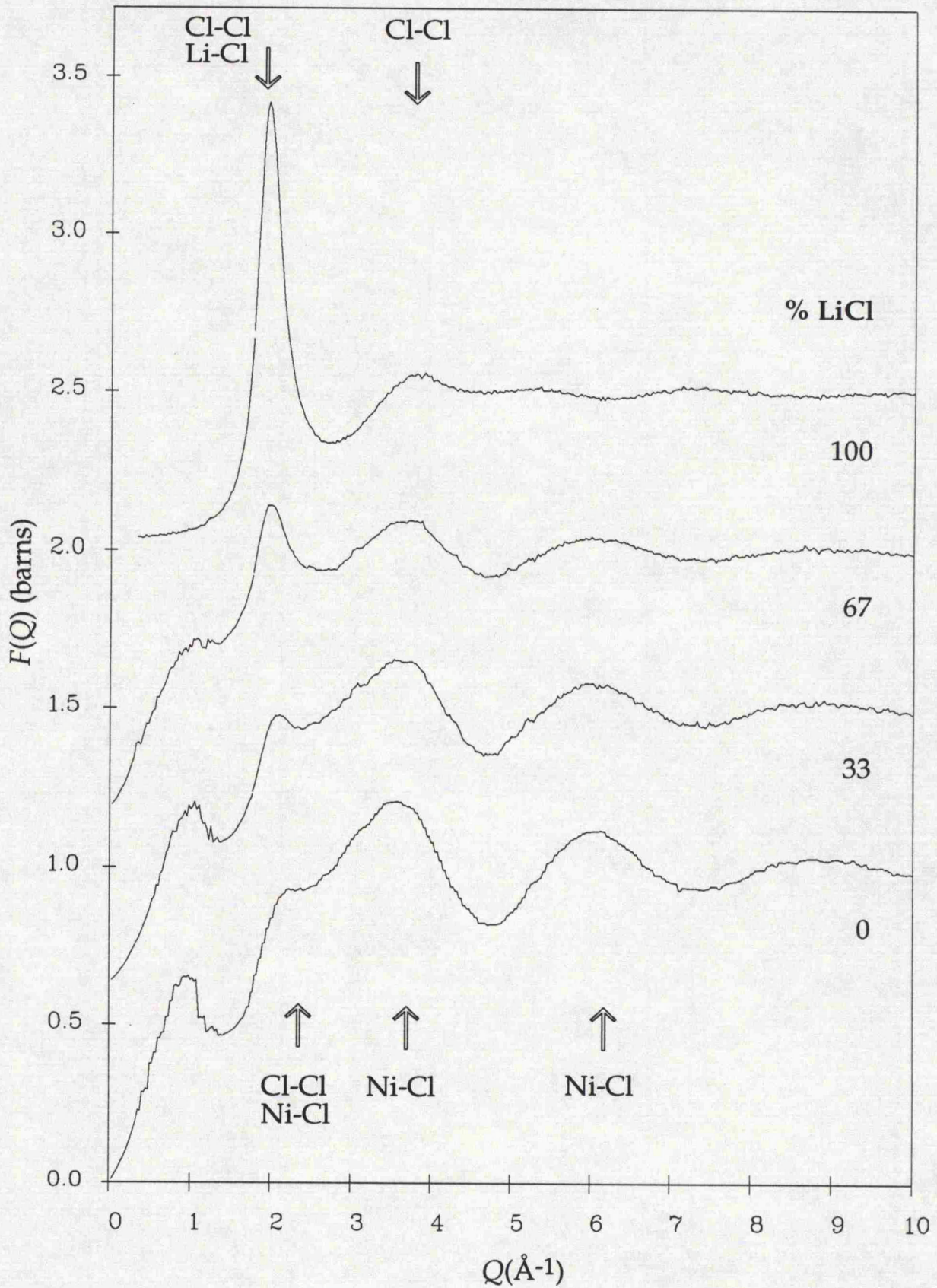


Figure 6.2. Total structure factors for molten NiCl_2 - LiCl mixtures. The main partial contributions to prominent peaks in the pure salts are indicated. The LiCl data is from McGreevy [6.22].

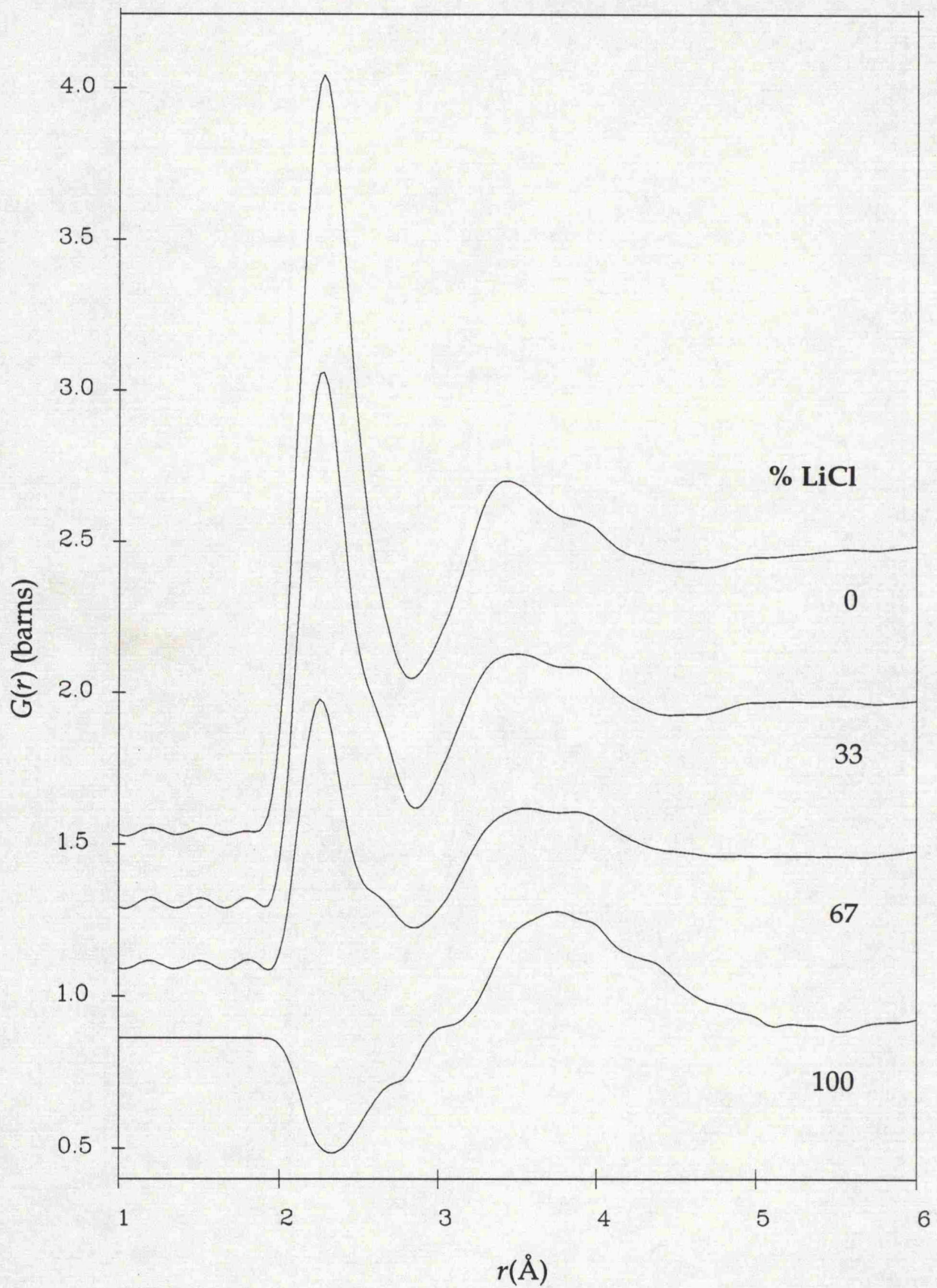


Figure 6.3. Total pair distribution functions for molten NiCl_2 -LiCl mixtures.

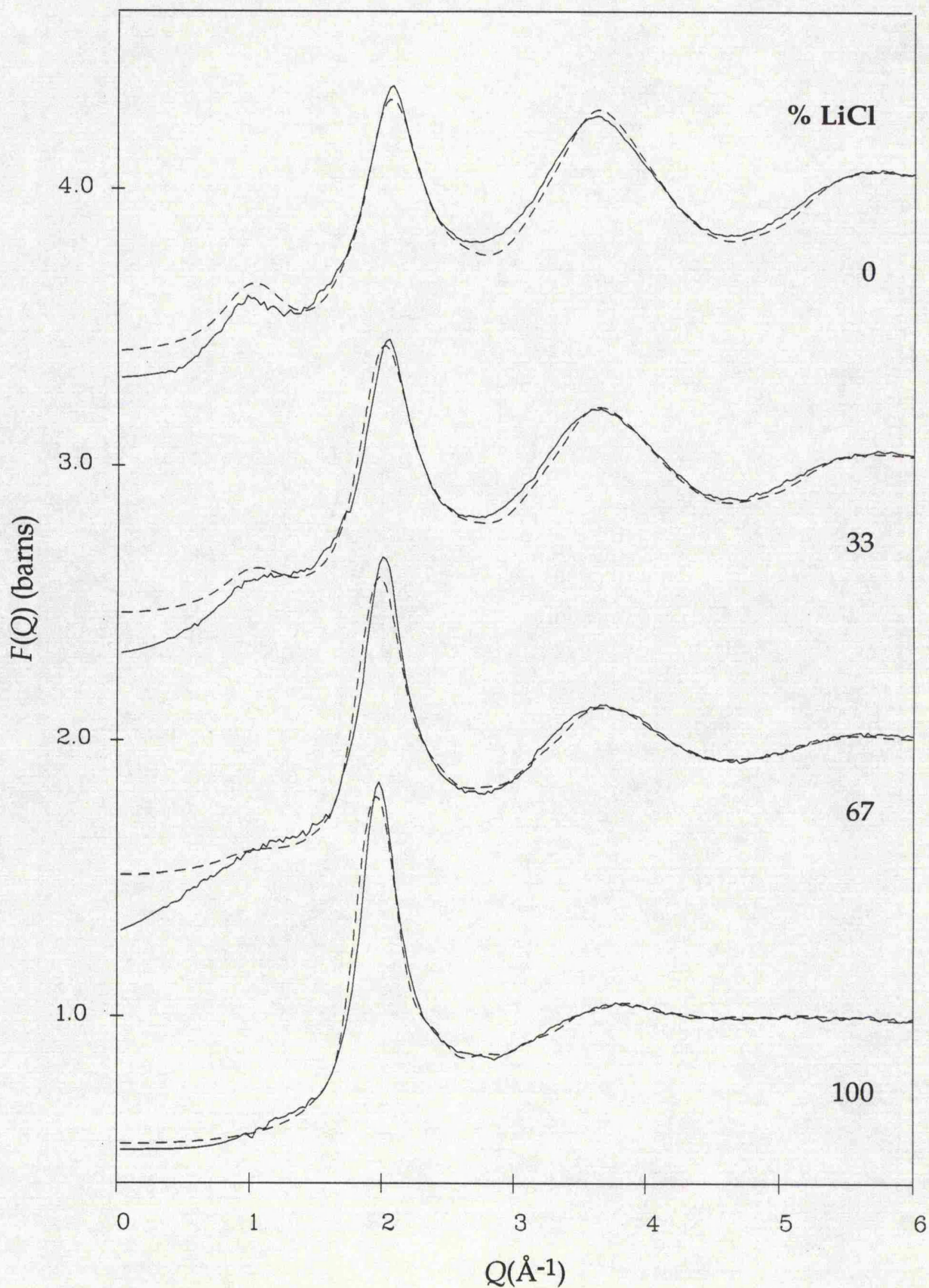


Figure 6.4. Comparison of total structure factor data (full curves) for molten $\text{ZnCl}_2\text{-LiCl}$ against model $F(Q)$ (broken curves) generated from the pure salt partials. The ZnCl_2 partials are from Biggin & Enderby [6.21] and for LiCl from McGreevy & Howe [6.22]. The divergence at low Q is probably due to the lack of a furnace correction in our data.

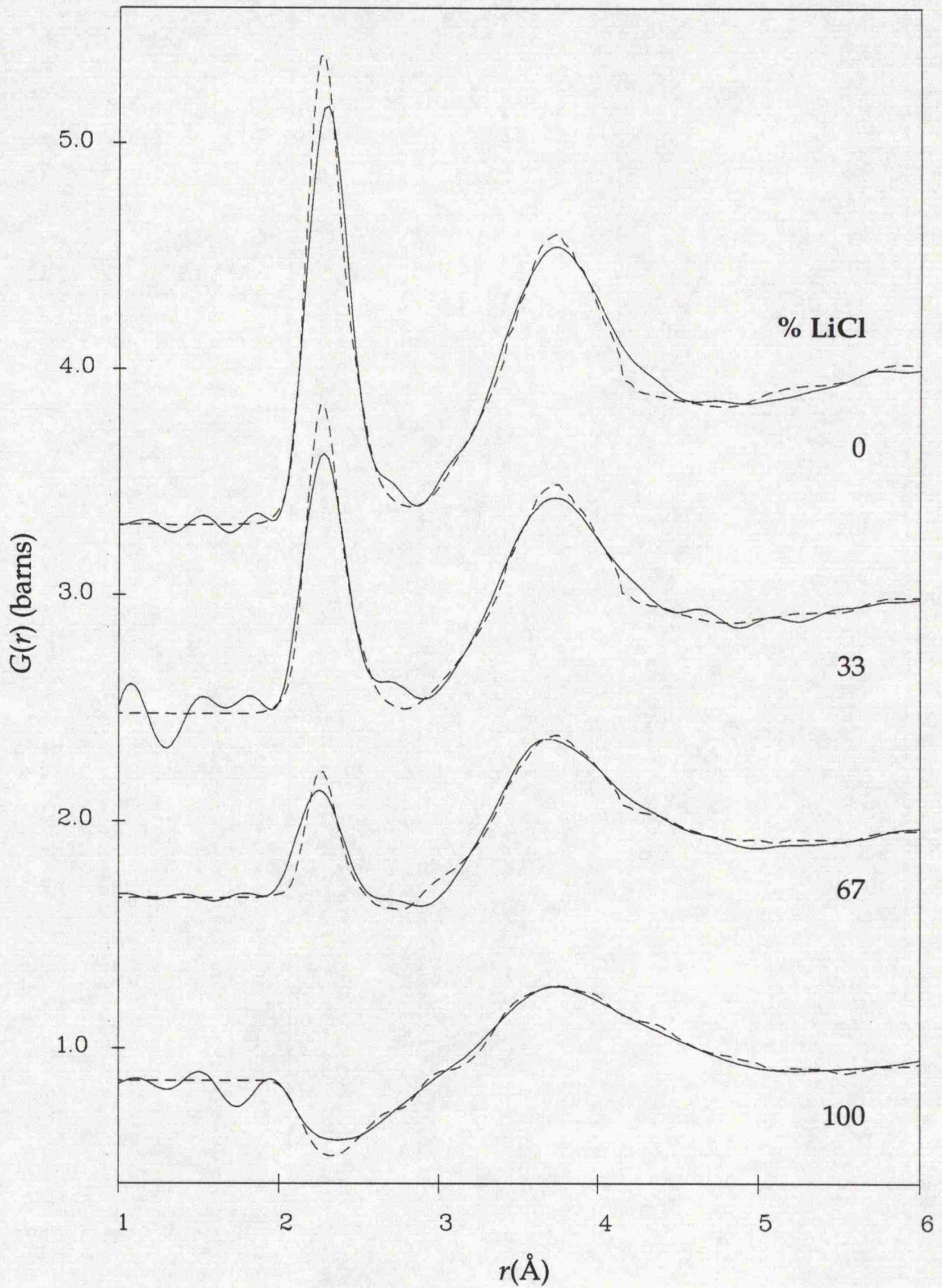


Figure 6.5. Comparison of real-space data (full curves) for molten $\text{ZnCl}_2\text{-LiCl}$ against model total pair distribution functions (broken curves) assembled from the pure salt partials. The discrepancy between model and data at the principal peak can be explained by the difference in temperature and the effects of Fourier ripple.

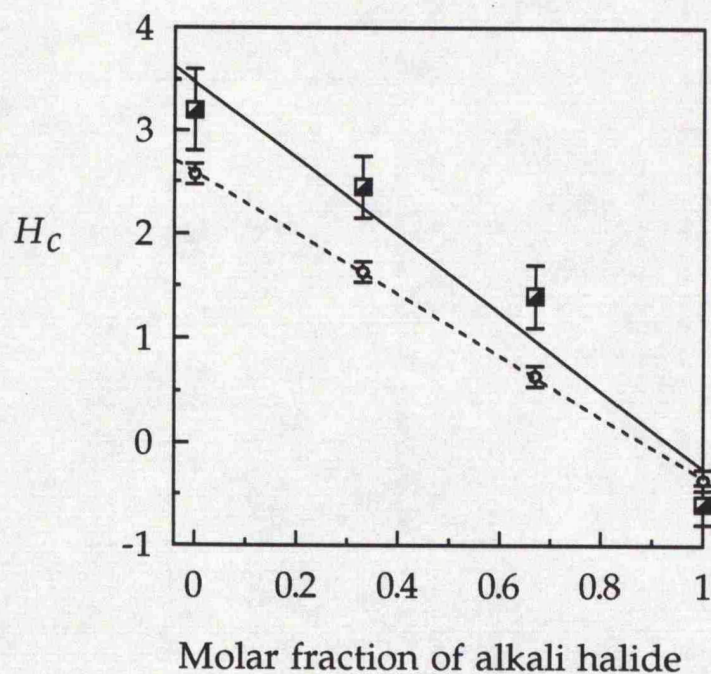


Figure 6.6. Normalised height H_c (eqn. 6.1) of the principal peak in $G(r)$ as a function of alkali halide concentration for $\text{NiCl}_2\text{-LiCl}$ (\blacksquare and full curve) and $\text{ZnCl}_2\text{-LiCl}$ (\circ and broken curve). Least-squares linear best fits are shown for the two systems.

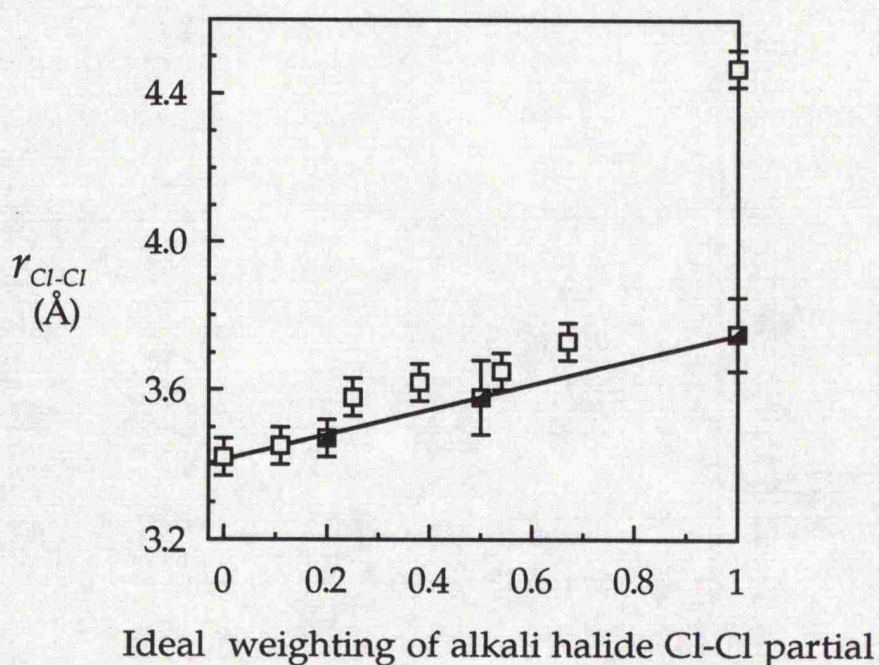


Figure 6.7. Position of the anion-anion peak $r_{\text{Cl-Cl}}$ as a function of *ideal* weighting of the alkali halide $g_{\text{Cl-Cl}}(r)$ partial for $\text{NiCl}_2\text{-KCl}$ (\square) and $\text{NiCl}_2\text{-LiCl}$ (\blacksquare and solid line).

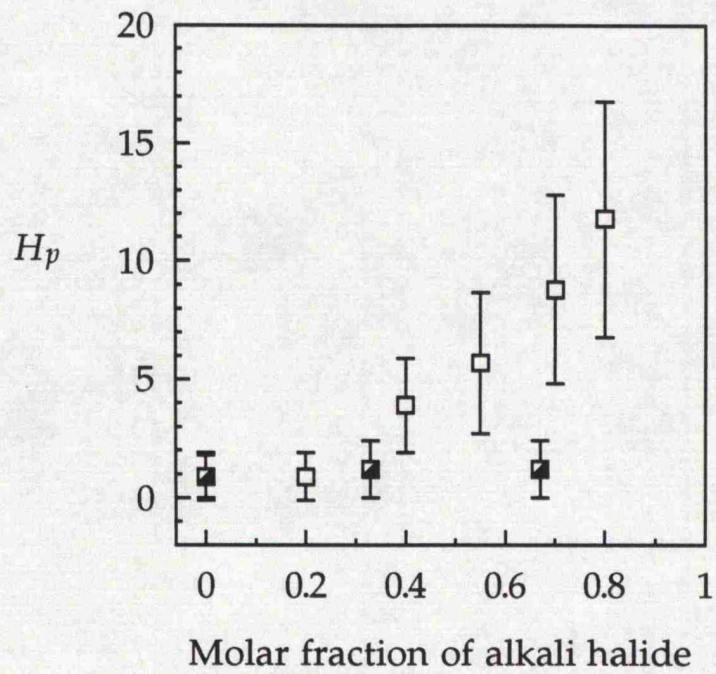


Figure 6.8. Estimated height H_p of the $S_{\text{Ni-Ni}}(Q)$ contribution to the FSDP as a function of alkali halide concentration for NiCl₂-KCl (\square) and NiCl₂-LiCl (\blacksquare).

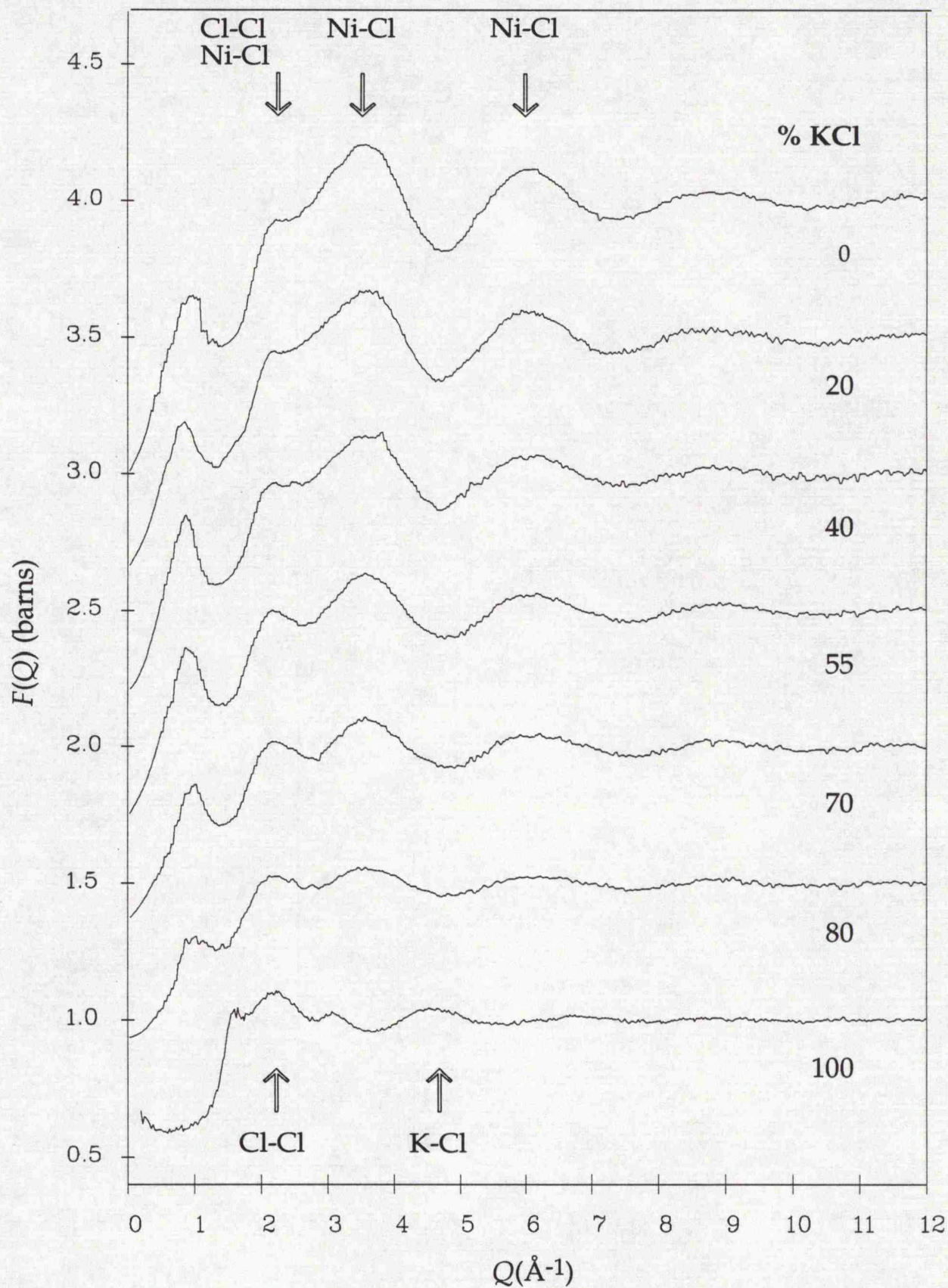


Figure 6.9. Total structure factors for the molten NiCl_2 - KCl mixtures. The main partial contributions to prominent peaks in the pure salts are indicated.

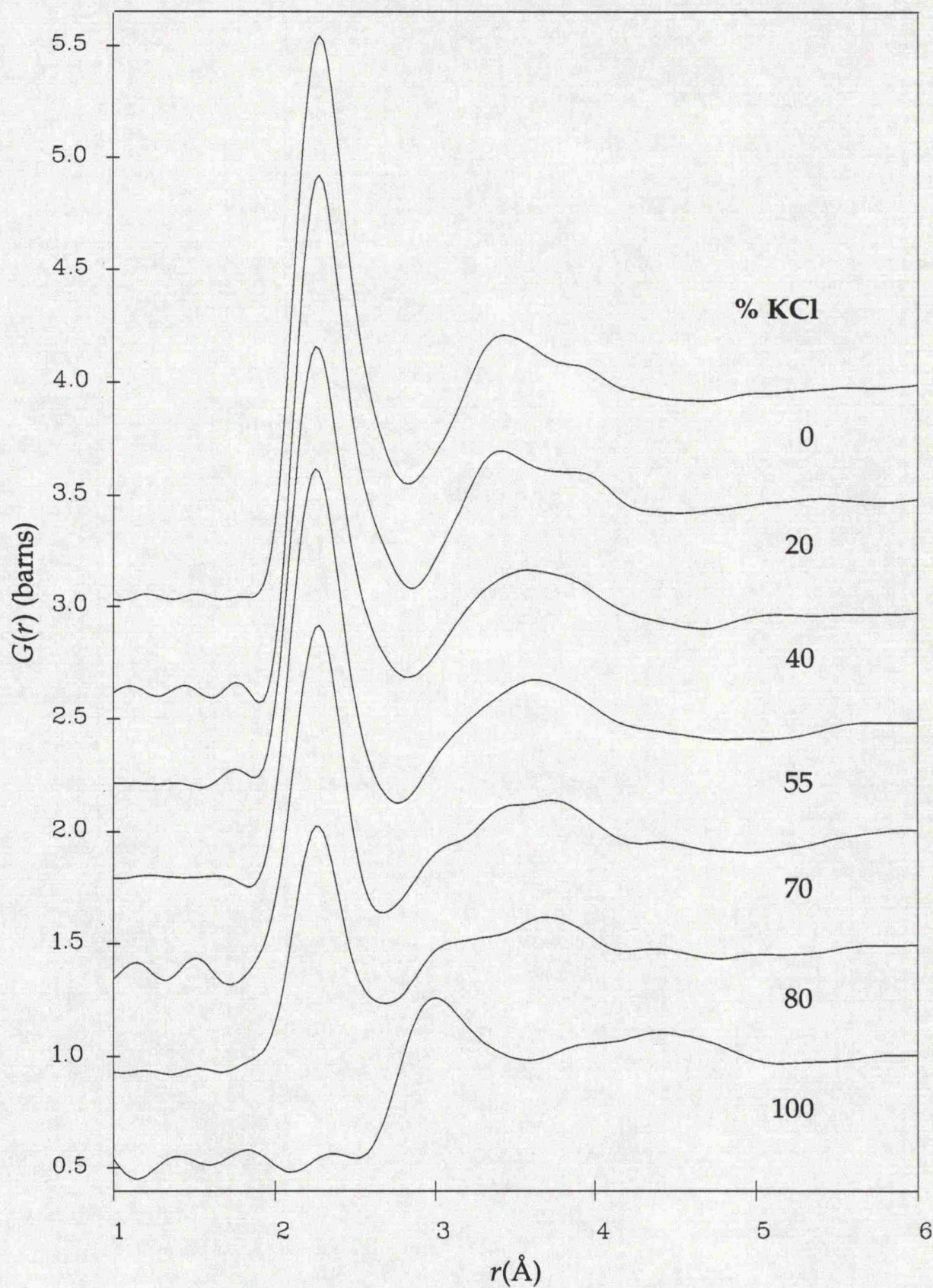


Figure 6.10. Total radial distribution functions for molten NiCl_2 -KCl mixtures.

Chapter 7

Isotopic substitution study of NiCl₂-KCl and ZnCl₂-KCl binary molten salt mixtures

(A shortened version is due to be published in J. Phys. : Condens. Mat., 1995)

Abstract

The scattering from ^xNiCl₂-KCl binary molten salt mixtures of nominally 2/3 alkali halide concentration, where x = 'natural', 'zero-scattering' and '62' enrichments of nickel, has been measured by time-of-flight neutron diffraction on ISIS LAD. A complementary experiment was performed on molten ZnCl₂-KCl samples, also of nominally 2/3 alkali halide concentration, using isotopic substitution of chlorine. In the case of NiCl₂-KCl, the results indicate a large first sharp diffraction peak (FSDP) in $S_{Ni-Ni}(Q)$ and $S_{Ni-Cl}(Q)$ but not in $S_{K-K}(Q)$. Reverse Monte Carlo (RMC) modelling indicates a well-ordered, almost regularly tetrahedral local structure for the Ni²⁺ ion, the preponderance of large K⁺ ions as next nearest neighbours to the metal cation and the apparent association of this with enhanced intermediate range order (IRO) in the mixtures. The results confirm the findings of the initial, composition study of this system and provide further support for the suggestion that enhanced IRO arises from ordering between tetrahedral units and alkali counter-ions. Modelling of the ZnCl₂-KCl data suggests a strong similarity with molten NiCl₂-KCl even though the pure NiCl₂ and ZnCl₂ molten salt structures are confirmed to be dissimilar.

7.1 Introduction

In the previous chapter, the results of a composition study of binary molten salt mixtures of divalent metal chlorides with alkali chlorides were described. The main conclusion was that the degree of structural modification was dependent on the relative size and polarising power of the alkali cation. The mixtures of NiCl₂ and ZnCl₂ with LiCl simply appeared to be admixtures of the two pure salt structures. In contrast, adding KCl to NiCl₂ led to the following structural changes :

- i) A more ordered local structure around the Ni²⁺ ion with the alkali cation appearing to occupy disordered sites.
- ii) A transition to a more regularly tetrahedral local coordination for the metal cation from one which is best described as disordered octahedral (with 1-2 vacancies) in pure molten NiCl₂.

iii) The dominance of the short-range anion structure by the metal cation, which is consistent with the formation of discrete NiCl_4^{2-} tetrahedral units.

iv) An enhanced FSDP at $Q \sim 1. \text{ \AA}^{-1}$ in the total structure factor, particularly at higher KCl concentrations, implying increased IRO.

Similar findings were reported by Allen *et al* [7.1] in their composition study of ZnCl_2 -KCl melts with one important difference ; little change was observed in the local geometry of the Zn^{2+} ion, which remains almost regularly tetrahedral just as in pure molten ZnCl_2 [7.2]. Intriguingly, Allen and co-workers also reported that enhancement of the FSDP seems to reach its maximum near the $2/3$ alkali halide concentration. At this critical composition, it is possible for the melt to consist exclusively of tetrahedral ZnCl_4^{2-} units and K^+ ions. Pure molten ZnCl_2 has a prominent FSDP in the Zn-Zn partial structure factor (PSF) [7.2] and it has been suggested by Wood and Howe [7.3] that this correlation is due to the angular dependence of interionic forces giving rise to IRO involving corner-linked ZnCl_4^{2-} tetrahedral units. Given this explanation, and contrary to the observations of Allen *et al*, the breakdown of the ZnCl_2 network structure upon the addition of alkali halide might have been expected to lead to a marked *reduction* in the size of the FSDP. In chapter 6, a simple model was proposed for molten NiCl_2 -KCl mixtures in which the large K^+ ions act to both space apart and charge order NiCl_4^{2-} units thus giving rise to a less random, more 'lattice-like' structure and hence *increased* IRO involving the metal cations. Such a model, it seems, could apply equally well to molten ZnCl_2 -KCl.

The central aim of the research described in this chapter was to study, in detail, the nature of the enhanced IRO in the mixtures. The simple model involving charge ordering between tetrahedral units and alkali counter-ions suggests there should be a sizeable FSDP arising not only from the metal-metal correlation but possibly also from metal-alkali and alkali-alkali correlations. By isotopic substitution of nickel in (nominally) $\text{NiCl}_2+2\text{KCl}$ melts it was possible to ascertain the precise contributions of some of the partials to the enhanced FSDP in the total scattering. In addition, a chlorine substitution study of (nominally) $\text{ZnCl}_2+2\text{KCl}$ melts was undertaken in an attempt to obtain details of the anion structure and, it was hoped (bearing in mind the similarities between the two systems), complementary information to that available from the nickel isotopes experiment. RMC modelling made it possible to extract the maximum structural information from the data. The wider aim of this study was to confirm the general trends highlighted in the previous composition studies of these systems.

7.2 Experimental details

The mixtures were prepared from the isotopically-enriched single salts heated gently under vacuum to minimise moisture content. The details of the vacuum drying procedure for the pure salts and the general method followed for preparing the mixtures have already been covered in chapter 3. The samples were 'pre-mixed' by heating to at least 25°C above the liquidus, as indicated in the phase diagrams for NiCl₂-KCl [7.4] and ZnCl₂-KCl [7.5], and maintained at that temperature for at least 18 hours. The prepared samples were loaded into fused quartz containers of approximately 6 mm internal diameter and 1 mm wall thickness before being sealed off under an argon pressure of ~ 0.5 atm. at room temperature.

The scattering from three isotopically-enriched samples of molten NiCl₂-KCl ('natural', 'zero-scattering' and '62' nickel enrichments), at a single nominal composition of 67% alkali halide and a temperature of 650°C, was measured by time-of-flight neutron diffraction on ISIS LAD. In a separate LAD experiment, measurements were made on three samples of molten ZnCl₂-KCl, also of nominally 67% alkali halide concentration, enriched in ³⁵Cl, ³⁷Cl and mixCl (an ~ 50:50 mixture of the two chlorine isotopes), all at a temperature of 480°C. As usual, multiple scans were taken for each sample to monitor any structural changes in sample or container due to incomplete mixing or chemical attack during data collection. Only scans that agreed to within statistical error were added together. Phase separation in the ³⁷Cl-enriched sample was evident in the form of persistent, small Bragg peaks that gradually decreased in size as the temperature was raised from 480°C and then increased again upon cooling. This sample was carefully recovered from its container and crushed to re-mix it before being re-tubed for a successful second measurement. Unfortunately, this problem meant there was no time remaining on the LAD instrument to measure a 'natural' ZnCl₂-KCl sample. In each experiment, data was collected for the empty container, furnace and instrument backgrounds as well as a vanadium calibration.

The raw data was analysed using the ATLAS package [7.6], with furnace corrections applied, in the manner described in chapter 4. The SUBSELF routine was used to remove the slopes at high Q and improve the agreement between detector groups. Composite $F(Q)$ s were obtained by merging those Q ranges of adjacent detector groups which matched well (see table 4.1). Except for the $\pm 5^\circ$ bank, there was good agreement between opposite pairs of detector groups. The lack of isothermal compressibility data precluded the use

of the long-wavelength limit as a check on normalisation. The missing low- Q portion of the data was simply extrapolated. Because of the Q^2 dependence of the Fourier transform this makes little difference to the real-space picture. The $G(r)$ functions were obtained by Fourier transformation of $F(Q)$ data smoothed at high Q (in the manner described in chapter 4). No window function was used. Comparison of the $G(r)$ from smoothed and unsmoothed $F(Q)$ data confirmed that mainly Fourier ripple was removed with marginal effect on real peaks. In addition, no obvious signs of excess or deficit of container scattering were noted in the $G(r)$ data.

The isotopic enrichments were checked, using the mass spectrometer at the Bristol isotope preparation unit, prior to data analysis and are shown in table 7.1. Because of the lack of published measurements, the number density initially used for molten $\text{NiCl}_2\text{-KCl}$ was linearly interpolated from those of the pure salt endpoints at 1040°C . The consistent renormalisation factor of approximately 0.95 found for *all* three $\text{NiCl}_2\text{-KCl}$ samples allowed a crude correction to be made to this figure. Given the similarity expected from the almost identical metal ion sizes in the two systems (see table 7.2), the corrected density value of 0.0285 \AA^{-3} is in satisfyingly good agreement with the known value of 0.028 \AA^{-3} for the $\text{ZnCl}_2\text{-KCl}$ mixture.

7.3 Discussion

7.3.1 *The structure of molten $\text{NiCl}_2\text{-KCl}$*

The total structure factors and corresponding total pair distribution functions for the three $\text{NiCl}_2\text{-KCl}$ samples are shown in figures 7.1 and 7.2, respectively. In order to extract the maximum structural information, the RMC method was used to model the data. Since the RMC method and its application are already described in detail in chapter 5, a brief outline will suffice here. Basically, RMC is a variant of the standard Metropolis Monte Carlo algorithm (see chapter 5 and references therein) and differs only in that a fit directly to the diffraction data is minimised rather than the total potential energy. The starting configuration was always a random one containing $N=2400$ atoms satisfying the appropriate geometrical constraints. The dimensions of the simulation cube gave an effective simulation size of $r \sim 21.9 \text{ \AA}$ (the maximum distance for calculating the model $G(r)$). Initially, modelling was confined to the real-space data in order to allow the closest approach distances to be fine tuned before restarting from a random configuration and fitting directly to the structure factors. As the model neared equilibrium, with χ^2

converging to a minimum, refinement of the fit by automatic renormalisation of the data was allowed. The renormalisation factor was usually close to unity (typically $\pm 2.5\%$). Statistically-independent configurations, each separated by at least $2N$ accepted moves, were collected for averaging of their properties once the model had clearly reached equilibrium.

Initial RMC modelling of the 'natural' sample alone, suggested the nominal $2/3$ alkali halide concentration was incorrect. Under-fitting of the first main peak in $G(r)$ resulted from modelling the real-space data, and a spurious spike in the leading edge of the RMC $g_{K-Cl}(r)$ partial was observed in subsequent modelling of the structure factor. These findings can be explained in terms of there being too few Ni^{2+} ions to allow a good match to the main Ni-Cl peak in real space and, conversely, too many K^+ ions so that these are pushed down to low r , where they have less effect on the back-transform, when fitting to the structure factor. Modifying the composition of the RMC model to 60% KCl led to a better fit to the first peak in $G(r)$ and the disappearance of the spurious spike in $g_{K-Cl}(r)$. Reducing the alkali halide concentration yet further to 55% KCl produced a worse match to the main Ni-Cl peak in real space. RMC modelling thus clearly favours the 60% KCl concentration as being more correct (see figure 5.1). Confirmation of this finding was provided by subsequent chemical analysis of the *entire* 'natural' sample which estimated the composition, based on the Ni:K ratio, as $59 \pm 1\%$ KCl. Equilibrium configurations were collected for the RMC model obtained assuming a 60% KCl composition. Although this represents only a *provisional* model (henceforth known as model P) found by fitting to a single structure factor, it will prove useful later in highlighting the key features of the full model (henceforth known as model F) obtained by exploiting the complete set of isotopic data.

The results, after adopting the 60% KCl composition¹, of a RMC fit simultaneously to all 3 $F(Q)$ data-sets are shown in figures 7.1 and 7.2. Although the composition of the ^{62}Ni - and ^{zero}Ni -enriched samples has not been checked independently, the existence of a RMC model physically

¹ A deficit of 10% in the amount of KCl in these samples is quite plausible given the details of sample preparation. As usual (see chapter 3), the vacuum-dried KCl was cast into a solid pellet for easier handling. However, solid KCl has a glassy appearance and is difficult to distinguish from container quartz. Consequently, some quartz fragments will inevitably have been incorporated, in place of KCl, when making up the mixtures. Fortunately, the KCl-deficient samples resulting from this systematic error are not likely to differ greatly in composition from each other.

consistent with all three data-sets strongly suggests there is no significant deviation from the assumed 60% KCl concentration. The structure factors expressed in terms of the appropriate Faber-Ziman coefficients for 'natural' (F_1), 'zero-scattering' (F_2) and ^{62}Ni (F_3) enrichments are

$$F_1 = 0.03A_{\text{Ni-Ni}} + 0.192A_{\text{Ni-Cl}} + 0.032A_{\text{Ni-K}} + 0.312A_{\text{Cl-Cl}} + 0.103A_{\text{Cl-K}} + 0.008A_{\text{K-K}}$$

$$F_2 = 0.0003A_{\text{Ni-Ni}} + 0.02A_{\text{Ni-Cl}} + 0.003A_{\text{Ni-K}} + 0.312A_{\text{Cl-Cl}} + 0.103A_{\text{Cl-K}} + 0.008A_{\text{K-K}}$$

$$F_3 = 0.013A_{\text{Ni-Ni}} - 0.126A_{\text{Ni-Cl}} - 0.021A_{\text{Ni-K}} + 0.312A_{\text{Cl-Cl}} + 0.103A_{\text{Cl-K}} + 0.008A_{\text{K-K}}$$

where $A_{\alpha\beta}$ corresponds to $(S_{\alpha\beta}(Q) - 1)$. In figures 7.3 and 7.4, the RMC solution is compared to the direct first-order and second-order differences. Compared with straight-forward isotopic differencing, the RMC method has the advantage of powerful additional constraints on ion size and density which ensure the solution partials are physically consistent with each other. This is best illustrated (see figure 7.4) for the case of the unique Ni-Ni partial, where using RMC enforces a physically realistic solution.

The RMC model-F partial structure factors are shown in figure 7.5. As expected, the unique $S_{\text{Ni-Ni}}(Q)$ partial exhibits a large peak at $Q \sim 1 \text{ \AA}^{-1}$ which makes a substantial contribution to the FSDP in the total scattering and is much larger than in pure NiCl_2 [7.8]. Rather surprising is the presence of a trough, rather than a peak, at approximately the same position in the $S_{\text{Ni-K}}(Q)$ partial. The $S_{\text{Ni-Cl}}(Q)$ PSF also exhibits a greatly enhanced FSDP compared to the pure salt. However, this partial is not unique although the weighting of the Ni-Cl term in the second-order difference F_7 (see figure 7.3) strongly suggests it is almost correct. There appears to be no obvious low- Q peak in $S_{\text{K-K}}(Q)$, which is consistent with the lack of a FSDP in the total structure factor for the 'zero-scattering' sample (no significant contribution was expected from $S_{\text{K-Cl}}(Q)$ and $S_{\text{Cl-Cl}}(Q)$ because of the absence of low- Q peaks in the same partials for the pure salts).

In order to identify the structural features induced by the additional isotopic information, particularly regarding the Ni-Ni correlation, available to the full RMC model, it is helpful to make comparisons with the provisional model. An advantage of this approach is that the differences between the two models will be virtually independent of the residual error in the estimated density (since the same value is used in both models). Figure 7.5 shows the model-P $S_{\text{Ni-Ni}}(Q)$ and $S_{\text{Ni-K}}(Q)$ partials and there clearly is a less prominent FSDP in the former and a correspondingly less pronounced trough in the latter,

compared to the model-F partials². To find out what this corresponds to in a 3-D model, the real-space Ni-Ni and Ni-K functions are compared in figure 7.6. This comparison suggests that modelling the prominent FSDP in the unique $S_{Ni-Ni}(Q)$ partial gives rise to an increase in the number of K^+ ions, and conversely a reduction in the number of metal cations, as next nearest neighbours to Ni^{2+} ions. This observation is confirmed by comparison of the mean coordination numbers, each averaged over five successive equilibrium configurations, as shown in table 7.3. Furthermore, as illustrated in figure 7.6, crudely removing the large FSDP in $S_{Ni-Ni}(Q)$ has the effect in real space of substantially increasing the size of the first (next nearest neighbour) peak. Clearly, RMC modelling suggests there is chemical ordering on the length scale of IRO, involving Ni^{2+} and K^+ ions, which is manifest as an anti-phase relationship between the peaks in $S_{Ni-Ni}(Q)$ and $S_{Ni-K}(Q)$ at low Q . This behaviour would seem to mirror the more familiar anti-phase relationship between peaks at $Q \sim 2 \text{ \AA}^{-1}$ in the metal-metal and metal-anion PSFs (as evident in the RMC partials and generally for pure molten salts) which is widely regarded as a signature of the Coulombic nature of interionic forces.

Further insight into the possible origins of the enhanced IRO can be gained from comparison of the bond angle distributions (again, averaged over several statistically-independent RMC configurations) for the two models as shown in figure 7.7. Modelling the prominent FSDP in $S_{Ni-Ni}(Q)$ leads to pronounced peaks at approximately 90° and 180° in the model-F Ni-Cl-Ni function. That this is consistent with an increase in the proportion of K^+ next nearest neighbours to Ni^{2+} cations can be visualised from figure 7.8 which illustrates the likely effect on the conformation of corner-linked and edge-sharing nickel-centred units. There is also some indication from the general depression of the Ni-Ni-Ni function at low angles of a 'straightening out' of linked units. Furthermore, because the main effect in real space of crudely removing the enhanced FSDP in $S_{Ni-Cl}(Q)$ (see figure 7.9) appears to be to shift the second peak to lower r , a large FSDP in this partial seems to be associated with relatively isolated nickel-centred units and is thus consistent with the concept of more rectilinear, linked chains of such units. Bond network analysis (see table 7.4) appears to be consistent with this simple picture, with the RMC structures shown to be dominated by branched chains and complex units (containing loops and rings) rather than entities corresponding to discrete $NiCl_4^{2-}$ tetrahedra. Visual inspection of a typical

² This is to be expected since a unique Ni-Ni partial can in principle only be obtained if all the isotopic data is used otherwise RMC will generate a much less structured solution.

'slice' through a model-F RMC configuration, as shown in figure 7.10, confirms this general impression.

Clearly, RMC modelling suggests that the prominent FSDP in the model-F $S_{Ni-Ni}(Q)$ partial arises (indirectly) from the increased numbers of K^+ ions as next nearest neighbours to Ni^{2+} ions. This is broadly consistent with, and lends support to, the model suggested in the preceding composition study (chapter 6). However, the lack of a clear peak at approximately 180° in the Ni-K-Ni bond angle distribution (figure 7.7), coupled with the small numbers of discrete $NiCl_4^{2-}$ tetrahedral units, indicates that *strong* charge ordering by the alkali counter-ions, in the manner illustrated in figure 8.19, is not a significant feature of the RMC model. The almost featureless K-K-K distribution would seem to imply that the K^+ ions occupy quite disordered sites in the structure. However, the increased order in the model-F Ni-K-Ni bond angle distribution, compared to that for model P, suggests that the alkali cations do begin to take up ordered positions relative to the Ni^{2+} ions. Thus the featureless K-K-K distribution would actually seem to reflect the random orientation of linked nickel-centred units and the random distribution of such chains with respect to each other. At this stage, it is worth pausing to note two points. Firstly, there is no *direct* information available from the isotopic data concerning the partials involving potassium so RMC may simply be under-estimating the order in the Ni-K, Cl-K and K-K correlations. Indeed, it should always be borne in mind that the discussion only ever refers to a particular model and that other, perhaps more obviously 'lattice-like' and charge-ordered, structures have *not* been ruled out. Secondly, the composition is known to fall short of the critical $2/3$ alkali halide concentration, which could explain the smaller than expected number of discrete tetrahedral units and hence also why a more strongly charge-ordered RMC structure is not apparent.

The findings from RMC modelling of molten $NiCl_2$ -KCl do share some similarities to those of Börjesson *et al* [7.9] for fast-ion conducting glasses. The addition of AgI to a phosphate or borate glass host material gives rise to a proportionate increase in the size of the FSDP at $Q \sim 0.7 \text{ \AA}^{-1}$ [7.10]. RMC modelling by Börjesson and co-workers suggests the enhanced FSDP arises not from correlations involving the additive, AgI, but from local density fluctuations in the phosphate network stemming from the requirement to maintain the connectivity of oxygen-sharing PO_4 tetrahedral units while the network is being diluted by the increasing salt content.

As regards the local structure of the Ni^{2+} ion, the results indicate the local coordination is mostly fourfold and almost regularly tetrahedral, in addition to being much better ordered than in pure NiCl_2 . The average anion coordination, estimated directly from the second-order difference G_7 (see figure 7.4), is approximately 3.6 ± 0.2 . A similar mean value of 3.7 ± 0.2 is obtained from RMC modelling and the distribution (figure 7.11) suggests most units are fourfold coordinated (although a sizeable proportion are threefold coordinated). From the position of the first, mainly Ni-Cl, peak at $r \sim 2.28 \text{ \AA}$ and the second, mainly Cl-Cl, peak at $r \sim 3.6 \text{ \AA}$ in the $G(r)$ data, a r_{-}/r_{+} ratio of approximately 1.58 is obtained, which is close to the value of $\sqrt{8/3}$ (≈ 1.63) expected for a regular close-packed tetrahedron. RMC bond angle distributions (see figures 7.11 and 7.12) confirm an almost regularly tetrahedral local geometry for the Ni^{2+} ion. The Cl-Ni-Cl function exhibits a single prominent peak at $\sim 98^\circ$. Although this is not very close to the 109.5° expected for a regular tetrahedron, a predominantly octahedral geometry can be ruled out because there is no large peak at 180° . The Cl-Cl-Cl function also exhibits a single peak at $\sim 53^\circ$ which, again, is not far off the expected value of 60° for a regular tetrahedron. The better ordered local structure is apparent from the comparison of radial distribution functions (RDFs) in figure 7.9. The Ni-Cl principal peak for molten $\text{NiCl}_2\text{-KCl}$ is clearly much taller, with a reduced FWHM and a deeper first minimum, at lower r , compared to molten NiCl_2 . These findings are wholly in accord with those of the preceding composition study.

7.3.2 The structure of molten $\text{ZnCl}_2\text{-KCl}$

The total structure factors and corresponding total pair distribution functions for the three $\text{ZnCl}_2\text{-KCl}$ molten salt samples are shown in figures 7.13 and 7.14, respectively. Attempts were made to model all three data-sets simultaneously using RMC in much the same manner as already described above for the nickel isotopes experiment. Unfortunately, the results (not shown) clearly indicated that the three structure factors were inconsistent with the same RMC structural model and hence with each other. This is borne out from modelling the data using the model-F RMC partials, obtained from fitting the nickel isotopes data, with the appropriate Faber-Ziman coefficients. It can be seen from figure 7.14 that while a good fit is obtained in real space to the Zn-Cl principal peak at $r \sim 2.3 \text{ \AA}$ for the ^{35}Cl -enriched sample, there is an increasingly poor match with the data for the other two samples as the total coherent scattering diminishes. The mismatch, particularly in the case of the weakly-scattering ^{37}Cl -enriched sample, is

thought to be due to errors in the container correction and associated errors in the normalisation of the data. Such errors provide an explanation of why there is a good match between model and data in the shape and size of the FSDP for the ^{35}Cl -enriched sample but not for the other two samples. The problem arises from using fused quartz, which is not a featureless scatterer, as the sample container material. In Q space, there is a quartz peak at approximately 1.5 \AA^{-1} so even a small error in the container correction will lead to either a deeper, or shallower, trough on the high- Q side of the FSDP and this will affect the apparent height and position of that feature - particularly if it is small. Unfortunately, TOF data invariably seems to contain spurious slopes in Q space manifest as features at low r in the Fourier transform and this makes it difficult to use the Si-O principal peak position in quartz of $r \sim 1.6 \text{ \AA}$ as a guide to the accuracy of container correction. Given the inconsistencies³ between the isotopic data-sets, the rest of this discussion will focus on the data for the ^{35}Cl -enriched sample, which will be least affected by errors in the container correction and for which a RMC structural solution providing an excellent fit in Q space was also obtained (see figure 7.13).

Again, a random RMC configuration containing $N=2400$ atoms satisfying the appropriate geometrical constraints was the starting point for modelling the structure factor data (the effective simulation size was approximately 21.6 \AA). Initial attempts at modelling indicated an error in composition similar to that encountered with the $\text{NiCl}_2\text{-KCl}$ data. Again, tests suggested the true composition was closer to 60% KCl - which was adopted in the final RMC model and for modelling using the model-F RMC partials - rather than the nominal 67% KCl. This is not surprising, since the same systematic error leading to KCl-deficient $\text{NiCl}_2\text{-KCl}$ samples is equally likely to affect the $\text{ZnCl}_2\text{-KCl}$ samples. The final RMC solution achieved a best-fit χ^2 of approximately 1.1. The fit in real space can be seen in figure 7.14 and although there is clearly some problem in resolving the K-Cl and Cl-Cl partial structures where they overlap at approximately 2.9 \AA , the RMC solution generally provides a good match to the data. As usual, several statistically-independent equilibrium configurations were collected for averaging of their structural properties.

³ The inconsistencies are confirmed by direct isotopic differencing, which reveals a large peak and a trough, respectively, at $r \sim 2.6 \text{ \AA}$ (corresponding to the O-O principal peak position in quartz) in the two second-order differences.

RMC coordination number and bond angle distributions relevant to the local structure of the metal cation are shown in figure 7.11, and these clearly indicate a regular tetrahedral geometry just as in pure molten ZnCl_2 . The mean anion coordination of Zn^{2+} ions is approximately 3.7 ± 0.1 , with the fourfold coordination being most likely. The Cl-Zn-Cl bond angle distribution peaks (almost symmetrically) around 104° and is little different to that obtained by RMC for pure ZnCl_2 [7.11]. The principal Zn-Cl and Cl-Cl peak positions in $G(r)$ of ~ 2.3 and 3.7 \AA , respectively, are also little different and confirm a similar r_-/r_+ ratio of ~ 1.61 . In addition, the height of the Zn-Cl principal peak in the RDF of approximately 18 ± 1 does not differ markedly from that for pure ZnCl_2 . Clearly, the results seem to confirm the persistence of the ZnCl_2 local structure in the mixtures as suggested by Allen *et al* [7.1]. Furthermore, the lack of change in the position of the Cl-Cl principal peak in the ZnCl_2 -KCl mixtures, in contrast to the shift to high r observed in the case of molten NiCl_2 -KCl, is consistent with the suggestion made in the preceding composition study that the local geometry of the metal cation in pure molten NiCl_2 is quite dissimilar to that in pure ZnCl_2 .

As regards the anion structure, the coordination number distribution in figure 7.12 highlights the dramatic reduction in density compared to molten ZnCl_2 , with the mean coordination number falling from ~ 10.6 down to ~ 8.5 . Molten ZnCl_2 -KCl does not appear to retain the dense, close-packed anion structure of the pure salt (a similar change does not occur in the case of the NiCl_2 -KCl melts largely because the anion structure in pure molten NiCl_2 is much less dense to begin with). This is not surprising given the evidence for the breakdown of the 'network liquid' structure of pure ZnCl_2 upon the addition of alkali halide (see [7.1] and references therein). The loss of connectivity appears to be confirmed by the disappearance of the peak present at $\sim 107^\circ$, and the diminution of the peak at $\sim 57^\circ$, in the Cl-Cl-Cl bond angle distribution for pure ZnCl_2 . Note that the apparent reduction in external constraints on the linkage of tetrahedral ZnCl_4^{2-} units seems to have little effect on the local structure of the Zn^{2+} cation, which appears remarkably stable and resilient.

In order to discuss intermediate range order, it is necessary to turn to modelling and make comparisons with the results for molten NiCl_2 -KCl. From figure 7.13, it can be seen that the FSDP in the structure factor for the ^{35}Cl -enriched sample is of a similar size and shape to the model FSDP but is positioned at slightly higher Q and appears to be somewhat narrower. Firstly, this implies a strong similarity between the two systems as regards

intermediate range order. Secondly, the relative sharpness and position of the feature in molten $\text{ZnCl}_2\text{-KCl}$ may possibly reflect the more efficient packing possible in this case due to the better ordered, more regularly tetrahedral local structure of the Zn^{2+} cation (see figure 7.11).

In general, a strong similarity between the structures of the two molten salt systems is evident from the excellent match between the amplitudes of all the main peaks in the total structure factors for model and data. The RMC partial structures for molten $\text{ZnCl}_2\text{-KCl}$ (see figure 7.15) are also very similar to those for model F (figure 7.5) especially in the case of those PSFs which contribute most to the total scattering. In addition, the bond angle and coordination number distributions (figures 7.11 and 7.12) suggest nearly similar local and anion structures. Any remaining differences between the mixtures appear to be vestiges of the dissimilar pure salt structures. For example, the Cl-Ni-Cl bond angle distribution in figure 7.11, when compared to the Cl-Zn-Cl distribution, appears to be slightly skewed towards that expected of an octahedral geometry. Differences in the results of bond network analysis (see table 7.4) can also be interpreted as arising from the dissimilar pure salt structures. The general similarity between the two molten salt systems is perhaps not surprising given the almost identical ion sizes of the two metal species. However, this naturally begs some questions as to the reasons for the clearly different structures of the pure salts, which are considered (briefly) next.

7.3.3 *The structures of the pure ZnCl_2 and NiCl_2 melts*

The Zn^{2+} cation has been found to have a tetrahedral coordination in crystalline polymorphs of pure ZnCl_2 and in the glass phase [7.12]. In contrast, the Ni^{2+} cation has an octahedral coordination within a layered CdCl_2 -type structure, in the crystalline phase of pure NiCl_2 [7.13]. RMC modelling by McGreevy and Pusztai [7.11] suggests that, in common with a range of other monovalent and divalent metal halide salts studied, the ZnCl_2 and NiCl_2 melts retained the basic local symmetries of the corresponding crystals from which they fused. This conclusion is, of course, wholly consistent with the current findings and the composition study discussed in the preceding chapter. Obviously, to explain the differing structures, effects other than simple ion size must be invoked. From a neutron diffraction study of the nickel halides, Wood and Howe [7.3] suggested a model involving reduced charge transfer arising from hybridisation of the metal d-band and anion p-band. The electronic structure of Ni^{2+} is d^8 and is therefore quite different to

that of Zn^{2+} which has a completely-filled d shell. It appears very likely that such differences play a part in determining structure. Indeed, it has been suggested [7.14] that the large deficit in the entropy of melting of pure ZnCl_2 is associated with the persistence of a strong network of partially covalent bonds arising from hybridisation of d states on Zn^{2+} with p states on Cl^- . More recently, Wilson and Madden [7.15] have put forward a simple ionic model which includes the effect of induced dipoles on the structure of divalent metal halide melts consisting of a small, highly polarising cation and a large, highly polarisable anion, such as ZnCl_2 . Computer simulation [7.16] shows that this polarisable anion model, unlike those based upon a rigid-ion assumption, can reproduce observed experimental features such as the overlap of principal peaks in $g_{++}(r)$ and $g_{--}(r)$ as well as the FSDP in $S_{++}(Q)$. However, given the almost identical metal ion sizes, it seems unlikely that the differences in structure of ZnCl_2 and NiCl_2 can be explained simply by including polarisation effects in a simple ionic model. It still seems necessary to invoke 'covalency' effects arising from the detailed electronic configuration as an explanation for the different melt structures and for such non-Coulombic features as adjacent layers of anions in the CdCl_2 structure of crystalline NiCl_2 .

7.4 Summary

The general trends in structural modification for NiCl_2 -KCl molten salt mixtures, first identified in the preceding composition study, have been confirmed by isotopic substitution of the nickel species at a specific composition. RMC modelling of the isotopic data-sets has made it possible to ensure a physically consistent set of PSFs. The unique $S_{\text{Ni-Ni}}(Q)$ partial obtained in this manner exhibits, unlike the corresponding PSF for molten NiCl_2 , a prominent FSDP thus confirming the existence of enhanced IRO in the mixtures. The RMC findings also confirm a better ordered, more regularly tetrahedral local structure around the Ni^{2+} ion and the dominance of the anion structure by the metal cation. Comparison of RMC models obtained by fitting to all or part of the isotopic data has made it possible to identify the structural features arising from modelling the prominent FSDP in $S_{\text{Ni-Ni}}(Q)$. The results suggest the enhanced IRO in the mixtures arises from increased numbers of K^+ ions as next nearest neighbours to Ni^{2+} ions. This is broadly consistent with, and lends support to, the model suggested in the preceding composition study in which the alkali cation plays a central role in promoting IRO. Although it was not possible to obtain detailed information about the anion structure in molten ZnCl_2 -KCl, RMC modelling of the

structure factor for the most strongly scattering ^{35}Cl enrichment did confirm the persistence of the tetrahedral ZnCl_2 local structure. Modelling also confirmed the general similarity to molten $\text{NiCl}_2\text{-KCl}$, with any residual differences between the two molten salt systems appearing to be vestiges of the dissimilar structures of the pure NiCl_2 and ZnCl_2 melts.

The somewhat narrower FSDP at slightly higher Q in molten $\text{ZnCl}_2\text{-KCl}$, compared to that in molten $\text{NiCl}_2\text{-KCl}$, hints at the importance of well-ordered local units as regards IRO in the mixtures. In this context, the study of structural modification in alkali chloro-aluminate melts, as detailed in the next chapter, is of particular interest.

7.5 References

- [7.1] D.A. Allen, R.A. Howe, N.D. Wood & W.S. Howells, 1992, *J. Phys. : Condens. Mat.*, **4**, 1407-1418
- [7.2] S. Biggin & J.E. Enderby, 1981, *J. Phys. C: Solid State Physics*, **14**, 3129
- [7.3] N.D. Wood & R.A. Howe, 1988, *J. Phys. C: Solid State Physics*, **21**, 3177
- [7.4] V.M. Bazhenov, S.P. Raspopin & Y.F. Chervinskii, 1984, *Russ. Journ. Inorg. Chem. (trans.)*, **29**(12), 1814
- [7.5] G.S. Perry, L.G. Macdonald & S. Newstead, 1983, *Thermochim. Acta.*, **68**, 341
- [7.6] A.K. Soper, W.S. Howells & A.C. Hannon, 1989, "ATLAS - analysis of time-of-flight diffraction data from liquid and amorphous samples", RAL report RAL-89-046
- [7.7] V.F. Sears, 1992, *Neutron News*, **3**(3), 26-37
- [7.8] R.J. Newport, R.A. Howe & N.D. Wood, 1985, *J. Phys.C: Solid State Physics*, **18**, 5249-5257
- [7.9] L. Börjesson, R.L. McGreevy & W.S. Howells, 1992, *Phil. Mag. B*, **65**, 261
- [7.10] L. Börjesson, L.M. Torrel, U. Dahlborg & W.S. Howells, 1989, *Phys. Rev. B*, **39**, 3404
- [7.11] R.L. McGreevy & L. Pusztai, 1990, *Proc. R. Soc.*, **430**(1878), 241-261
- [7.12] J.A.E. Desa, A.C. Wright, J. Wong & R.N. Sinclair, 1982, *J. Non. Cryst. Solids*, **51**, 57
- [7.13] R.W.G. Wyckoff, 1963, "Crystal Structures", 2nd edition, vol. 1, New York: Interscience
- [7.14] Z. Akdeniz & M.P. Tosi, 1992, *Proc. R. Soc. A*, **437**, 85
- [7.15] M. Wilson & P.A. Madden, 1994, *J. Phys. : Condens. Mat.*, **6**, A151-A155
- [7.16] M. Wilson & P.A. Madden, 1993, *J. Phys. : Condens. Mat.*, **5**, 6833-6844

	NiCl ₂ -KCl			ZnCl ₂ -KCl		
	natNi	zeroNi	⁶² Ni	³⁵ Cl	mixCl	³⁷ Cl
\bar{b}_{coh} (fm)	10.31	1.045	-6.75	11.59	7.41	3.68

Table 7.1. Coherent scattering lengths for the isotopic enrichments used in each sample. The individual scattering lengths of each isotope were taken from Sears [7.7].

Salt	Ionic radii (Å)	r_+/r_-
NiCl ₂	0.72	0.43
ZnCl ₂	0.74	0.46

Table 7.2. Comparison of crystal ionic radii for the divalent metal cation in the solid phases, and ratios of ionic radii (r_+/r_-) in the liquid phases, of NiCl₂ and ZnCl₂. A close similarity in metal ion sizes is also suggested by the almost identical first-peak positions in $G(r)$ for the two molten salts (see table 6.2).

Neighbour type	Mean Coord. number	
	Model P	Model F
Ni ²⁺	3.5 ± 0.2	3.0 ± 0.2
K ⁺	6.3 ± 0.2	6.7 ± 0.2

Table 7.3. Next nearest neighbour coordinations of Ni²⁺ averaged over several equilibrium configurations (r_{max} of 6 Å in all cases) for molten NiCl₂-KCl. The error bars have been estimated from the variation in coordination number between successive RMC configurations so the true errors in the mean values shown above are probably less than indicated.

RMC model		<u>Branched chains</u>		<u>Complex units</u>
		(all ≥ 3 atoms size)	5 atoms size	all sizes
NiCl ₂ -KCl	P	95	27	15
-	F	104	35	31
ZnCl ₂ -KCl		68	28	16
Pure NiCl ₂		25	3	15
Pure ZnCl ₂		4	0	1

Table 7.4. The results of bond network analysis (averaged over several equilibrium configurations) for the RMC models. The total numbers of branched chains and complex units (containing loops and rings) formed by neighbouring metal cations and anions, separated by no more than 2.8 Å, are shown. The branched chains of 5 atoms size correspond to discrete tetrahedra. The much greater numbers of such discrete units, in addition to branched chains and complex units, in the mixtures compared to the corresponding pure molten salts is consistent with the 'network-breaker' role of the alkali halide as supported by previous composition studies. Any quantitative differences between the mixtures in the degree of network breakdown e.g. the smaller number of branched chains in molten ZnCl₂-KCl, appear largely to be vestiges of the structural differences between the pure molten salts.

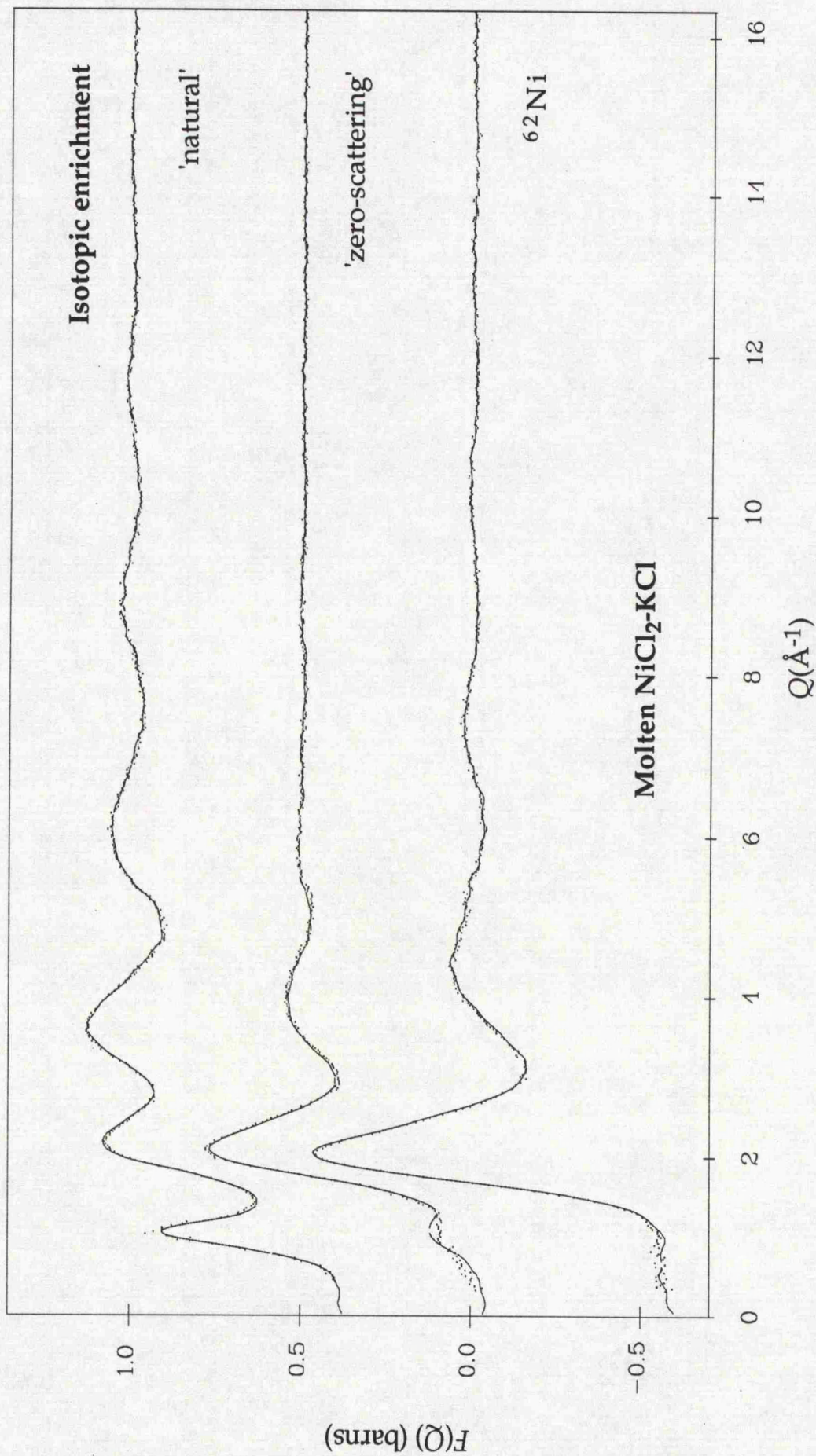


Figure 7.1. Total structure factor data (dotted curves) for the $\text{NiCl}_2\text{-KCl}$ samples compared with their respective RMC fits (solid curves). The deviations between model and data are most pronounced at low Q but this is to be expected since corrections for absorption and inelasticity are greatest in this region.

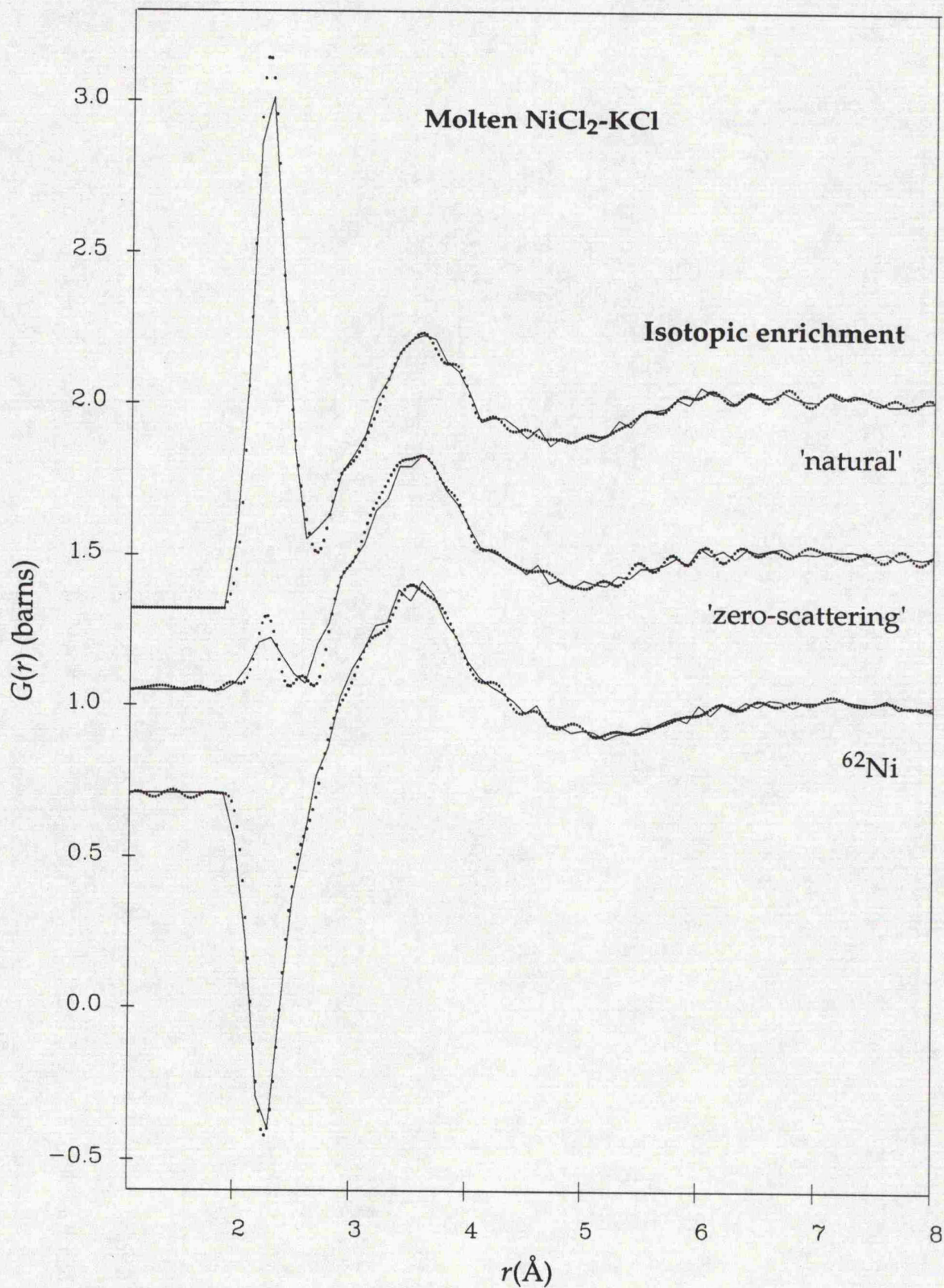


Figure 7.2. Total pair distribution functions (dotted curves) for the NiCl₂-KCl samples compared against the corresponding RMC fits (solid curves). Note that the 'zero-scattering' sample clearly does not have a coherent scattering length of exactly zero for nickel because a small Ni-Cl principal peak is still visible at $r \sim 2.3 \text{ \AA}$.

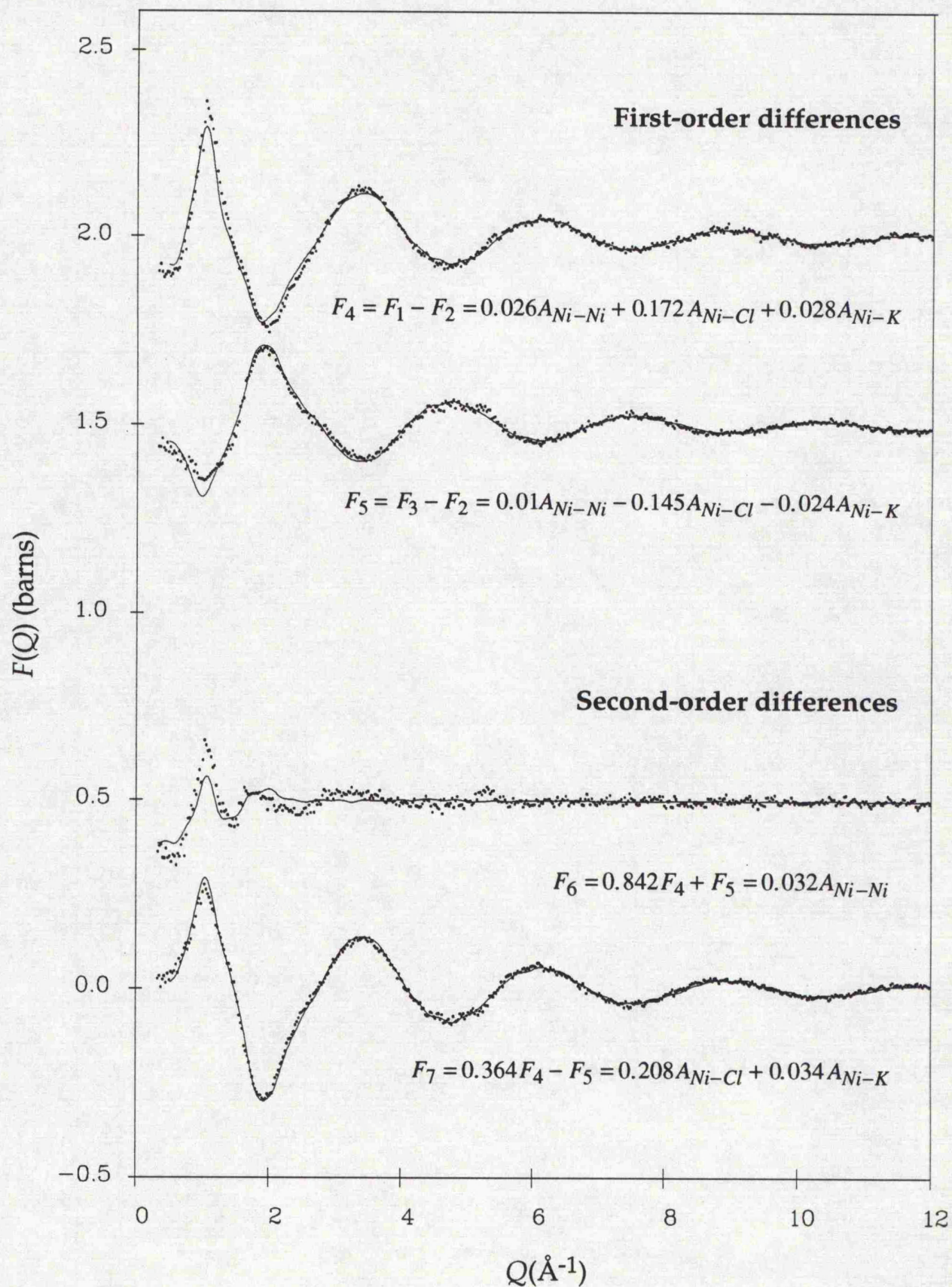


Figure 7.3. Comparison of the direct first- and second-order differences (dotted curves) against the model-F RMC solution (solid curves), for the NiCl₂-KCl data.

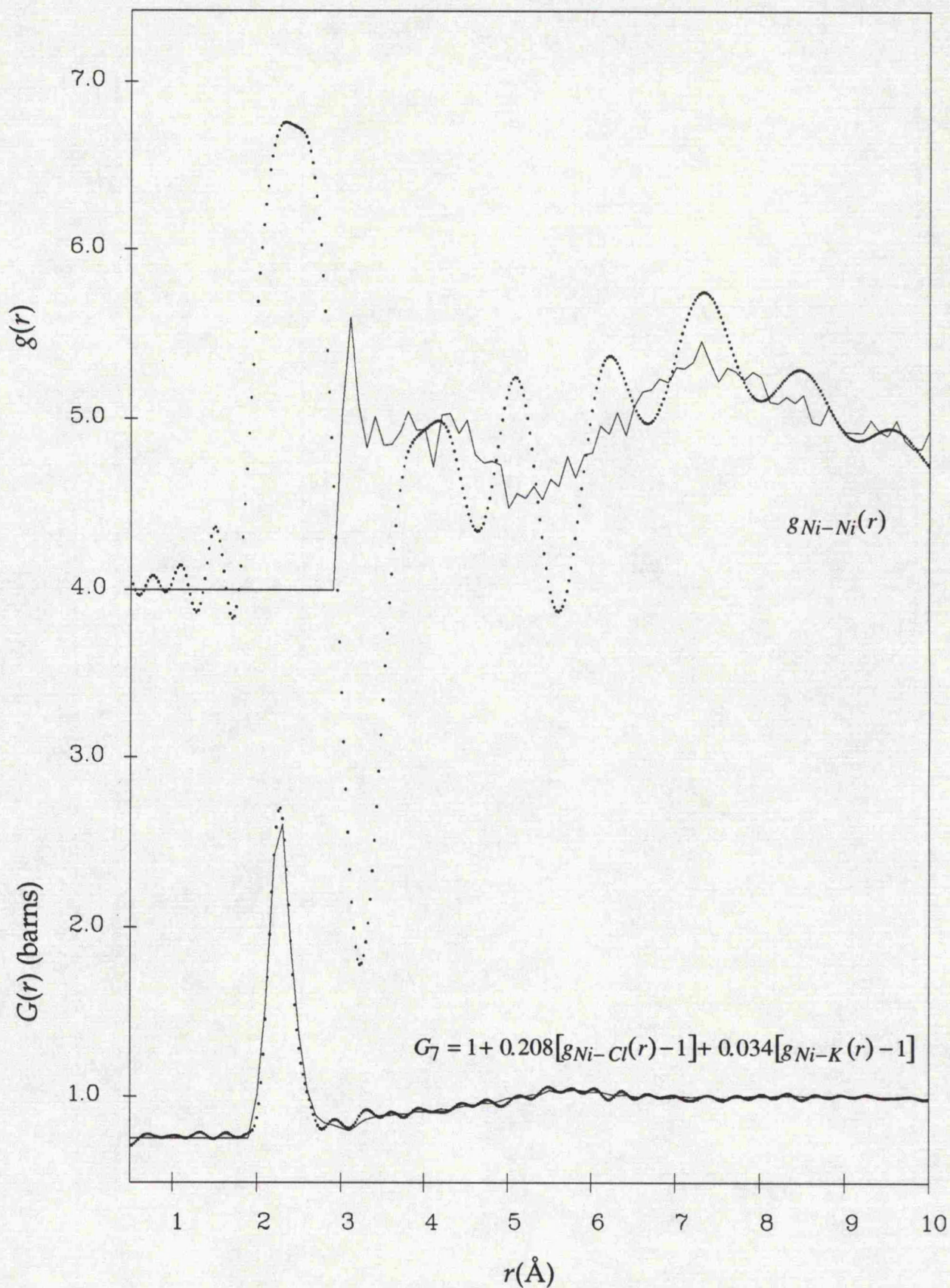


Figure 7.4. Comparison of the real-space functions obtained from the direct second-order differences (dotted curves) shown in figure 7.3 and the RMC solution (solid curves). Note that the Ni-Ni partial is clearly unphysical at low r and RMC is essential to obtaining a realistic solution. The spurious peak and trough at $r \sim 2.3$ and 3.4 \AA , respectively, appear to correspond to the features between $Q \sim 2$ and 6 \AA^{-1} in F_6 (see figure 7.3) which are not modelled by RMC.

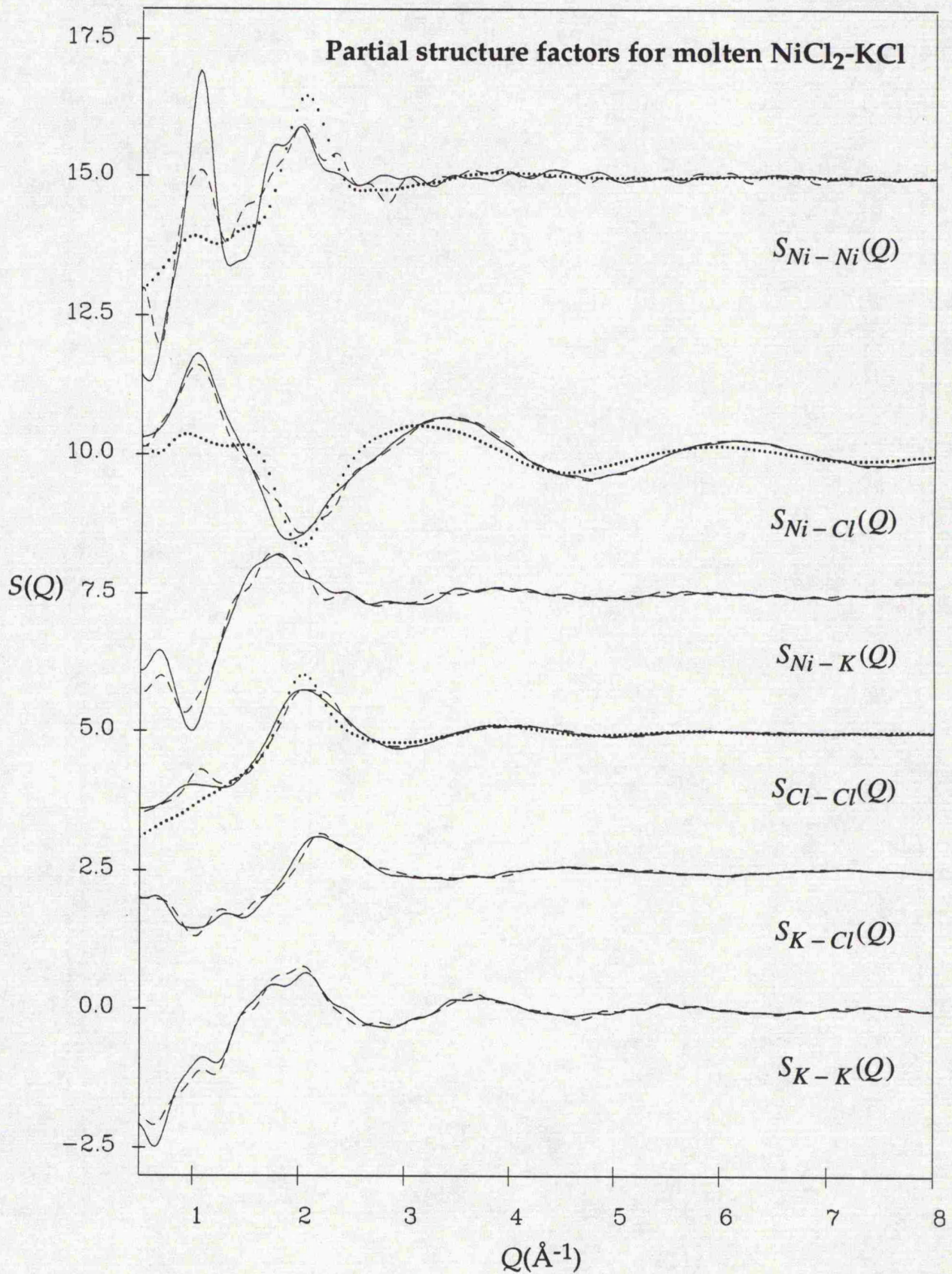


Figure 7.5. Comparison of RMC partial structure factors for model F (solid curves) and model P (dashed curves). The three PSFs for pure molten NiCl₂, from the isotopic study of Newport *et al* [7.8], are also shown as dotted curves.

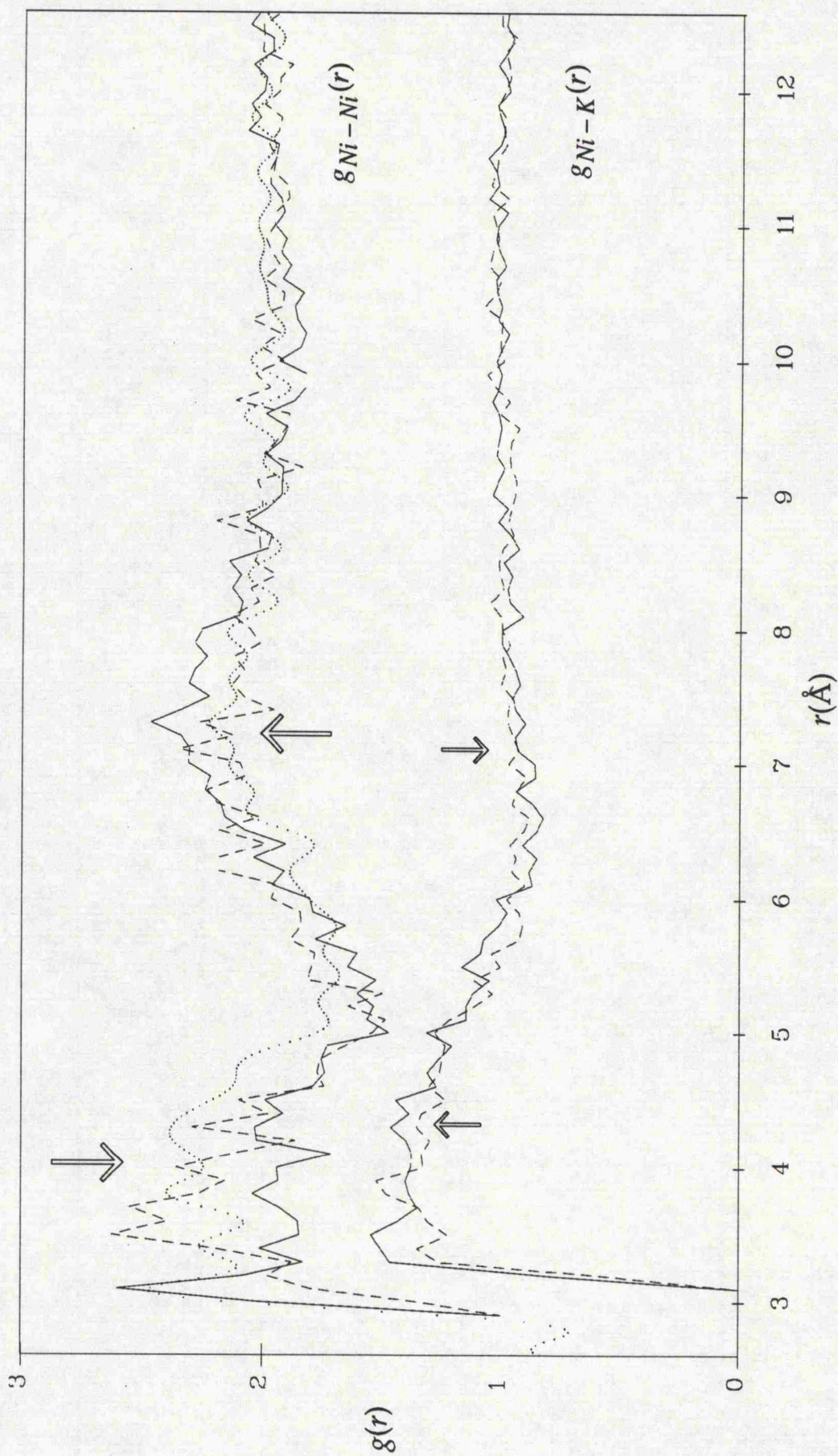


Figure 7.6. Comparison of Ni-Ni and Ni-K pair distribution functions for RMC models F (solid curves) and P (dashed curves). It is apparent from the changes highlighted by the arrows, that modelling the FSDP in the Ni-Ni PSF gives rise to a reduction in the number of Ni^{2+} ions, and conversely an increase in the number of K^+ ions, as next nearest neighbours to the metal cation. The dotted curve shows the effect in real space of crudely removing the large FSDP in the Ni-Ni PSF prior to Fourier transformation.

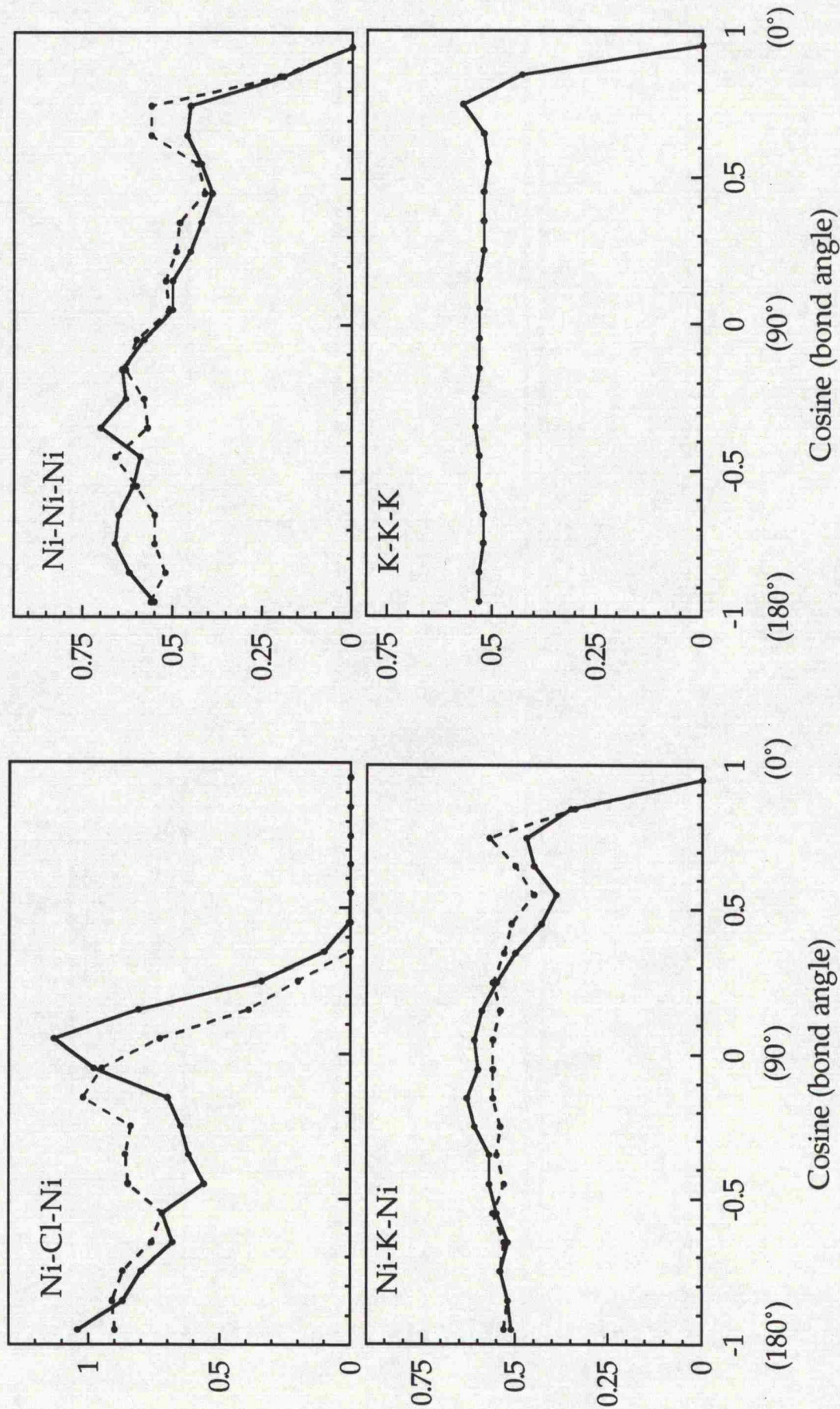


Figure 7.7. Comparison of RMC bond angle distributions pertaining to IRO for models F (solid curves) and P (dashed curves).

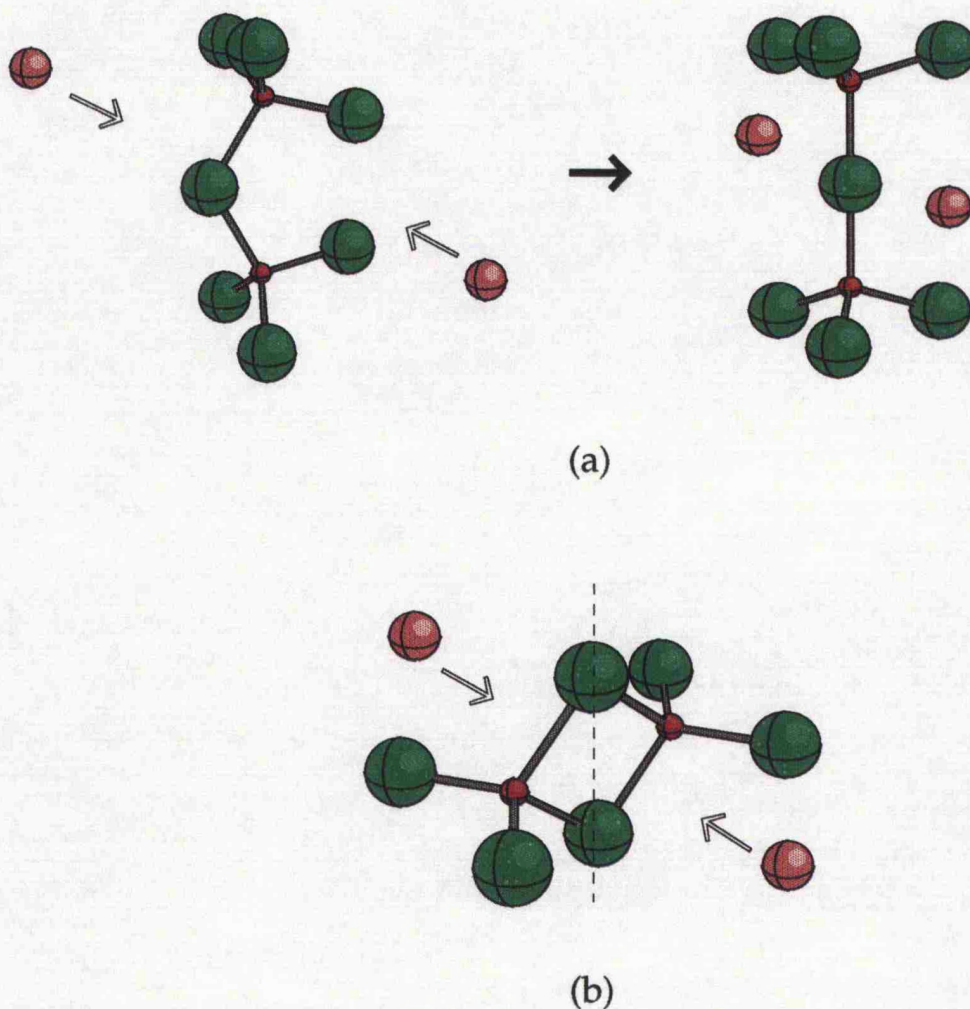


Figure 7.8. Illustration (exaggerated) of the apparent effect of increased numbers of K^+ ions as next nearest neighbours to nickel, on the conformation of a) corner-linked and b) edge-sharing $NiCl_4^{2-}$ tetrahedral units in molten $NiCl_2$ - KCl . The atoms are shown to reduced scale (for clarity) with chlorine coloured green, nickel coloured red and potassium coloured orange. The 'bonds' do not imply the existence of actual bonds but simply serve to highlight the geometry of (mainly) ionic complexes. In (a) it can be seen how the large K^+ ions promote a more rectilinear conformation of corner-linked tetrahedral units (although only two linked units are shown, the same will be true of larger linked chains). In (b) a similar process can be seen at work in the case of edge-sharing tetrahedra, where the large K^+ ions will limit the movement of the two 'wings' around the axis joining the bridging chlorine atoms (dotted line) thus giving rise to a more symmetrical structure.

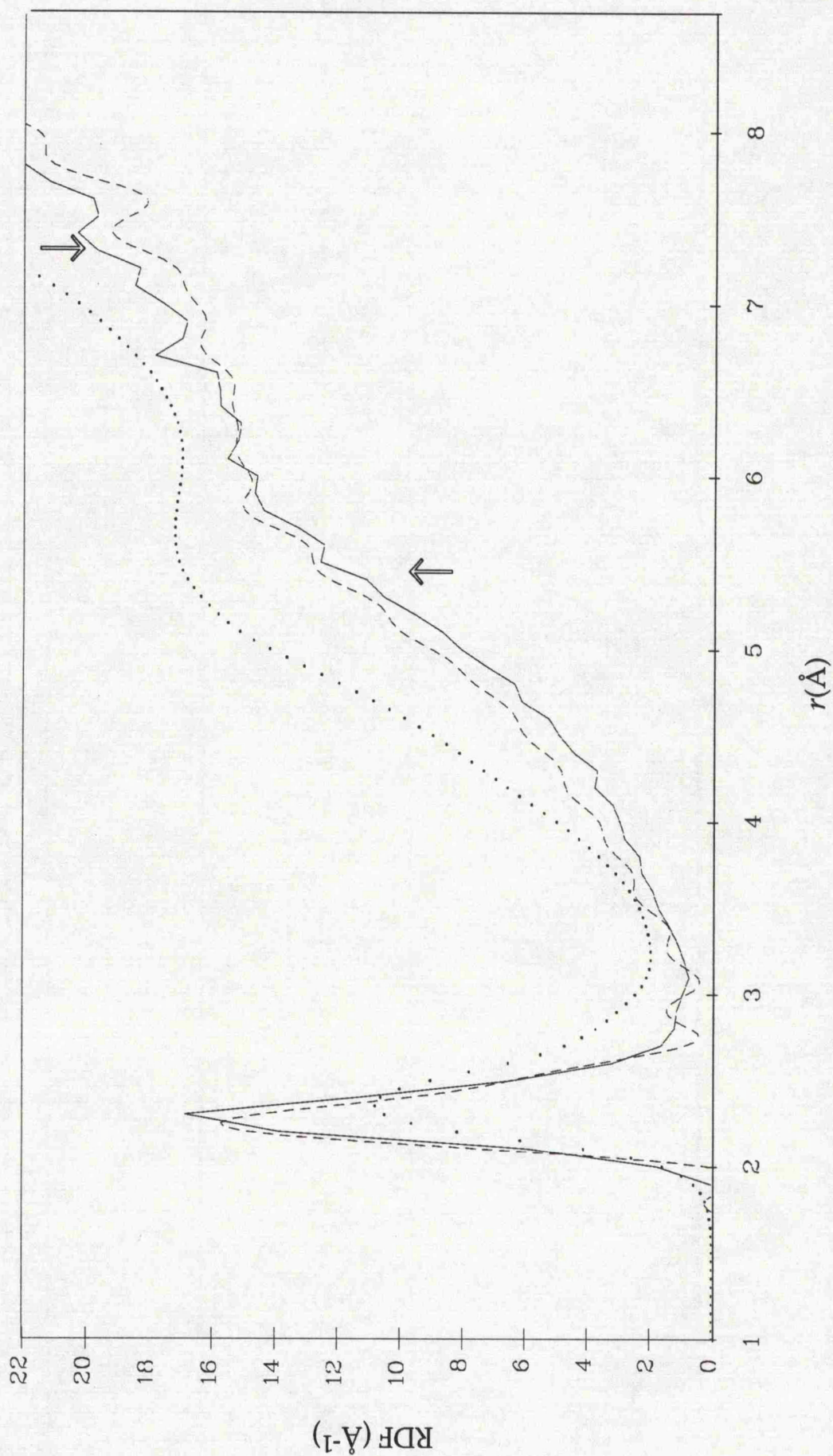


Figure 7.9. Comparison of RDFs (defined as $4\pi\rho_0 r^2 g(r)$) for the Ni-Cl correlation. The solid curve is the RDF using the model-F $g_{\text{Ni-Cl}}(r)$ function and the dotted curve is the corresponding RDF for pure molten NiCl_2 from the data of Newport *et al* [7.8]. The dashed curve shows the effects (highlighted by the arrows) in real space of crudely removing the FSDP in the corresponding model-F PSF prior to Fourier transformation.

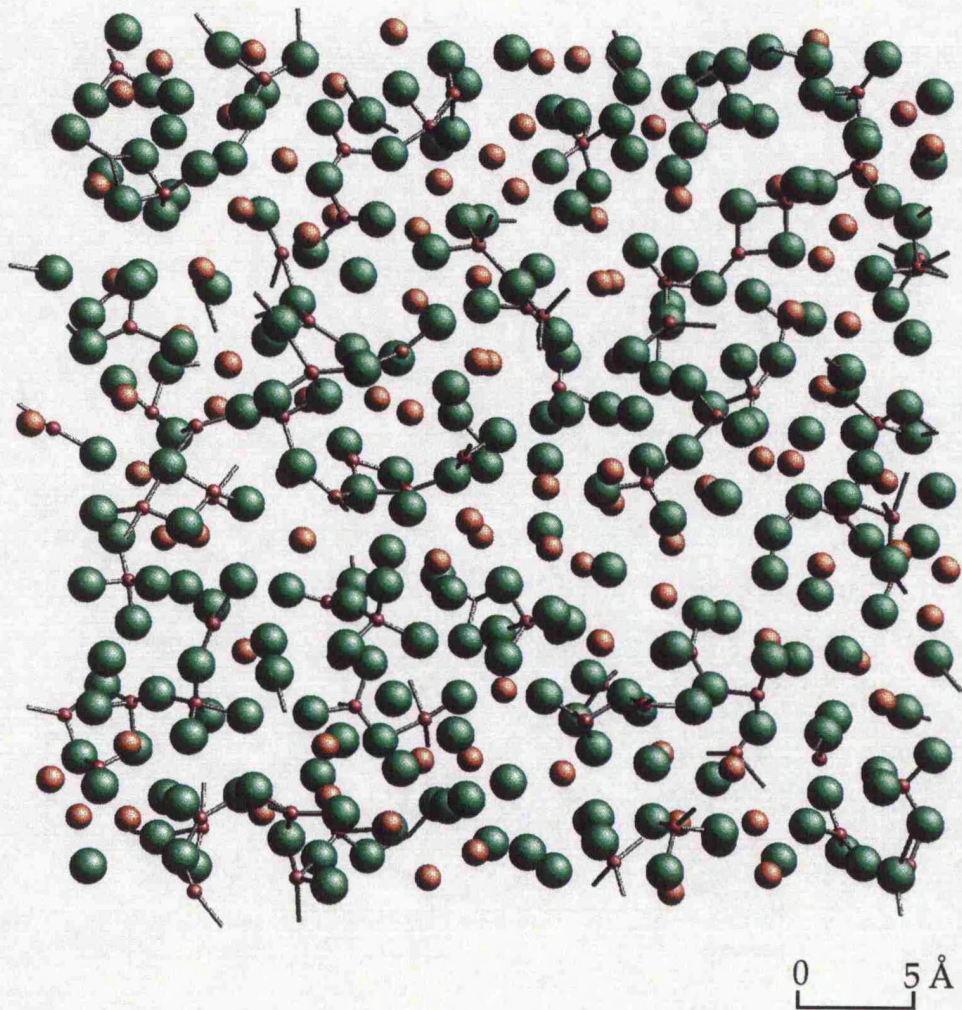


Figure 7.10. A 'slice' (8 Å thick) through the middle ([200] plane) of a typical RMC model-F equilibrium configuration. The large green spheres represent chlorine atoms, the orange spheres the potassium and the small red spheres correspond to nickel. The diameters (based on crystal ionic radii) of all the atoms have been scaled by 0.5 in order to enable the 'bonds' (a purely geometric definition), drawn between all Ni and Cl atoms with separations of less than 3 Å, to be clearly seen. Note the relatively short chains of nickel-centred units and the disordered distribution of potassium ions.

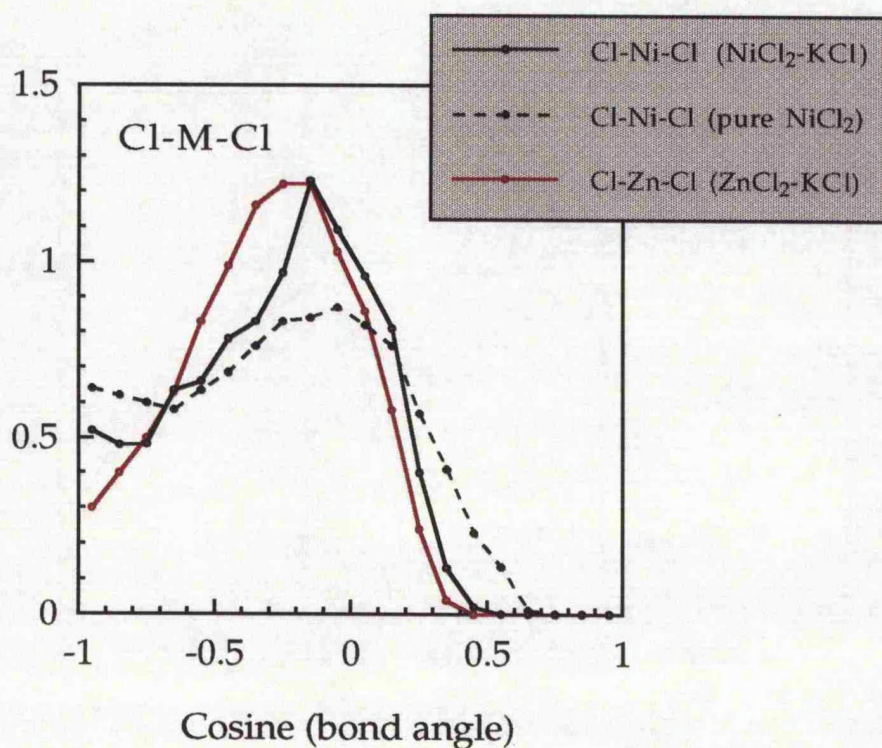
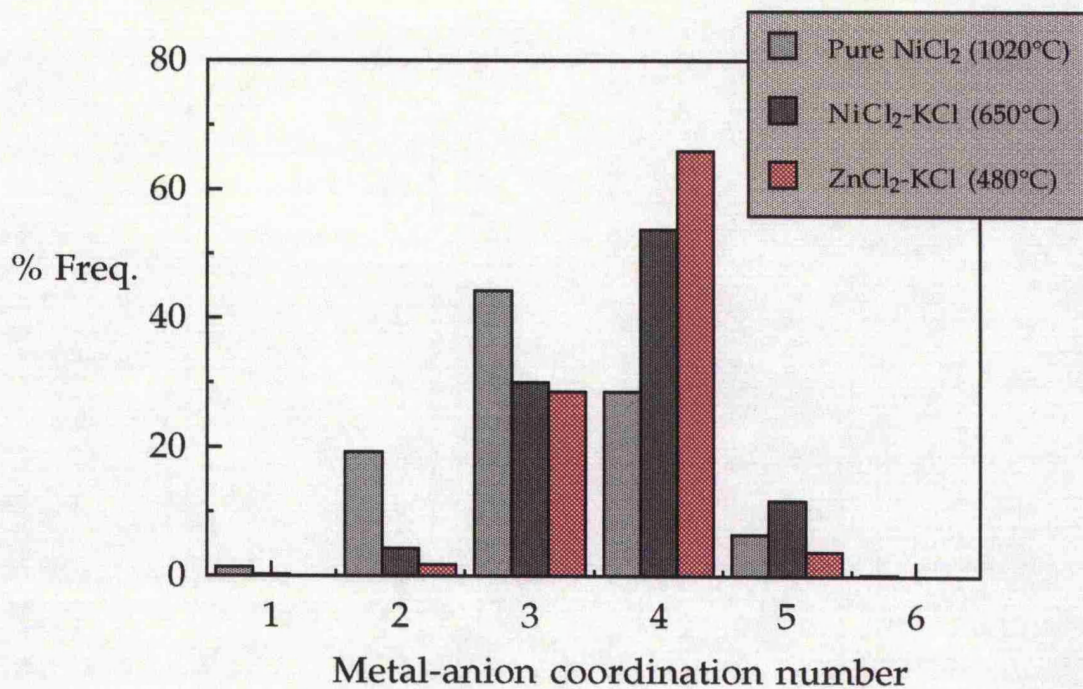


Figure 7.11. RMC coordination number and bond angle distributions relevant to the local structure of the metal (M) cation in NiCl₂-KCl and ZnCl₂-KCl molten salt mixtures. Comparison is made with the corresponding functions from a RMC configuration (courtesy of R.L. McGreevy [7.11]) obtained by fitting to isotopic data for pure molten NiCl₂ [7.8].

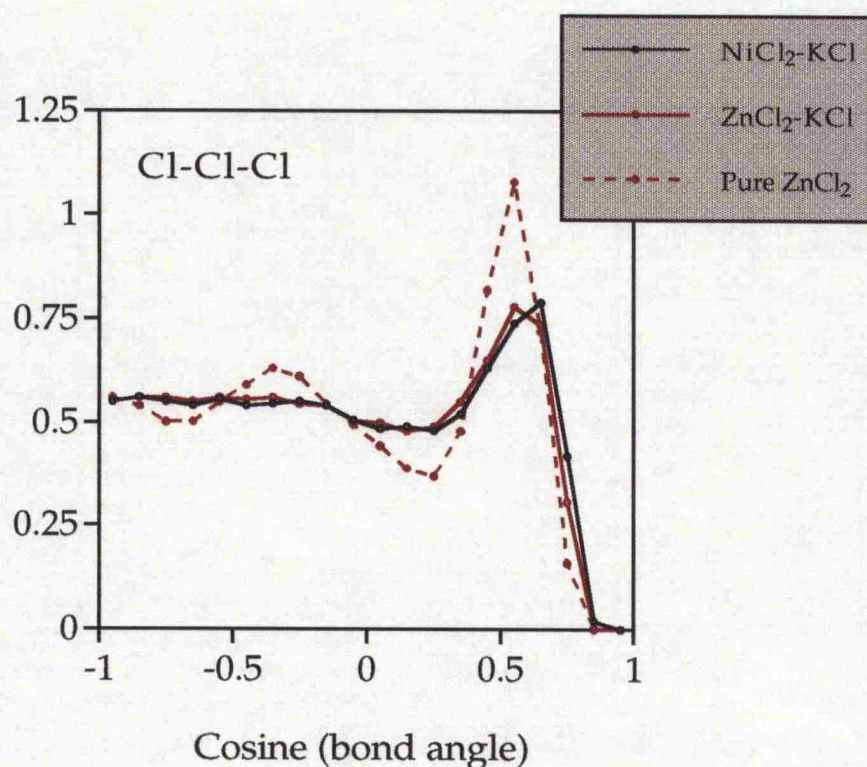
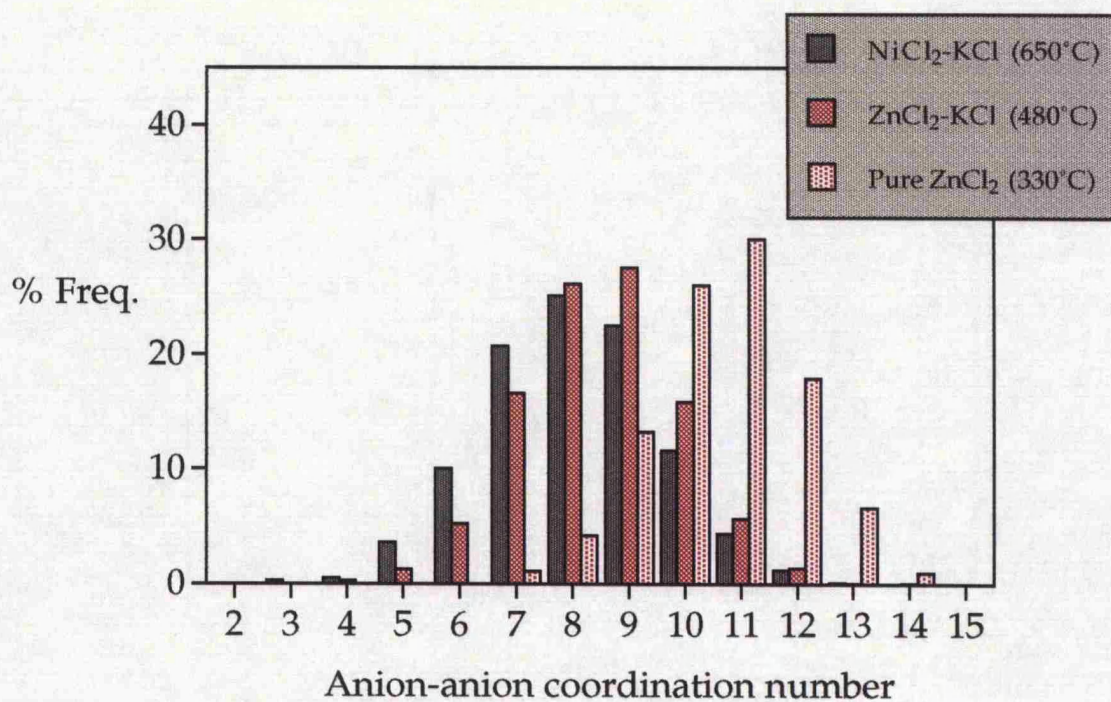


Figure 7.12. RMC coordination number and bond angle distributions pertaining to the anion structure in NiCl₂-KCl and ZnCl₂-KCl molten salt mixtures. Comparison is also made with the corresponding functions from a RMC configuration (courtesy of R.L. McGreevy [7.11]) obtained by modelling isotopic data for pure molten ZnCl₂ [7.2].

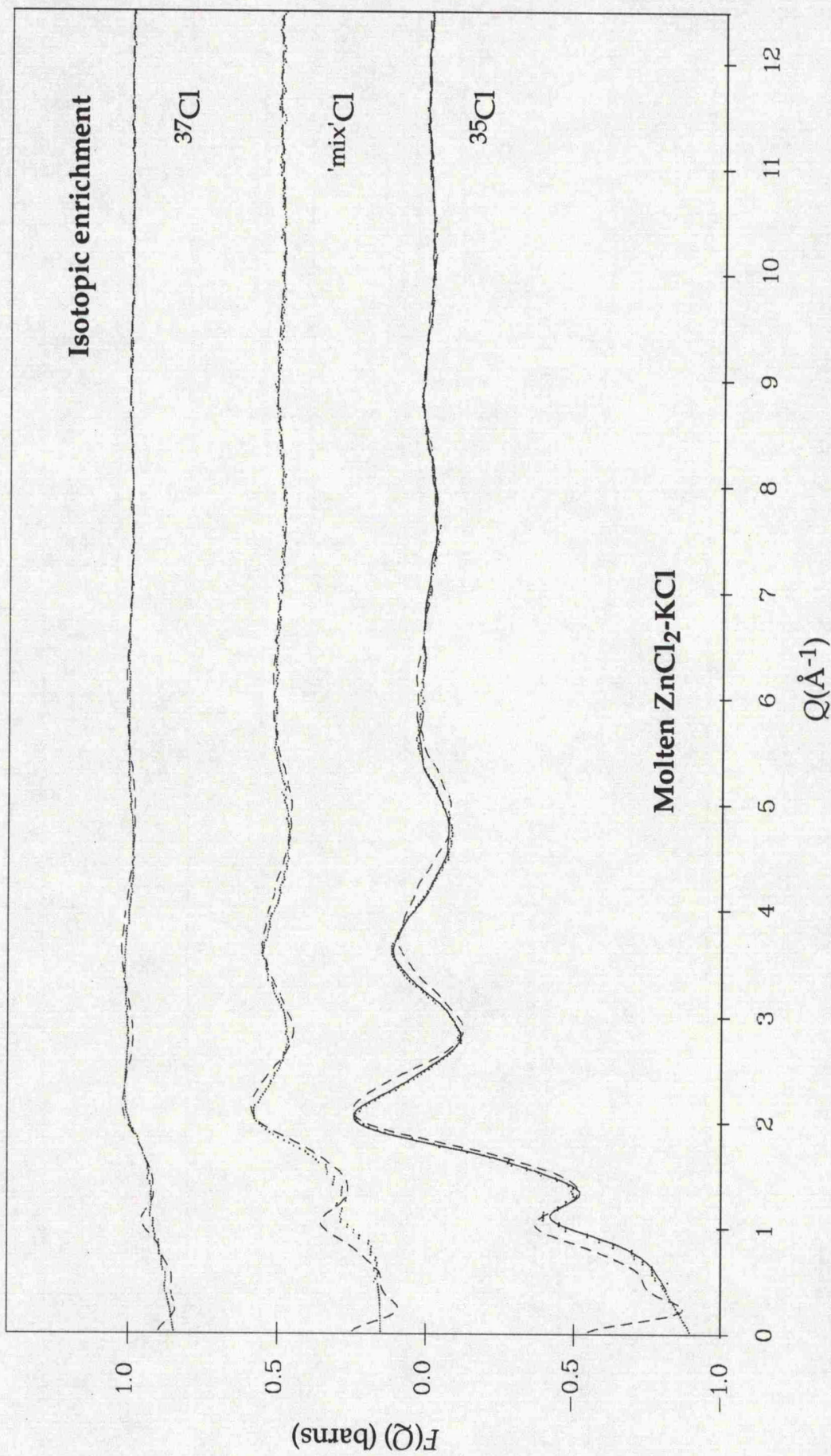


Figure 7.13. Total structure factors for the three isotopic enrichments of molten $\text{ZnCl}_2\text{-KCl}$ (dotted curves) compared with model $F(Q)$ assembled using the RMC partials found from modelling the nickel isotopes data (dashed curves). The model partials were of course weighted with the appropriate Faber-Ziman coefficients (the composition was taken to be 60% KCl in all cases). The RMC fit directly to the ^{35}Cl data is also shown (solid curve).

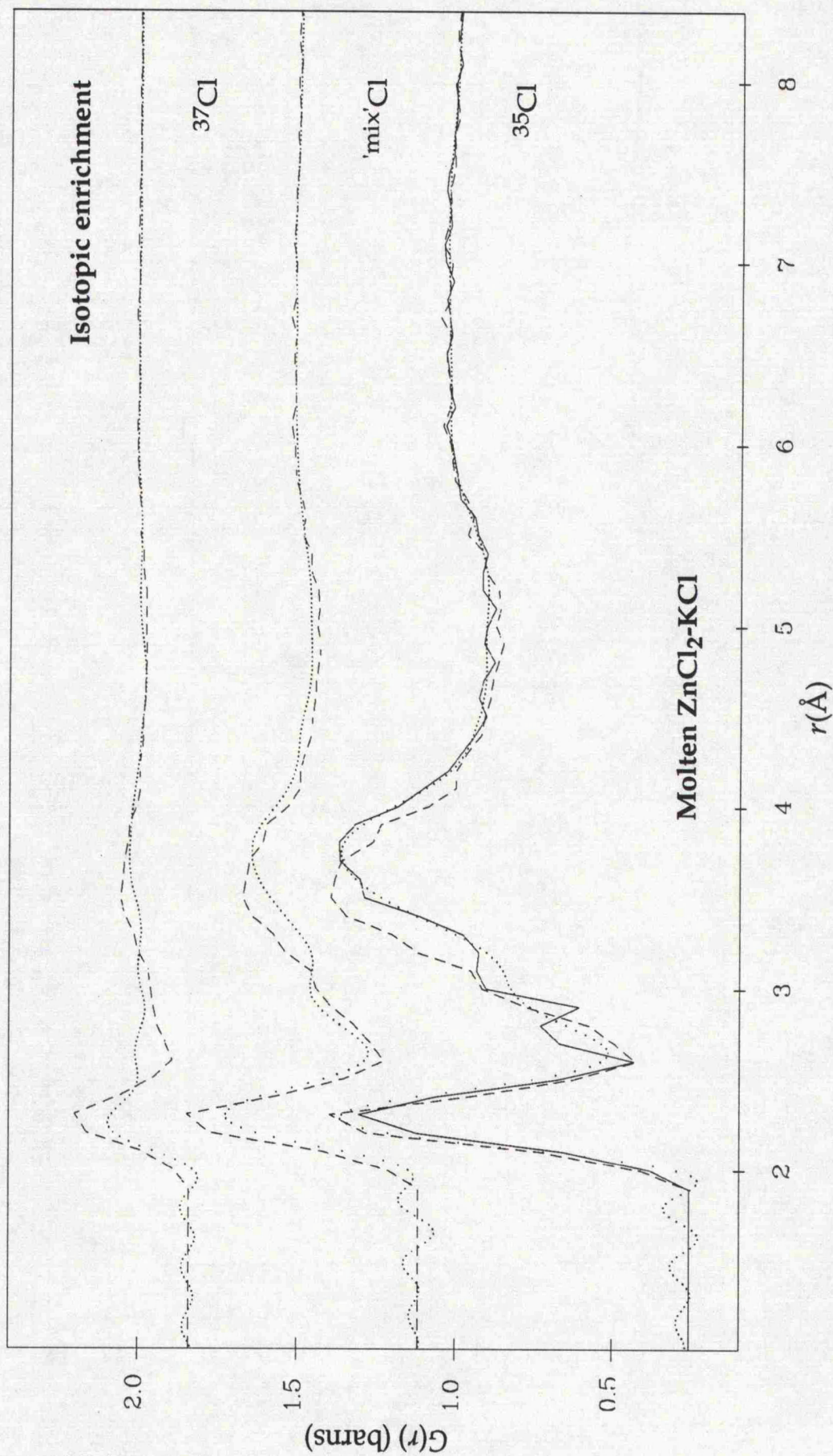


Figure 7.14. Total pair distribution functions for the three isotopic enrichments of molten $\text{ZnCl}_2\text{-KCl}$ (dotted curves) compared against the model functions (dashed curves) assembled from the RMC partials obtained for the nickel isotopes data. The mismatch between model and data for the ^{37}Cl -enriched sample, especially in the region of the first minimum at approximately 2.7 \AA , clearly suggests a problem with the correction for container scattering. The real-space RMC fit to the data for the ^{35}Cl -enriched sample is also shown (solid curve).

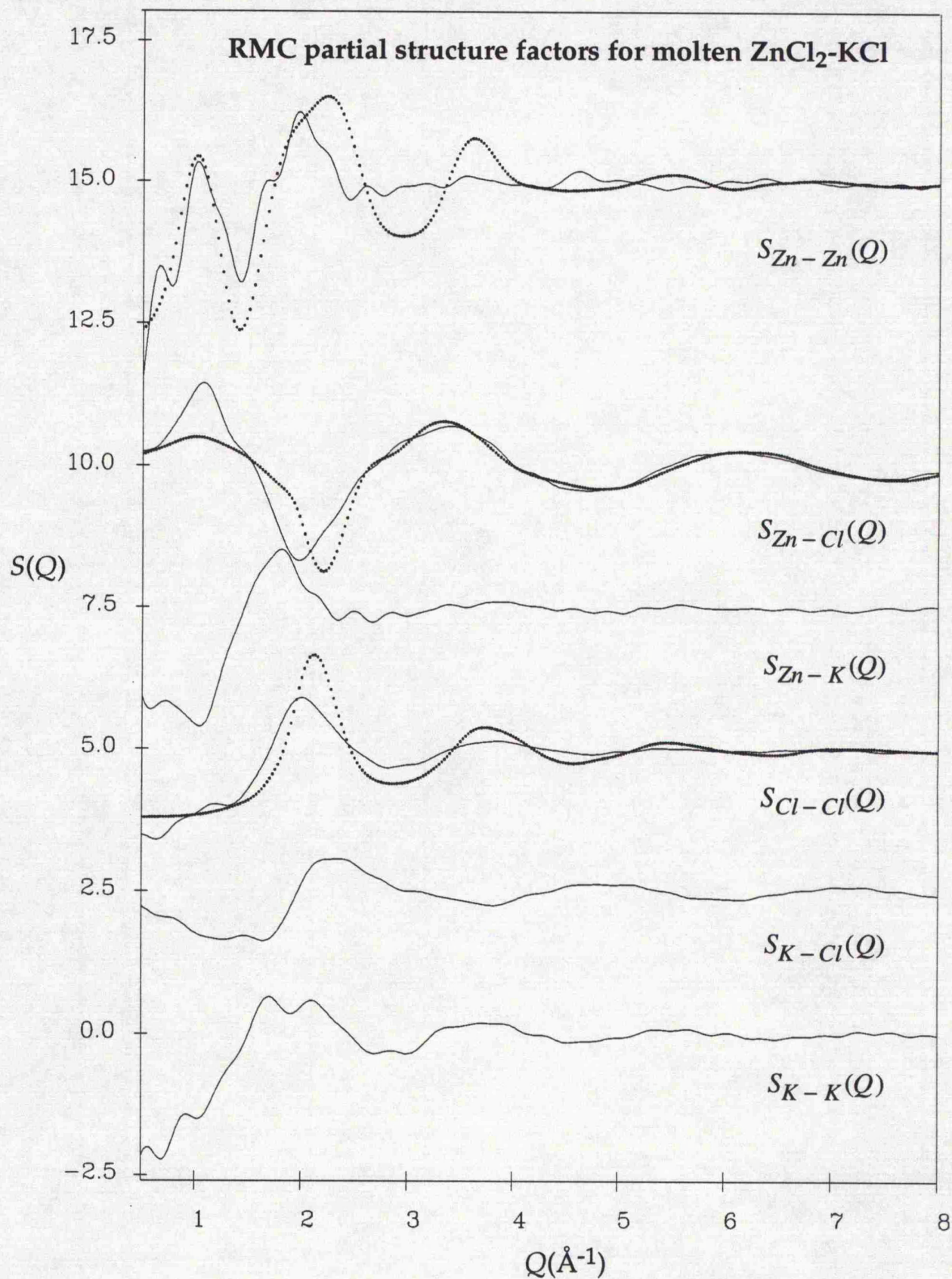


Figure 7.15. RMC partial structure factors for molten ZnCl₂-KCl obtained from fitting the $F(Q)$ data for the ³⁵Cl-enriched sample (solid curves). Partial structure factors for pure molten ZnCl₂, from the isotopic study of Biggin & Enderby [7.2], are also shown (dotted curves).

Chapter 8

The structure of liquid AlCl_3 and structural modification in $\text{AlCl}_3\text{-MCl}$ ($\text{M}=\text{Li,Na}$) molten salt mixtures

(Expanded version of article published in J. Phys. : Condens. Mat., 1994, 6(47), 10193-10220)

Abstract

The scattering from pure liquid AlCl_3 and $\text{AlCl}_3\text{-MCl}$ ($\text{M}=\text{Li,Na}$) binary molten salt mixtures has been measured by time-of-flight neutron diffraction. Reverse Monte Carlo simulation of the AlCl_3 data, whilst confirming a regular tetrahedral local geometry for the Al^{3+} ion, challenges the accepted view of the structure as consisting (predominantly) of discrete Al_2Cl_6 dimers. The data for the mixtures suggests the connectivity in the structure of pure AlCl_3 , formed by Al-Cl-Al bridges, is proportionately reduced upon the addition of alkali halide as isolated AlCl_4^- units are created. In addition, a gradual shift in the position of the first sharp diffraction peak to higher Q is observed, implying a systematic reduction in the length scale of intermediate range order. The findings for the mixtures are generally consistent with those from previous structural studies using X-ray diffraction and also with Raman and electrochemical measurements.

8.1. Introduction

There is considerable evidence for the existence of a series of complex ions ; AlCl_4^- , Al_2Cl_7^- and $\text{Al}_3\text{Cl}_{10}^-$ in alkali chloro-aluminate melts for acidic (i.e. > 50% AlCl_3) compositions. The presence of such structural units was first reported in studies of $\text{AlCl}_3\text{-NaCl}$ melts by Raman spectroscopic analysis [8.1] and thermodynamic measurements [8.2]. The proportion of Al_2Cl_7^- ions was found to increase with AlCl_3 concentration, and at compositions close to the pure salt endpoint the presence of an additional species, most likely $\text{Al}_3\text{Cl}_{10}^-$, was indicated. The proportion of isolated AlCl_4^- tetrahedra was also shown to increase with temperature at all compositions. More recently, these trends have been confirmed for $\text{AlCl}_3\text{-NaCl}$ and $\text{AlCl}_3\text{-KCl}$ molten salt mixtures by X-ray [8.3] and neutron diffraction [8.4] studies, respectively. All the complex ion species are essentially polymeric - being based on the same fundamental unit of AlCl_4^- tetrahedra sharing corners. However, the precise structures are not well established and there is some disagreement as to whether the higher-order species (Al_2Cl_7^- etc.) have a linear or, as suggested by *ab initio* molecular orbital

(MO) calculations [8.5] which take into account the effects of bond polarisation, a bent Al-Cl-Al bridge. Blander *et al* [8.4] achieved optimum fits to structure factor data for acidic AlX_3-KX ($X=Cl, Br$) melts using a bent-bridge angle of approximately 110° for $Al_2X_7^-$ which was consistent with MO calculations and the X-ray diffraction analysis of crystalline KAl_2Br_7 [8.6].

In contrast to the $AlCl_3$ -rich melts, the equimolar compositions are regarded as relatively simple systems consisting mainly of $AlCl_4^-$ tetrahedra and alkali cations. The EMF measurements of Boxall *et al* [8.2] indicate this is the case for the $AlCl_3-NaCl$ system and also suggest a high degree of charge ordering between complex anions and alkali counter-ions ; a model which appears to be confirmed by analysis of X-ray diffraction data for equimolar $AlCl_3 + LiCl$ [8.7] and $AlCl_3 + NaCl$ [8.8] molten salt mixtures.

In earlier studies (see chapters 6 and 7) of divalent metal chloride - alkali chloride melts, similar charge-ordered structures were reported for systems such as $NiCl_2-KCl$ near the critical $2/3$ alkali halide concentration. The formation of a charge-ordered structure in mixtures involving 2:1 molten salts appears to be dependent on the type of alkali cation - large ions such as K^+ promote structural modification whereas small ions such as Li^+ give rise to admixtures of the pure salt structures - and also seems to be associated with enhanced intermediate range order (IRO). In order to explore the effects of reducing the size of metal cation and greatly increasing its polarising power, studies have been extended to the trivalent metal chloride - alkali chloride molten salt mixtures which are the subject of the present chapter.

The secondary aim of the investigation was to gain further insight into the structure of pure liquid aluminium chloride, not only by measurement of the total structure factor for the pure salt but also from the structural modification observed in the mixtures. The 'established' model of molten $AlCl_3$ is that of a fluid of Al_2Cl_6 dimers each formed by edge sharing of two somewhat distorted $AlCl_4^-$ tetrahedra. The anomalously large volume increase upon melting from an octahedral coordination in the crystal ([8.9] and references therein) and the results of an early (1951) X-ray diffraction study of the liquid [8.10] are often cited in support of this rather idealised model. However, both $AlCl_3$ and $ZnCl_2$, which is believed to have a very different 'network liquid' structure made up of corner-linked $ZnCl_4^{2-}$ tetrahedra, share some intriguing similarities in their physical properties e.g. a low melting point and very low conductivity in the melt. In the light of this observation, detailed analysis, including reverse Monte Carlo (RMC) modelling, of neutron diffraction data for liquid $AlCl_3$ has been

undertaken. RMC has also provided partial structure factor (PSF) information which has facilitated analysis of the data for the mixtures.

8.2. Experimental details

The mixtures were prepared using pure ($\geq 99.99\%$) anhydrous single salts heated under vacuum to minimise their moisture content. However, vacuum drying could not be used for AlCl_3 because of its high vapour pressure. Instead, a method of sublimation drying was employed (see section 3.2.1) with the salt being heated gradually, over a period of about 3 days, to approximately 150°C whilst being continually evacuated by a diffusion pump. The sublimed salt vapour was collected in a condensation trap ($\sim -5^\circ\text{C}$) leaving most of the water vapour to continue to the pump. Microanalysis gave an *upper* limit for the concentration of water in the sublimed AlCl_3 of $\sim .5\%$ by weight. Mixtures of the desired composition were obtained by weighing out the appropriate masses of the dried salts. The general sample preparation procedure is detailed in chapter 3. The lithium chloride used in mixtures with aluminium chloride was isotopically enriched ($\geq 99.99\%$) in ^7Li to avoid the very large absorption cross-section for neutrons of the ^6Li isotope.

The data was collected in two separate time-of-flight (TOF) neutron diffraction experiments using the SANDALS instrument at Rutherford ISIS. In the first, the scattering was measured for samples of 0(200°C), 30(300°C), 45(300°C), 70(740°C) and 100%(820°C) NaCl with AlCl_3 . In the second experiment, measurements were made for samples of 25(280°C), 50(280°C), 70(625°C) and 100%(640°C) LiCl with AlCl_3 . Multiple scans were performed for each sample to check whether structural changes in sample or container, from incomplete mixing or chemical attack, occurred during data collection. Only scans that agreed to within statistical error were integrated. In both experiments, data was collected for the empty container (at low and high temperatures close to the pure salt melting points), furnace backgrounds and a vanadium calibration.

The raw SANDALS data was analysed using the Rutherford ATLAS package [8.11] in the manner described in chapter 4. Reliable furnace corrections were essential because of the very large furnace background on SANDALS. Even with appropriate corrections (details of the precise parameters and how they were chosen are given in section 4.4) there was marked disagreement between the vanadium-calibrated scattering from different detector groups. This is believed to be due to sample-dependent background scattering which, fortunately, appears to be mostly in the form of monotonic Q -space slopes evident as

spurious features at low r in real space. The problem was minimised using a program, SUBSELF [8.12], which effectively corrected the scattering by fitting a theoretical low- r base-level (based on sample composition) to the Fourier transform (FT) and then back-transforming. The resulting excellent agreement between detector groups made inelasticity corrections redundant, and also meant that data could be merged over a wide Q range thus generating composite $F(Q)$ functions with improved statistics. Because of the lack of isothermal compressibility data, the experimentally inaccessible low- Q portion of the data was simply extrapolated. Fortunately, because of the Q^2 dependence of the FT this makes little difference to the real-space picture.

The $G(r)$ functions were obtained by Fourier transformation of $F(Q)$ data smoothed at high Q . No window function was employed. In each case, comparison of the $G(r)$ derived from the smoothed and unsmoothed $F(Q)$ data confirmed that mainly Fourier ripple was removed with marginal effect on real peaks (see figures 8.1-8.2).

The data analysis parameters for the pure salts are given in table 8.1. The density data used for the AlCl_3 -rich mixtures with LiCl and NaCl were taken from Carpio *et al* [8.15] and Boston [8.16], respectively. In the absence of published measurements, the number densities for the 70% alkali halide compositions were linearly interpolated from temperature-extrapolated values for the equimolar and pure alkali halide melts.

8.3 Discussion

8.3.1 The structure of pure liquid AlCl_3

The local structure of the Al^{3+} ion appears to be well defined with a regular, fourfold coordinated tetrahedral geometry. The $F(Q)$ and corresponding $G(r)$ functions for liquid AlCl_3 are shown in figures 8.1 and 8.2, respectively. There is clearly a deep first minimum after the well-resolved Al-Cl principal peak in real space, implying little movement of anions into and out of the first shell. The mean anion coordination number for this peak is $\sim 4.0 \pm .2$ (the deep first minimum means this is a fairly reliable estimate). The r_{-}/r_{+} ratio in $G(r)$ of ~ 1.66 is also close to that of a regular tetrahedron. However, comparison of the radial distribution functions (RDFs) for $g_{\text{Al-Cl}}^{\text{AlCl}_3}(r)$ and $g_{\text{Zn-Cl}}^{\text{ZnCl}_2}(r)$ (the superscript refers to the pure salt), as in figure 8.3, shows that although the principal peak in AlCl_3 is at lower r , it is shorter and broader with an FWHM of $\sim .42 \pm .05$ compared with $\sim .27 \pm .02$ Å for ZnCl_2 . The reason for this is apparent from the

Al_2Cl_6 molecular structure shown in figure 8.4(a) and the corresponding structural parameters in table 8.2. The Al-Cl principal peak is actually a combination of two overlapping peaks due to shorter, terminal, Al-Cl^T and longer, bridging, Al-Cl^B bonds.

However, some details of the total pair distribution function appear to be inconsistent with the 'established' view of the structure as consisting, predominantly, of such discrete Al_2Cl_6 dimers. In this regard, it should be noted that the only previous structural study, by Harris *et al* [8.10] using X-ray diffraction, is fundamentally flawed. The radial distribution curve presented in this earlier study is clearly affected by large FT truncation errors - the first minimum after the Al-Cl principal peak dips well below zero indicating a sizeable FT ripple amplitude (see figure 8.5). This error means the shape and position of the peaks must be deemed inaccurate and even puts into doubt the existence of those at high r . The absence in the neutron data of peaks corresponding to those at $r \sim 5.6$ and $r > 7.5$ Å, as claimed by Harris *et al*, appears to confirm the systematic errors in the earlier study. Unfortunately, Harris *et al* used their dubious values of peak position to deduce the structural parameters of the assumed Al_2Cl_6 dimer and obtained good agreement with the results of an electron diffraction study of the vapour phase [8.18] (for which there is strong evidence for the existence of dimers) thus 'confirming' their initial assumption. However, duplicating the approach of Harris *et al* and using the current peaks at $r \sim 6.3$ and 7.0 Å (instead of 5.6 and 6.5 Å), whose positions were verified using the Maximum Entropy Method (see [8.19] and references therein), for the interatomic distances 4-6 and 3-6 respectively in figure 8.4, leads to dimers with a structure even more distorted in the Al-Al direction. The shape of the Al-Cl peak on the high- r side is not consistent with Al-Cl^B bond lengths significantly greater those in table 8.2, which implies the additional distortion would involve a reduced distance between the two bridging chlorine atoms. This would further intensify the 'overlap' problem of these atoms and makes such a structure appear unlikely. An alternative model involving corner sharing, in place of edge sharing, of tetrahedral units would seem more probable. The peaks at $r \sim 6.3$ and 7.0 Å agree quite closely with the two Cl-Cl distances of 6.13 and 7.0 Å obtained in a modelling study of AlCl_3 -n-BPC mixtures [8.21] at a composition known to consist primarily of corner-sharing Al_2Cl_7^- units. In addition, simple weighted averaging of the Al-Cl^T and Al-Cl^B bond lengths in table 8.2 provides a better match to the Al-Cl peak position of ~ 2.11 Å if polymeric corner-sharing tetrahedral units are assumed. For example, an estimate of ~ 2.13 Å is obtained for $\text{Al}_3\text{Cl}_{10}^-$ units compared with ~ 2.18 Å for discrete dimers. Furthermore, the peak positions for Al-Cl and Cl-Cl (2.11 and

3.5 Å) are close to those quoted for the isolated tetrahedral AlCl_4^- species believed to predominate in the equimolar $\text{AlCl}_3 + \text{NaCl}$ melt [8.8] (2.13 and 3.48 Å), which would be consistent with a corner-linked structure involving less distortion of the tetrahedral units compared to edge-sharing dimers.

These observations call for a critical reassessment of some of the arguments usually made in support of the 'established' model :

i) **Electron diffraction studies of the vapour** [8.18] ; as pointed out above, the only direct structural study [8.10] suggesting a strong similarity between the liquid and vapour phases is seriously flawed. The vapour phase inevitably favours bound molecular states but the liquid environment and hence structure may be very different. In this context, it is interesting to note that the electron diffraction data [8.18] also indicates a trend of increasing deformation, and hence decreasing stability, for the halide series Al_2X_6 , $\text{X}=\text{I}\rightarrow\text{Br}\rightarrow\text{Cl}$, in the vapour phase. This implies that, of the three trihalides, AlCl_3 is *least likely* to have a dimer structure in the liquid.

ii) **Raman scattering experiments** ; these only provide indirect evidence on structure and the usual approach to interpretation, that of iteratively refining a self-consistent force model, often depends on arbitrary initial assignments of experimentally identified modes. Even a study [8.20] (see figure 8.6) which uses *ab initio* MO calculations to show an apparently excellent agreement between model and experiment is based on the assumption of gas-phase dimers - alternative models which could fit the data equally well, or better, do not appear to have been considered.

iii) **The large increase in specific volume (~ 88%) and entropy upon melting of AlCl_3 , more than twice that observed for AlBr_3** ; this is certainly evidence of a unique structural transition but not necessarily for dimers in the liquid. The volume increase is usually explained entirely in terms of the dramatic change in coordination of the Al^{3+} ion from octahedral in the crystal [8.9] to tetrahedral in the melt [8.10]. In the case of AlBr_3 , the Al^{3+} ion starts off with a tetrahedral coordination in a crystal molecular lattice of Al_2Br_6 dimers which appear to be retained in the melt ([8.22] and references therein). Clearly, other fourfold coordinated structures, such as the corner-sharing tetrahedral units suggested earlier, would be as consistent with this explanation as Al_2Cl_6 dimers. A further weakness in the conventional explanation is to assume the difference in crystal structure of the two salts accounts entirely for the melting behaviour. Comparison of the packing fractions for liquid AlCl_3 (~ 40%) and AlBr_3 (~ 50%) reveals the substantially greater void volume in the former which, in the opinion of the author, is difficult to reconcile with the notion of a similar dimer structure in both melts.

It is clear from the above, that while the evidence is strong for a dramatic change in structure from the crystal state upon melting, it is very weak for specifically a dimer structure in the melt. Indeed, reconsideration of the historical arguments would actually seem to point to alternative structures.

Because the use of specific features of $G(r)$ to make inferences about structure can be misleading, modelling of the data has been attempted. Details of the chosen method, RMC, can be found in chapter 5 so only an outline of the method and its application will be given. The RMC algorithm is a variant of the standard Metropolis Monte Carlo (MMC) algorithm - the distinction being that RMC minimises the χ^2 fit directly to the diffraction data whereas MMC minimises the total potential energy. A random initial configuration containing $N=2400$ atoms satisfying the necessary closest approach and density constraints was always used. The size of the simulation cube allowed the model $G(r)$ to be calculated up to $r \sim 23.6$ Å. An initial fit was attempted to $G(r)$ data, which allowed the closest approach distances to be fine tuned, before restarting from a random configuration and fitting directly to the structure factor. As the model neared equilibrium (χ^2 fluctuating about a minimum), automatic renormalisation of the data, to improve the fit with the model $F(Q)$, was allowed as a refinement. The renormalisation factor never exceeded $\pm 5\%$. Statistically-independent configurations, each separated by at least $2N$ accepted moves, were collected for averaging of their properties once the model had clearly reached equilibrium.

The initial results of RMC modelling (henceforth known as model I), whilst confirming an almost regular tetrahedral local geometry for the Al^{3+} ion, further challenge the accepted view of the wider structure. The model-I fit to the $F(Q)$ data is shown in figure 8.7, along with the Faber-Ziman (F-Z) weighted contributions of the RMC partials to the total scattering. The corresponding comparison in real space is shown in figure 8.8. The bond angle distributions (averaged over five independent configurations) relevant to local structure are shown in figure 8.9. The prominent peaks at $\sim 107^\circ$ in the Cl-Al-Cl function, at $\sim 60^\circ$ in the Cl-Cl-Cl and at $\sim 37^\circ$ in Cl-Cl-Al agree closely with the values of 109.5 , 60 and 35.25° , respectively, of a regular tetrahedron. The coordination number distribution (figure 8.10) indicates strong physical constraints against anion coordinations greater than four, with the average being ~ 3.6 . The tendency of the RMC to produce a solution with maximum configurational entropy means that observed anion coordinations of less than four are not necessarily features of the 'correct' solution - the structure may simply be insufficiently ordered. Given this characteristic, it is perhaps not surprising that the RMC structure

contains few *discrete* molecules resembling Al_2Cl_6 dimers. Bond network analysis (see table 8.3) reveals a large number of connected units but the majority ($\sim 75\%$) are branched chains and of the remainder - complex units containing loops and rings - only a few ($\sim 5\%$) appear to resemble Al_2Cl_6 dimers. However, this analysis also indicates few instances of the essential edge-sharing feature of the dimer. This was confirmed by visual inspection of thin 'slices' through the model, thus proving that a 3-D structure quantitatively consistent with the data and known physical constraints can include almost no units corresponding to dimers. The 'slice' of a model-I RMC configuration shown in figure 8.11 illustrates the predominance of long, branched, mainly corner-linked chains of tetrahedral units with edge sharing occurring mostly within units larger than dimers.

The model-I RMC structure resembles the picture of polymeric, corner-linked tetrahedra suggested earlier from semi-quantitative analysis of the $G(r)$ data. The principal peak in the model-I $g_{\text{Al}-\text{Al}}^{\text{RMC}}(r)$ partial (the superscript denotes a RMC partial which, in this case, has been obtained by fitting to a single data-set) is centred at $r \sim 3.7 \text{ \AA}$ implying a mean Al-Al separation significantly greater than quoted for the vapour and quasicrystal dimer structures (see table 8.2). The bond angle distributions shown in figure 8.12 are also consistent with predominantly corner-linked tetrahedral units. The broad peaks at $\sim 120^\circ$ in the Al-Cl-Al function and at $\sim 25^\circ$ in Al-Al-Cl, both indicating a bent bridge, are clearly inconsistent with the corresponding angles of $\sim 90^\circ$ and $\sim 45^\circ$ characteristic of the dimer. Naturally, the RMC angles are geometrically consistent with the position of the principal peak in $g_{\text{Al}-\text{Al}}^{\text{RMC}}(r)$.

Although only a single $F(Q)$ data-set was available, the RMC method can apparently (through the use of physical constraints) extract a great deal of information about the structure of liquid AlCl_3 . The most striking sign of this is the remarkably structured $g_{\text{Al}-\text{Al}}^{\text{RMC}}(r)$ partial. RMC might be expected to generate an almost unstructured Al-Al partial because of the low F-Z weighting i.e. there is little *direct* information about this partial in $F(Q)$, which implies the Al-Al structure is being 'deduced' using the more directly accessible Al-Cl and Cl-Cl partial structures. Furthermore, the mean bridging angle of $\sim 120^\circ$ suggested by the peak in the Al-Cl-Al bond angle distribution is close to values obtained from *ab initio* MO calculations [8.4] for Al_2Cl_7^- (125.8°) and similar corner-linked units. However, notwithstanding the apparently high information content of the data, there remains a question as to what information about the 'correct' structure is absent and how this affects the RMC solution? Clearly, it was necessary to try

and explore the *range* of possible solution structures especially since isotopic data, and hence a unique set of PSFs, were unavailable.

The first tests conducted were on the effects of varying number density by $\pm 10\%$. It was particularly important to check this because of the likely systematic errors in published density measurements due to the difficulties of purifying and handling liquid AlCl_3 . The main effect of varying the number density was on the vacancies in the local structure of the Al^{3+} ion. For example, reducing the density by 10% generated approximately 10% more vacancies in the local structure and a proportionate reduction in the mean anion coordination number. However, the local geometry of the Al^{3+} ion, as characterised by the relevant bond angle distributions, was scarcely affected. In addition, bond network analyses and the Al-Cl-Al and Al-Al-Cl bond angle distributions indicated that the predominance of chains of mainly corner-linked tetrahedral units was preserved.

However, the critical question to be addressed was whether significant numbers of dimers, or even units possessing the characteristic edge-sharing attribute, were possible in a RMC structure? An attempt was made to answer this question by reducing the mean Al-Al separation from $\sim 3.7 \text{ \AA}$, as in model I, to the $\sim 3.3 \text{ \AA}$ expected for dimers thereby forcing increased edge sharing. This was done by fitting to an artificial $S_{\text{Al-Al}}(Q)$ data-set in addition to the original $F(Q)$. The more direct approach of explicitly including dimers in the initial configuration, and using coordination constraints to preserve these discrete molecules during random moves, had the drawback of requiring a great deal more computer time. The fit to the total structure factor obtained in this case (henceforth referred to as model II) is equally as good as for model I (see figures 8.7-8.8). Comparison of bond angle and coordination number distributions with those of model I (see figures 8.9-8.10) reveals little change to the local structure. Increased edge sharing is evident from bond network analysis (table 8.3) with a larger proportion of connected units containing loops and rings. This appears to be confirmed by the bond angle distributions (figure 8.12) with a prominent peak emerging at $\sim 90^\circ$ in the Al-Cl-Al function and with the peak in Al-Al-Cl shifting closer to 45° , just as expected for edge-sharing dimers. However, the Al-Cl-Al function still exhibits a broad peak at $\sim 115^\circ$ and the peak in Al-Al-Cl falls slightly short of 45° . This indicates corner sharing is still a significant feature of the structure. Visual inspection of a series of thin configuration 'slices' (not shown) confirms that although there are at least 50% more instances of edge sharing in the model-II structure compared to model I, chains of mainly corner-linked tetrahedral units still predominate (see figure 8.13). As regards the

possibility of discrete dimers, the RMC results suggest the structure of liquid AlCl_3 may be only partially dimerised.

Although the model of liquid AlCl_3 as predominantly a fluid of dimers has not been disproved by RMC modelling, it has been shown that an alternative structure consisting mainly of polymeric, mostly corner-linked tetrahedral units is consistent with the data even after allowing for some uncertainty in the $g_{\text{Al-Al}}(r)$ partial. If isotopic data were available, the consequent reduction in the range of RMC solutions might make it possible to determine which of the above models is 'correct', particularly if the position of the principal peak in $g_{\text{Al-Al}}(r)$ were to become more rigidly constrained¹.

Having noted earlier the similarities in some properties of molten AlCl_3 and ZnCl_2 , the general structure suggested by RMC may be best described as a 'sparse network liquid'. In this context, it is interesting to note that the comparison of RDFs (figure 8.3) shows the second peak in the RMC Al-Cl function to be lower than for the Zn-Cl function of liquid ZnCl_2 , just as expected from the comparatively more isolated, corner-linked tetrahedral units in liquid AlCl_3 . The new model is favoured over the 'established' one because of the greater plausibility of the former when considering the indirect evidence. For example, the greater void volume in liquid AlCl_3 compared with AlBr_3 can be explained more readily if a skeletal network structure is assumed instead of discrete dimers. Furthermore, because corner-linked Al_2Cl_7^- units have been shown to predominate in AlCl_3 -KCl melts [8.4], even at compositions close to pure AlCl_3 (75%), and the suggestions of higher-order species like $\text{Al}_3\text{Cl}_{10}^-$ at the AlCl_3 -rich end, a distribution of corner-linked tetrahedral polymers in the pure molten salt appears eminently plausible. It should also be pointed out that the low viscosity and conductivity of liquid AlCl_3 does not necessarily support the existence of discrete molecules; a 'sparse network liquid', containing voids and large polymeric units of low ionic mobility, would also be consistent with these observations. For the above reasons, the 'sparse network liquid' model of AlCl_3 is preferred in the remainder of the discussion on molten salt mixtures and is wholly consistent with the findings.

¹ Intriguingly, reducing the Al-Al separation for model II had the effect of greatly increasing the number of rings based on Al 'triplets'. This is shown by the emergence of a peak close to the equilateral 60° angle in the Al-Al-Al bond angle distribution (figure 8.12) and confirmed by visual inspection (see figure 8.13). Reduced uncertainty in the $g_{\text{Al-Al}}(r)$ principal peak position would also make it possible to check whether such 'triplets' are a significant feature of the structure.

8.3.2 Structural modification in the mixtures

The total structure factors and corresponding total pair distribution functions for the molten salt mixtures are shown in figures 8.14-8.17. It is apparent from the real-space data that the already well-defined local coordination of the Al^{3+} ion becomes better ordered upon the addition of alkali halide while retaining its tetrahedral geometry. Table 8.4 reveals how the normalised height of the Al-Cl principal peak, estimated from the first peak in $G(r)$, for the AlCl_3 -NaCl mixtures increases with alkali halide concentration up to at least 45% NaCl. There is also a corresponding reduction in the FWHM despite an increasing contribution on the high- r side from the $g_{\text{Na-Cl}}(r)$ partial. In the AlCl_3 -LiCl mixtures, the height of the first peak in $G(r)$ (which also has its main contribution from the Al-Cl partial) diminishes less rapidly with increasing alkali halide than expected from the simple approximately linear effect of reduced concentration on the F-Z coefficient. For example, the peak height in 50% LiCl is clearly more than half the size in pure AlCl_3 , and is unusually sharp. This is all the more remarkable considering the expected negative contribution from the overlapping Li-Cl partial (assuming the principal peak position remains the same as in pure LiCl). The overlap with the $g_{\text{M-Cl}}(r)$ ($\text{M}=\text{Li}, \text{Na}$) principal peak makes it difficult to reliably estimate the anion coordination from the Al-Cl peak so this has not been attempted. However, evidence for a tetrahedral geometry is provided by the main peak positions which remain generally unchanged. In the AlCl_3 -NaCl mixtures, the Al-Cl principal peak remains at a position characteristic of pure AlCl_3 ($\sim 2.11 \text{ \AA}$) across the composition range as does the Cl-Cl peak ($\sim 3.5 \text{ \AA}$), implying no change in the approximately tetrahedral r_{-}/r_{+} ratio. For the AlCl_3 -LiCl mixtures, it is harder to draw a similar conclusion because of the proximity of other peaks but the Al-Cl peak position is unaltered at 25% LiCl and the Cl-Cl peak shows no shift even up to 70% alkali halide suggesting a tetrahedral geometry is also retained in this case. The lack of change in peak positions, especially at the AlCl_3 -rich concentrations, is wholly consistent with the 'sparse network liquid' model. The Al-Cl principal peak becomes better ordered because of the reduction in longer bridging bonds as large, mainly corner-linked species are broken up.

Modelling studies indicate the Al^{3+} ion dominates the anion structure in the mixtures - this is consistent with the formation of isolated AlCl_4^- units from the breakdown of larger linked species. The data for the mixtures was modelled using the pure salt partials (those for AlCl_3 were from RMC) weighted with F-Z coefficients appropriate to each composition. The unavailable M-Al ($\text{M}=\text{Li}, \text{Na}$) partial could be neglected because of its small weighting. The distinctive Cl-Cl

partial structures for the pure salts, $S_{Cl-Cl}^{MCl}(Q)$ and $S_{Cl-Cl}^{AlCl_3}(Q)$, were both used and their weightings adjusted to obtain the best fit initially to the structure factors. By first working in Q space and only then Fourier transforming using the appropriate number density for the mixtures, it was possible to compensate for the significant effect of density on the partial structures. The FTs of the model structure factors were checked against the real-space data to confirm an optimum fit in the region of the main anion-anion peaks (see figures 8.14-8.17 for a comparison of model fits and data). The resulting best-fit weightings (table 8.5) consistently favour the $g_{Cl-Cl}^{AlCl_3}(r)$ partial over $g_{Cl-Cl}^{MCl}(r)$ when compared to the *ideal* weightings expected for simple admixtures of the pure salts. This indicates a dominance of the overall anion structure by the Al^{3+} ion and implies the formation of isolated tetrahedral units from the break-up of larger linked units. However, the best-fit weightings for compositions close to equimolar (50% LiCl and 45% NaCl) do not indicate a complete breakdown i.e. the reaction $AlCl_3 + MCl \rightarrow AlCl_4^- + M^+$, which suggests there is still a distribution of species. In addition, given the uncertainty in the modelling process (for example, due to errors in the partials² and nominal compositions) the best-fit weightings do not suggest a quantitative difference between the molten salt systems. The results are broadly consistent with the findings of earlier X-ray diffraction studies of the equimolar melts [8.7, 8.8]. The weightings for 70% alkali halide, however, are not far short (given the likely errors) of those expected from a complete breakdown into isolated $AlCl_4^-$ units. The high temperatures of these mixtures would be expected to promote such a process. Incidentally, modelling using the pure salt partials also confirms the increased ordering of the Al-Cl principal peak in the mixtures - it is clearly taller than predicted even for the high-temperature 70% alkali halide samples.

The diffraction data also confirms the strong charge ordering in these systems particularly near the equimolar composition. Charge ordering is suggested by the presence of prominent peaks at $r \sim 6.65, 9.85$ and possibly 12.9 \AA in 50% LiCl as well as a weaker peak apparent at $r \sim 6.8 \text{ \AA}$ in 45% NaCl. These peaks do not appear to correspond to features in the pure molten salts and this is illustrated in figure 8.18 by the deviations from model $G(r)$ generated using the pure salt partials. The new peaks are likely to be associated with the formation of isolated $AlCl_4^-$ tetrahedra, and the size and position suggests they arise mainly from Cl-

² The partials in the mixtures will not of course be identical to those in the pure salts. However, the significant effect of density has been taken into account and the findings from best-fit modelling are in general agreement with those of earlier experiments, which suggests the remaining errors are not large.

Cl correlations³ between these units. From modelling of X-ray diffraction data for equimolar $\text{AlCl}_3 + \text{LiCl}$ [8.7] and $\text{AlCl}_3 + \text{NaCl}$ [8.8], Takahashi *et al* suggested a charge-ordered structure with average inter-unit distances of 6.75 and 6.98 Å, respectively, which appear to be consistent with the peaks observed in the current data. The units were assumed to be MAlCl_4 ($M=\text{Li,Na}$) hard spheres with the alkali ion located in, or near, face-centre sites of AlCl_4^- tetrahedra. In the case of 50% LiCl, we can extend this model by assuming a close-packed anion coordination around the Al^{3+} ion. Close packing is implied by the RMC coordination number distribution in figure 8.10 and is plausible given the small size of the cation. It is now possible to predict the minimum inter-unit distance as occurring when the faces of neighbouring tetrahedra interlock in a hexagonal close-packed arrangement, with the Li^+ ion occupying the gap in the centre, as shown in figure 8.19. The central, singly-charged Li^+ ion is unlikely to significantly disturb the faces of neighbouring tetrahedra so it is possible to assume an approximately regular octahedral cage for the alkali cation and thus estimate the *minimum* average Li-Cl separation to be $\approx r_{\text{---}}/\sqrt{2} = 2.47$ Å - clearly larger than evident in $G(r)$ for pure LiCl. The divergence between model and data for 50% LiCl in the region of the first minimum (see figure 8.15) appears to support this simple picture⁴. Furthermore, the remarkable sharpness and height of the Al-Cl principal peak in $G(r)$, as well as the absence of the expected shift in position to low r (see table 8.4), is difficult to explain without some movement to higher r of the inverted Li-Cl principal peak from its position in pure LiCl. The picture is less clear for 45% NaCl (primarily because of the inconsistency between the current TOF results and earlier isotopic data) but the larger size of the Na^+ ion suggests close-packing of tetrahedra would not be possible in this case. Comparison of model and data for 45% NaCl indicates the local structure of the Na^+ ion remains at least as disordered as in pure NaCl, regardless of which of the possible Na-Cl principal peak positions is assumed. This is consistent with the Na^+ ion occupying disordered sites not precisely in the face centres of tetrahedra, just as suggested by Takahashi *et al* [8.8].

Geometrical calculations based on the simple idealised model of interlocking tetrahedra as the predominant structure in 50% LiCl suggest distances which

³ Support for this suggestion is provided by an isotopic experiment on equimolar $\text{AlCl}_3+\text{LiCl}$ [8.26] indicating the main contribution to the high- r peaks is from $g_{\text{Cl-Cl}}(r)$, although this study should not be regarded as conclusive [8.27].

⁴ Possible over-subtraction of container scattering was discounted as a cause of the divergence because tests showed the effect of this to be more closely localised around 2.6 Å than is evident (the difference between model and data extends over the range $r \sim 2.4 - 3.0$ Å).

may correspond to the peaks at high r . Pairs of chlorine atoms on adjacent tetrahedra with separations of $\sim 6.$, 8.6 and 10.6 Å have been identified. These figures imply the tetrahedra are not quite interlocking but actually spaced apart by, on average, approximately 0.8 Å which would then give Cl-Cl distances of 6.7 , 9.5 and $12.$ Å - close to those suggested by the observed peaks in $G(r)$.

The question now arises as to which features of the structure factor data correspond to the prominent peaks at high r in real space? In order to answer this question the effects in Q space of removing the high- r peaks were estimated for 50% LiCl by splicing together the data ($r \leq 5.5$ Å) and model ($r \geq 5.5$ Å) $G(r)$ functions and then back-transforming (see the inset of figure 8.18). One effect is to produce a lower, broader peak at $Q \sim 2.$ Å⁻¹ just as expected from the period of ~ 3.1 Å of the observed r -space peaks. Thus the increase in height and narrowing of the main peak at $Q \sim 2$ Å⁻¹ noted in both sets of mixtures near the equimolar composition appears to be a consequence, and possibly a characteristic signature, of the strong charge ordering in these systems. The other main effect is a deviation at low Q indicating the additional presence of shallow oscillations of period $\sim 5.$ Å in the original $G(r)$ giving rise to the particularly narrow FSDP at $Q \sim 1.2$ Å⁻¹ in the unmodified structure factor. The charge-ordered model as discussed above has obvious implications for the intermediate range structure to which we shall now turn our attention.

8.3.3 Intermediate range order

The predominant contribution to the FSDP in the total structure factor for liquid AlCl₃ is from $S_{Al-Cl}(Q)$ and not $S_{Cl-Cl}(Q)$. This is evident from the approximately 40% greater height of the FSDP in the X-ray diffraction data [8.10] compared to the current neutron data. The difference is not far short of the $\sim +60\%$ expected from the change in fractional F-Z coefficient for $S_{Al-Cl}(Q)$, assuming no contribution from $S_{Cl-Cl}(Q)$ or $S_{Al-Al}(Q)$. Clearly, there is a large FSDP in the $S_{Al-Cl}(Q)$ partial which has an estimated (absolute) height of ~ 3.5 - much greater than in $S_{Zn-Cl}^{ZnCl_2}(Q)$ [8.17]. There is also a prominent FSDP in $S_{Al-Al}^{RMC}(Q)$ which, because the partial has a very small F-Z coefficient, must be essential to fulfilling the additional physical constraints imposed by RMC. The height of the feature is lower than in $S_{Zn-Zn}^{ZnCl_2}(Q)$ [8.17] but is probably underestimated by the RMC method.

A gradual shift in position of the FSDP to higher Q , and a narrowing, is observed up to approximately 50% alkali halide, which implies a systematic

reduction in the length scale of IRO in the mixtures. The shift appears to be associated with the formation of a charge-ordered structure because the movement of the FSDP seems to reach its maximum near the equimolar composition (see table 8.6). A subsequent shift back to lower Q with increased alkali halide, apparent in 70% LiCl at least, can be explained by the increase in temperature and the effects of thermal expansion on the charge-ordered structure. The notable sharpness of the FSDPs at 50% LiCl and 45% NaCl is also consistent with a strongly charge-ordered structure because it suggests IRO extends over many repetition lengths. Despite the expected increase in the average Al-Al separation for such a structure compared to the mainly corner-linked model for pure AlCl₃, a reduction in the length scale of IRO in the mixtures is plausible given the possibility of improved packing of tetrahedral units. The packing fractions are close to 50% for both the 50% LiCl and 45% NaCl mixtures, compared to ~ 40% for pure AlCl₃. The charge-ordered model also implies an obvious correlation between the maximum FSDP shift and alkali cation size - the smaller Li⁺ ion may be expected to force a lower average inter-unit distance between neighbouring tetrahedra and thus IRO on a shorter length scale, compared to the Na⁺ ion. However, although the FSDP position in 45% NaCl is at lower Q than in 50% LiCl, this is not conclusive evidence of such a correlation. The comparison needs to be made at exactly the same equimolar concentration because of the strong compositional dependence of charge ordering in these systems.

It is useful to compare these chloro-aluminate melts to other systems in which charge ordering also appears to be linked to IRO, such as molten NiCl₂-KCl near the 2/3 alkali halide concentration (see chapters 6 and 7). Although little or no shift in FSDP position was observed between pure NiCl₂ and 60% KCl + NiCl₂, given the large size of the K⁺ ion and the high temperature of the samples (640°C), this would still appear to be consistent with the suggested correlation between FSDP position and alkali cation size in the mixtures. The isotopic study of equimolar AlCl₃ + LiCl by Biggin & co-workers [8.26] indicated that $S_{Al-Cl}(Q)$ makes the main contribution to the FSDP in the total scattering, which is also likely to be true of 45% NaCl because of the similar size and shape of the feature to that in 50% LiCl. The metal-chlorine partial, $S_{Ni-Cl}(Q)$, in 60% KCl + NiCl₂ also makes the main contribution to the FSDP in the total scattering which remains as prominent as in pure NiCl₂. In contrast, the clearly diminished size, compared to pure AlCl₃, of the FSDP in the 50% LiCl and 45% NaCl mixtures suggests little enhancement of the feature in $S_{Al-Cl}(Q)$ and is consistent with there already being strong IRO in the pure salt.

8.4. Concluding remarks

From the neutron diffraction data for molten AlCl_3 , it has been possible to confirm the well-defined tetrahedral coordination of the Al^{3+} ion. However, analysis of the total pair distribution function and a review of the historical arguments casts doubt on the 'established' view of the liquid as consisting almost entirely of Al_2Cl_6 dimers. Instead, RMC modelling suggests a 'sparse network liquid' structure which gives both a quantitative fit to the data and is physically consistent. Consideration of the indirect evidence, in particular the much greater void volume in liquid AlCl_3 compared to AlBr_3 , leads the author to favour the new model over the 'established' one. The 'sparse network liquid' model appears even more plausible given the similarities in some of the physical properties of AlCl_3 and ZnCl_2 . The proposed structure for liquid AlCl_3 can be regarded as the equivalent of the ZnCl_2 'network liquid' only with much reduced connectivity (a 3:1 salt requires less anion sharing, compared with a 2:1 salt, to achieve fourfold coordination). The reduced connectivity and the strong covalent character of bonding readily suggests a sparse network structure with substantial void volume.

Compared with the divalent metal chloride - alkali chloride mixtures, the main effect of having a smaller, trivalent metal cation in $\text{AlCl}_3\text{-MCl}$ ($\text{M}=\text{Li,Na}$) melts appears to be to greatly weaken the dependence of structural modification on alkali cation type. With either type of alkali, the already well-defined local coordination of the Al^{3+} ion becomes even better ordered in the mixtures and retains its tetrahedral geometry. In addition, modelling using the pure salt partials indicates the Al^{3+} ion dominates the anion structure (hence confirming the formation of isolated AlCl_4^- units from the breakdown of larger linked species) with no clear quantitative difference with alkali cation type being discerned. The diffraction data also confirms the strong charge ordering particularly near the equimolar composition. A gradual shift in the position of the FSDP to higher Q , and a narrowing, is observed upon the addition of alkali halide up to the 50% concentration. This shift, implying a systematic reduction in the length scale of IRO, appears to be associated with the formation of a charge-ordered structure.

The above findings can be accommodated within the same simple model⁵, involving competition between two types of cation for anions and hence

⁵ It should be noted that the actual behaviour is certainly more complex than suggested by a simple physical model able to qualitatively explain the facts.

influence over their respective local structures, used to explain structural modification in divalent metal chloride - alkali chloride mixtures. In competition against the highly polarising, triply-charged Al^{3+} cation, even the small Li^+ ion can only exert limited influence on the Cl^- ions and hence on the overall anion structure. This simple model does, however, imply that the highest degree of charge ordering between well-ordered AlCl_4^- tetrahedra and alkali counter-ions would occur with the more strongly polarising Li^+ ion. Because of the strong compositional dependences exhibited by the alkali chloro-aluminate systems it has not been possible to confirm this hypothesis in the present study.

8.5 References

- [8.1] G. Torsi, G. Mamantov & G.M. Begun, 1970, *Inorg. Nucl. Chem. Lett.*, **6**, 553-560
- [8.2] L.G. Boxall, H.L. Jones & R.A. Osteryoung, 1973, *J. Electrochem. Soc.*, **120**(2), 223-231
- [8.3] S. Takahashi, K. Maruoka, N. Koura & H. Ohno, 1986, *J. Chem. Phys.*, **84**(1), 408-415
- [8.4] M. Blander, E. Bierwagen, K.G. Calkins, L.A. Curtiss, D.L Price & M.-L. Saboungi, 1992, *J. Chem. Phys.*, **97**(4), 2733-2741
- [8.5] L.A. Curtiss, 1987, *Proceedings of the Joint International Symposium on Molten Salts*, vol 87(7), *Electrochem. Soc.*, 185-194
- [8.6] E. Rytter, B.E.D. Rytter, H.A. Øye & J. Krogh-Moe, 1973, *Acta. Cryst. B*, **29**, 1541-1543
- [8.7] S. Takahashi, T. Muneta, N. Koura & H. Ohno, 1985, *J. Chem. Soc. Faraday. Trans. 2*, **81**, 319-326
- [8.8] S. Takahashi, T. Muneta, N. Koura & H. Ohno, 1985, *J. Chem. Soc. Faraday. Trans. 2*, **81**, 1107-1115
- [8.9] K.N. Semenenko & T.N. Naamova, 1964, *Russ. Journ. Inorg. Chem. (trans.)*, **9**(6), 718-722
- [8.10] R.L Harris, R.E. Wood & H.L. Ritter, 1951, *J. Am. Chem. Soc.*, **73**, 3151-3155
- [8.11] A.K. Soper, W.S. Howells & A.C. Hannon, 1989, RAL report RAL-89-046
- [8.12] A.K. Soper, ISIS, Rutherford Appleton Laboratory, Chilton, Didcot U.K.
- [8.13] V.F. Sears, 1992, *Neutron News*, **3**(3), 26-37
- [8.14] L.A. King & D.W. Seegmiller, 1971, *J. Chem. Eng. Data*, **16**, 23-26
- [8.15] R.A. Carpio, L.A. King & A.A. Fannin Jr., 1979, *J. Chem. Eng. Data*, **24**(1), 22-24
- [8.16] C.R. Boston, 1966, *J. Chem. Eng. Data*, **11**(2), 262-263
- [8.17] S. Biggin & J.E. Enderby, 1981, *J. Phys. C: Solid State Physics*, **14**, 3129
- [8.18] K.J. Palmer & N. Elliott, 1938, *J. Am. Chem. Soc.*, **60**, 1852-1857
- [8.19] D.A. Allen, R.A. Howe, N.D. Wood & W.S. Howells, 1992, *J. Phys. C: Condens. Mat.*, **4**, 1407-1418
- [8.20] A.D. Alvarenga, M.-L. Saboungi, L.A. Curtiss, M. Grimsditch & L.E. McNeil, 1994, *Mol. Phys.*, **81**(2), 409-420
- [8.21] S. Takahashi, N. Koura, M. Murase & H. Ohno, 1986, *J. Chem. Soc. Faraday. Trans. 2*, **82**, 49-60
- [8.22] M.-L. Saboungi, M.A. Howe & D.L. Price, 1993, *Mol. Phys.*, **79**(4), 847-858
- [8.23] R.L. McGreevy & M.A. Howe, 1989, *J. Phys. C: Condens. Mat.*, **1**, 9957

-
- [8.24] R.L. McGreevy & L. Pusztai, 1990, Proc. Royal. Soc. Lond. A, **430** (1878), 241-261
- [8.25] S. Biggin & J.E. Enderby, 1982, J. Phys. C: Solid State Phys., **15**, L305
- [8.26] S. Biggin, S. Cummings, J.E. Enderby & M. Blander, 1985, Proceedings of the 5th International Symposium on Molten Salts, vol. **86**, Electrochem. Soc., 81-96
- [8.27] M. Blander, 1993, private communication

Pure salt	Number density $\rho_o(\text{\AA}^{-3})$	Faber-Ziman coefficients		
		M-M	M-Cl	Cl-Cl
AlCl ₃	0.023 (200°C) ^a	0.007	0.124	0.516
NaCl	0.032 (820°C)	0.031	0.171	0.229
LiCl	0.042 (640°C)	0.009	-0.091	"
⁷ LiCl	-	0.012	-0.104	"
	σ_c (barns)	σ_s (barns)	σ_a (barns) @ 1.8 Å	
Aluminium	1.49	1.5	0.23	
Sodium	1.61	3.28	0.53	
Lithium	0.45	1.36	70.5	
⁷ Lithium	0.62	1.40	0.045	
Chlorine	11.52	16.8	33.5	

The scattering cross-sections are from Sears [8.13].

^a From King & Seegmiller [8.14].

Table 8.1. Data analysis parameters for the pure salts. The temperatures corresponding to the density figures are in brackets. The symbol M denotes the relevant metal species in the case of each pure salt.

Al ₂ Cl ₆ state	Bond lengths (Å)					Bond angles (°)	
	Al-Cl ^B	Al-Cl ^T	Al-Al	Cl ^B -Cl ^B	Cl ^T -Cl ^T	Cl ^B -Al-Cl ^B	Cl ^T -Al-Cl ^T
Vapour ^a	2.25	2.07	3.21	3.16	3.64	91.0	123.4
Quasicrystal ^b	2.29	2.08	3.26	3.21	3.64	89.1	121.8

^a From the electron diffraction measurements of Palmer and Elliott [8.18].

^b From quantum-chemical calculations [8.20].

Table 8.2. Parameters for the Al₂Cl₆ molecular structure. Cl^B and Cl^T denote the bridging and terminal chlorine atoms, respectively. The bond angles have been defined by specifying a triplet of atoms - the required angle is formed by the central atom with respect to the other two.

RMC model	Branched chains (≥ 3 atoms size)	Complex units (with loops and rings)	
		all sizes	6-10 atoms size
I	85	28	5
II	48	42	5

Table 8.3. Comparison of the results of bond network analysis (averaged over several configurations) for RMC models I and II. The complex units of 6-10 atoms size are the only ones which can be said to resemble discrete dimers. A small number (≈ 20) of branched chains of 5 atoms size, corresponding to isolated AlCl_4^- tetrahedra, are also apparent in both models.

	Peak position (\AA)	Peak height (\AA^{-1})	FWHM
AlCl_3	2.11 ± 0.02	12.5 ± 1.4	0.37 ± 0.04
% NaCl			
30	2.12 ± 0.02	16.3 ± 1.4	0.35 ± 0.04
45	2.11 ± 0.02	19.1 ± 1.0	0.28 ± 0.04
70	2.11 ± 0.02	18.5 ± 2.0	0.34 ± 0.04
% LiCl			
25	2.11 ± 0.02		
50	2.14 ± 0.02		
70	2.15 ± 0.03		

Table 8.4. Structural parameters for the Al-Cl principal peak in real space. The peak positions and FWHM values were taken directly from the $G(r)$ functions. The peak height (in $4\pi\rho_0r^2g_{\text{Al-Cl}}(r)$) for the NaCl mixtures was obtained using the $g_{\text{Al-Cl}}(r)$ partial estimated by assuming, at least up to the principal peak position, an approximately nil contribution to the total $G(r)$ from the other partials.

	% LiCl			% NaCl		
	25	50	70	30	45	70
$S_{Cl-Cl}^{AlCl_3}(Q)$	0.97 (0.9)	0.85 (0.75)	0.7 (0.56)	0.96 (0.88)	0.92 (0.79)	0.7 (0.56)
$S_{Cl-Cl}^{MCl}(Q)^a$	0.03 (0.1)	0.15 (0.25)	0.3 (0.44)	0.04 (0.12)	0.08 (0.21)	0.3 (0.44)

^a M denotes an alkali metal (M=Li, Na).

Table 8.5. Best-fit weightings of the Cl-Cl pure salt partial structures from modelling the data for the mixtures. The *ideal* weightings expected for admixtures of the pure salts are shown in brackets. Some indication of the errors in the weighting coefficients is provided by the sensitivity of the fitting process ; typically, a variation of approximately ± 0.05 in the best-fit weightings gave a 10% larger χ^2 than the minimum.

% LiCl	FSDP position (Å)	% NaCl	FSDP position (Å)
25	0.94 ± 0.03	30	1.01 ± 0.02
50	1.18 ± 0.02	45	1.10 ± 0.03
70	1.08 ± 0.02	70	1.12 ± 0.04
AlCl ₃	0.92 ± 0.02		

Table 8.6. The systematic shift in position of the FSDP.

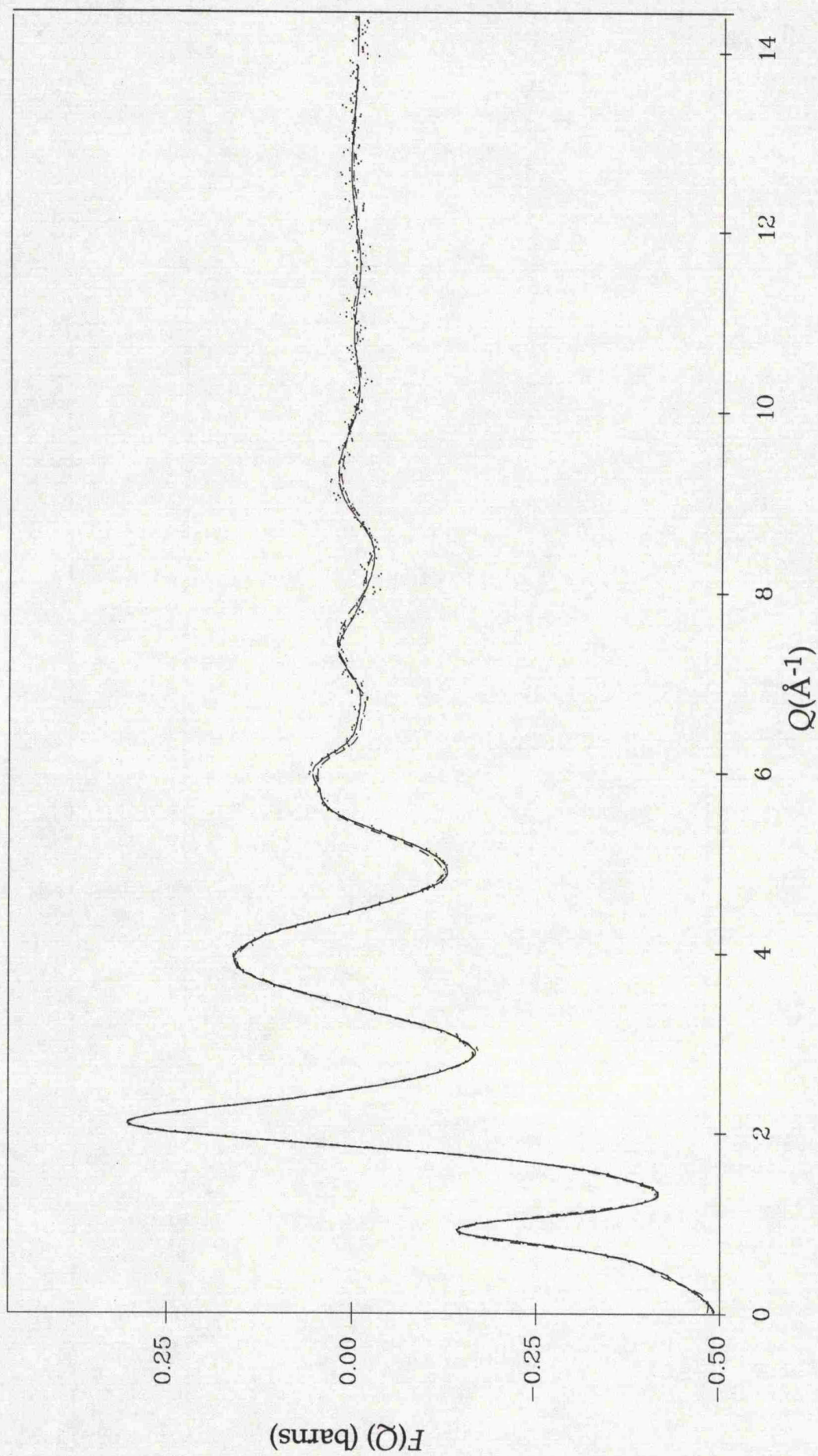


Figure 8.1. The total structure factor data (dotted curve) for pure liquid AlCl_3 compared with the function obtained by smoothing at high Q (solid) and the fit obtained using the Maximum Entropy method (dashed). Note that although only a limited data range is shown in this and other figures (for clarity), the Q_{max} actually used in Fourier transformation was typically 20-24 \AA^{-1} .

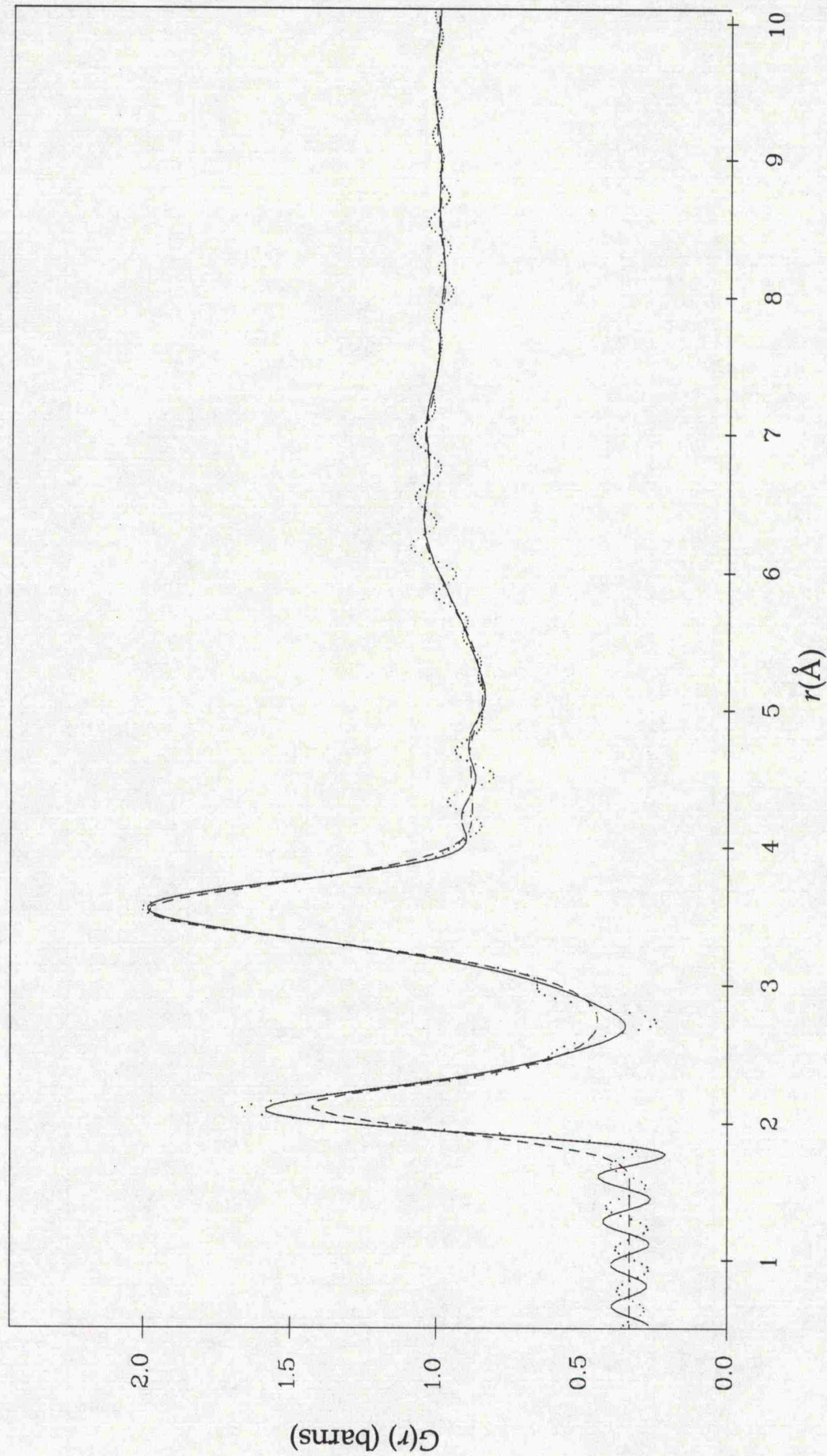


Figure 8.2. The total pair distribution functions for pure liquid AlCl_3 corresponding to the functions in figure 8.1. The $G(r)$ obtained from a smoothed $F(Q)$ (solid curve) is clearly less affected by spurious ripple than the transform of the original data (dotted). The Maximum Entropy solution (dashed) has a noticeably broader first peak but this often the case with this method although the agreement with the smoothed $F(Q)$ transform is very good at higher r .

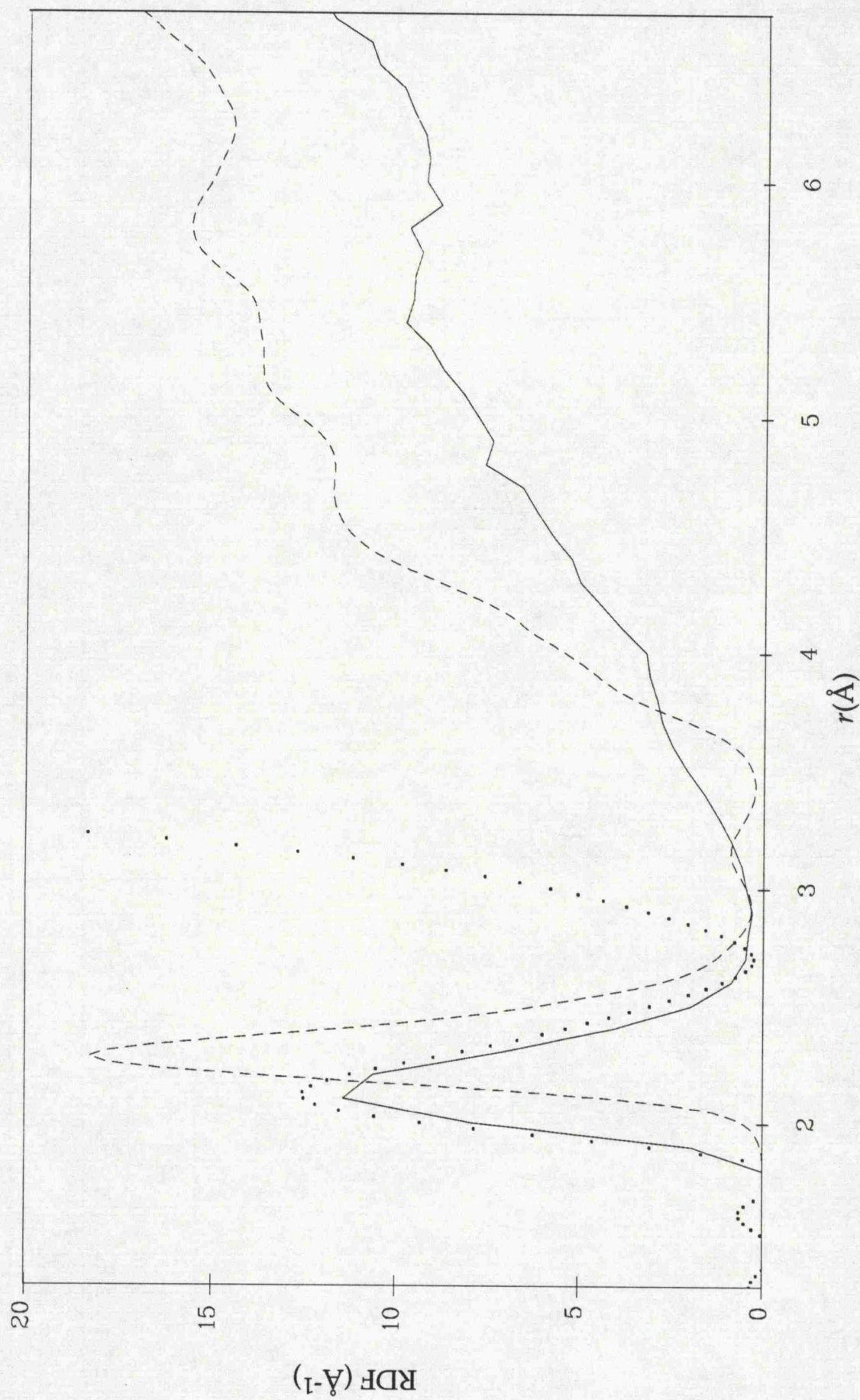
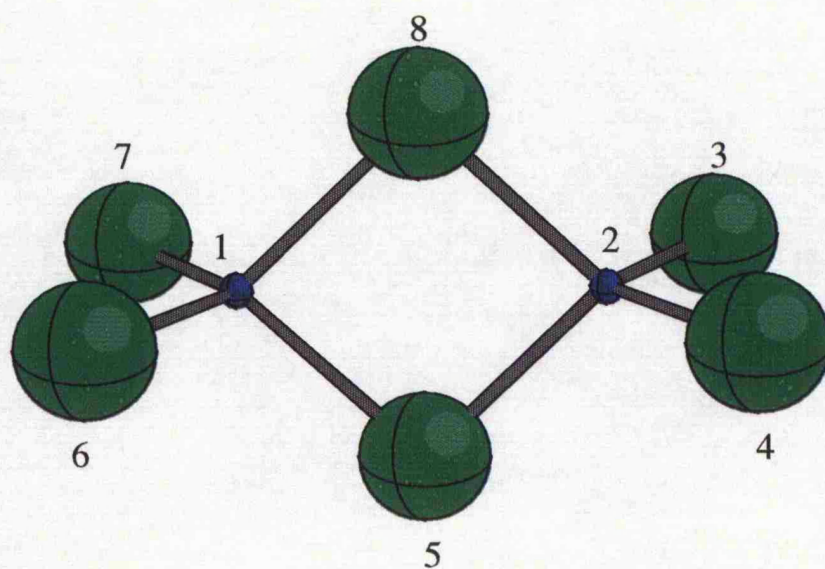
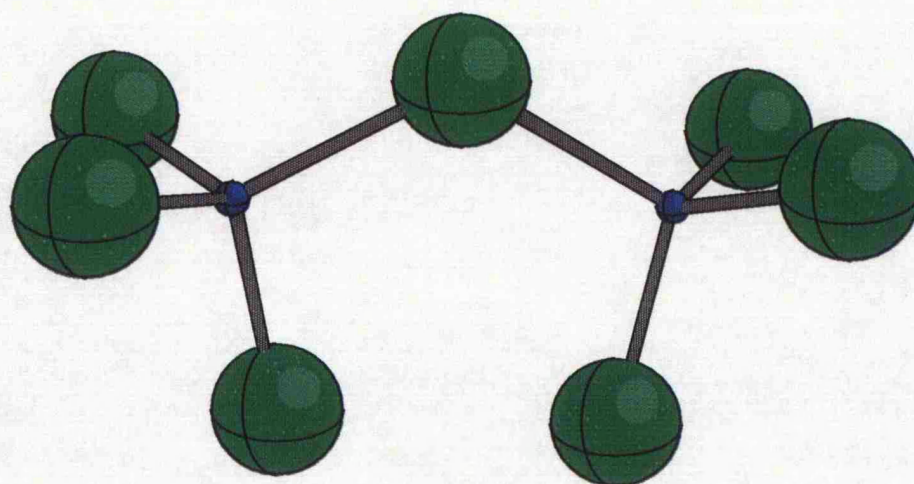


Figure 8.3. Comparison of RDFs, defined as $4\pi\rho_0 r^2 g(r)$, for $g_{Al-Cl}^{AlCl_3}(r)$ (dotted curve) and $g_{Zn-Cl}^{ZnCl_2}(r)$ [8.17] (dashed curve). The RDF for the Al-Cl function has been determined directly from the $G(r)$ data and is obviously incorrect beyond $r \sim 2.7 \text{ \AA}$. For this reason, the RDF derived from the RMC Al-Cl partial is also shown, as a solid curve.



(a)



(b)

Figure 8.4.(a) The Al_2Cl_6 molecular structure of liquid AlCl_3 as suggested by Harris *et al* [8.10] from X-ray diffraction measurement. The diagram has been drawn according to the parameters given in table 8.2, with the large chlorine and the smaller aluminium atoms shown at $1/3$ scale. The dimeric molecule consists of two edge-sharing tetrahedra distorted in the Al-Al direction such that the angles formed by atoms 8-1-5 and 8-2-5 are reduced from 109.5° to approximately 90° . (b) The Al_2Cl_7^- unit thought to predominate in acidic chloro-aluminate melts. This unit comprising two corner-sharing tetrahedra is shown in the eclipsed C_{2v} configuration although the non-eclipsed C_2 structure is more stable [8.4]. It may be thought of as a 'broken' dimer with the Al atoms able to move further apart.

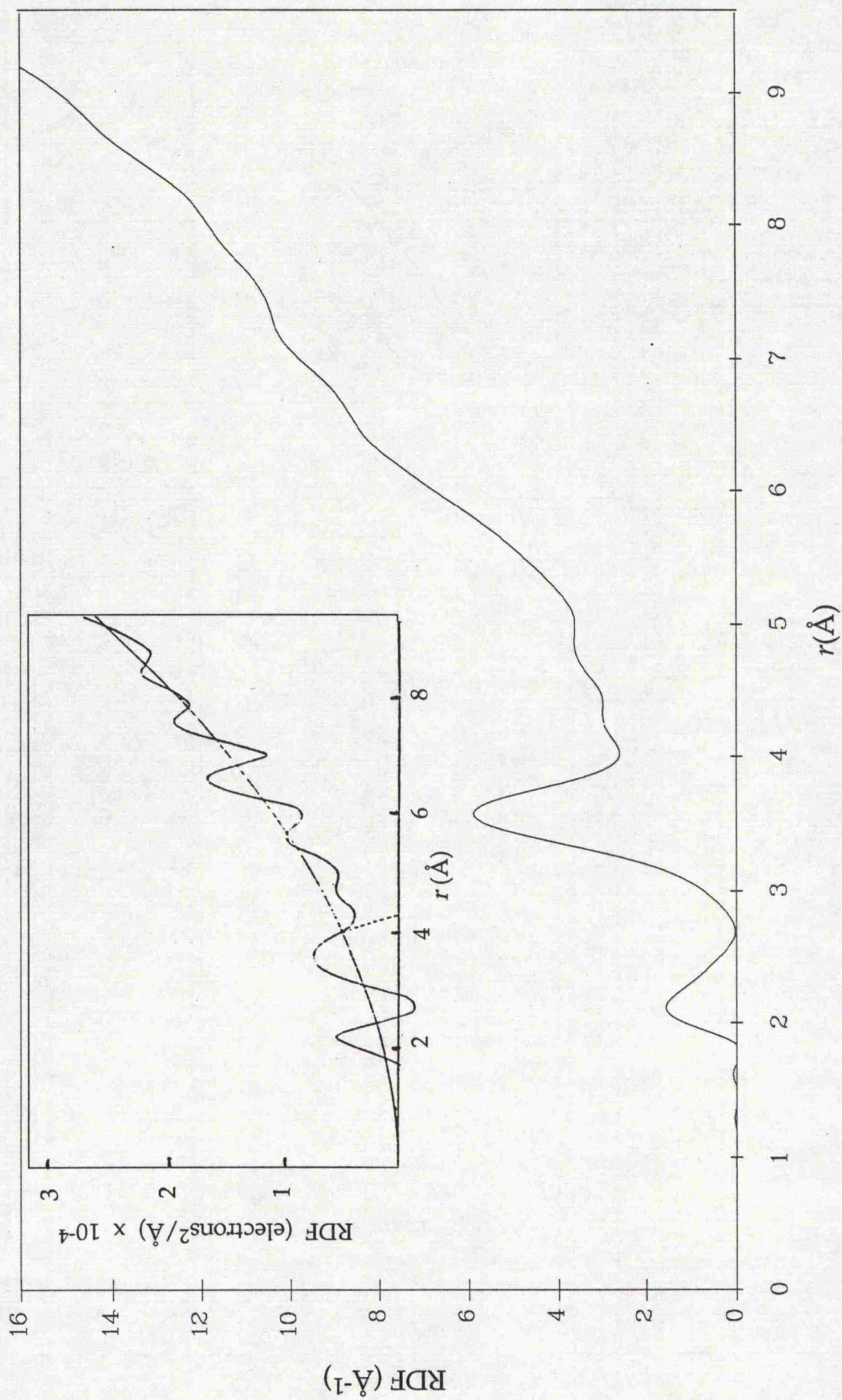


Figure 8.5. RDF ($4\pi\rho_0r^2 [G(r)-\bar{b}^2]$) from our neutron data for pure liquid AlCl_3 . Compare this to the corresponding RDF from the earlier X-ray diffraction study by harris *et al* [8.10] (inset figure).

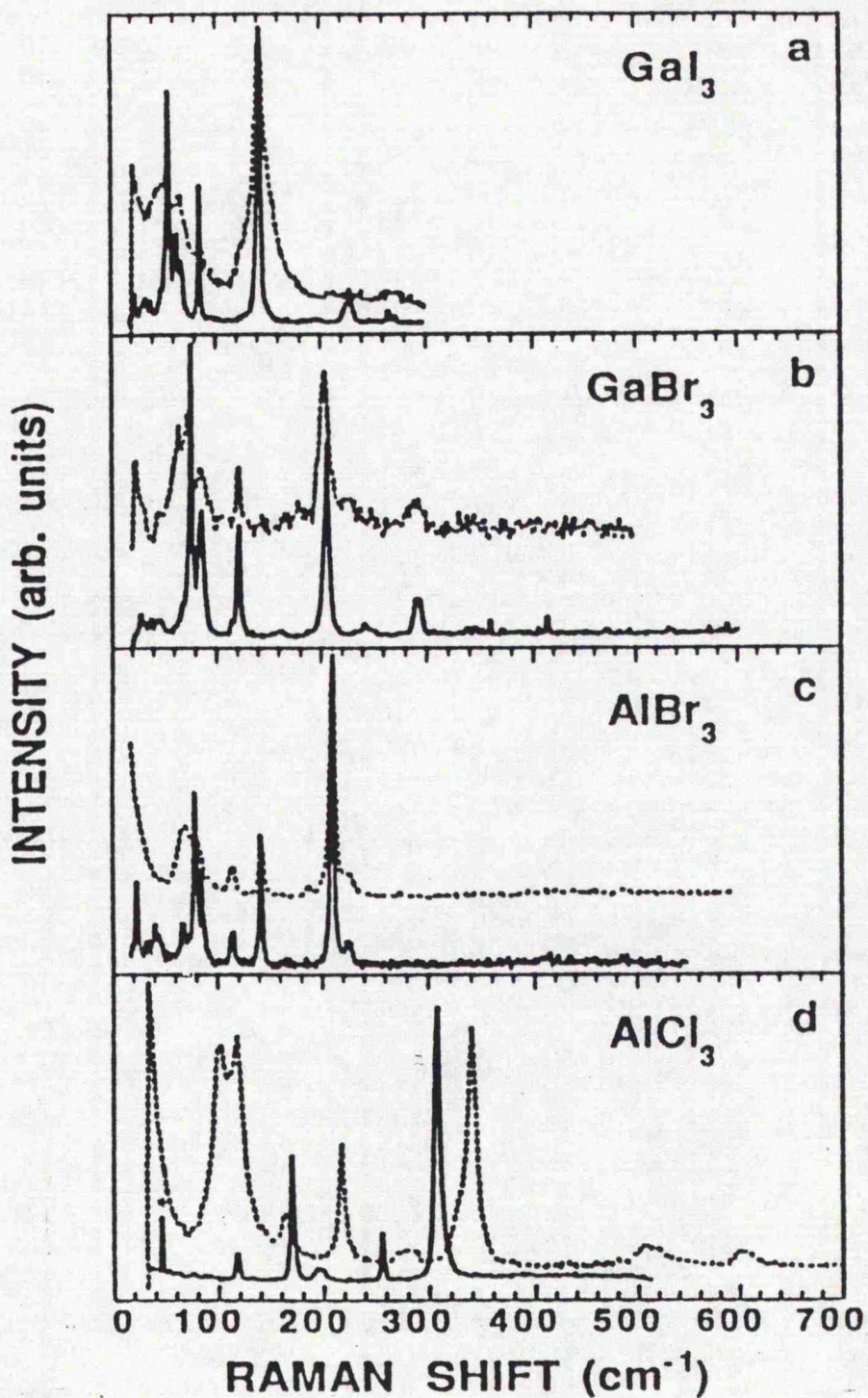


Figure 8.6. Raman spectra of GaI_3 , GaBr_3 , AlBr_3 and AlCl_3 in both the solid (solid curves) and liquid (dotted) phases. Note the similarity between solid and liquid spectra for the first three trihalides (a, b and c). In contrast, the spectra for liquid AlCl_3 differs markedly from that in the solid phase. Furthermore, the liquid AlCl_3 spectra does not seem to resemble those for liquid GaBr_3 and AlBr_3 both of which are believed to consist of molecular dimers in the solid. The figure is reproduced from Alvarenga *et al* [8.20].

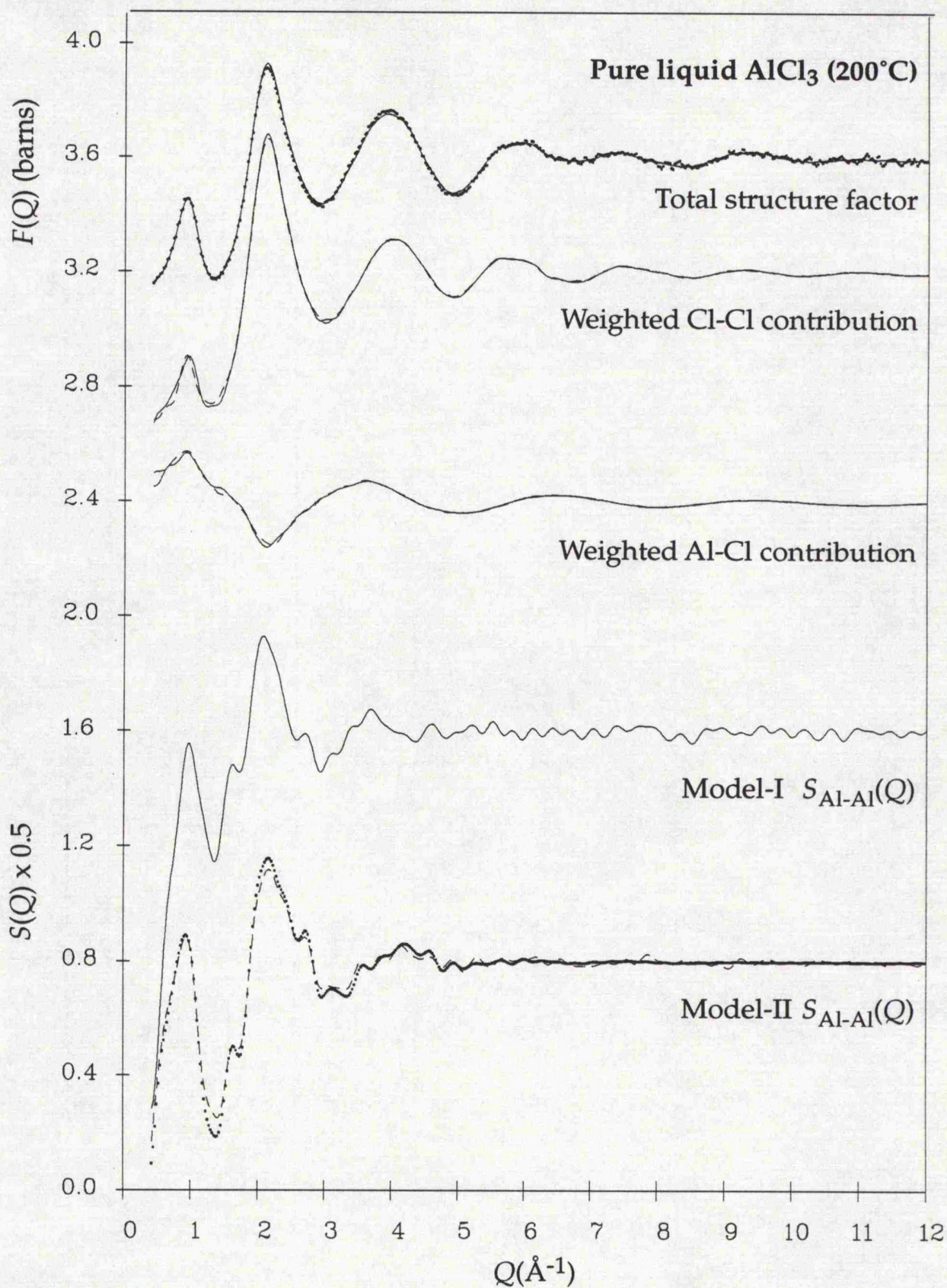


Figure 8.7. Total structure factor data for pure liquid AlCl_3 (topmost curve, dotted) compared with the RMC model fits : model I, solid curve ; model II, dashed curve. The fits to the structure factor data for both models are nearly indistinguishable and the corresponding RMC Cl-Cl and Al-Cl partial structures (shown weighted by their respective F-Z coefficients) are also little different. The RMC $S_{\text{Al-Al}}(Q)$ functions are shown scaled by 0.5 for display purposes. The artificial $S_{\text{Al-Al}}(Q)$ data-set used as an additional constraint for model II is shown as a dotted line and compared against the fit, in the bottom set of curves.

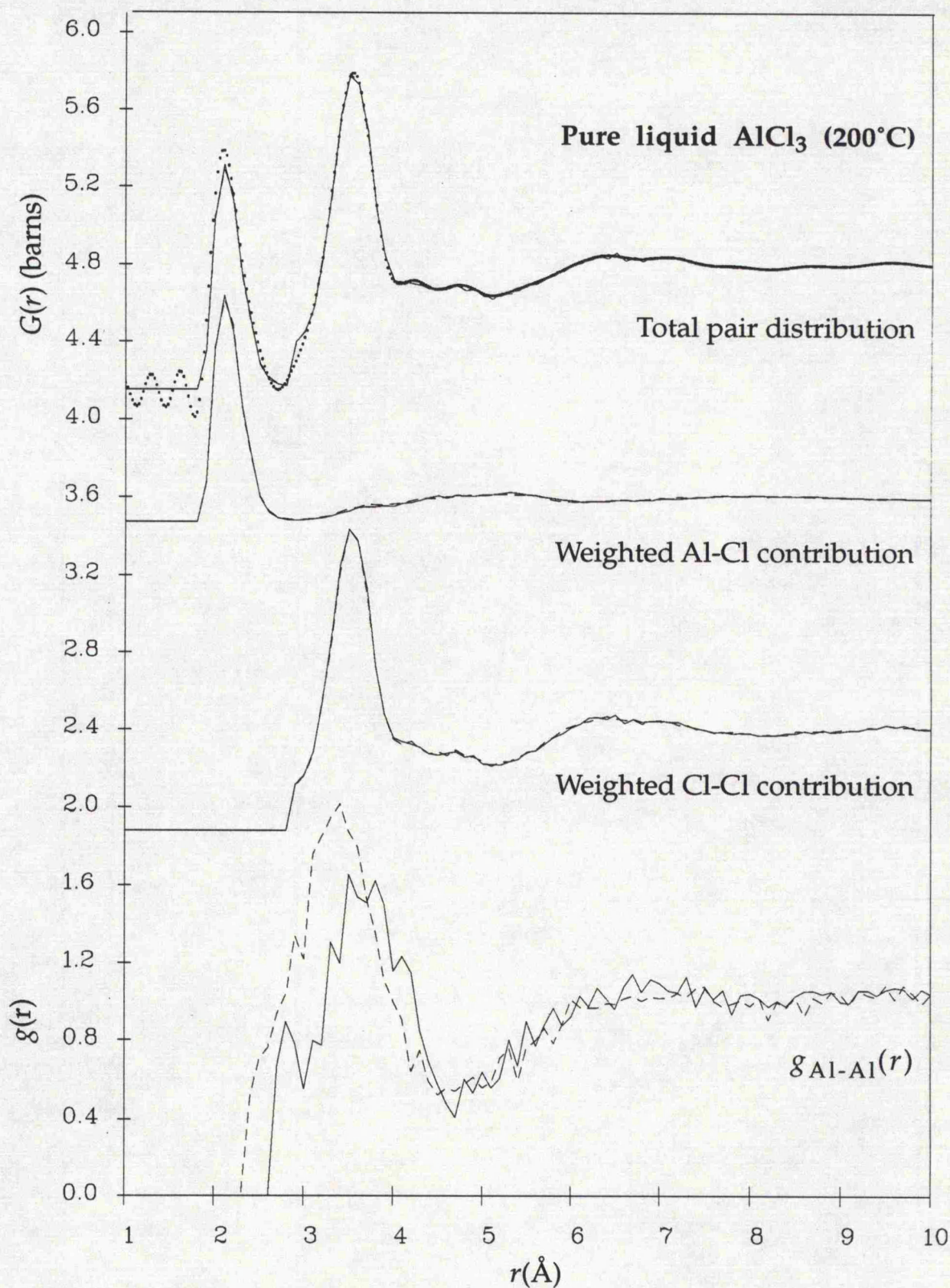


Figure 8.8. Total pair distribution function for pure liquid AlCl_3 (topmost curve, dotted) compared with the RMC model fits : model I, solid curve ; model II, dashed curve. The difference between the two models is in the position of the principal peak in the $g_{\text{Al-Al}}(r)$ partial (bottom) although the Al-Cl and Cl-Cl partial structures (shown weighted by their F-Z coefficients), and hence the fits to the total scattering, are almost indistinguishable.

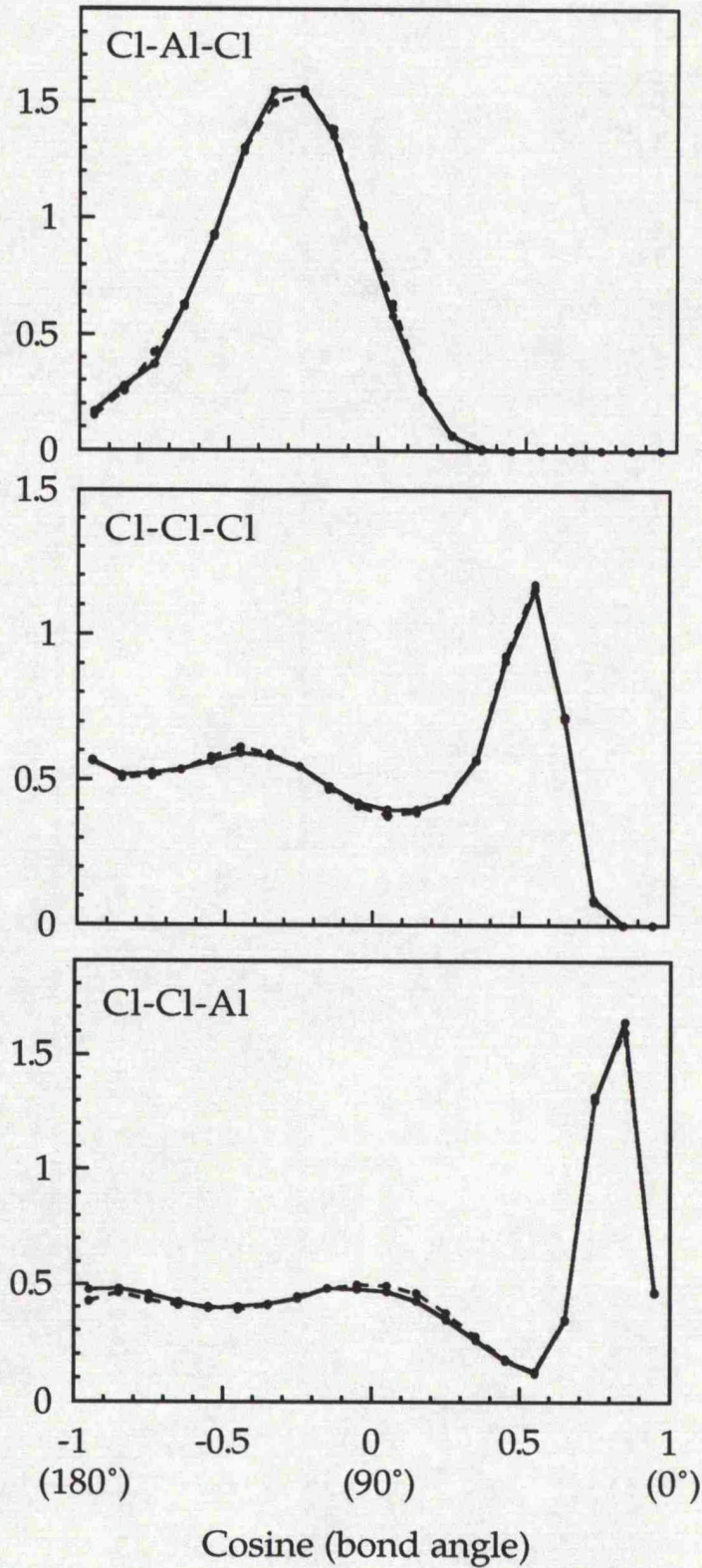


Figure 8.9. RMC bond angle distributions relevant to local structure for model I (solid curves) and model II (dashed curves).

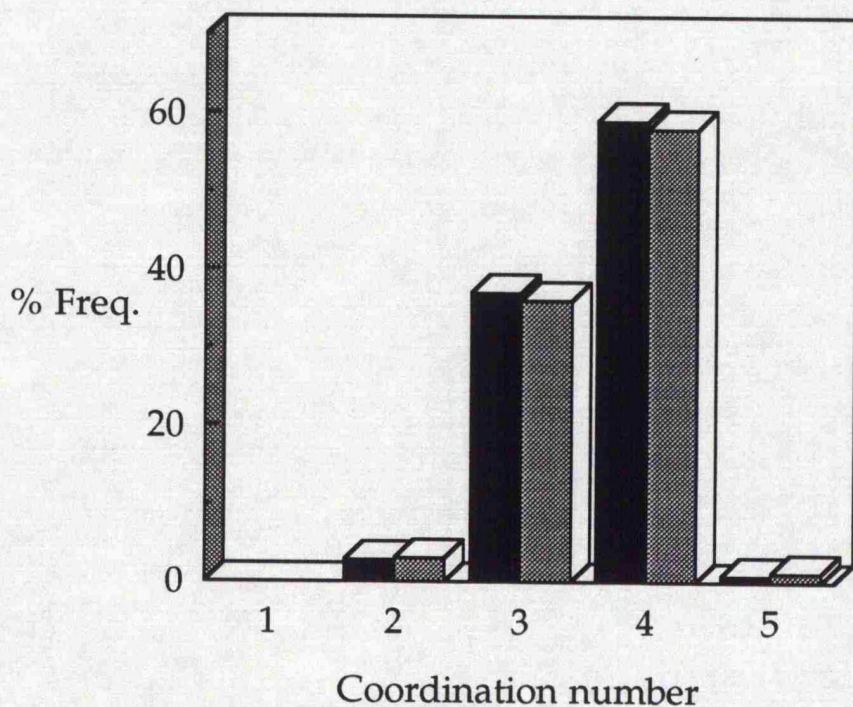


Figure 8.10. Coordination number distribution of chlorine anions around aluminium (r_{\max} of 2.8 Å) for model I (black histogram) and model II (grey). The most common coordination is fourfold and the physical constraints against coordinations greater than this are apparent from the small proportion of fivefold coordinated species.

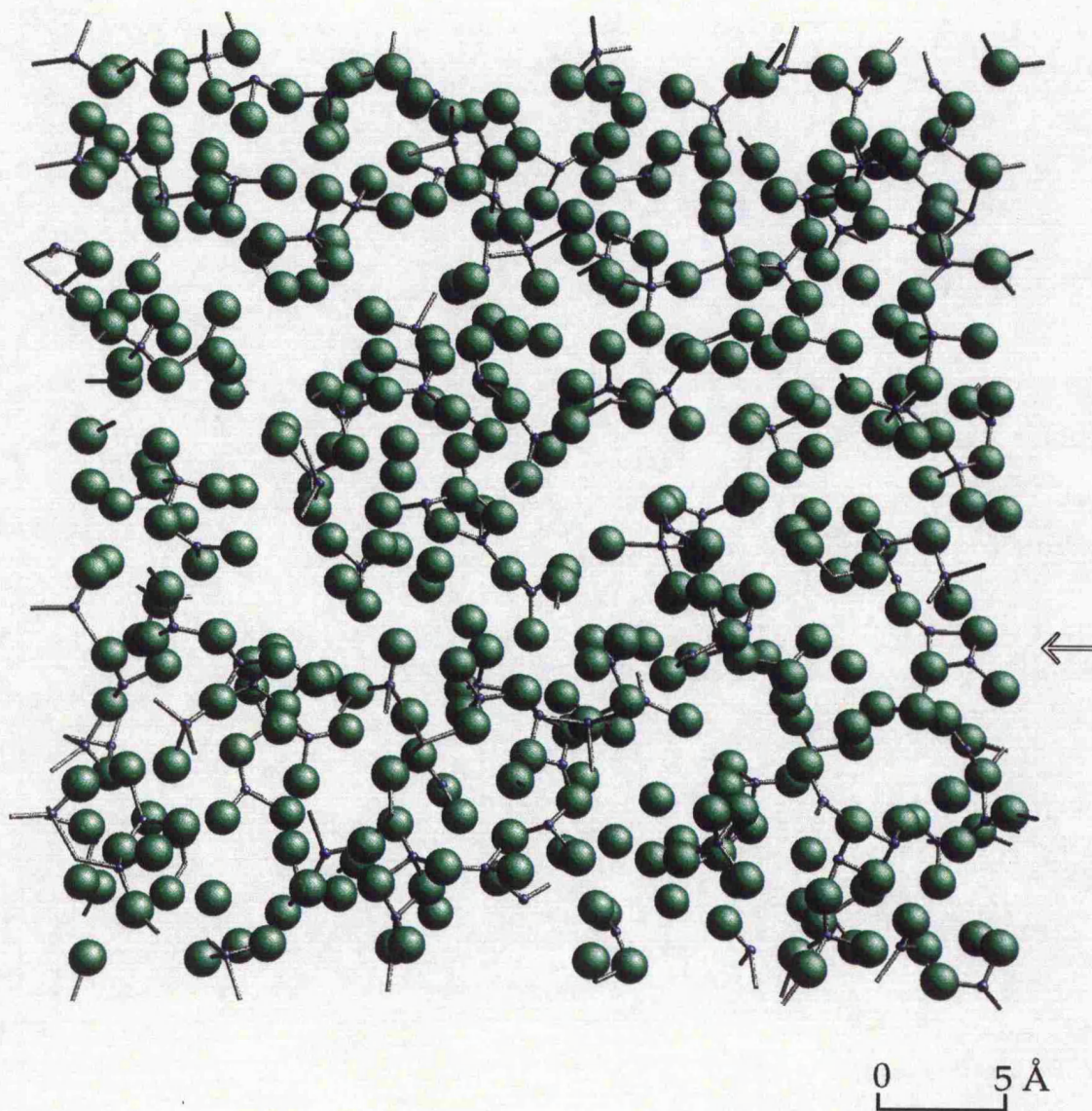


Figure 8.11. A thick (10 Å) 'slice' through the middle ([200] plane) of a model-I RMC configuration for liquid AlCl_3 . The 'slice' includes approximately 20% of all the atoms in the simulation cube. The large green spheres represent the chlorine atoms and the smaller blue ones the aluminium ; both types have their diameters scaled by 0.5 in order to allow the 'bonds' (a purely geometric definition), between all Al and Cl atoms with separations of less than $r_{\text{max}} \sim 2.8 \text{ \AA}$, to be clearly seen. However, this does have the drawback of making it difficult to appreciate the true void volume. The predominance of mainly corner-linked chains is readily apparent although a few instances of edge-sharing are visible (a specific example is indicated by the arrow).

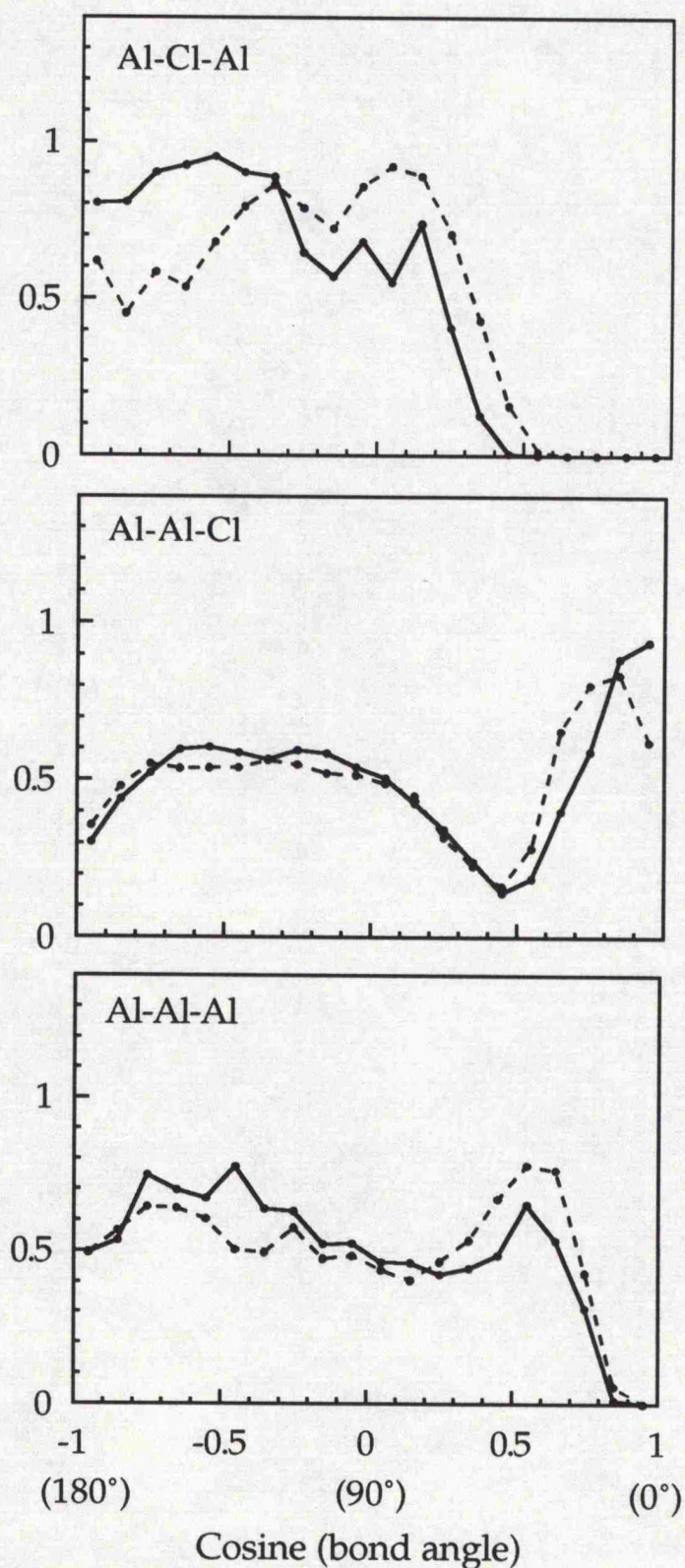


Figure 8.12. Bond angle distributions relevant to the wider structure for model I (solid curves) and model II (dashed curves). The Al-Cl-Al function shows the correlations in the bridging angle i.e. the angle formed by atoms 1-8-2 in figure 8.4(a). The bridging angle is related by simple geometry to the angle for the Al-Al-Cl function i.e. the angle formed by atoms 8-1-2 in the same figure.

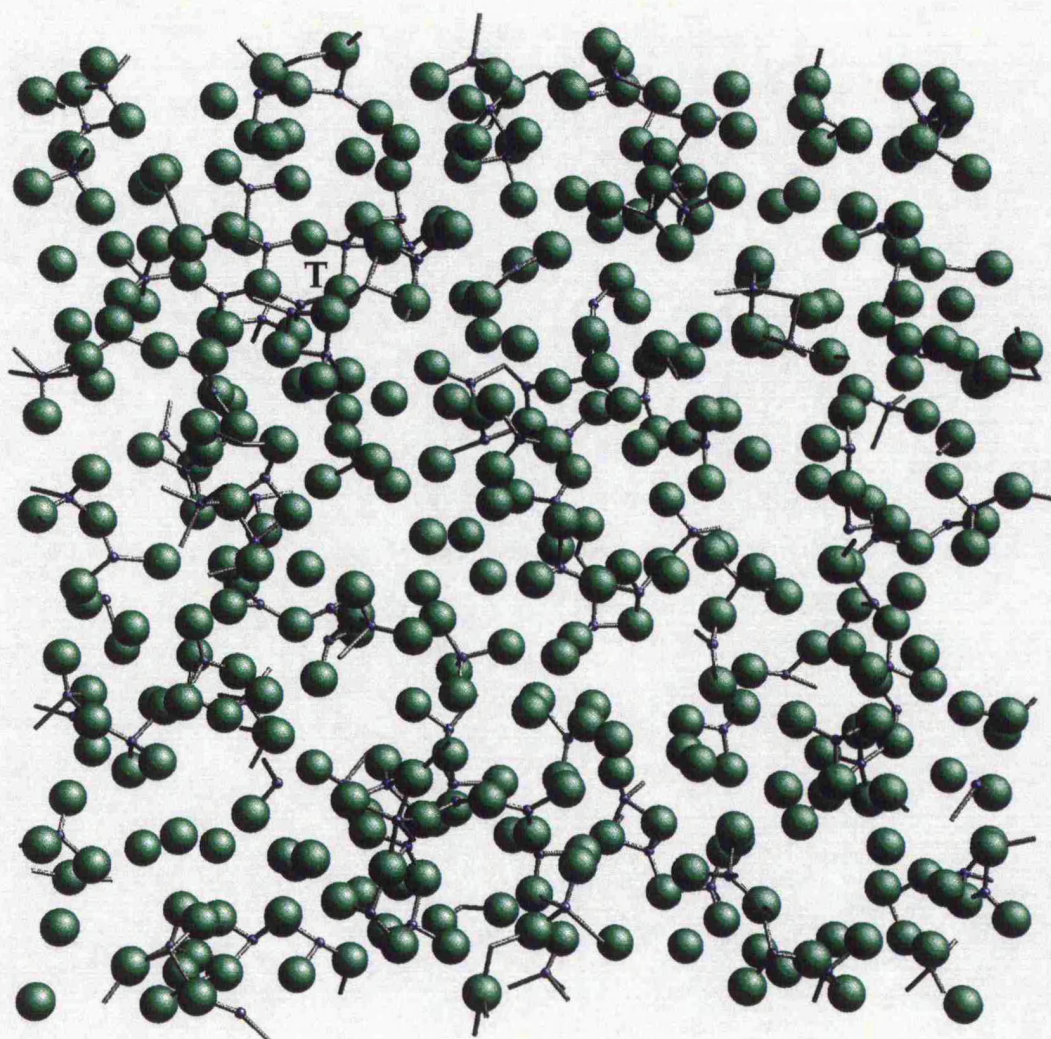


Figure 8.13. A 'slice' through a model-II RMC configuration corresponding to that for model I in figure 8.11 (same thickness, plane etc.). Although there are now clearly more instances of edge sharing, the overall impression is still of chains of mainly corner-linked, tetrahedral units. What appears to be a 'triplet' of Al atoms (forming part of a larger connected unit) is visible in the top left of the picture and is marked by the symbol 'T' in the middle of the distinctive 'triplet' loop.

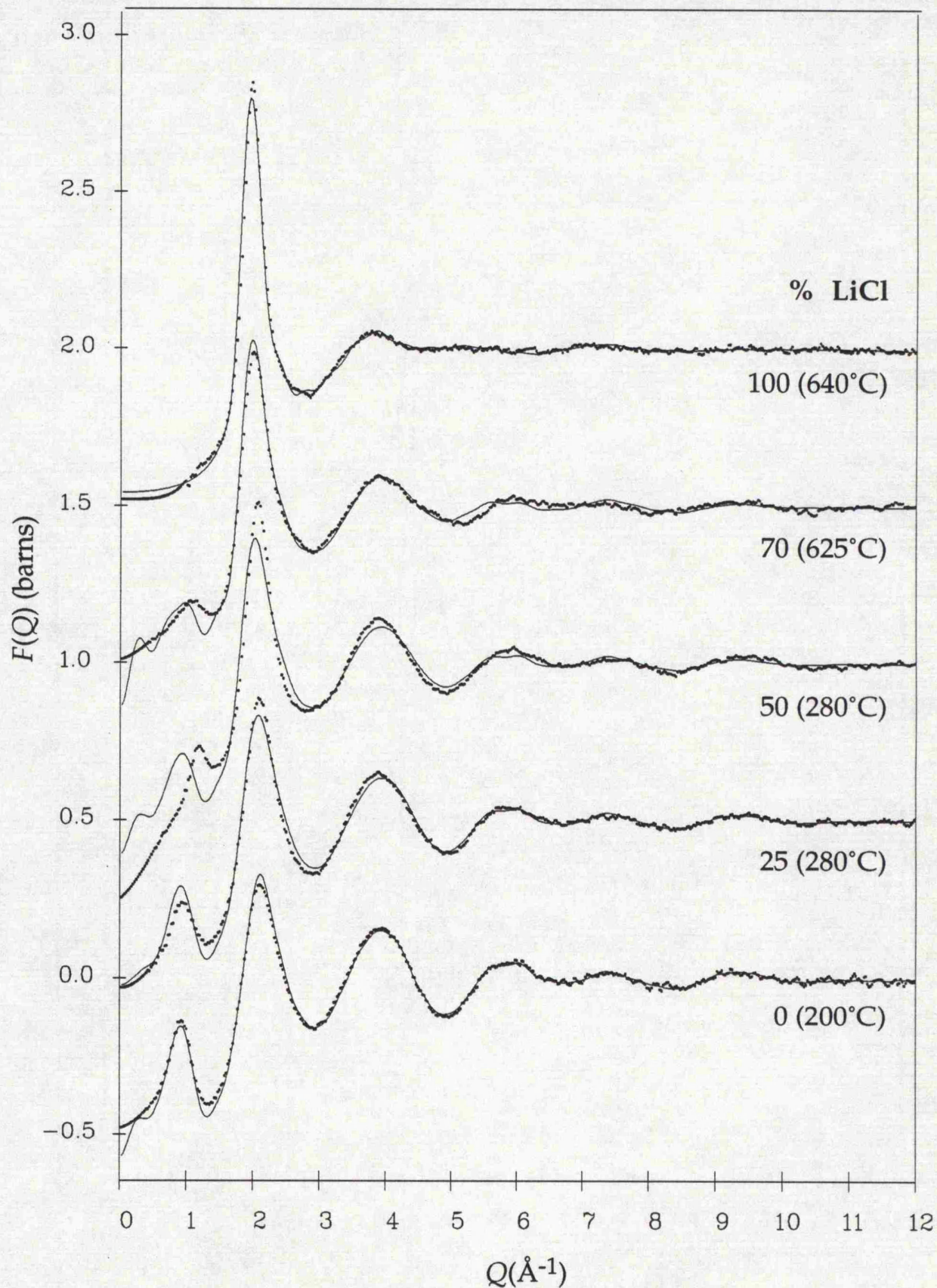


Figure 8.14. Total structure factor data (dotted curves) for the AlCl_3 - LiCl molten salt mixtures compared with model functions (solid curves) generated using the pure salt partials. The partials for pure AlCl_3 were from the RMC model-I fit to a single structure factor whereas the partials for pure LiCl were from a RMC fit to isotopic data [8.23].

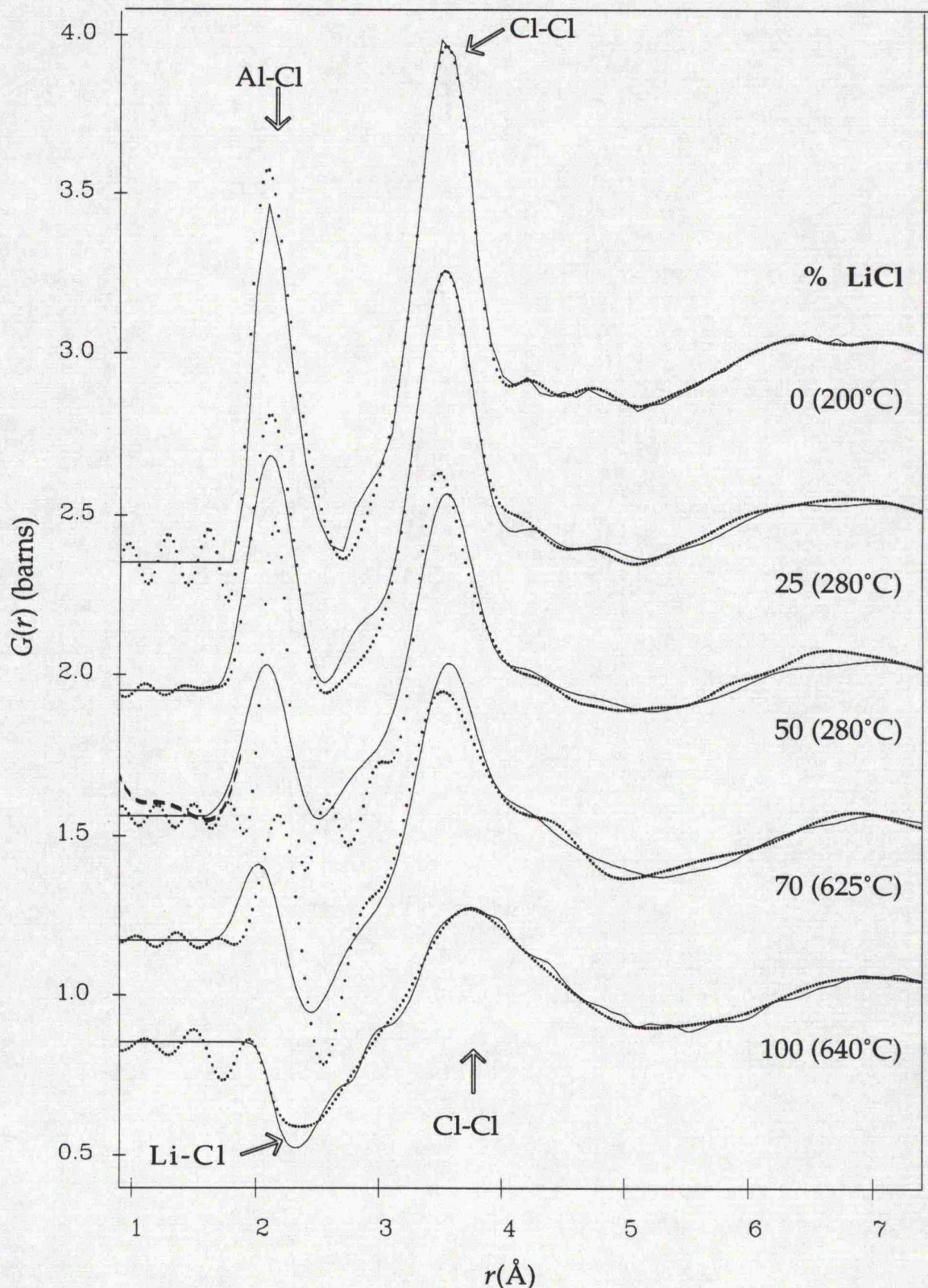


Figure 8.15. Total pair distribution functions (dotted curves) for the AlCl_3 - LiCl molten salt mixtures. The FTs of the model structure factors in figure 8.14 are shown (solid curves) for comparison. The partial structures giving rise to the main peaks in the pure salts are also indicated. In the case of 50% LiCl , the low- r portion of the FT of $F(Q)$ prior to correction for spurious slopes, is shown as a dashed line. The absence of a clear peak or trough at $r \sim 1.6 \text{ \AA}$ confirms that container subtraction was performed correctly.

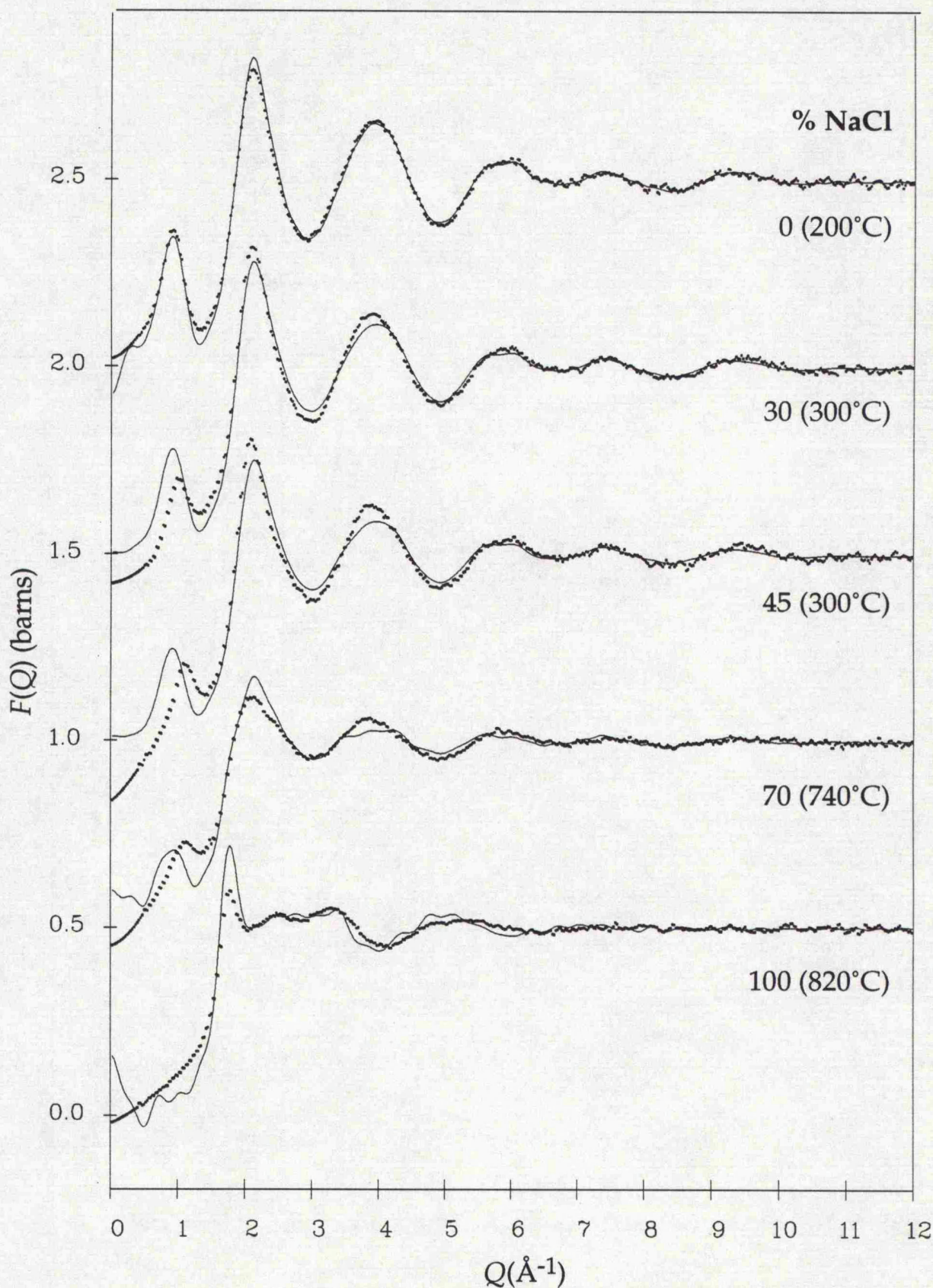


Figure 8.16. Total structure factor data (dotted curves) for $\text{AlCl}_3\text{-NaCl}$ molten salt mixtures compared with model functions (solid curves) assembled using the pure salt partials. The partials for pure NaCl are from a RMC fit [8.24] to the isotopic data of Biggin & Enderby [8.25]; there is clearly some disagreement with our total structure factor data particularly in the region of the main peak at $Q \sim 1.8 \text{ \AA}^{-1}$.

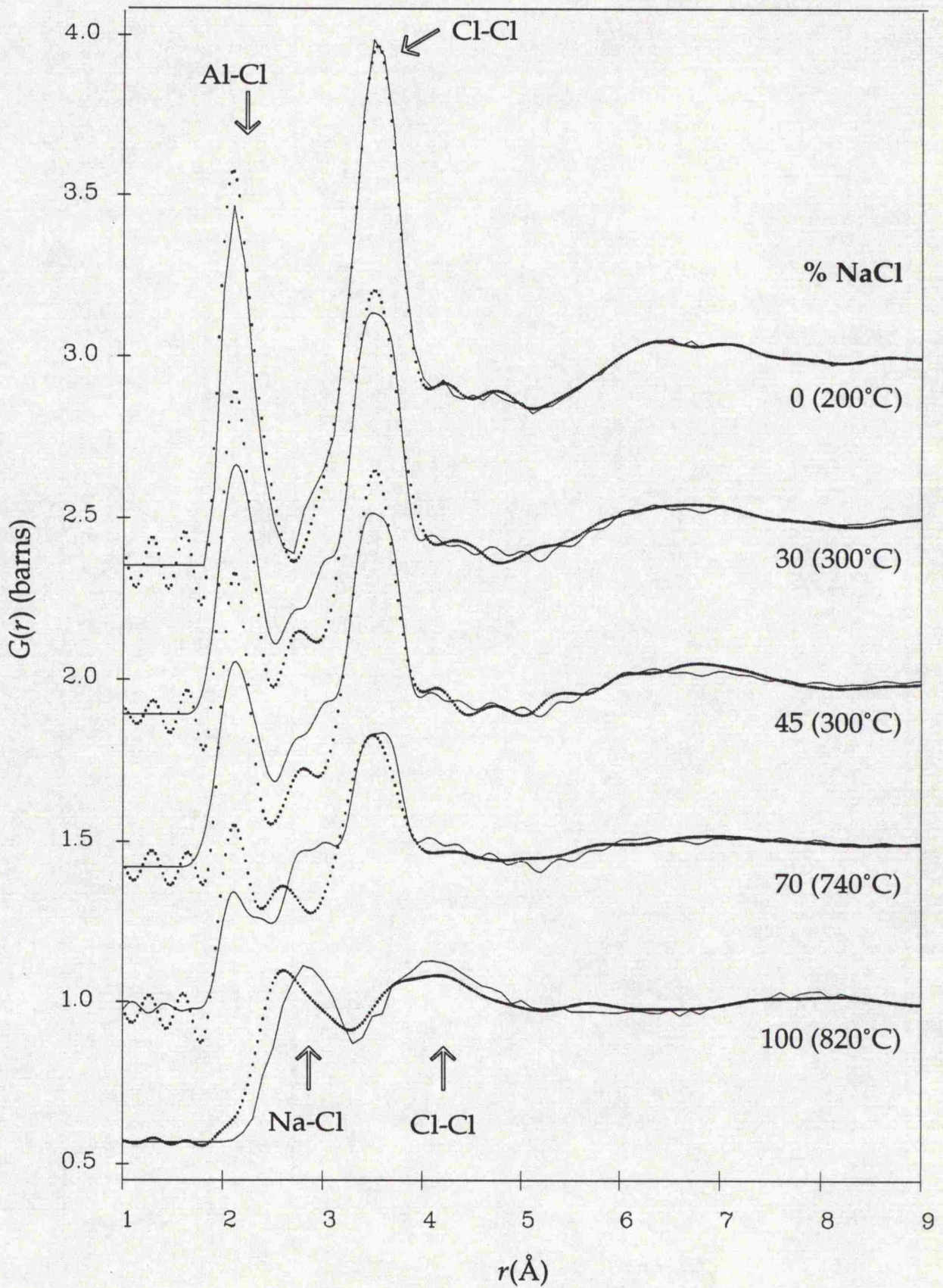


Figure 8.17. Comparison of actual (dotted curves) and model (solid curves) total pair distribution functions for the AlCl_3 - NaCl molten salt mixtures. The partial structures giving rise to the main peaks in the pure salts are indicated. The discrepancy between our $F(Q)$ for pure NaCl and that of Biggin & Enderby [8.25] is apparent in real space mainly as a difference in the Na-Cl principal peak position. Fortunately, the deviation in the region of the main Cl-Cl peak in the mixtures is small and thus has little effect on modelling of the anion structure.

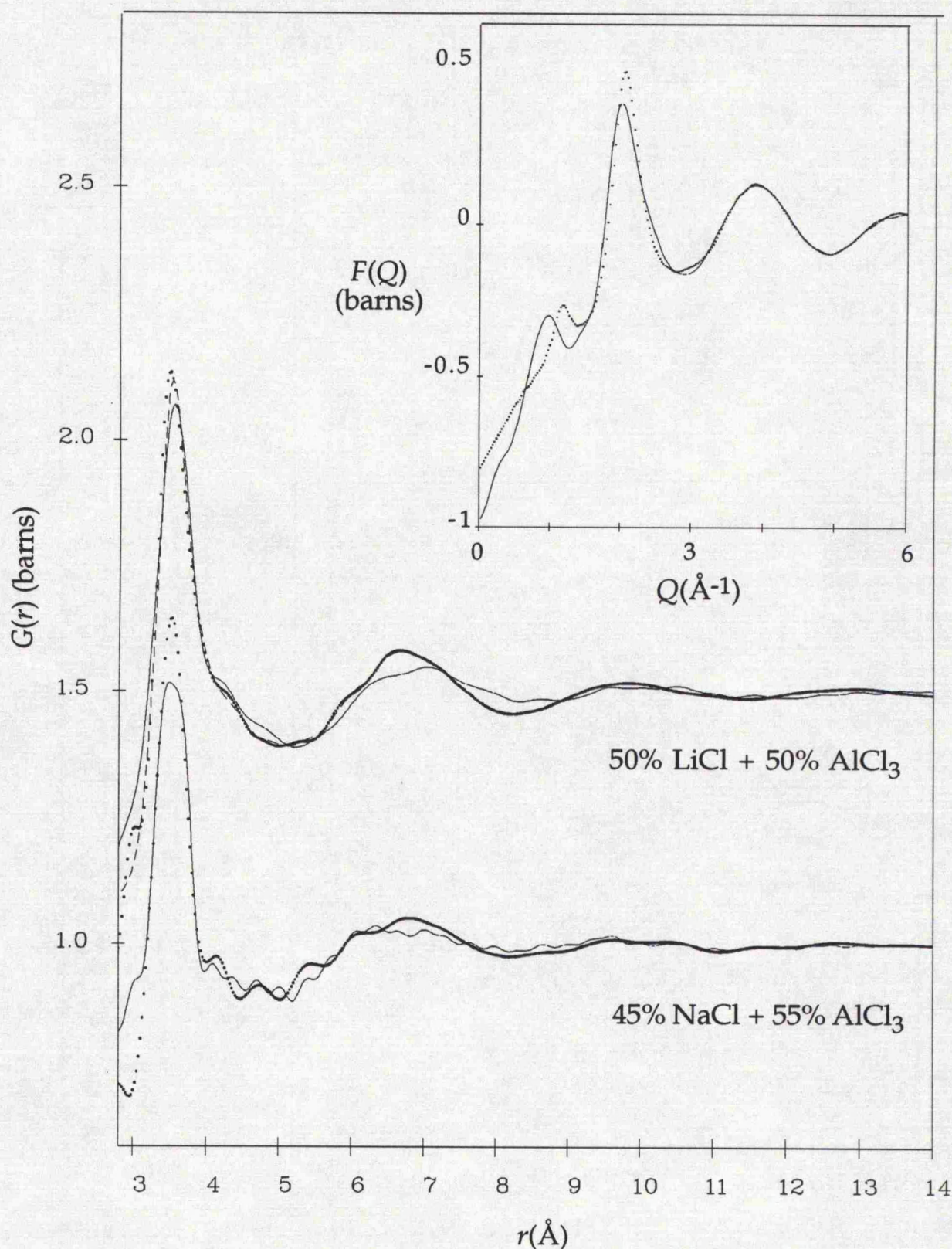


Figure 8.18. The high- r regions of the $G(r)$ data (dotted curves) for 50% LiCl and 45% NaCl mixtures compared with their respective model fits using the pure salt partials (solid curves). The Maximum Entropy solution for 50% LiCl is also shown (dashed curve) and is almost indistinguishable from the data beyond the main anion-anion peak at $r \sim 3.6$ Å. The inset figure compares the original $F(Q)$ for 50% LiCl (dotted curve) with the back-transform of the composite $G(r)$ (solid curve) formed by splicing together model ($r \geq 5.5$ Å) and data ($r \leq 5.5$ Å) real-space functions.

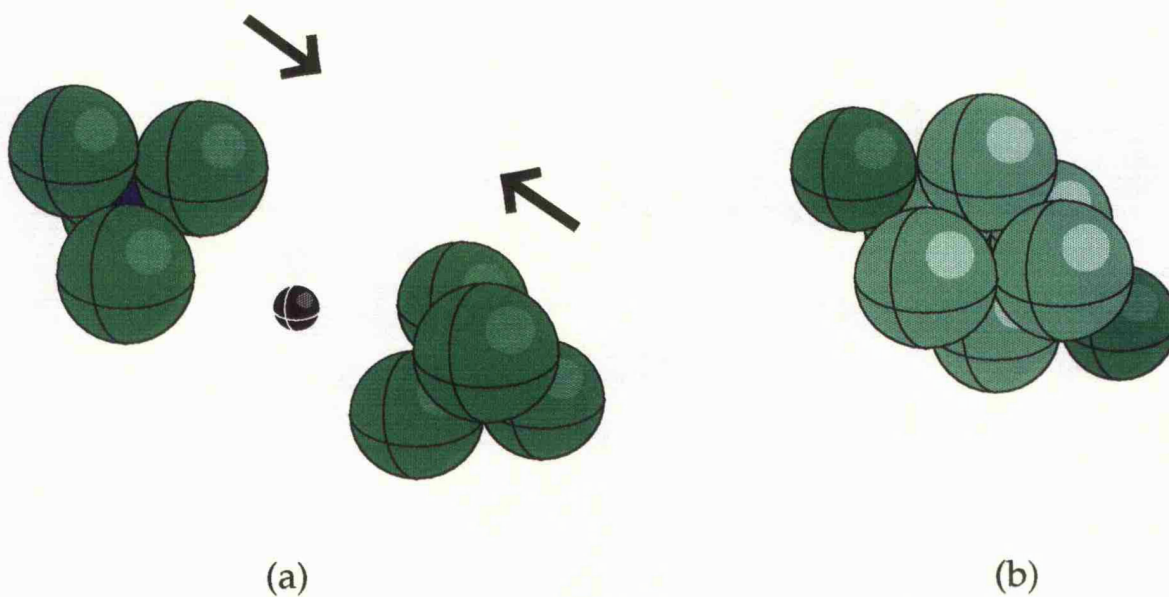


Figure 8.19. (a) The 'approach' of two neighbouring AlCl_4^- tetrahedra as a result of charge ordering by the central Li^+ cation (black), and (b) the regular octahedron resulting if the tetrahedra interlock in an AC hexagonal close-packed arrangement (the chlorine atoms forming the octahedron have been given a lighter shade of green for clarity). All atoms are shown approximately to scale.

Chapter 9

Summary and further work

9.1 Summary of main research findings

Structural modification in divalent metal chloride - alkali chloride binary molten salt mixtures has been investigated using the pulsed neutron diffraction technique. The findings of the initial composition study have been confirmed using the combined techniques of isotopic substitution and neutron diffraction on molten $\text{NiCl}_2\text{-KCl}$ and $\text{ZnCl}_2\text{-KCl}$ samples at a specific composition. In addition, a composition study of trivalent metal chloride - alkali chloride binary molten salt mixtures has been undertaken, again, using the neutron diffraction technique. In all the studies, particular attention was paid to the first sharp diffraction peak (FSDP) and intermediate range order (IRO). The reverse Monte Carlo (RMC) modelling technique has been applied to some of the data and has proved to be invaluable in extracting the maximum structural information. The use of the RMC technique has also made it possible to visualise the likely structural origin of the enhanced intermediate range order observed in the mixtures. In addition, RMC has played an important role in the reassessment of the structures of the pure molten salts, in particular that of liquid AlCl_3 .

The main research findings can be briefly summarised as :

For divalent metal chloride - alkali chloride binary molten salt mixtures ;

- a) The dependence of the degree of structural modification on the type of alkali cation. The mixtures of NiCl_2 , and ZnCl_2 , with LiCl largely appear to be admixtures of the two pure salt structures, whereas adding KCl to NiCl_2 results in a better ordered, more regularly tetrahedral local structure around the metal cation and enhancement of the FSDP.
- b) Charge ordering involving structural units and alkali counter-ions, evident near critical compositions for the mixtures with KCl , appears to be associated with the enhanced intermediate range order.
- c) The strong structural similarity between $\text{NiCl}_2\text{-KCl}$ and $\text{ZnCl}_2\text{-KCl}$ molten salt mixtures near the critical $2/3$ alkali halide concentration even though the structures of the pure divalent salts are confirmed to be dissimilar.

For trivalent metal chloride - alkali chloride binary molten salt mixtures ;

d) The resilience of the tetrahedral coordination of the small metal cation species to the addition of alkali halides.

e) The systematic change in the length scale of intermediate range order which also seems to be linked to the formation of strongly charge-ordered structures near the critical equimolar composition.

f) The lack of evidence for the 'established' model of pure liquid AlCl_3 as consisting mainly of discrete dimers. The alternative 'sparse network liquid' model, which emphasises the similarities to molten ZnCl_2 , proposed in this thesis has been shown to be a feasible RMC structure and appears more plausible considering the indirect evidence.

For details, the reader should refer to the appropriate chapter.

Whilst the work described in this thesis has undoubtedly contributed to the understanding of many features in the structural properties of molten salt mixtures, it has also shown that several issues remain unresolved, particularly regarding the precise relationship between charge ordering and IRO. The programme of further study outlined in the next section aims to address some of these outstanding issues and would also extend the study of commercially significant systems based on chloro-aluminates.

9.2 Further work : charge-ordered structures in molten salts

A programme of study is described which focuses on exploring, in further detail, the links between strongly charge-ordered structures in molten salts and intermediate range order. The suggestions for further work are summarised under five main headings.

9.2.1 *Structural modification in divalent metal chloride-alkali halide melts*

The structural study of alkali halides in divalent molten salts, largely initiated in this doctoral research, can be usefully extended. In particular, the effects of further increasing the size of alkali cation may be investigated by composition studies of ZnCl_2 - CsCl and NiCl_2 - CsCl melts. A discernible effect on the local structure of the metal cation is to be expected with such a large alkali cation (Cs^+ is similar in size to Cl^-). Current ideas suggest the weakly polarising alkali cation will lead to a weakening of the charge ordering between alkali counter-ions and tetrahedral MCl_4^{2-} ($\text{M}=\text{Zn},\text{Ni}$) units and, consequently, weaker intermediate range order in the mixtures. If a significant broadening of the FSDP is observed

for these mixtures, compared to the mixtures with KCl, then this will provide confirmation of the relationship between charge ordering and IRO. As with previous such studies, the availability of the partial structure factors for the pure salts will facilitate analysis of the data for the mixtures.

Pure molten MgCl_2 is believed to have fourfold, planar coordination of anions around the Mg^{2+} ion [9.1]. Initial studies of molten MgCl_2 -KCl mixtures suggest little change to this upon the addition of alkali halide, although difficulties were encountered in data analysis which resulted in structure factor data of relatively poor quality [9.2]. RMC modelling, however, suggests the structure of molten MgCl_2 is similar to, although not as disordered as, that of molten NiCl_2 i.e. approximately octahedral with 1-2 vacancies [9.3]. The RMC solution is more realistic and is consistent with the common crystal structure of the two salts. In view of the change in local geometry observed in the composition study of molten NiCl_2 -KCl (see chapter 6), in-depth studies of MgCl_2 -KCl and MgCl_2 -CsCl melts are proposed. Such studies are likely to shed further light on the structure of pure molten MgCl_2 . If the coordination around the Mg^{2+} ion is actually planar in the pure salt and remains so in the mixtures then this could be expected to have consequences for the charge ordering between cation-centred structural units and alkali counter-ions.

The effect of temperature on the charge-ordered structures evident at critical compositions of certain binary molten salt mixtures remains to be investigated. In this context, it would be useful to repeat the (highly successful) nickel isotopes study of molten NiCl_2 -KCl (see chapter 7) at higher temperatures. The effect of higher temperature on the FSDP in the Ni-Ni partial structure would be of particular interest.

9.2.2 Structural modification in chloro-aluminate melts

The initial studies of AlCl_3 -LiCl and AlCl_3 -NaCl molten salt mixtures described in this thesis (see chapter 8) have revealed a systematic change in the length scale of intermediate range order, which appears to be associated with the formation of strongly charge-ordered structures in these melts. By measuring total structure factors for equimolar AlCl_3 -MCl ($M=\text{Li,Na,K,Cs}$) molten salt samples, it should be possible to confirm (from the shape and position of the FSDP) the expected role of alkali cation size and polarising power upon the degree of charge ordering and associated intermediate range order. The experiment is also expected to reveal the systematic effects of alkali cation size on the tetrahedral coordination of the Al^{3+} ion. It should be noted that this will

be a difficult experiment to perform since high accuracy in composition is essential (because of the strong compositional dependences exhibited by these mixtures).

The equimolar $\text{AlCl}_3\text{-LiCl}$ mixture appears to be the most highly charge-ordered system that has been studied to date and is amenable to chlorine substitution. The availability of reliable isotopic data would make it possible to obtain, using RMC, a realistic 3-D structure in which some of the more detailed features could be unambiguously established.

Given that the degree of charge ordering in the mixtures is believed to be closely linked to the type of alkali cation, replacing these by divalent metal cations would allow the effects of ion size and polarising power to be distinguished. Hence compositional studies of $\text{AlCl}_3\text{-MCl}_2$ ($M=\text{Mg,Sr,Zn}$) molten salt mixtures are proposed. The $\text{AlCl}_3\text{-ZnCl}_2$ system is of particular interest because of the similarity in some of the thermodynamic and physical properties of the pure polyvalent molten salts as well as the similar ionicity of the metal cation species. Einarsrud and Rytter [9.4] in their infra-red reflectance study of these melts suggest, primarily on the basis of the almost equal ionicity of the metal species and (presumably) the 'established' dimers model for liquid AlCl_3 , the existence of trimeric species incorporating zinc. However, the 'sparse network liquid' model proposed in this thesis raises other possibilities. For example, at the AlCl_3 -rich end of the composition range, ZnCl_2 may be able to retain some of its pure salt structure by occupying the large voids between chains of linked AlCl_4^{2-} units.

9.2.3 *Trivalent metal halides and their mixtures*

As already noted in the summary, the thesis findings for molten AlCl_3 strongly challenge the 'established' view of the structure as consisting predominantly of discrete Al_2Cl_6 dimers and, instead, support a 'sparse network liquid' model similar to that for molten ZnCl_2 . Furthermore, the results for the $\text{AlCl}_3\text{-LiCl}$ and $\text{AlCl}_3\text{-NaCl}$ molten salt mixtures are wholly consistent with this 'sparse network liquid' model. In view of the commercial significance of chloro-aluminate systems, the structure of liquid AlCl_3 clearly merits further investigation. Accordingly, a full isotopic substitution experiment using chlorine isotopes is proposed. The availability of accurate partial structure factor data would provide a sound basis for further RMC modelling aimed at exploring the reduced range of feasible structures, and would also facilitate analysis of the molten salt mixtures proposed for study in the preceding section. However, it

must be acknowledged that obtaining reliable partial structure information, particularly about the all-important Al-Al correlation, will pose a considerable experimental challenge.

A detailed investigation of AlCl_3 is also of special interest in any attempts to determine the precise origin and nature of intermediate range order in ionic liquids. Although the FSDP is often prominent in Q -space, it is notoriously difficult to identify corresponding features in the real space transforms. Consequently, the precise structural origin of the FSDP remains controversial (see chapter 1). It has been suggested that the feature arises from the existence of low-density regions or voids in the structure [9.5]. In this regard, AlCl_3 is a good candidate for investigation because it undergoes a very large decrease in density upon melting and the resulting large void volume suggests obvious opportunities for studying void-volume effects on IRO. Hence measurements on natural enrichments of molten AlCl_3 over a range of temperatures are proposed. Sealed sample cells and the volatility of the salt will ensure that varying the temperature would also generate a wide range of pressures.

Given the diversity of melting behaviours, there is obvious interest in systematically comparing the structure of liquid AlCl_3 with that of other molten trihalides [9.6]. Hence, in order to determine the effect of increasing anion size, a diffraction study of molten AlI_3 and its mixtures with alkali iodides is proposed. The crystal structure of AlI_3 and the relatively large anion size suggests a dimers structure in the liquid is quite possible and this could be checked by RMC modelling. Diffraction data for AlI_3 taken together with that for AlCl_3 and AlBr_3 [9.7] would enable a systematic comparison of the halide series, with the size and position of the FSDP being of particular interest. In order to investigate the effects of altering the size of trivalent cation, a study of molten InCl_3 and its mixtures with alkali chlorides is suggested. Such a study would be of special interest because InCl_3 has a similar crystal structure to AlCl_3 and also exhibits a large increase in volume upon melting. Finally, in order to distinguish between the effects of cation size and polarising power, it would be useful to compare the structure of liquid GaI_3 with that of AlCl_3 since the former is almost a scaled-up version of the latter in terms of ion sizes.

9.2.4 *Thermodynamic-related studies*

AlCl_3 sublimates under normal atmospheric pressure at a temperature (180°C) which is just a few degrees below the melting point (192°C). It is conceivable that in the liquid phase just above the melting point that AlCl_3 may exhibit density

fluctuations (because of the proximity to the triple point) which might be sensitive to small changes in pressure and/or temperature. Hence additional measurements on AlCl_3 close to the melting point are proposed. The pressure can be adjusted independently of the temperature by varying the amount of blanket gas, usually argon, included when sealing off the sample at room temperature. Obviously, such a study will require a furnace with excellent thermal stability and homogeneity. A successful outcome would pave the way for a similar investigation of NiCl_2 which also sublimes before fusion. Interestingly, there is some disagreement (see chapter 6) on the size of the FSDP in molten NiCl_2 close to the melting point, which may be related to the effect of small differences in pressure so a study of this salt would seem particularly promising.

9.2.5 *Quasi-elastic and inelastic studies*

Diffraction studies of Ni-NiI_2 and Ni-NiBr_2 metal-molten salt mixtures have shown that when nickel metal is dissolved in the salts the excess nickel occupies existing vacant tetrahedral sites within an unperturbed anion structure [9.8]. Furthermore, the full isotopic substitution study of molten Ni-NiBr_2 has revealed a reduction in the ordering of the nickel species, contrary to what might be expected from the filling of vacant cation sites [9.9]. This behaviour has been attributed to a reduction of the Coulomb interaction between nickel ions, due perhaps to electronic screening, which would lead to greater ionic mobility. In order to test this hypothesis, a quasi-elastic neutron scattering study of this type of system, exploiting the unique isotopic properties of nickel, has been proposed in the past [9.10]. Unfortunately, the question of cation mobility in these tetrahedrally coordinated systems remains, as yet, unresolved although it is known that there is a correlation between fast-ion conduction in the hot solid phase and the existence of collective motions in the liquid. In view of its continuing significance, this problem clearly merits further study.

The structural relaxation and weaker charge ordering apparent in the metal-molten salt systems described above, contrasts sharply with the enhanced local structure and strong charge ordering observed for some binary molten salt mixtures. Since both types of system seem to feature prominent FSDPs, an investigation of cation mobility in strongly charge-ordered molten salt mixtures would be of interest in order to determine any relationship with enhanced IRO. Hence quasi-elastic neutron scattering studies of molten NiCl_2 -KCl mixtures are proposed. In addition, because of the possibility of phonon modes associated with the strongly charge-ordered, 'lattice-like' structure of the mixtures near the

critical $2/3$ alkali halide concentration, an inelastic study would also be worthwhile.

9.3 Concluding remarks

It has been implicitly assumed in the programme of further work discussed above, that neutron scattering methods will be adopted. This preference stems largely from the limitations imposed by the use of bulk samples (the high vapour pressures and corrosive properties of many molten salts dictates thick-walled quartz containers and hence large amounts of sample in order to achieve acceptable signal-to-noise ratios). Furthermore, neutron scattering can be combined with isotopic substitution to yield partial structure factor information.

More recently, however, the potential for using X-ray techniques has begun to attract increasing attention. Total X-ray diffraction has been successfully used to study several chloro-aluminate melts (see chapter 8) so clearly the sample containment problems arising from the use of X-rays, which are more strongly scattering and absorbing than neutrons, can be surmounted. It is also possible to exploit the different coherent scattering lengths for X-rays and neutrons to obtain information about the partial structures by combining the results of both diffraction techniques using a method such as RMC. The RMC method also provides a means of dealing with the systematic errors in the complementary techniques (for example, the absolute normalisation of neutron data is usually better than for X-rays and can be used to correct the latter). Anomalous X-ray scattering can, in principle, also provide information about partial structures but is in practise a very difficult technique to apply successfully because it requires a finely tuneable and exceptionally stable X-ray beam. Small angle neutron scattering and small angle X-ray scattering have obvious potential to be used in studying void-volume effects in liquid AlCl_3 , although excessive furnace scattering could pose a problem.

Practical problems have also limited the use of extended X-ray absorption fine structure spectroscopy (EXAFS), a chemically-specific probe of the local structure of atoms, particularly the requirement for a slab geometry which makes it difficult to contain volatile samples. Recently, Bras *et al* [9.11] have developed a new sample chamber designed for EXAFS experiments on highly corrosive liquids at high temperatures, which has been used successfully to study liquid K-Pb alloys at 600°C . However, analysis of the data using the standard EXAFS data analysis packages (e.g. EXCURV92) was not possible because of the poor signal-to-noise ratio. Instead, the data was analysed using

RMC and was shown to be consistent with the corresponding neutron diffraction data thus demonstrating that useful information on high-temperature liquids could be obtained using EXAFS.

The RMC method is generally of great benefit to the study of complex multicomponent systems such as molten salts and their mixtures. RMC makes it possible to combine the results of different experimental techniques and allows the maximum structural information to be extracted from the data (see, for example, [9.12]). Note that the full potential of using RMC to make inferences about the structure of materials (for example, by using coordination constraints) has not been exploited in the work presented in this thesis. There is also no published work on the use of RMC with interaction potentials as constraints, even though this would address the complaint that RMC solutions do not conform to thermal equilibrium and an equation of state. The continuing improvement in computation speeds will, in due course, ease the computational burden imposed by the use of such additional constraints and lead to the realisation of the full potential of RMC as a method of structural modelling.

9.4 References

- [9.1] S. Biggin, M. Gay & J.E. Enderby, 1984, *J. Phys. C: Solid State Physics*, **17**, 977
- [9.2] D.A. Allen, 1990, 'ISIS Annual Report 1990', RB1441, A86
- [9.3] R.L. McGreevy & L. Pusztai, 1990, *Proc. R. Soc. Lond. A*, **430**, 241-261
- [9.4] M.A. Einarsrud & E. Rytter, 1987, *Proceedings of the International Symposium on Molten Salts*, ed. G. Mamantov *et al*, vol. 87-7, The Electrochemical Society, Pennington, N.J.
- [9.5] S.R. Elliott, 1992, *J. Phys. : Condensed Matter*, **4**, 7661
- [9.6] M.P. Tosi, 1994, *J. Phys. : Condensed Matter*, **6**, A13-A28
- [9.7] M.-L. Saboungi, M.A. Howe & D.L. Price, 1993, *Mol. Phys.*, **79**(4), 847-858
- [9.8] D.A. Allen & R.A. Howe, 1991, *J. Phys. : Condensed Matter*, **3**, 97-110
- [9.9] D.A. Allen & R.A. Howe, 1992, *J. Phys. : Condensed Matter*, **4**, 6029-6038
- [9.10] D.A. Allen, 1989, 'A neutron diffraction study of the structure and structural modification of molten zinc halides and nickel halides', Ph.D thesis, University of Leicester, chapter 9
- [9.11] W. Bras, R. Xu, J.D. Wicks, F. van der Horst, M. Oversluizen, R.L. McGreevy & W. van der Lugt, 1994, *Nuc. Inst. Meth. Phys. Res. A*, **346**, 394-398
- [9.12] J.D. Wicks, 1993, 'Studies of disordered materials', Ph.D thesis, Oxford University (Lincoln College), chapter 10

Appendices

A1 Calculating the differential cross-section : case I

Below is the sequence of steps for calculating the differential cross-section (DCS) for the simple case of a sample in a container. The superscript *Tot* refers to the total scattering, *Sin* to single scattering, and the subscripts *s*, *c* and *b* to sample, container and background, respectively. In addition, the symbol *I* refers to normalised scattering and *M* denotes the calculated multiple scattering.

- 1) Subtract background.

$$I_{sc}^{Tot}(Q) = I_{scb}^{Tot}(Q) - I_b^{Tot}(Q)$$

$$I_c^{Tot}(Q) = I_{cb}^{Tot}(Q) - I_b^{Tot}(Q)$$

- 2) Normalise to vanadium.

$$I_{sc}^{Tot}(Q) \Rightarrow \frac{I_{sc}^{Tot}(Q)}{CAL_v(Q)}$$

$$I_c^{Tot}(Q) \Rightarrow \frac{I_c^{Tot}(Q)}{CAL_v(Q)}$$

- 3) Subtract multiple scattering.

$$I_{sc}^{Sin}(Q) = I_{sc}^{Tot}(Q) - M_{sc}(k)$$

$$I_c^{Sin}(Q) = I_c^{Tot}(Q) - M_c(k)$$

- 4) Apply attenuation corrections.

$$I_s^{Sin}(Q) = \frac{\left(I_{sc}^{Sin}(Q) - I_c^{Sin}(Q) \frac{A_{c,sc}}{A_{c,c}} \right)}{A_{s,sc}}$$

- 5) Normalise for the amount of sample.

$$DCS(Q) = \frac{I_s^{Sin}(Q)}{N_s}$$

A2 Calculating the differential cross-section : case II

Below is the modified sequence for calculating the DCS in the case of having to apply a furnace correction. The new subscript f refers to the furnace otherwise the nomenclature is as for case I (appendix A1).

- 1) Subtract background.

$$I_{scf}^{Tot}(Q) = I_{scfb}^{Tot}(Q) - I_b^{Tot}(Q)$$

$$I_{cf}^{Tot}(Q) = I_{cfb}^{Tot}(Q) - I_b^{Tot}(Q)$$

$$I_f^{Tot}(Q) = I_{fb}^{Tot}(Q) - I_b^{Tot}(Q)$$

- 2) Normalise to vanadium.

$$I_{scf}^{Tot}(Q) \Rightarrow \frac{I_{scf}^{Tot}(Q)}{CAL_v(Q)}$$

$$I_{cf}^{Tot}(Q) \Rightarrow \frac{I_{cf}^{Tot}(Q)}{CAL_v(Q)}$$

$$I_f^{Tot}(Q) \Rightarrow \frac{I_f^{Tot}(Q)}{CAL_v(Q)}$$

- 3) Subtract multiple scattering.

$$I_{scf}^{Sin}(Q) = I_{scf}^{Tot}(Q) - M_{scf}(k)$$

$$I_{cf}^{Sin}(Q) = I_{cf}^{Tot}(Q) - M_{cf}(k)$$

$$I_f^{Sin}(Q) = I_f^{Tot}(Q) - M_f(k)$$

- 4) Subtract furnace scattering (corrected for attenuation).

$$I_{sc}^{Sin}(Q) = I_{scf}^{Sin}(Q) - I_f^{Sin}(Q) \frac{A_{f,scf}}{A_{f,f}}$$

$$I_c^{Sin}(Q) = I_{cf}^{Sin}(Q) - I_f^{Sin}(Q) \frac{A_{f,cf}}{A_{f,f}}$$

P.T.O

- 5) Subtract corrected container scattering.

$$I_s^{Sin}(Q) = \frac{\left(I_{sc}^{Sin}(Q) - I_c^{Sin}(Q) \frac{A_{c,scf}}{A_{c,cf}} \right)}{A_{s,scf}}$$

- 6) Normalise for the amount of sample.

$$DCS(Q) = \frac{I_s^{Sin}(Q)}{N_s}$$

"The intellect of man is forced to choose
Perfection of the life, or of the work."

W.B. Yeats *The Choice* (*Collected Poems of W.B. Yeats*) (1933)

Via ovicipitum dura est
The way of the egghead is hard.

Adlai E. Stevenson (1900-1965), attributed